Brno 2016

Organická hmota sedimentárních hornin v naftové geologii a environmentálních vědách

Eva Geršlová

Ústav Geologických věd

MASARYKOVA UNIVERZITA

PŘÍRODOVĚDECKÁ FAKULTA

Ústav Geologických věd

Organická hmota sedimentárních hornin v naftové geologii a environmentálních vědách

Habilitační práce

Eva Geršlová

Brno 2016

Bibliografický záznam

Habilitační práce

Autor:	Mgr. Eva Geršlová, Ph.D. Přírodovědecká fakulta, Masarykova univerzita Ústav geologických věd
Název práce:	Organická hmota sedimentárních hornin v naftové geologii a environmentálních vědách
Počet stran:	201
Klíčová slova:	odraznost vitrinitu; pyrolýza RockEval; kerogen; tepelná a subsidenční historie; geochemické fosílie; polyaromatické uhlovodíky; variský orogen; mikulovské slínovce;

Eva Geršlová, Masarykova univerzita, 2016

Bibliographic Entry

Author: Mgr. Eva Geršlová, Ph.D.
Faculty of Science, Masaryk University
Ústav geologických věd
Title: Sedimentary organic matter in oil geology and environmental sciences
Number of pages: 201
Keywords: vitrinite reflectance; pyrolyses RockEval; kerogen; thermal and subsidence history; geochemical fossils; polyaromatic hydrocarbons; variscan orogeny; mikulov marls;

Eva Geršlová, Masaryk University, 2016

Poděkování

Na tomto místě bych ráda poděkovala své rodině za trpělivost a podporu, a také svým kolegům za pomoc a nekonečné odborné diskuse, bez kterých by práce nevznikla.

Obsah

Abstrakt

Předkládaná habilitační práce představuje metody studia organické hmoty sedimentárních hornin. V první části je uvedena základní terminologii oboru geochemie a hlavní metodické principy. Druhá část na příkladu tří regionálních studií dokumentuje využití metod při studiu geologického vývoje Českého masivu.

První příkladová studie autorky shrnuje výsledky hodnocení tepelné přeměny svrchně karbonských sedimentů východního okraje Českého masivu. Na základě analýzy hloubkové závislosti odraznosti vitrinitu bylo prokázáno, že dosažený stupeň tepelné přeměny odráží geologickou pozici během posledních fází variského orogenu a je dán mocností chybějících paleozoických jednotek nikoliv odlišným geotermálním gradientem. V české části hornoslezské pánve se předpokládá mocnost erodovaných jednotek v době maximálního pohřbení v závěru variského orogenu – 3 000 m v předhlubni a 1 800 m na platformě.

Jako druhá příkladová studie je uveden výzkum paleoteplotních podmínek vývoje kulmských sedimentů jihovýchodního okraje Českého masivu, kterému se autorka dlouhodobě systematicky věnovala. Současná distribuce odraznosti vitrinitu dokládá pokles tepelné přeměny kulmských sedimentů moravsko-slezské oblasti ve směru Z-V. Tepelná zralost neklesá kontinuálně, ale v oblasti Drahanské vrchoviny vykazuje skokovitý pokles. Prostorové sblížení oblastí s vysokým a nízkým stupněm teplotní přeměny je vysvětleno kontaktem zóny s tektonicky řízeným pohřbením s oblastí s původní sedimentárním sledem.

Třetí studie hodnotí sedimentární prostředí mikulovských slínovců na základě výzkumu geochemických fosilií a macerálového složení organické hmoty. Výsledky dokládají neměnné složení přítomné organické hmoty s dominantním podílem řas a kladou předpokládaný počátek ropného okna do hloubky 3 491 m.

Poslední kapitola je věnována novému vědnímu směru, který využívá znalosti klasických geologických metod, pro hodnocení kontaminace životního prostředí na příkladu Brněnské přehrady. Zde tento přístup prokázal dominantní transportní mechanismy radionuklidů, persistentních organických polutantů typu DDT a HCB, polychlorovaných bifenylů a polyaromatických uhlovodíků.

Abstract

The present habilitation thesis introduces methods used to study the sedimentary organic matter. The first part provides the basic terminology for the organic geochemistry along with the main methodological principles. The second part documents applicability of these methods in three regional evolution studies from the Bohemian Massif.

The first case study of the author summarises the results of the thermal evaluation of Upper Carboniferous sediments. The organic matter thermal maturity reflects the geological setting during the end of the Westphalian and is related to different thickness of the Palaeozoic units rather than to different thermal regime. The expected thickness of the molasses association varies between 1,800 and 3,400 m towards the west and east.

The second case study presents the research of the burial and thermal history of Lower Carboniferous siliciclastic rocks in the Rhenohercynian zone of the Variscan orogeny in Moravia, which is what the author has been dedicated to in the long-term on a systematic basis. The current distribution of vitrinite reflectance shows a decline of thermal conversion of Culm sediments of the Moravian-Silesian Zone in the W to E direction. Thermal maturity is not decreasing continuously; rather, it exhibits a stepwise/incremental decline in the region of the Drahanská vrchovina upland. The spatial approximation of the areas featuring the high and low thermal conversion degree can be explained through a contact of the zone with tectonically controlled burial with an area of original sedimentary sequence.

The third study is assessing the sedimentary environment of Mikulov marls on the basis of the microscopic study and geochemical fossils. The results show the homogenous composition of the present organic matter with a dominant proportion of algae and determine the expected onset of the crude oil window to occur at a depth of 3,491 metres.

The last section covers a new branch of science which makes use of knowledge of conventional geological methods of studies when assessing environmental contamination; here, the dam of Brněnská přehrada is discussed and the approach showed using this instance that uranium-enriched minerals form the dominant source of radionuclides in sediments. DDT and HCB were also demonstrated to be bound to the clay fraction with which the compounds enter the River Svratka through runoff to continue into the reservoir, where they are deposited. Conversely, polychlorinated biphenyls and polyaromatic hydrocarbons are not bound to the grain class and enter the dam through either runoff from the immediate vicinity or atmospheric deposition, where applicable.

1. Úvod

Předložená habilitační práce se zabývá organickou hmotou a jejím výzkumem v naftové geologii a environmentálních vědách. Organická hmota představuje spojnici mezi minulostí a současností. Biologický materiál může být inkorporován do sedimentárních hornin a zachován po miliony let. Na zemský povrch se pak dostává jednak působením přirozených geologických procesů, ale také lidskými aktivitami, např. těžbou, a opětovně tak vstupuje do biologických systémů. Tento cyklus zahrnuje široké spektrum biochemických a geochemických transformací, které jsou úzce spjaty s původem a vývojem života a rolí uhlíku v něm. První část předložené práce představuje přístupy hodnocení a studia organické hmoty v geologii. Zde jsou také uvedeny tři příkladové studie, které komplexně hodnotí paleozoické a jurské sedimenty.

Druhá část je věnována využití geologických poznatků při studiu znečištění životního prostředí. Na příkladu hodnocení kontaminace sedimentů Brněnské přehrady je prezentována přínosnost znalostí o sedimentárním prostředí, jeho dynamice a dominujícím mechanismu transportu.

2. Organická hmota v naftové geologii

Organická hmota je důležitou složkou řady hornin a patří také k podstatné složce půdy. V širším slova smyslu reprezentuje organická hmota uhlík a jeho cyklus, který tvoří jeden ze základních cyklů životního prostředí. Oxid uhličitý patří mezi hlavní formy výskytu uhlíku a je fotosyntézou transformován do biologického materiálu, ten po odumření vstupuje do sedimentárních hornin, kde může být v různé podobě zachován po miliony let. Působením rostoucí teploty a v menší míře i litostatického tlaku na organickou hmotu, dochází k strukturním a chemickým změnám při současném zachování některých biologických sekvencí. Výzkum těchto specifických organických sloučenin (tzv. *biologických markerů*) poskytuje informace o původním sedimentárním prostředí, jeho faciálním členění, dosaženém stupni tepelné přeměny, a následně také umožnuje korelaci uhlovodíkových akumulací se zdrojovými horninami (Killops & Killops 2005, Peters et al. 2005, Taylor et al. 1998, Tissot & Welte 1984).

Organickou hmotou bohaté sedimenty nebyly během geologického vývoje ukládány kontinuálně a se stejnou intenzitou. Jejich výskyt je vázán na specifické podmínky sedimentárních prostředí, jako je dostatečně vysoká biologická produkce (vyšší rostliny, fytoplankton), nízkoenergetické sedimentární prostředí a pomalá sedimentace anorganických složek doprovázená nízkou rychlostí rozkladných procesů (Killops & Killops 2005, Pedersen & Calvert 1990, Tissot & Welte 1984,). Podle Peters et al. (2005) je minimální obsah organického uhlíku (TOC) v potenciálních zdrojových horninách dán hodnotou vyšší než 0,5 hm. %. Horniny s obsahem TOC pod 0,5 hm. % jsou označovány jako chudé, interval od 0,5–2 hm. % je vyhovující, 2 hm. % a více je velmi dobré. Hodnoty TOC vyšší než 5 hm. % jsou přiřazovány roponosným břidlicím (oil shale).

V organické geochemii se termínem ***diageneze*** označují procesy probíhající po uložení a během prvních stádií pohřbení za podmínek nízkých teplot a tlaků, na rozdíl od klasického geologického pojetí, kde termín diageneze probíhá za vyšších teplot a tlaků. Během diageneze roste hloubka pohřbení a sediment prochází stádiem kompakce, dominujícím mechanismem je biologický rozklad, minimálně se projevují chemické změny a katalytické působení minerální matrix. Dochází k postupnému snižování obsahu vody a nárůstu teploty. Rostoucí teplota omezuje biologickou aktivitu a postupně dochází k rozpadu chemických vazeb. Tento proces je dominující ve fázi ***katageneze.*** Hranice mezi diagenezí a katagenezí není ostrá a jasně daná. Často je korelována s počátkem tvorby uhlovodíků a obvykle koresponduje s teplotou okolo 60 °C (Taylor et al. 1998, Tissot & Welte 1984).

2.1 Klasifikace organické hmoty

Pro určení zda daná hornina představuje potenciální zdroj uhlovodíků, ať plynných či kapalných, je důležité stanovit typ výchozí organické hmoty tzn. složení vstupujícího biologického materiálu. Na základě rozpustnosti (resp. nerozpustnosti při nízkých teplotách, do 80 °C) v organických a alkalických rozpouštědlech, je organická hmota sedimentů dělena na ***bitumen*** a ***kerogen***.

Kerogen sedimentárních hornin je v rámci tzv. van Krevelenova diagramu (obr. 1) klasifikován podle zastoupení hlavních prvků organické hmoty (vodík, uhlík a kyslík) na čtyři základní typy I-IV.

Kerogen I – dominantní složkou jsou lipidy, obvykle vzniká v jezerním, popřípadě mořském sedimentárním prostředí s nízkým obsahem kyslíku a vysokým obsahem řas (např. r. *Tasmanites*). Kerogen je méně hojný, ale tvoří řadu významných světových zdrojů ropy a roponosných břidlic, protože je nabohacen vodíkem a dosahuje atomárního poměru H/C>1,5.

Kerogen II – atomární poměr H/C je nižší než 1,5. Je více hojný než kerogen I. Původní organická hmota pochází ze směsi mořského fytoplanktonu a zooplanktonu s příměsí bakteriálních zbytků. Běžně vzniká fyzikálním mísením kerogenu I a III.

Kerogen II/III – přechodový typ, který bývá vyčleňován, tehdy když poměr H/C je vyšší než 1. Jedná se o směs terigenních a mořských uloženin v paralické sekvenci s vyšším potenciálem pro tvorbu uhlovodíků ve srovnání s klasickým kerogenem III.

Kerogen III – je specifický vysokým poměrem O/C a nízkým poměrem (nižším než 1) H/C. Původní organická hmota pochází z terestrických rostlin. Má omezenou schopnost tvořit kapalné uhlovodíky, je výchozím materiálem pro uhlí, popřípadě plyn.

Kerogen IV – je velmi ochuzen o vodík, protože pochází z oxidované a přepracované organické hmoty. Nemá téměř žádný uhlovodíkový potenciál, jedná se o tzv. mrtvý kerogen s nulovou perspektivou pro tvorbu uhlovodíků.

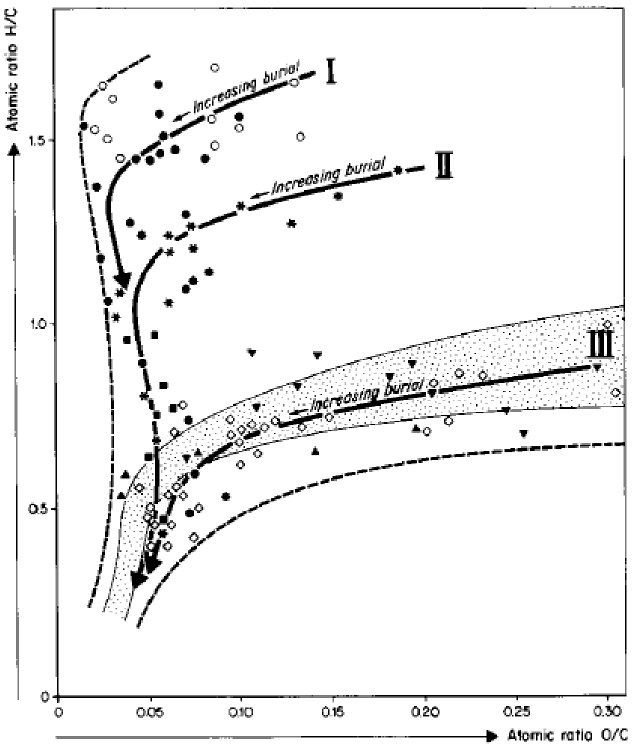

Obr. 1 Klasifikace kerogenu v pojetí van Krevelenova diagramu, O = kyslík, C = uhlík, H = vodík (Tissot & Welte 1984).

Během tepelné přeměny organické hmoty dochází ke změnám jejich chemických a fyzikálních vlastností. Tento proces lze charakterizovat jako nabohacování uhlíkem a ochuzování vodíkem. Po pohřbení do větších hloubek a teplot nedochází ke kompletní přeměně kerogenu na ropu a plyn. Obvykle jsou uváděny hodnoty kolem 50 % přeměn z celkové hmoty materiálu pro kerogen I-III (Littke & Leythaeuser 1993, Rullkötter et al. 1988).

2.2 Organická hmota jako indikátor tepelné zralosti sedimentárních pánví

Pro hodnocení hornin a jejich schopností vytvářet uhlovodíky je klíčová znalost nejen obsahu a původu organické hmoty, ale také stupeň jejich současné tepelné zralosti a průběh teplotní historie. Označení „***zralost organické hmoty***“ je v tomto pojetí chápáno jako dosažené stádium tepelné přeměny původní organické hmoty sedimentu. Je dáno společným působením teploty a času expozice (Carr 1999, Huang 1996, Burnham & Sweeney 1989). V převážné většině sedimentárních pánví je současná teplota nižší, než byla v geologické minulosti.

Nejlepší způsob rekonstrukce teplotní historie v kontextu pánevního vývoje je numerické počítačové modelování, které umožnuje přímou vizualizaci geologického vývoje a zároveň nabízí možnost srovnat měřené hodnoty s modelovými (Allen & Allen 2005, Littke et al. 2008, Příloha 1, Příloha 2). Míra spolehlivosti výsledného modelu je dána kvalitou vstupních dat a kalibračních parametrů. Informaci o maximální dosažené teplotě je možno získat pomocí metod, které hodnotí změny v organické hmotě, jílových minerálech (Příloha 3, Velde 1995), fluidních inkluzích (Samson et al. 2003), a dobu rozpadu radioaktivních minerálů – metoda fission track (Wagner & Haute 1992).

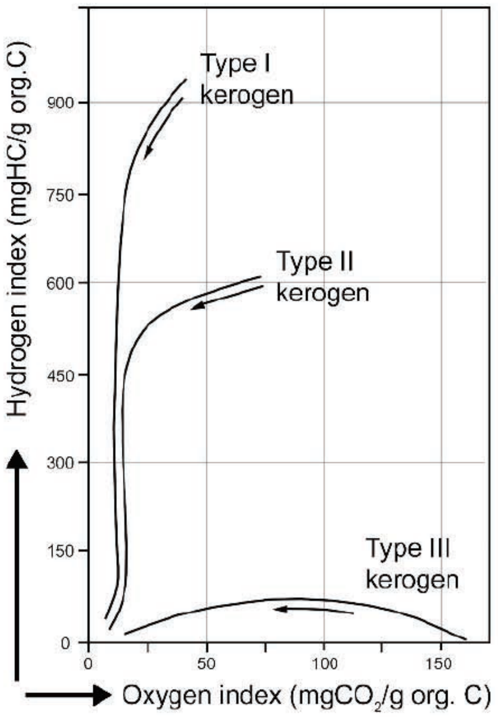

Obr. 2 Modifikovaný van Krevelenův diagram (Killops & Killops 2005).

Hodnocení organické hmoty z pohledu identifikace původního biologického materiálu je klíčové pro predikci tvorby ropy a plynu. Jako základní hodnotící parametr se používá obsah organické hmoty (TOC) v kombinaci s pyrolýzou RockEval (Behar et al. 2001, Tissot & Welte 1984). Při analýze se přítomná organická hmota rozkládá v inertní atmosféře za současného plynulého zvyšování teploty. Výsledkem stanovení je teplota maxima pyrolytické odezvy (T_{max}) a obsah volných (S1) a vázaných (S2) uhlovodíků. Odvozeným parametrem je vodíkový index (HI) vypočítaný podle vztahu HI=100*S2/TOC, který vypovídá o relativním obsahu vodíku v kerogenu a umožnujem tak základní klasifikaci kerogenu a stanovení uhlovodíkového potenciálu horniny. Vzájemný poměr HI : OI (obr. 2) bývá používán jako alternativa van Krevelenova diagramu. Srovnání indexů pyrolýzy RocEval s dalšími teplotními parametry bylo publikováno souhrnně v Peters et al. (2005) a Taylor et al. (1998).

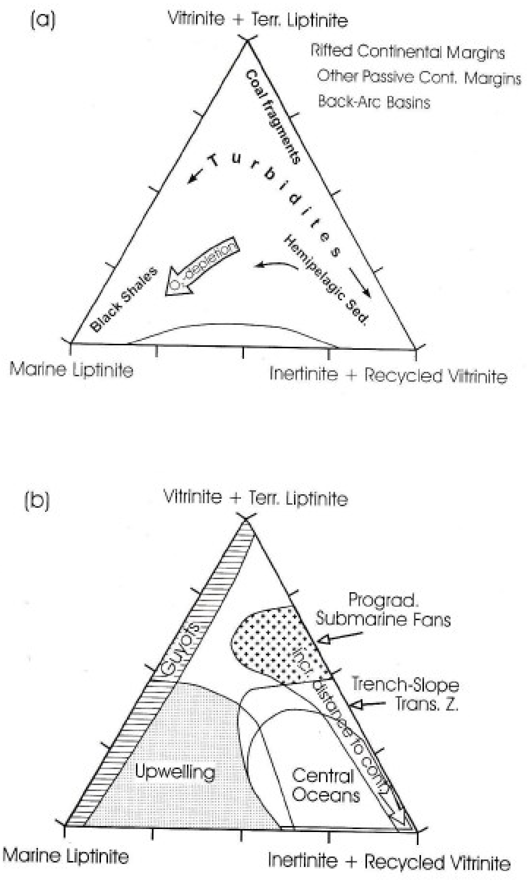

Obr. 3 Charakteristické macerálové složení organické hmoty uložené v oceánských pánvích a podél pasívních kontinentálních okrajů (a), v centrálním oceánu, guyotách, podmořském kuželu a hlubokomořských příkopů (b) podle Littke & Sachsenhofer (1994).

Klasifikace organických částic sedimentárních hornin vychází z názvosloví uhelné petrografie, kde jsou mikroskopické složky uhlí označovány termínem ***macerál***. Rozlišujeme tři základní skupiny macerálů: sk. Liptinitu, Vitrinitu a Inertinitu (Taylor et al. 1998). Jejich vzájemné zastoupení je využíváno při rekonstrukci podmínek sedimentárního prostředí (obr. 3). Vitrinit pochází z vyšších rostlin které jsou hlavní složkou uhlí, ale vyskytuje se také hojně v sedimentárních horninách. Chemické vlastnosti, barva, tvrdost, fluorescence a množství odraženého světla jsou funkcí teploty a času. Množství odraženého světla je vyjadřováno jako odraznost (% R) a tento parametr je nejčastěji využívaný paleoteplotní indikátor (obr. 4).

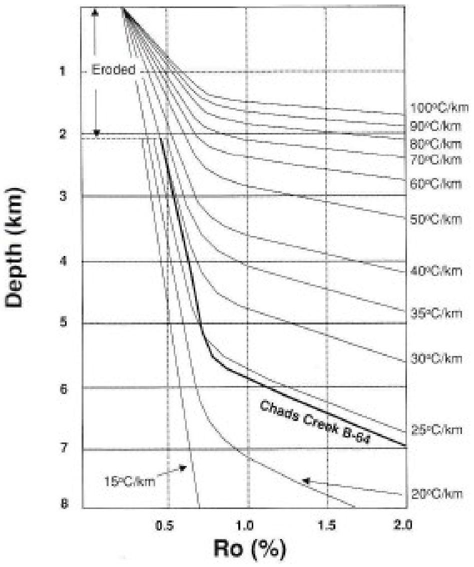

Obr. 4 Generalizovaný vztah mezi odrazností vitrinitu (% R_r), maximální hloubkou pohřbení a paloegeotermickým gradientem (Suggate 1998).

V odborné literatuře se můžeme setkat s vyjádřením „střední“ odraznost (“random” R_r) měřená v nepolarizovaném světle, „maximální“ (R_{max}) a „minimální“ (R_{min}) odraznost měřená v polarizovaném světle. Používání těchto parametrů souvisí se změnami organické hmoty v průběhu tepelné přeměny, kdy přibližně při hodnotách vyšších než 1,6 % R_r dochází ke vzniku optické anizotropie (obr. 5). Změny organické hmoty s rostoucí teplotou jsou nevratné a v nezralém stádiu nabývají hodnot v intervalu 0,2–0,5 % R_r což odpovídá rašelině, lignitu a hnědému uhlí. Ve stádiu ropného okna střední světelná odraznost nabývá hodnot 0,5–1,3 % R_r, a ve stádiu plynového okna 1,3–2 % R_r. Hodnoty střední odraznosti nad 2 % R_r odpovídají suchému plynovému oknu až antracitu (Taylor et al. 1998). V současné době je výpočet teploty z odraznosti vitrinitu založen na algoritmu publikovaném Sweeney & Burnham (1990).

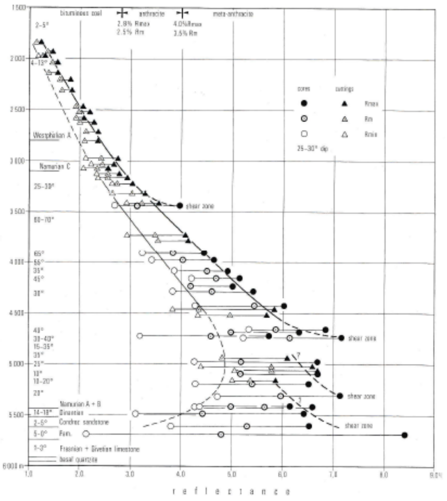

Obr. 5 Nárůst anisotropie (dvojodrazu) vitrinitu, vyjádřeného jako maximální (R_{max}) a minimální (R_{min}) odraznost ve vrtu Munsterland 1 (Teichmuller & Teichmuller 1979).

Dalšími alternativními mikroskopickými parametry tepelné zralosti jsou barva konodontů, spor, odraznost pevného bitumenu případně graptolitů. Metody jsou využívány pro stanovení tepelné zralosti hornin starších než devonských, hornin s dominujícím mořským planktonem, případně řasovým kerogenem (Goodarzi et al. 1992).

2.3 Využití organické hmoty k určení typu sedimentárního prostředí

Geochemické fosílie (biomarkery) jsou sloučeniny, které pochází z biochemických, zejména lipidních, složek dříve žijích organismů. Vyskytují se v sedimentech, horninách, ropě a vykazují žádné nebo malé změny ve své struktuře ve srovnání s původní biologickou molekulou. Určující pro výslednou skladbu přítomných biomarkerů je povaha vstupující organické hmoty a depoziční prostředí. Z těchto důvodů je na základě znalostí biomarkerů možno zpětně interpretovat podmínky během sedimentace a vlastnosti jednotky jako je např. litologie, charakter organické hmoty, množství kyslíku, stáří jednotky (obr. 6). Z pohledu chemického uspořádání rozdělujeme biomarkery na alkany a acyklické isoprenoidy, sterany a diasterany, terpany, aromatické steroidy, hopanoidy a porfyriny. Za určitých okolností mohou velké populace organismů produkovat typické diagnostické biomarkery, které umožnují korelace zdrojových hornin a ropy (Killops & Killops 2005, Peters et al. 2005, Horsfield 1997).

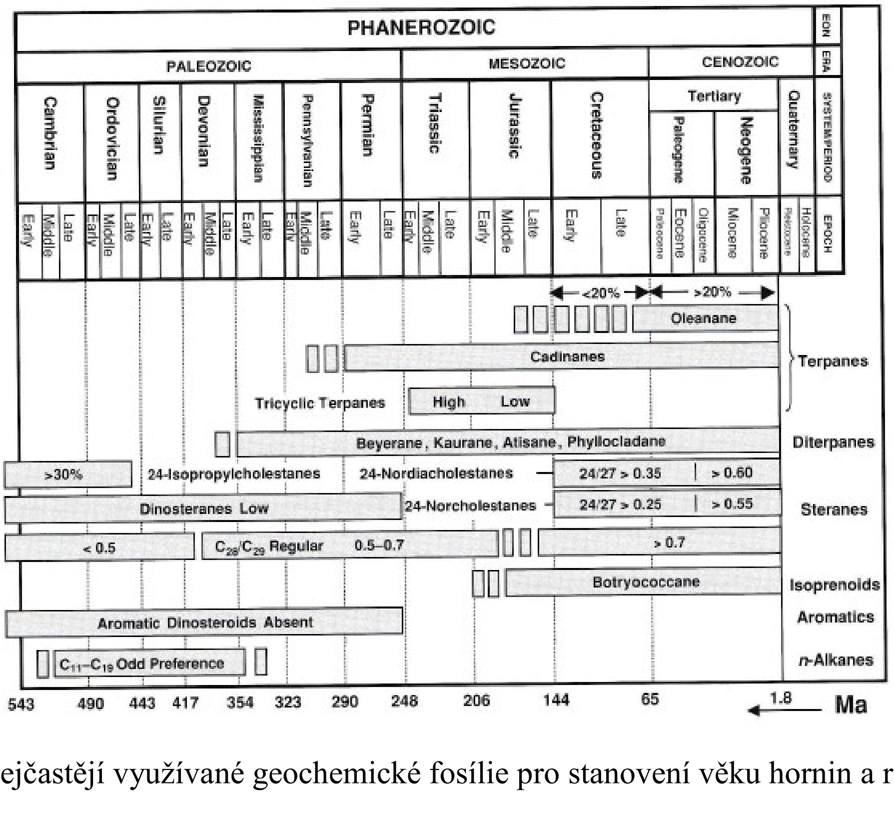

Obr. 6 Nejčastější využívané geochemické fosílie pro stanovení věku hornin a rop.

2.4 Využití organické hmoty k vyhledání uhlovodíkových akumulací

Jako podpůrný nástroj vyhledávání uhlovodíkových akumulací jsou využívány metody povrchové geochemické prospekce (Příloha 4, Abrams et al. 2004, Abrams et al. 2001). Princip geochemické prospekce vychází z konceptu, který předpokládá výstup ropy nebo plynu k povrchu a vznik tzv. „**petroleum seep**“ (Conan et al. 1996, Kross & Leytheuser 1996, Leythaeuser et al. 1983). Petroleum seeps se hojně vyskytují podél zlomových linií, násunových ploch a často doprovázejí bahení vulkány a solné pně. Analytické metody zahrnují odběr vzorků v přípovrchové zóně v systematickém odběrovém schématu. Následné laboratorní analýzy vychází z předpokladu, že přítomnost vyšších uhlovodíků vyvolává změny v zastoupení dalších složek půdy. Podle analytické metody a analytu rozlišujeme následující stanovení:

1) volných uhlovodíků v pórech půdy nebo ve vodě metodou headspace

2) uhlovodíků sorbovaných na půdní částice pomocí sorbčních materiálů

3) fluorescence vzorku metodou total scaning fluorescence (TSF)

4) přítomných bakteriálních společenství

5) stopových a radioaktivní prvků

6) karbonátů vytvořených bakteriální oxidací methanu

Geochemická data poskytují dva druhy informací: absolutní obsah (intenzitu) a vzájemné zastoupení analyzovaných složek. Intenzita signálu je kontrolována permeabilitou (propustností) migrační cesty, nasycením pórů, ložiskovým a atmosférickým tlakem. Síla signálu tedy nemusí být v přímé korelaci s velikostí ložiska a následným ekonomickým úspěchem v hodnocené oblasti. Vzájemné zastoupení složek je výrazně ovlivněno přítomností recentní organické hmoty a odlišení těchto je klíčové pro zhodnocení pravděpodobnosti výskytu zdroje uhlovodíků. Interpretace dat povrchové prospekce ale není možná bez návaznosti na geofyzikální měření, geologický vývoj a tektonickou situaci oblasti. Nejčastějším problémem je neporozumění procesům které způsobují měřené uhlovodíkové anomálie a snaha lokalizovat přesné místo výskytu ložiska pouze na základě těchto metod (Tedesco 2012, Price 1996, Schumacher 1996).

3. Případové studie využití vlastností organické hmoty

3.1 Moravskoslezské paleozoikum

Geologická stavba evropských variscid je výsledkem složitého tektonicko-sedimentárního vývoje během paleozoika (Kalvoda et al. 2008, McCann et al. 2008). Pro centrální Evropu bylo Kossmatem navrženo již v roce 1927 rozdělení na čtyři geotektonické zóny - moldanubikum, saxothuringikum, rhenohercynikum a subvariscikum. Toto rozdělení vychází z průběhu metamorfní zonality, magmatických pásů a sedimentárních facií. Navržené členění je dodržováno s malými obměnami dodnes (Littke et al. 2012, Dallmeyer et al. 1992).

Moravskoslezské paleozoikum je interpretováno jako akreční klín variského orogenu (Babek et al. 2006, Příloha 1, Grygar & Vavro 1995, Kumpera & Martinec 1995) a popisováno jako imbrikační sled k sz. upadajících tektonických šupin. Komplikovaná geologická stavba oblasti je dána šikmou kolizí mezi lugodanubickou skupinou teránů na jedné straně a subdukujicím brunovistulickým teránem na straně druhé (Kalvoda et al. 2008, Fritz & Neubauer 1995). Ohnutí orogenu na současný směr SV-JZ z orientace Z-V je široce diskutováno v odborné literatuře (Kalvoda et al. 2008, Edel et al. 2003, Tait et al. 1996, Finger & Steyer 1995). Hlavní etapa vrásnění a sešupinatění se předpokládá ve svrchním karbonu na hranici vestfál/stefan. Během posledních fází kolize došlo k přechodu z kompresního do transpresního tektonického stylu, v důsledku kterého vznikl mocný imbrikační sled na západě brunovistulického teránu (Schulmann et al. 2000, Stípská & Schulmann 1995). Ve stejném období se předpokládá i dosažení maximálních mocností v oblastech variské předhlubně (Příloha 2).

Podloží moravsko-slezského paleozoika je tvořeno katazonálně metamorfovanými horninami brunovistulika (Belka et al. 2002, Dudek 1980). Východní okraj brunovistulika je překryt mezozoickými a terciérními sedimenty Vnějších Západních Karpat (Pícha et al. 2006), na severu dosahuje brunovistulikum ke zlomové zóně Hamburg – Krakov, západní hranice je tvořena lugodanubikem (Chlupáč & Vrána 1994) a na jihu se přimyká ke krystalickým horninám Alp (Finger et al. 1993, Neubauer & Frisch 1993).

Nejstarší sedimenty oblasti jsou spodně kambrického (vrty Měnín 1, Němčičky 3 a 6; Jachowicz & Přichystal 1997) a silurského stáří (Stínava; Kettner & Remeš 1935). Sedimentace většího rozsahu je reprezentována devonskými bazálními klastiky stáří spodní až střední devon (Nehyba et al. 2001). Následná devonská sedimentace probíhala ve třech základních vývojích a to – Moravského krasu, drahanském a přechodném (Zukalová & Chlupáč 1982, Zukalová 1976). Mělkovodní sedimenty ***vývoje Moravského krasu*** jsou reprezentovány macošským souvrstvím, stáří eifel-frasn, které je děleno na tři stratigrafické členy: josefovské, lažánecké a vilémovické vápence.

Vývoj přechodný (ludmírovský) vystupuje v úzkém pruhu při východním okraji brněnského masivu (němčicko-vratíkovský pruh) a v konicko-mladečském pruhu a začíná sledem bazálních klastik které přechází do stínavsko-chabičovského souvrství a následně do ponikevského souvrství.

Vývoj pánevní (drahanský) začíná sedimentací bazálního klastického souvrství, pokračuje sedimentací převážně prachovitého stínavsko-chabičovského souvrství s polohami bazických vulkanitů. Nadložní jesenecké vápence (eifel-tournai) obsahují také polohy vulkanitů a ve svrchní části se laterálně zastupují s ponikevským souvrstvím (famen – tournai) tvořeným převážně břidlicemi s radiolarity (Přichystal 1993, Chlupáč 1959).

V oblasti Drahanské vrchoviny jsou ve svrchním visé vyčleňovány siliciklastické sedimenty kulmu, ke kterým náleží **protivanovské** souvrství, jenž se na východě tektonicky stýká s **rozstáňským** souvrstvím tvořeným na severu převážně břidlicemi a na jihu břidlicemi a drobami. Nejmladší jednotkou kulmu je **myslejovické** souvrství, tvořené břidlicemi, drobami a na jihu račickými a lulečskými slepenci.

V oblasti Nízkého Jeseníku jsou vyčleňovány **andělskohorské** souvrství, s pravidelným střídáním drob a prachovců s polohami slepenců, které přechází do **hornobenešovského** souvrství, které je považováno za ekvivalent protivanovského souvrství. Následující **moravické** souvrství reprezentuje turbidity a bývá korelováno s myslejovickým souvrstvím. Sedimentace je zakončena **hradecko-kyjovickým** souvrstvím, ve kterém převažují droby, jenž přechází do prachovito-jílovitých rytmitů (Dvořák 1994).

Kulmská sedimentace plynule přechází do paralické uhlonosné molasy, která představuje sedimentární výplň hornoslezské pánve (HP). HP představuje jednu z nejvýznamnějších pánví evropských variscid. Doposud známý rozsah byl zdokumentován na více než 7 000 km^2, z čehož cca 1 550 km^2 leží na území ČR (Dopita et al. 1997). Původní rozsah pánve byl podstatně větší (obr. 7), zejména s ohledem na předpokládanou vazbu na svrchnokarbonské sedimenty jižní Moravy (Opletal & FiIák 2013). Nedořešenou otázkou je také pokračování výplně HP jižním a jihovýchodním směrem pod vněkarpatské příkrovy. Rozšíření svrchnokarbonských uhlonosných sedimentů je zde známo pouze na základě výsledků několika hlubokých vrtů (Jablůnka1, Tyra, Jablunkov1). Západní vymezení uhlonosné výplně je erozní a probíhá v linii Poruba – Nový Jičín – Valašské Meziříčí (Ptáček et al. 2012).

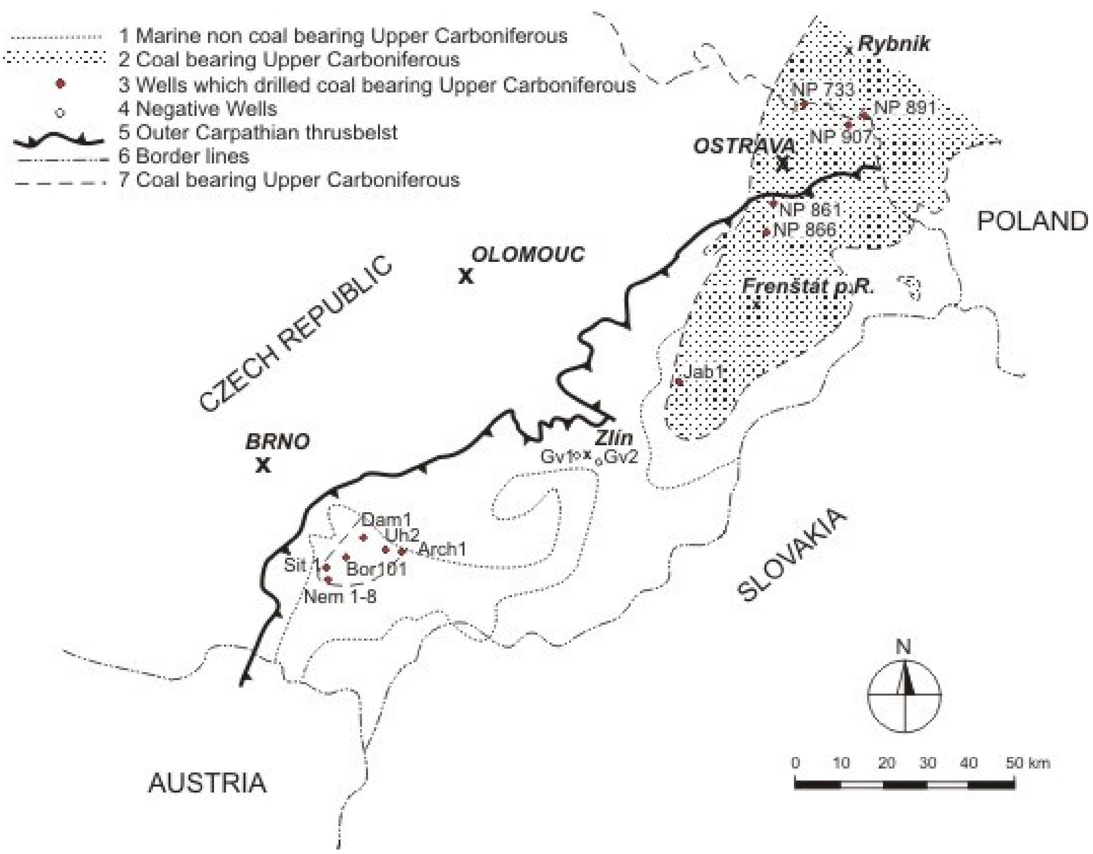

Obr. 7 Rozšíření svrchnokarbonských sedimentů podél jv. okraje Českého masivu (Opletal & Filák 2013).

Sedimentární výplň HP je tradičně dělena na paralické ostravské a limnické karvinské souvrství. V ostravském souvrství jsou vymezeny petřkovické, hrušovské, jaklovecké a porubské vrstvy. Karvinské souvrství je členěno na sedlové, sušské a doubravské vrstvy.

Pro ostravské souvrství jsou význačné opakující se eustatické mořské transgrese a regrese (Skoček 1989). V maximech transgresí zpravidla vznikaly významné korelační faunistické horizonty. K nejvýznamějším transgresím došlo na území HP v období končící sedimentace hrušovských vrstev (sk.f.h. Enny) a ve svrchní části jakloveckých vrstev (sk.f.h. Barbory). Ostravské souvrství je litologicky velmi různorodé a obsahuje faciálně pestrý sled pískovců, prachovců, jílovců, vulkanoklastik a uhelných slojí. Nejčastější jsou jemnozrnné až střednozrnné pískovce (40–60 % mocnosti). Ostravské souvrství obsahuje více než 170 uhelných slojí s průměrnou mocností 0,73 m (Dopita & Kumpera 1993).

Po sedimentaci paralického ostravského souvrství následuje krátký hiát a následné ukládání čistě kontinentálního karvinského souvrství, které začíná ukládáním hrubozrnných sedlových vrstev a pokračuje sušskými a doubravskými vrstvami. Nejmladším doloženým členem karvinského souvrství na území ČR jsou vyšší doubravské vrstvy. Spodní část karvinského souvrství je tvořena převážně hrubozrnnými sedimenty zastoupenými slepenci a pískovci, ve svrchní části převažují prachovité sedimenty. Podobně jako v ostravském souvrství se zde vyskytují polohy vulkanogenních horizontů (Martinec et al. 1989). Dopita et al. (1985) uvádí v karvinském souvrstí 87 uhelných slojí o průměrné mocnosti 1,76 m. Uhlonosnost karvinského souvrství je čtyřikrát větší než ostravského souvrství (Dopita et al. 1997).

3.1.1 Tepelná přeměna svrchně karbonských sedimentů východního okraje ČM

Stupeň prouhelnění v oblasti HP byl studován již na počátku minulého století (Stahl 1933, Patteisky 1928). Tyto pionýrské práce přinesly základní představu o rozložení tepelné přeměny v pánvi. První ucelené zhodnocení stupně prouhelnění uhlí v ostravsko-karvinské oblasti zachycující horizontální a vertikální změny (Dopita & Zeman 1960, Petránek & Dopita 1955), prokázalo postupný pokles stupně přeměny od Z k V, s výjimkou oblasti kolem orlovské struktury. Pro potřeby praxe byl další výzkum více soustředěn na macerálové složení uhlí a jeho chování v technologických procesech (Holubář 1975, Malán et al. 1966). Weiss (1976, 1975) sledoval závislost stupně prouhelnění vyjádřený obsahem prchavé hořlaviny (V^{daf}) na hloubce v profilech několika set vrtů a konstatoval pozoruhodnou podobnost jednotlivých gradientů v různých částech české části HP. Pozorované odchylky od všeobecného trendu dával do souvislosti s tektonickými jevy (sklon vrstev, poklesy, přesmyky), oxidací uhlí (pestré vrstvy), kontaktní přeměnou na styku s magmatickými tělesy a odlišným prostředím vzniku uhelné hmoty (skok na hranici ostravského a karvinského souvrství). Upozornil na skutečnost, že rozptyl hodnot dosud nejčastěji používaného parametru V^{daf} limituje možnost postižení drobných rozdílů mezi jednotlivými vrty. Odlišné sedimentární prostředí karvinského souvrství se projevuje jednak vyšším obsahem inertinitu a liptinitu (Chudý 1992, Dopita 1988), ale také zvýšenými hodnotami kyslíkového indexu a nižším vodíkovým indexem (Příloha 2).

Během posledních třiceti let bylo vytvořeno několik map prouhelnění české části hornoslezské pánve, které se navzájem liší svým pojetím (Pešek et al. 1998, Adamusová et al. 1992, Chudý 1992, Jurina & Weiss 1982, Dopita & Zeman 1960). Z publikovaných výsledků vyplývá nárůst tepelné přeměny ve směru V-Z.

Mapa tepelné přeměny Peška et al. (1998) je ve srovnání s mapou vytvořenou Adamusovou et al. (1992) méně členitá a uvádí vyšší hodnoty maximální odraznosti R_{max} na povrch ostravského souvrství. Zdánlivý rozpor je vyvolán odlišným způsobem prezentace dat, kdy Pešek et al. (1998) používá průměrnou hodnotu R_{max} pro celé souvrství zatímco Adamusová vykresluje interpolované hodnoty na povrch. Zhodnocení tepelné zralosti na základě odraznosti vitrinitu a teploty maximální pyrolytické odezvy (Příloha 2) dokládá nárůst teplotní zralosti od východu (variská platforma) k západu (variská předhluběň). Na základě analýzy hloubkové závislosti bylo prokázáno, že stupeň tepelné přeměny odráží geologickou pozici během posledních fází variského orogenu a je dán mocností chybějících paleozoických jednotek, nikoliv odlišným geotermálním gradientem. V české části HP se předpokládá mocnost erodovaných jednotek v době maximálního pohřbení v závěru variského orogenu – 3 000 m v předhlubni a 1 800 m na platformě (Příloha 2). Tyto výsledky velmi dobře korelují se závěry studia, publikovanými z polské části HP (Narkiewicz 2007).

Z oblasti jihovýchodních svahů Českého masivu byla publikována data odraznosti vitrinitu a prchavé hořlaviny svrchního karbonu zachyceného ve vrtech Němčičky 1, 2, 5 a 6 (Dvořák et al. 1997). Střední světelná odraznost nabývá v uvedených vrtech hodnot 0,57–0,90 % R_r a koreluje s obsahem prchavé hořlaviny V^{daf} (37,1–41,5). Oba parametry dokumentují nízké prouhelnění organické hmoty.

Střední světelná odraznost vitrinitu v uhelných polohách svrchního karbonu v novějších vrtech Archlebov 1, Šitbořice 1 a Borkovany 101 (obr. 8) dosahuje hodnot 0,64–0,90 % R_r, což odpovídá nízkému stupni prouhelnění černého uhlí tzv. plynovému uhlí.

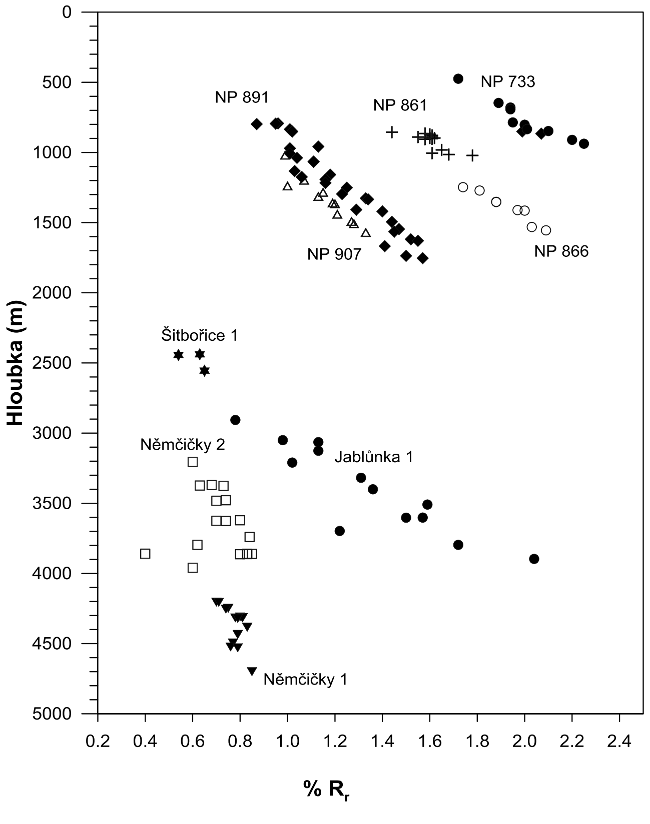

Obr. 8 Změna odraznosti vitrinitu (% R_r) svrchně karbonských sedimentů hornoslezské pánve a jihovýchodních svahů Českého masivu.

Pokud vzájemně srovnáme hodnoty střední světelné odraznosti spodnonamurských sedimentů HP (0,75–2,34 % R_r) s daty z jižního okraje klasické části HP (vrt Jablůnka 1, 0,78–

2,04 % R_r) a z vrtů na jižní Moravě (do 0,85 % R_r), zjistíme, že méně přeměněné horniny jsou uloženy ve větších hloubkách (obr. 8). Měřená odraznost vitrinitu dokládá stav v době nejvyššího pohřbení tj. v paleozoiku. V oblasti jižní Moravy tedy musely být horniny svrchního karbonu při stejném teplotním gradientu uloženy v mnohem nižších hloubkách ve srovnání s HP (Příloha 2).

3.1.2 Tepelná přeměna sedimentů kulmu jv. okraje ČM

Výzkumem tepelné přeměny organické hmoty v sedimentech variského flyše (kulmu) na jihovýchodním okraji Českého masivu, v oblasti Drahanské vrchoviny a Nízkého Jeseníku se zabývali Franců (2000), Příloha 1, Příloha 3, Příloha 5, Příloha 6, Příloh7, Dvořák et al. (1997), Krejčí et al. (1994), Dvořák (1989), Müller (1987), Dvořák & Wolf (1979), Skoček (1976), Dvořák & Skoček (1975).

Skutečnost, že z původního rozsáhlého sedimentačního prostoru moravskoslezského kulmu zůstaly zachovány jen izolované relikty (Bábek et al. 2008, Kalvoda et al. 2008) komplikuje rekonstrukci původního teplotního gradientu v období maximálního pohřbení. V první ucelené interpretaci tepelné zralosti (Dvořák & Wolf 1979) jsou společně hodnocena data odraznosti vitrinitu a krystalinity illitu z devonských vápenců, sedimentů kulmu a svrchního karbonu. Toto zjednodušení nezohledňuje výrazné tektonické sblížení devonských a karbonských sedimentů a roli násunové tektoniky.

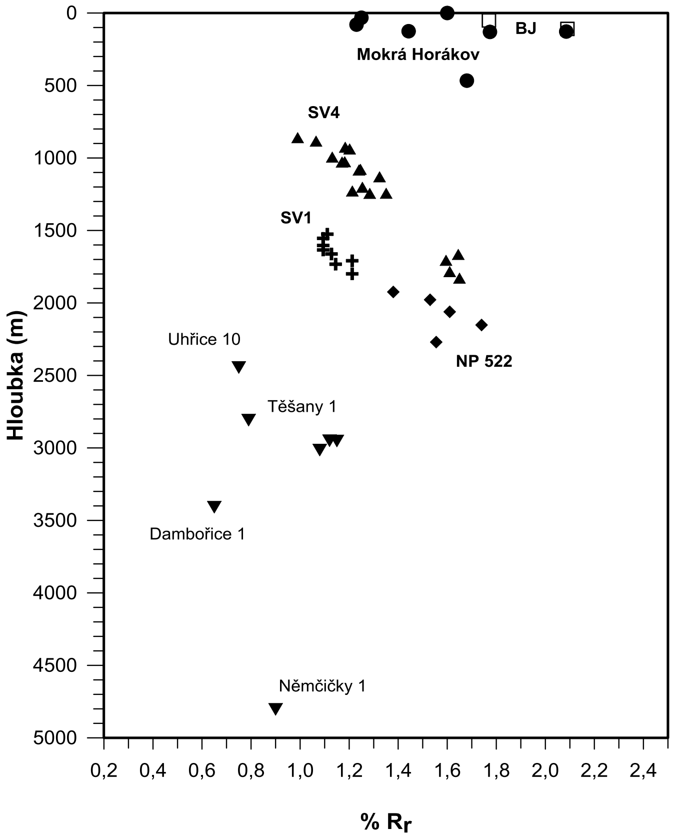

Obr. 9 Změna odraznosti vitrinitu (% R_r) spodně karbonských sedimentů hornoslezské pánve a jihovýchodních svahů Českého masivu.

V kulmských sedimentech zachycených ve vrtech Dambořice 1, Těšany 1, Němčičky 1 a Uhřice 10 pod příkrovy vnějších Západních Karpat, dosahují hodnoty střední odraznosti vitrinitu 0,65–1,65 % R_r (Müller 1987). Srovnatelné hodnoty střední odraznosti vitrinitu byly také zjištěny v myslejovickém souvrství zachyceném mělkými vrty v oblasti Mokrá-Horákov (1,23–2,05 % R_r) a Skalka BJ (1,77–2,09 % R_r). V stejném intervalu hodnot střední světelné odraznosti (1,37–2,10 % R_r) se pohybují vzorky z povrchových výchozů myslejovického souvrství – lokality Olšany, Vyškov a Luleč (Příloha 1). Tepelná zralost kulmských sedimentů (hradecko-kyjovické s.) zastižených ve vrtech v HP dosahuje hodnot střední odraznosti vitrinitu 0,91–2,55 %R_r (obr. 9).

Vrt Potštát 1 zachytil 2 866 m mocný sled sedimentů moravického souvrství v oblasti s variskou příkrovou stavbou (Čížek & Tomek 1991). Tepelná přeměna je vysoká, a proto byla stanovena maximální (R_{max}) a minimální (R_{min}) odraznost (Müller 1987). Tyto hodnoty byly přepočítány na střední odraznost (R_r) podle vztahu $R_r = (2*R_{max} + R_{min})/3$ (Taylor et al. 1998). Tento přepočet umožnil vzájemně srovnávat oblasti s nízkou a vysokou tepelnou přeměnou. Střední světelná odraznost vitrinitu ve vrtu Potštát 1 nabývá hodnot od 4,49–6,18 % R_r. Změna R_r s hloubkou ve vrtu Potštát 1, dokládá tektonické opakování sedimentárních sledů a prokazuje, že k dosažení tepelné zralosti došlo před dosunutím kulmských jednotek (obr. 10).

Tomuto scénáři také odpovídá tepelná přeměna organické hmoty měřená na povrchových vzorcích z blízkého okolí (4,56–5,66 % R_r, Franců & Otava 1998) a v přilehlých vrtech oderských vrchů (3,32–5,22 % R_r). Stejný stupeň tepelné přeměny je doložen ve vzorcích z protivanovského a rozstáňského souvrství severní části Drahanské vrchoviny (lokality Horní Štěpánov, Kořenec, Okrouhlá, Dzbel, Buková, Nová Ves u Litovle, Okluky, Stínava, Repešský žleb, Stražisko, Vícov, Sloup, Studnice), kde střední světelná odraznost dosahuje hodnot 3,08–4,96 %R_r (Příloha 7, Příloha 3).

Prezentovaná data dokládají pokles tepelné přeměny kulmských sedimentů moravsko-slezské oblasti ve směru Z-V. Tepelná zralost neklesá kontinuálně, ale v oblasti Drahanské vrchoviny vykazuje skokovitý pokles z hodnot střední odraznosti 3,17–5,23 % R_r na hodnoty 0,62–2,10 % R_r (Příloha 1). Prostorové sblížení oblastí s vysokým a nízkým stupněm teplotní přeměny je možné vysvětlit kontaktem zóny s tektonicky řízeným pohřbením a oblasti s původním sedimentárním sledem (Příloha 1, Kalvoda et al. 2008).

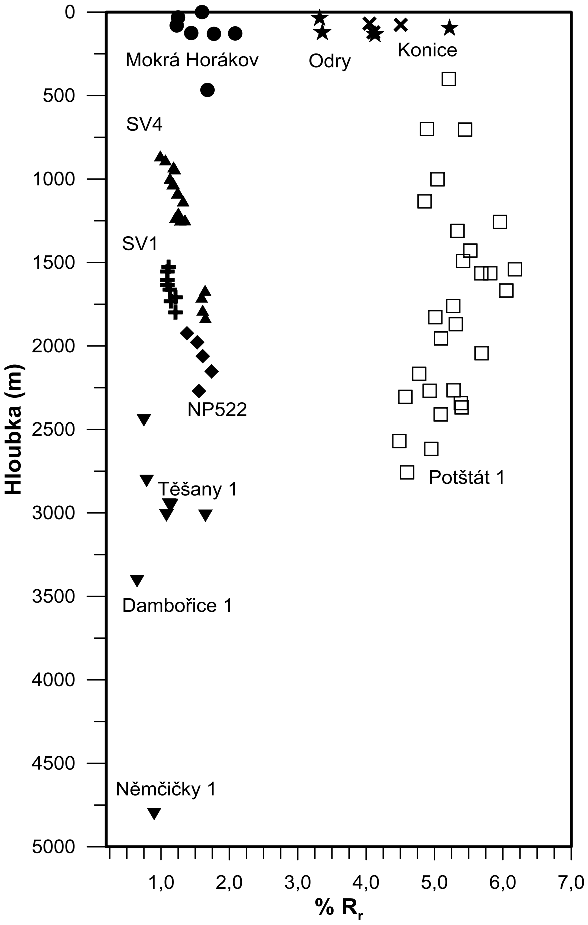

Obr. 10 Změna odraznosti vitrinitu (% R_r) svrchně karbonských sedimentů hornoslezské pánve, Oderských vrchů, Drahanské vrchoviny a jihovýchodních svahů Českého masivu.

3.2 Organicko-geochemická charakteristika mikulovských slínovců

Mikulovské slínovce patří ke sledu autochtonních mezozoických sedimentů v oblasti jižní Moravy a přilehlé části Rakouska (Pícha et al. 2006). Jsou považovány za hlavní zdrojovou horninu ropy a plynu ve vídenské pánvi a přilehlé oblasti (Pícha et al. 2006, Blížkovský et al. 1994, Eliáš & Wessely 1990, Ladwein 1988). Mocnost mikulovských slínovců roste od západu (200–400 m), kde mikulovské slínovce přechází do jurského platformního vývoje směrem na východ s vrtně doloženými mocnostmi až 1 500 m. Tmavé slínovce představují pánevní facii (Adámek 2005) svrchně jurského stáří a byly ukládány na kontinentálním svahu jako monotónní sekvence organickou hmotou bohatých slínovců s proměnlivým obsahem karbonátů (Eliáš & Wessely 1990). Občasná laminace je projevem odlišné zrnitostní skladby úzce spjaté s proměnlivým obsahem křemene, mikritu a jílové frakce (Stráník et al. 1993, Eliáš 1974).

Přítomná organická hmota je homogenní a tvoří ji převážně planktonické a bentické řasy s minoritním podílem terestrického materiálu (nepřesahujícím 11 hm. %). Podle výsledků macerálové analýzy představuje organická hmota klasický kerogen II (obr. 11).

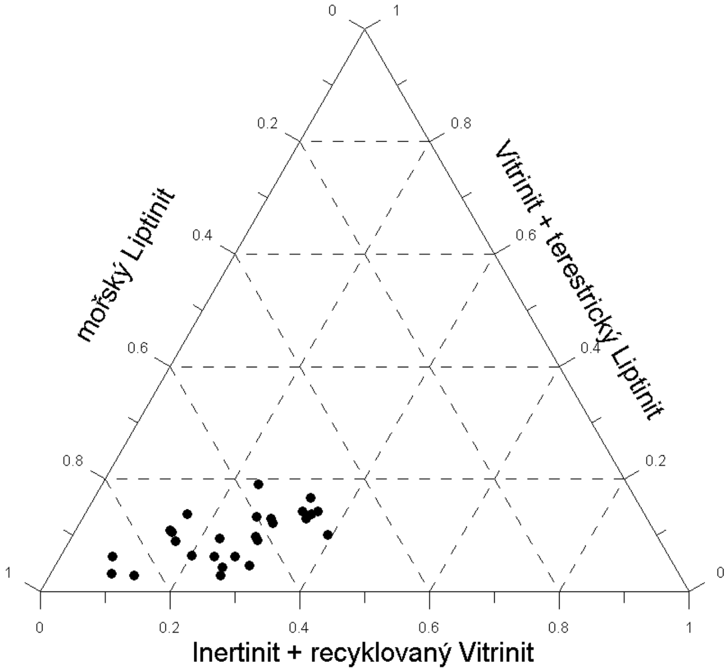

Obr. 11 Petrografické složení organického hmoty mikulovských slínovců v diagramu podle Littke & Sachsenhofer (1994).

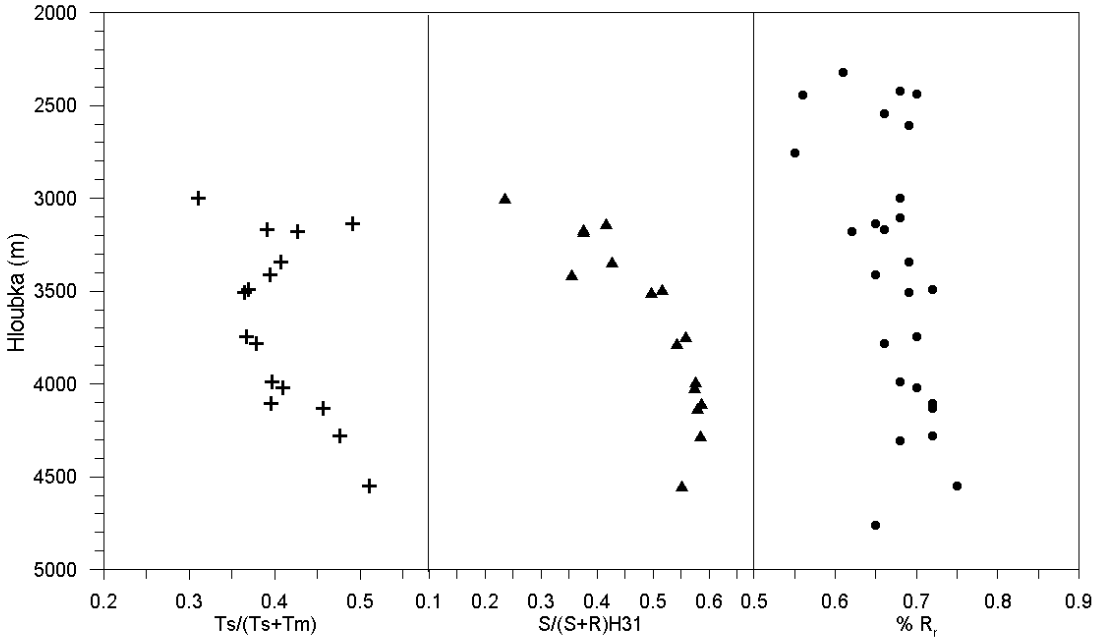

Obr. 12 Změna v zastoupení hopanů (parametry Ts/(Ts+Tm) a S/(S+R)H31) a střední světelné odraznosti vitrinitu (% R_r) s hloubkou v mikulovských slínovcích.

Dominantní podíl řas limituje využití parametrů pyrolýzy RockEval a vybraných biomarkerů, které jsou založeny na přítomnosti terestrické organické hmoty. Neměnné složení přítomné organické hmoty v hodnoceném sedimentárním sledu umožnilo využití hopanů (parametry Ts/(Ts+Tm) a S/(S+R)H31). Na základě těchto indexů byl stanoven předpokládaný počátek ropného okna na hloubku 3 491 m (obr. 12). Odraznost vitrinitu pro mikulovské slínovce zde dosahuje vyšších hodnot (0,7 % R_r) něž odpovídá ropnému oknu, což je způsobeno přítomností malého množství měřitelné organické hmoty a její částečnou oxidací. Velký rozptyl hodnot maximální pyrolytické odezvy (T_{max}) v intervalu 0 – 3 500 m souvisí s přítomností nepřeměněné organické hmoty (Příloha 8) a jílových minerálů skupiny smektitu a illitu (Dembecki 1992, Peters 1986, Davis et al. 1982).

4. Organická hmota v environmentálních vědách

Vzájemné propojení geologických aspektů dynamiky transportu a ukládání sedimentů s detailní geochemií jak původní organické hmoty, tak vybraných organických kontaminantů, umožňuje vyhodnotit a posoudit ekologickou zátěž prostředí a vymezit stupeň významnosti jednotlivých složek systému. Uvedený přístup využívá molekulární a isomerickou distribuci ekologicky indikativních látek ve vztahu ke geologickým a geomorfologickým charakteristikám hodnocené oblasti. Tento přístup je důležitý nejen v oblastech se starou zátěží a probíhající těžbou nerostů, ale také v říčním systému, do kterého uvedené látky mohou vstupovat jednak přímým splachem, ale také v důsledku atmosférické depozice (Murphy & Morrison 2002, Speight 1991).

Z organickou hmotou bohatých sedimentárních látek jsou nejčastějším zdrojem kontaminace uváděny uhlí a ropa. Získávání obou surovin ovlivňuje životní prostředí způsobem technického řešení těžby, transportem a návazným způsobem zpracování. Uhlí a ropa mají dané primární geochemické rysy, které odráží sedimentační prostředí a podmínky během diageneze (Peters et al. 2005, Murphy & Morrison 2002, Taylor et al. 1998, Tissot & Welte 1984). Jednotlivé typy uhlí a ropy se liší z pohledu chemického složení, tepelné zralosti a množství a složení anorganických příměsí (Stout & Emsbo-Mattingly 2008). Obě suroviny jsou přirozeným zdrojem polyaromatických uhlovodíků (PAU) a vykazují specifickou distribuci tzv. „fingerprint“ – pyrogenní a petrogenní (Pies et al. 2008, Douglas et al. 2007, Yunker et al. 2002, Wang et al. 1999, Douglas et al. 1996). Obě skupiny PAU byly velmi intenzivně studovány z pohledu jejich primární distribuce, mechanismu transportu, degradace a uchování v různých složkách životního prostředí (Kim et al. 2009, Gogou et al. 2000). Podle posledních výzkumů je možné prokázat souvislost mezi potenciálním zdrojem a výskytem kontaminace pomocí distribuce PAU pouze na základě příkladové studie oblasti, kdy jsou jasně definovány vstupy a potenciální zátěže. Problematice rozlišení primárního zdroje PAU kontaminace v říčním systému se dlouhodobě věnoval (Yunker & Macdonald 2003, Yunker et al. 1999). Ve svých pracech detailně popsal zákonitosti distribuce méně stabilních a více stabilních PAU a doložil, že v kombinaci s biomarkery je možné rozlišit látky pocházející ze spalování, ropné kontaminace, případně přirozeného biologického pozadí. Toto bylo potvrzeno řadou regionálních studií (např. Příloha 9, Farias et al. 2008, Yunker & Macdonald 2003, Faure et al. 2000, Wang et al. 1999).

Od 60. let minulého století, kdy se ochrana životního prostředí dostala do popředí zájmu širší veřejnosti, jsou znalosti o tzv. historické kontaminaci stále velmi limitované. Analytická data jsou dostupná ve velmi omezeném množství v tzv. přírodních archívech, které jsou klíčové pro výzkum historie znečištění dané oblasti. Jako přírodní archívy jsou využívány akvatické sedimenty (Heim & Schwarzbauer 2013, 2012). Geochronologický výzkum antropogenních polutantů je využíván jako nástroj rekonstrukce variability zastoupení a změn kontaminantů v čase a umožnuje vyhodnotit stupeň znečištění akvatických systémů. Pro sestrojení hodnověrného obrazu je potřebné mít k dispozici neporušený sedimentární záznam v rozmezí od 10 do 100 let (Schwarzbauer & Heim 2013, Warren et al. 2003, Alderton 1985) a zároveň s rychlostí sedimentace cca. 2 cm za rok (Ciszewski 2003). Většina studií v říčních systémech je zaměřena na estuárie případně břehové mokřady (Xu et al. 2015, Woodruf et al. 2013, Gosar & Zibret 2011, Götz et al. 2007) a na kovy vzhledem k jejich vyšší stabilitě a menší pohyblivosti v prostředí (např. Niencheski et al. 2014, Zhao et al. 2014, Bing et al. 2013, Gan et al. 2013) a existuje jen omezené množství zabývající se persistetními organickými polatnty (Kwan et al. 2014).

4.1 Změny v zastoupení organických kontaminantů v sedimentech Brněnské přehrady

Brněnská přehrada byla vybudována na řece Svratce v letech 1936–1939. Hodnocený vrtný profil zachytil neporušený sedimentární sled od vzniku přehrady a umožnil detailní zhodnocení vývoje sedimentace a změn v obsahu kontaminantů. Studium makroskopických texturních znaků sedimentů, obsahu organického uhlíku (TOC) a magnetické susceptibility (MSS) umožnilo vyčlenit jednotlivá stádia vývoje depozičního prostředí Brněnské přehrady za celou dobu její existence (Příloha 10).

Obsah organického uhlíku vykazuje cyklické změny, kde jsou vyšší obsahy TOC spojovány s klidnější sedimentací ze suspense a naopak dynamičtější sedimentace (povodně, jarní tání) vykazuje nižší hodnoty TOC. Magnetická susceptibilita odráží rozdílný přínos feromagnetických minerálů řekou Svratkou a je dobře srovnatelná se změnami v zrnitosti. Velmi nízké hodnoty MSS ve spodní části odpovídají postupnému plnění přehrady v letech 1939–1941. Rychlost sedimentace byla stanovena na základě mocnosti sedimentů a datování dílčích částí profilu pomocí ^{137}Cs, pro období 1986–2007 na 3,0 cm za rok, v období 1963–1986 na 3,4 cm za rok a v období 1954–1963 na 1,9 cm za rok. Na základě zrnitosti, MSS a TOC byly identifikovány hlavní povodňové události.

Začátek intenzivní těžby uranu v horním rozvodí řeky Svratky byl jasně prokázán v podobě zvýšeného obsahu ^{238}U, ^{226}Ra a ^{210}Pb v hloubce 150 cm. Jsou doloženy obzvláště vysoké obsahy ^{238}U v sedimentech z roku 1967. Rozdíly v koncentracích ^{238}U, ^{226}Ra a ^{210}Pb odráží vyšší rychlost sedimentace po dokončení přehrady v porovnání s jezerním prostředím. Výsledky prokázaly, že transport minerálů obohacených uranem z rozvodí do nádrže je hlavní zdroj radionuklidů v sedimentech, méně významným mechanismem je transport adsorbovaných radionuklidů na plavenině (Příloha 10).

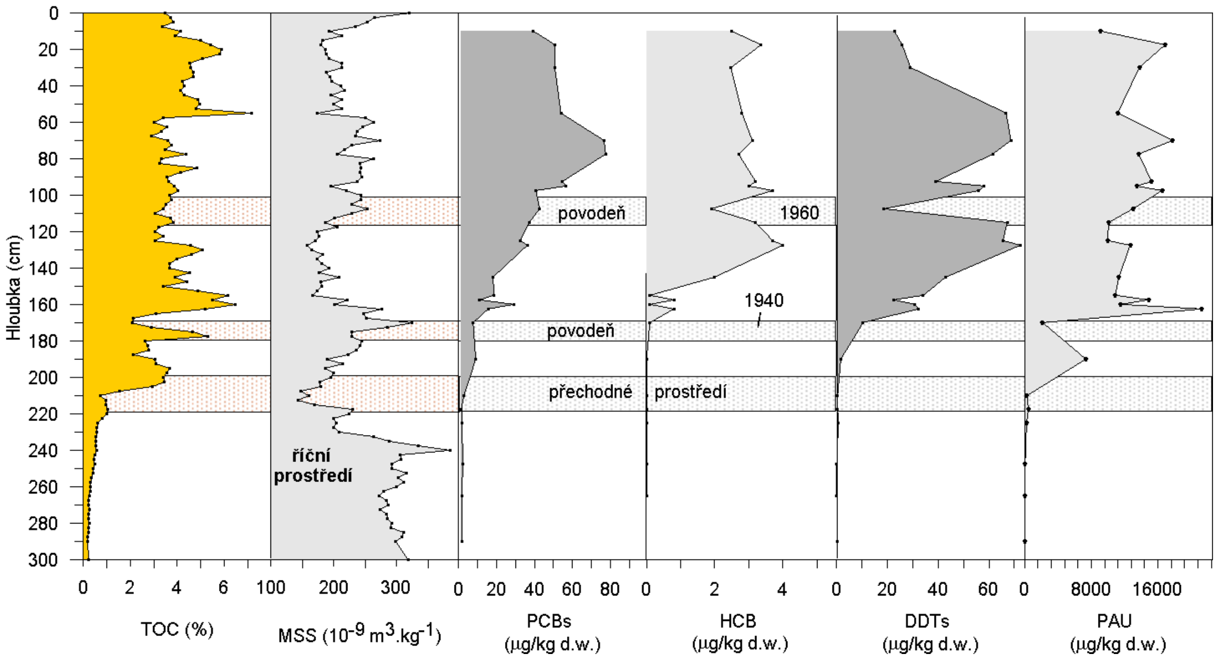

Obr. 12 Změna obsahu organického uhlíku (TOC), polychlorovaných bifenylů (PCB), hexachlorbenzenu (HCB), DDT a polycyklických uhlovodíků (PAU) v profilu vrtu BP4 v brněnské přehradě.

Analýza persistentních organických polutantů (POP) v sedimentárním profilu Brněnské přehrady ((Příloha 11) zdokumentovala vývoj znečištění v čase a prokázala odlišný mechanismus transportu hodnocených POP v říčním systému. Uvedený závěr vychází ze zhodnocení změn zastoupení POP s hloubkou. Zatímco u DDT a HCB dochází k poklesu koncentrace v povodňových pískových vrstvách, koncentrace PCB a PAU se v závislosti na litologii nemění. Pozorovaný jev souvisí s odlišným způsobem transportu DDT a HCB, které jsou vázány na jílovou frakci, se kterou se splachem dostávají do řeky Svratky a dále do přehrady, kde se ukládají. V době povodní, kdy byl zvýšený průtok a v přehradě sedimentovala pouze písčitá frakce, se tyto kontaminanty usadily dále po toku. Naopak PCB a PAU nejsou vázány na zrnitostní frakci a vstupují do přehradní nádrže spíše splachem z bezprostředního okolí přehrady případně atmosférickou depozicí.

5. Literatura

Abrams M. A., Segall M. P., Burtell S. G. (2001) Best practices for detecting, identifying, and characterizing near-surface migration of hydrocarbons within marine sediments. - Offshore Technology Conference Proceedings, OTC paper 13039.

Abrams M.A., Dahdah N., Francu E. (2004) Evaluationg petroleum systems elements and processes in frontier exploration areas using seabed geochemistry. – World Oil, June, 53-60.

Adámek J. (2005) The Jurassic floor of the Bohemian Massif in Moravia – geology and paleogeography. – Bulletin of Geosciences. 80, 4, 291-305.

Adamusová M., Dopita M., Foldyna J., Kalendová J., Kumpera O., Strakoš Z. (1992) Mapy mocností a prouhelnění uhlonosných molas čs. části hornoslezské černouhelné pánve. – Sbor. věd. prací VŠB Ostrava 1, XXXVIII, ř. hornicko-geologická, 27-38.

Alderton, D.H.M. (1985) Sediments. In: Historical Monitoring, MARC: Monitoring and Assessment Research Centre, No. 31, ISBN 0-905918-28-2, Technical Report. University of London.

Allen P.A., Allen J.R. (2005) Basin analysis. Principles and Applications. – Blackwell Publishing, Oxford, 2nd Edition.

Babek O., Tomek C., Melichar R., Kalvoda J., Otava J. (2006) Structure of unmetamorphosed Variscan tectonic units of the southern Moravo–Silesian zone, Bohemian Massif: a review. – N. Jb. Geol. Palaont. Abh., 239, 37–75.

Behar, F.V., Beaumont, B. De, Penteado H.L. (2001) Rock-Eval 6 technology: performances and developments: Oil & Gas Science and Technology – Revue du l'Institute Français du Petrole, 56, 111-134.

Belka Z., Valverde-Vaquero P., Dorr W., Ahrendt H., Wemmer K., Franke W., Schafer J. (2002) Accretion of first Gondwana-derived terranes at the margin of Baltica. - In: Winchester JA, Pharaoh TC, Verniers J (eds) Palaeozoic amalgamation of Central Europe. Geological Society, London, Special Publications, 201, 19–36.

Bing H, Wu Y, Liu E, Yang X (2013) Assessment of heavy metal enrichment and its human impact in lacustrine sediments from four lakes in themed-low reaches of the Yangtze river, China. – J. Environ. Sci., 25, 1300-1309.

Blížkovský M., Kocak A., Morskovský M., Novotný A., Gaza B., Kostelníček P., Hlavatý V., Lunga S., Vass D., Franců J., Müller P. (1994) Exploration History, Geology and Hydrocarbon Potential in the Czech Republic and Slovakia. In: Popescu, B. M. (Ed.), Hydrocarbons of Eastern Central Europe, Habitat, Exploration and Production History. – Springer-Verlag, Berlin, pp. 71-117.

Burnham A.K., Sweeney J.J., (1989) A chemical kinetic model of vitrinite maturation and reflectance. - Geochimica et Cosmochimica Acta, 53, 10, 2649-2657.

Carr A. D. (1999) A vitrinite reflectance kinetic model incorporating overpressure retardation. – Mar. Petrol. Geol., 16, 355-377.

Ciszewski D. (2003) Heavy metals in vertical profiles of the Middle Odra river overbank sediments: evidence for pollution changes. – Water Air Soil Pollut, 143, 81.

Conant B.H., Gillham R.W., Mendoza C.A. (1996) Vapor transport of trichloroethylene in the unsaturated zone: Field and numerical modeling investigations. - Water Resources Research, 32, 9-22.

Čížek P., Tomek Č. (1991) Large-scale thin-skinned tectonics in the eastern boundary of the Bohemian Massif. – Tectonics, 10, 2, 273-286.

Dallmeyer R.D., Neubauer F., Hock V. (1992) Chronology of late Paleozoic tectonothermal activity in the southeastern Bohemian Massif, Austria (Moldanubian and Moravo–Silesian zones) $^{40}Ar/^{39}Ar$ mineral age controls. – Tectonophysics, 210, 135–153.

Davis, J.B., and Stanley, J.P., 1982. Catalytic effect of smectite clays in hydrocarbon generation revealed by pyrolysis-gas chromatography. Journal of Analytical and Applied Pyrolysis, 4, 227-240.

Dembecki, H. Jr., 1992. The effects of the mineral matrix on the determination of kinetic parameters using modified Rock-Eval pyrolysis. Organic Geochemistry. 18, 531-539.

Dopita M. (1988) Sedlové vrstvy ostravsko-karvinského revíru. – MS, doktorská disertační práce, HGF VŠB-TU Ostrava.

Dopita M., Aust J., Brieda J., Černý I., Dvořák P., Fialová V., Foldyna J., Grmela A., Grygar R., Hoch I., Honěk J., Kaštovský V., Konečný P., Kožušníková A., Krejčí B., Kumpera O., Martinec P., Merenda M., Müller K., Novotná E., Ptáček J., Purkyňová E., Řehoř F., Strakoš Z., Tomis L., Tomšík J., Valterová P., Vašíček Z., Vencl J., Žídková S. (1997) Geologie české části hornoslezské pánve. – Ministerstvo životního prostředí ČR. Praha, 278 s.

Dopita M., Havlena V., Pešek J. (1985) Ložiska fosilních paliv. Státní nakladatelství

Dopita M., Kumpera O. (1993) Geology of the Ostrava - Karviná coalfield, Czech Republic, and its influence on mining. – Inter. J. Coal Geol., 23, 291-321.

Dopita M., Zeman J. (1960) Uwęglenie pokladów w Górnośląskim Zaglębiu Węglowym. – Kwart. geol., 3, 565-575.

Douglas G. S., Bence A. E., Prince R. C., McMillen S. J., Butler E. L. (1996): Environmental stability of hydrocarbon source and weathering ratios.- Environ. Sci. Technol., 30, 2332-2339.

Douglas GS, Stout SA, Uhler AD, McCarthy KJ, Emsbo-Mattingly SD (2007) Advantages of quantitative chemical fingerprinting in oil spill source identification. – In: Wang Z, Stout SA (eds) Oil spill environmental forensics. Fingerprinting and source identification. Elsevier, Boston, MA, pp. 257–292

Dudek A. (1980) The crystalline basement block of the Outer Carpathians in Morava. - Rozpr. Čs. Akad. Věd, Ř. mat.-přír. Věd., 90, 1-85. Praha.

Dvořák J. (1989) Anchimetamorphism in the Variscan tectogene in Central Europe - its relationschip to tectogenesis. – Věst. Ústř. Úst. Geol., 64, 1, 17-30.

Dvořák J., Honěk J., Pešek J., Valterová P. (1997) Deep borehole evidence for a southward extension of the Early Namurian deposits near Němčičky, S. Moravia, Czech Republic: implication for rapid coalification. In: Gayer R., Pešek J. (Eds.) European Coal Geology and Technology, Geological Society Special Publication, 125, 179-193.

Dvořák J., Skoček V. (1975) Reconstruction of the paleo-heat flow regime in two areas of the Variscan orogene. – N. Jb. Geol. Paleont. Mh., 517-527.

Dvořák J., Wolf M. (1979) Thermal metamorphism in the Moravian Paleozoic (Sudeticum, ČSSR). – N. Jb. Geol. Paleont. Mh., 10, 596-607.

Dvořák, J. (1994): Variský flyšový vývoj n Nízkém Jeseníku na Moravě a ve Slezsku. – Práce Čes. geol. Úst., 3., 80 str. Praha.

Edel J.B., Schulmann K., Holub F.V. (2003) Anticlockwise and clockwise rotations of the Eastern Variscides accommodated by dextral lithospheric wrenching: palaeomagnetic and structural evidence. – J. Geol. Soc., 160, 209-218.

Eliáš M. (1974) Mikrofaciální výzkum karbonátů naftonadějných oblastí na příkladě autochtonní jury jihovýchodních svahů českého masívu. - Zem. Plyn Nafta, XX, 3, 359-374. Hodonín.

Eliáš M., Wessely G. (1990) The autochtonous Mesozoic on the east flank of the Bohemian Massif – an object of mutual geological efforts between Austria and Czechoslovakia. In: Minaříková, H., Lobitzer, H. (Eds.), Thirty years of geological cooperation between Austria and Czechoslovakia. – Federal Geological Survey Vienna – Geological Survey Prague, pp. 78-83.

Farias C-O, Hamacher C, Wagener A de L-R, Scofield A de L (2008) Origin and degradation of hydrocarbond in mangrove sediments (Rio de Janeiro, Brazil) contaminated by an oil spill. Org Geochem., 39(3):289-307

Faure P, Landais P, Schlepp L, Michels R (2000) Evidence for diffusive contamination of river sediments by road asphalt particles. Environ Sci Technol., 34(7):1174-1181.

Finger F., Frasl G., Haunschmid B., Lettner H., Quadt A. von, Schermaier A., Schindlmayr A.O., Steyrer H.P. (1993) The Zentralgneisse of the Tauern Window (eastern Alps): insight into an intra- Alpine Variscan batholith. In: Raumer von J, Neubauer F (Eds) The Pre-Mesozoic geology in the Alps. – Springer, Berlin Heidelberg New York, 375–391.

Finger F., Steyer H.P. (1995) A tectonic model for the eastern Variscides: indications from a chemical study of amphibolites in the southeastern Bohemian Massif. – Geol. Carpathica, 46, 137–150.

Franců E (2009) Organic pollutants and their natural analogs in suspended particulate matter in the Bilina River. Internal report MZP.

Francu E. (2000) Optical properties of organic matter in Devonian and Lower Carboniferous black shales in the northern Drahany Upland. – Bulletin of the Czech Geological Survey, 75, 2, 115-120.

Franců E., Otava J. (1998) Odraznost vitrinitu břidlic „mírovského kulmu" a drahanského kulmu. – Geol. výzk na Mor. a Slez., 5, 44-46.

Fritz H., Neubauer F. (1995) Moravo–Silesian Zone; Autochthon; Structure. In: Dallmeyer RD, Franke W, Weber K (Eds.) Pre-Permian geology of Central and Eastern Europe. – Springer, Berlin Heidelberg New York, 490–494.

Gan H, Lin J, Liang K, Xia Z (2012) Selected trace metals (As, Cd, and Hg) distribution and contamination in the coastal wetland sediments of the northern Beibu Gulf, South China Sea. – Mar Pollut Bull 66, 252-258.

Gogou A, Bouloubassi I, Stephanou EG (2000) Marine organic geochemistry of the Eastern Mediterranean: 1. Aliphatic and polyaromatic hydrocarbons in Cretan Sea surficial sediments. – Mar Chem 68, 265–282.

Goodarzi F., Fowler M.G., Bustin M., McKirdy D.M. (1992) Thermal maturity of early Paleozoic sediments as determinated by the optical properties of marine-derived organic matter - a review. - In: Schidlowski M. et al.(eds.) Early organic evolution: implications for mineral and energy resources. Springer -Verlag Berlin, 279-295.

Gosar M, Zibret G (2011) Mercury contents in the vertical profiles through alluvial sediments as a reflection of mining in Idrijy (Slovenia). – J Geochem Exploration., 110, 81-91.

Götz, R., Bauer, O-H., Friesel, P., Herrmann, T., Jantzen, E., Kutzke, M., Lauer, R., Paepke, O., Roch, K., Rohweder, U., Schwartz, R., Sievers, S., Stachel, B. (2007): Vertical profile of PCDD/Fs, dioxin-like PCBs, other PCBs, PAHs, chlorobenzenes, DDX, HCHs, oganotin compounds and chlorinated ethers in dated sediment/soil cores from flood-plains of the river Elbe, Germany. – Chemosphere, 67, 592-603.

Grygar R., Vavro M. (1995) Evolution of Lugosilesian Orocline (North-Western periphery of the Bohemian Massif): Kinematics of Variscan deformation. – Čas. Mineral. Geol., 40, 65-90. Praha.

Heim S, Schwarzbauer J (2012) Geochronology of anthropogenic contaminants in aquatic sediment archives: historical trends of marine, limnic and fluvial sediment contamination. – In: Environmental Chemistry for a Sustainable World Vol. 1: Nanotechnology and Health Risk, Lichtfouse, Schwarzbauer, Robert (Eds), Springer Verlag, Berlin/Heidelberg, 209-257

Heim S, Schwarzbauer J (2013) Reconstructing pollution history by geochronology of anthropogenic contaminants in aquatic sediment archives - a review. – Environ Chem Lett 11, 255-270

Holubář, V. (1975) Inertinit v uhlích OKR. – MS, ÚSMH AV ČR, Výzkumná zpráva II-6-3/6, Praha.

Horsfield B. (1997) The Bulk Composition of First-Formed Petroleum in Source Rocks. In: Welte et al. (Eds.) Petroleum and Basin Evolution.Springer, Berlin, Heidelberg, 337-402.

Huang W.L. (1996) Experimental study of vitrinite maturation: effects of temperature, time, pressure, water, and Hydrogen Index. – Org. Geochem. 24, 233-241.

Chlupac I., Vrana S. (Eds.) (1994) Regional geological subdivision of the Bohemian Massif on the territory of the Czech Republic. – J. Czech Geol. Soc., 39, 1, 127-144.

Chlupáč, I. (1959): Stratigraphy of the Drahany development of the Moravian Devonian.- Věst. ÚÚG, XXXV, 329-332.

Chudý, J., 1992. Maceral composition and coalification of bitumenous coals from Karviná Basin. MS VŠB Ostrava, 135 pp.

Jachowicz M., Přichystal A. (1997) Lover Cambrian in deep boreholes in south Moravia. – Věst. Čes. geol. Úst., 72, 4, 329-332. Praha.

Jurina C., Weiss G. (1982) K rozčlenění stupně prouhelnění v karbonu čs. části hornoslezské pánve. – Sborník GPO, 26, 85-89.

Kalvoda J., Bábek O., Fatka O., Leichmann J., Melicahr R., Nehyba S., Špaček P. (2008) Brunovistulian terrane (Bohemian Massif, Central Europe) from late Proterozoic to late Paleozoic: a review (2008) – Int. J. Earth Sci. (Geol. Rundsch.), 97, 497-518.

Kettner R., Remeš M. (1935) Objev silurských břidlic s graptolitovou fanou na Moravě. – Věst. Král. Čes. Spol. Nauk., Tř. II, 16, 1-8.

Killops S., Killops V. (2005) Introduction to Organic Geochemistry. – Blackwell Publishing, Oxford.

Kim D, Kumfer BM, Anastasio C, Kennedy IM, Young TM (2009) Environmental aging of polycyclic aromatic hydrocarbons on soot and its effect on source identification. – Chemosphere, 76, 1075–1081

Krejčí O., Franců J., Müller P., Pereszlényi M., Stráník Z. (1994) Geologic structure and hydrocarbon generation in the Carpathian Flysch Belt of southern Moravia. – Věstník ČGÚ, 69, 4, 13-27.

Kross B. M., Leythaesser D. (1996) Molecular diffusion of light hydrocarbons in sedimentary rocks and its role in the migration and dissipation of natural gas. - In: D. Schumacher and M. A. Abrams (eds.) Hydrocarbon Migration and Its Near Surface Effects: American Association Petroleum Geology Memoir, 66, 173-184.

Kumpera O., Martinec P. (1995) The development of the Carboniferous accretionary wedge in the Moravian-Silesian Paleozoic Basin. – J. Czech Geol. Soc., 40, 47-60.

Kwan CS, Takada H, Boonyatumanond R, Kato Y, Mizukawa K, Ito M, Dung LQ, Zakaria MP, Santiago EC (2014) Historical occurrences of polybrominated diphenyl ethers and polychlorinated biphenyls in Manila Bay, and the upper Gulf of Thailand. – Sci Total Environ 470-471, 427-437.

Ladwein H. W. (1988) Organic Geochemistry of Vienna Basin. Model for Hydrocarbon Generation Overthrust Belts. – AAPG Bull. 72, 586-599.

Leythaeuser D., Schaefer R. G., Pooch H. (1983) Diffusion of light hydrocarbons in subsurface sedimentary rocks. – AAPG Bulletin, 67, 6, 889–895.

Littke R., Bayer U., Gajewski D., Nelskamp S. (2008) Dynamics of complex intracontinental basins. The example of the Central European Basin System. – Springer-Verlag, Berlin-Heidelberg, 519 p.

Littke R., Leythaeuser D. (1993) Migration of oil and gas in coals. – AAPG Studies in Geology, 38, 219-236.

Littke R., Urai J.L., Uffmann A.K., Risvanis F. (2012) Reflectance of dispersed vitrinite in Palaeozoic rocks with and without cleavage: Implications for burial and thermal history modeling in the Devonian of Rursee area, northern Rhenish Massif, Germany. – Int. J. Coal Geol., 89, 41-50.

Littke, R., Sachsenhofer, R. F. (1994) Organic petrology of deep sea sediments: a compilation of results from the Ocean Drilling Program and the Deep Sea Drilling Project. Energy and Fuels. 8, 1498-1512.

Malán O., Kessler M.F., Valeška F. (1966) Výskyt pyritu a inertinitu v OKR a možnosti jejich využití pro korelaci a identifikaci slojí. – Uhlí, 14, 8, 6-9.

Martinec P., Weiss, Z., Horák J., Špachman L. (1989): Problematika identifikace a klasifikace tonsteinů. – Sborník prací "Tonsteiny a tufogenní horniny uhelných pánví" I. 3-8. Ostrava.

McCann T. (ed), 2008 The Geology of Central Europe, The Geological Society London, 2008, vol. 1: Precambrian and Palaeozoic; vol. 2: Mesozoic and Cenozoic

Müller P. (1987) Zdrojové horniny ropy a plynu jihovýchodních svahů Českého masívu a Vídeňské pánve. – MS ČGÚ.

Murphy B. L., Morrison R. D. (2002) Introduction to environmental forensics.-London p. 558

Narkiewicz M. (2007) Development and inversion of Devonian and Carboniferous basins in the eastern part of the Variscan foreland (Poland). – Geological Quarterly 51, 231–256.

Nehyba S., Leichmann J., Kalvoda J. (2001) Depositional environment of the „Old Red'' sediments in the Brno area (South-eastern part of the Rhenohercynian zone, Bohemian massif). – Geol Carpathica, 52, 195–203.

Neubauer F., Frisch W. (1993) The Austro-Alpine metamorphic basement east of the Tauern window. In: Raumer J von, Neubauer F (Eds.) The Pre-Mesozoic geology in the Alps. – Springer, Berlin Heidelberg New York, 515–536.

Niencheski LF, Moore WS, Windom HL (2014) History of human activity in coastal southern Brazil from sediment. – Mar Pollut Bull 78, 209-212.

Opletal V., Filák P. (2013): Upper Carboniferous Strata reached by the Exlopration Well Sitborice 1 beneath the Carpathian Thrustbelt Units in the Area of south-eastern margin of Bohemian massif. - – Documenta Geonica 2013, 1, 1-9

Patteisky K. (1928) Chemical properties of coal in the Ostrava and Karvina districts. In: Bituminous coal mines in the Ostrava-Karviná district, I, Ostrava.

Pedersen T.F., Calvert S.E. (1990) Anoxia vs. productivity: What controls the formation of organic-carbon-rich sediments and sedimentary rocks? – AAPG Bulletin, 74, 4, 454-466.

Pešek J., Kumpera O., Holub V., Skoček V. (1998) Paleogeographic atlas: Late Paleozoic and Triassic Formations, Czech Republic. – Český geologický ústav, Praha.

Peters K.E., Walters C.C., Moldowan J.M. (2005) The biomarker guide; I, Biomarkers and isotopes in the environment and human history. II, Biomarkers and isotopes in petroleum systems and Earth history. – 2 ed. Cambridge University Press. Cambridge, United Kingdom. 1155 pp.

Peters, K.E., 1986. Guidelines for evaluating petroleum source rock using programmed pyrolysis. AAPG Bulletin, 70, 318-329.

Petránek J., Dopita M. (1955) Prouhelnění slojí v ostravsko-karvínském revíru a jeho závislost na geologických činitelích. – Sbor. Ústř. Úst. Geol., odd. geol. 22, 593-634.

Pies C, Hoffman B, Petrowsky J, Yang Y, Ternes TA, Hofmann T (2008) Characterization and source identification of polycyclic aromatic hydrocarbons (PAHs) in river bank soils. – Chemosphere, 72, 1594–1601

Picha F.J., Stranik Z., Krejci O. (2006) Geology and hydrocarbon resources of the Outer Western Carpathians and their foreland, Czech Republic, In: Golonka, J., Picha, F. J. (Ed.), The Carpathians and their foreland: Geology and hydrocarbon resources. – AAPG Memoir 84, 49-175.

Price L. C. (1996) Research-derived insights into geochemical hydrocarbon exploration, in D. Schumacher and M.A. Abrams (eds.), Hydrocarbon migration and its near-surface expression: AAPG Memoir, 66, 285-307.

Přichystal A. (1993) Vulkanismus v geologické historii Moravy a Slezska od paleozoika do kvartéru. In: Přichystal A, Obstova V and Suk M (Eds.) Geologie Moravy a Slezska (Sbor. Přispev. 90. Výr. naroz. prof. dr. K. Zapletala), 59–70.

Ptáček J., Grygar R., Koníček P., Waclawik P. (2012) The impact of Outer Western Carpathian nappe tectonics on the recent stress-strain state in the Upper Silesian Coal Basin (Moravosilesian Zone, Bohemian Massif). – Geologica Carpathica, 63, 1, 3-11.

Rullkötter J., Leythaeuser D., Littke R., Mann U., Müller P.J., Radke M., Schaefer R.G., Schenk H.J., Schwochau K., Witte E.G., Welte D.H. (1988) Organic matter maturation under the influence of a deep intrusive heat source: A natural experiment for quantitation of hydrocarbon generation and expulsion from a petroleum source rock (Toarcian shale, Northern Germany). In: Mattavelli L, Novelli L (eds) Advances in Org Geochem 1987. – Org. Geochem., 13, 4-6, 847-856.

Samson I., Anderson A., Marshall D.D. (2003) Fluid Inclusions: Analysis and Interpretation. - Mineralogical Association of Canada, p. 374.

Schulmann K., Gayer R. (2000) A model for a continental accretionary wedge developed by oblique collision: the NE Bohemian Massif. – J. Geol. Soc. Lond., 157, 401–416.

Schumacher D. (1996) Hydrocarbon-induced alteration of soils and sediments. – In D. Schumacher and M. A. Abrams, eds., Hydrocarbon migration and its nearsurface expression: AAPG Memoir 66, 71–89.

Skoček V. (1976) Regional and geological interpretation of organic matter coalification in the Late Paleozoic sediments of the Bohemian Massif. – J. Czech Geol. Soc., 51, 13-24.

Skoček, V. (1989): Indications of early carboniferous events in Paleozoic sequences of Moravia, Czechoslovakia. – Čas. Mineral. Geol., 34, 4, 373-384.

Speight J.G. (1991) The chemistry and technology of petroleum, 2nd edn. Marcel Dekker, New York.

Stahl A. (1933) Inkohlung und Flözlagerung in ostsudetischen Steinkohlen. – Jahrbuch der reussischen geol. Landesanstalt, LIV.

Stípska P., Schulmann K. (1995) Inverted metamorphic zonation in a basement-derived nappe sequence, eastern margin of the Bohemian Massif. – Geol. J., 30, 385-413.

Stout SA, Emsbo-Mattingly SD (2008) Concentration and character of PAHs and other hydrocarbons in coals of varying rank – implications for environmental studies of soils and sediments containing particulate coal. – Org. Geochem., 39, 801–819

Stráník Z., Menčík E., Eliáš M., Adámek J. (1993): Flyšové pásmo Západních karpat, autochtonní mesozoikum a paleogén na Moravě a ve Slezsku. In: Přichystal A. - Obstová V. - Suk M. (eds.), Geologie Moravy a Slezska, Moravské Muzeum, Brno, 107-122.

Suggate R.P. (1988) Relations between depth of burial, vitrinite reflectance and geothermal gradient. – Journal of Petroleum Geology, 21, 1, 5-32.

Sweeney J.J., Burnham A.K. (1990) Evaluation of a simple model of vitrinite reflectance based on chemical kinetics. AAPG Bull. 74, 1559-1570.

Tait J.A., Bachtadse V., Soffel H. (1996) Eastern Variscan fold belt; paleomagnetic evidence for oroclinal bending. – Geology, 24, 871-874.

Taylor G.H., Teichmüller M., Davis A., Diessel C.F.K., Littke R., Robert P. (1998) Organic petrology. – Gebrüder Borntraeger, Berlin, 704 pp.

Tedesco, S. A. (2012). Surface geochemistry in petroleum exploration. Springer Science & Business Media.

Teichmüller M., Teichmüller R. (1979) Diagenesis of coal (coalification). - In: Larsen G., Chilingar G.V. (eds.). Diagenesis in sediments and sedimentary rocks, Elsevier, Amsterdam, 207-246.

Tissot B.P., Welte D.H. (1984) Petroleum formation and occurrence. – 2nd edn. Springer, Berlin Heidelberg New York, 699 pp.

Velde B. (1995) Origin and mineralogy of clays. – Springer, New York.

Wagner, G., van den Haute, P.(1992) Fission-Track Dating. - Kluwer Academic Publishers, 285 pp.

Wang Z, Fingas M, Page DS (1999) Oil spill identification. – J. Chromatogr. A., 843, 369–411

Wang Z, Fingas M, Shu Y-Y, Sigouin L, Landriault M, Lambert P (1999) Quantitative characterization of PAHs in burn residue and soot samples and differentiation of pyrogenic PAHs from petrogenic PAHs –The 1994 Mobile Burn Study. - Environ Sci Technol 33 (18):3100-3109.Warren, N., Allan, I.J., Carter, J.E., House, W.A., Parker, A. (2003) Pesticides and other micro-organic contaminants in freshwater sedimentary environments - a review. – Appl. Geochem. 18, 159-194.

Weiss G. (1975) Surovinová studie čs. části hornoslezské pánve. – MS, Unigeo Ostrava, II. etapa část 1., svazek 2, 1-135.

Weiss G. (1976) K průběhu změn stupně prouhelnění s hloubkou v čs. části hornoslezské pánve. – Sborník GPO, 11, 7-34.

Woodruff JD, Martini AP, Elzidani EZH, Naughton TJ, Kekacs DJ, MacDonald DG (2013) Off-river waterbodies on tidal rivers: Human impact on rates of infilling and the accumulation of pollutants. – Geomorphol., 184, 38-50.

Xu W, Ni S, Gao Y, Shi Z (2015) Reconstruction of the cadmium contamination history of a floodplain from Maoniuping mining area (china) by gamma ray spectroscopy and inductively coupled plasma mass spectrometry. – Spectroscopy Lett 48, 542-552.

Yunker M.B., Macdonald R.W., Vingarzan R., Mitchell H.R., Goyette D., Sylvestre S. (2002) PAUs in the Fraser River basin: critical appraisal of PAU ratios ad indicators of PAU source and composition.- Organic Cheochemistry, 33, 489-515.

Yunker M-B, Macdonald R-W (2003) Petroleum biomarker sources in suspended particulate matter and sediments from the Fraser river Basin and Strait of Georgia, Canada. Org Geochem., 34, 11, 1525-1541.

Yunker, M.B., Macdonald, R.W., Goyette, D., Paton D.W., Fowler B.R., Sullivan D., Boyd J., 1999. Natural and antropogenic inputs of hydrocarbons to Strait of Gerogia. – Sci. Total Environ., 225, 191-209.

Zhao J, Hu B, Li J, Yang J, Bai F, Dou Y, Yin X (2014) One hundred-year sedimentary record of heavy metal accumulation in the southeastern Liaodong Bay of China. – Environ Erath Sci 71, 1073-1082.

Zukalova V. (1976) Biostratigraphy of the Paleozoic in the basement and foreland of the Carpathians east of Brno (In Czech). – Čas. Mineral. Geol. 21, 369-385.

Zukalová V., Chlupáč I. (1982) Stratigrafická klasifikace nemetamorfovaného devonu moravskoslezské oblasti. – Časopis pro mineralogii a geologii, 27, 3, 225-241.

6. Přílohy

Příloha 1

Francù E., Francù J., Kalvoda J., Poelchau H.S., Otava J. (2002) Burial and uplift hitory of the Palaeozoic Flysch in the Variscan foreland basin (SE Bohemian Massif, Czech Republic) In: Bertotti G., Schulmann K., Cloetingh S., eds.: Continental collision and the tectono-sedimentary evolution of forelands. European Geophysical Society - Stephan Mueller Special Publication Series, Vol. 1, 259-278.

Příloha 2

Geršlová E., Goldbach M., Geršl M., Skupien P. (2016) Heat flow evolution, subsidence and erosion in Upper Silesian Coal Basin, Czech Republic. – . – International Journal of Coal Geology International Journal of Coal Geology 154-155, 30-42.

Příloha 3

Francu E., Francu J., Kalvoda J. (1999) Illite crystallinity and vitrinite reflectance in Paleozoic siliciclastics in the SE Bohemian Massif. Geologica Carpathica. 50, 5, 365-372.

Příloha 4

Abrams, M.A. , Dahdah, N.F. , Franců, E. (2009) Development of methods to collect and analyze gasoline range (C5–C12) hydrocarbons from seabed sediments as indicators of subsurface hydrocarbon generation and entrapment. Applied Geochemistry 24, 10, 1951-1970.

Příloha 5

Čopjaková R., Franců E., Novák M. (2011) Formation of authigenic monazite-(Ce) to monazite-(Nd) from Upper Carboniferous graywackes of the Drahany Upland: Roles of the chemical composition of host rock and burial temperature. Lithos 127, november, 373-385.

Příloha 6

Bábek O., Franců E., Kalvoda J., Neubauer F. (2008) A digital image analysis approach to measurement of the conodont colour alteration index (CAI): a case study from the Moravo-Silesian Zone, Czech Republic. - N. Jb. Geol. Paläont., 249/2: 185-201;

Příloha 7

Špaček P., Kalvoda J., Franců E., Melichar R. (2001) Variation of deformation mechanisms within the progressive-retrogressive mylonitization cycle of limestones:

Brunovistulian sedimentary cover (The Variscan orogeny of the souteastern Bohemian Massif). – Geologica Carpathica. 52, 5, 263-275.

Příloha 8

Geršlová E., Opletal V., Sýkorová I., Sedláková I., Geršl M. (2015) A Geochemical and Petrographical Characterization of Organic Matter in the Jurassic Mikulov Marls from the Czech Republic. International Journal of Coal Geology 141-142, 42-50.

Příloha 9

Geršlová E., Schwarzbauer J. (2014) Hydrocarbon-based indicators for characterizing potential sources of coal-derived pollution in the vicinity of the Ostrava City. Environmental Earth Sciences, Springer, 71, 7,

Příloha 10

Nehyba S., Nyvlt D., Schkade U., Kirchner G., Francu E. (2010) Depositional rates and dating techniques of modern deposits in the Brno reservoir (Czech Republic) during the last 70 years. J Paleolimnol 45, 1, 41-55.

Příloha 11

Franců E., Schwarzbauer J., Lána R., Nývlt D., Nehyba S. (2009) Historical Changes in Levels of Organic Pollutants in Sediment Cores from Brno Reservoir, Czech Republic. Water, Air and Soil Pollution 209, 1-4, s. 81-91.

Příloha 1

Franců E., Franců J., Kalvoda J., Poelchau H.S., Otava J. (2002) Burial and uplift hitory of the Palaeozoic Flysch in the Variscan foreland basin (SE Bohemian Massif, Czech Republic) In: Bertotti G., Schulmann K., Cloetingh S., eds.: Continental collision and the tectono-sedimentary evolution of forelands. European Geophysical Society - Stephan Mueller Special Publication Series, Vol. 1, 259-278.

EGU Stephan Mueller Special Publication Series, 1, 167–179, 2002

Burial and uplift history of the Palaeozoic Flysch in the Variscan foreland basin (SE Bohemian Massif, Czech Republic)

E. Francu[1], **J. Francu**[1], **J. Kalvoda**[2], **H. S. Poelchau**[3, *], **and J. Otava**[1]

[1]Czech Geological Survey, Leitnerova 22, 658 69 Brno, Czech Republic
[2]Dept. of Geology, Masaryk University, Kotlárská 2, Brno, Czech Republic
[3]Inst. für Chemie und Dynamik der Geosphäre, Forschungszentrum Jülich, 52425 Jülich, Germany
[*] currently at: Kansas Geological Survey, USA

Received: 4 April 2001 – Revised: 15 October 2001 – Accepted: 29 October 2001

Abstract. Organic and clay indicators were measured to characterise the burial and thermal history of Devonian through Upper Carboniferous siliciclastic and carbonate rocks in the Rheno-Hercynian zone of the Variscan orogeny in Moravia (eastern Czech Republic). The very low-grade metamorphism is documented by the illite crystallinity (IC) and vitrinite reflectance (R_r) in the inner part of the thrust and fold belt in the NNW. Application of forward thermal modelling suggests maximum palaeo-temperature of 240–360°C and burial depth of 4–9 km. In the Variscan foreland in the SSE the IC and R_r values are typical of diagenetic conditions with maximum palaeo-temperature of 80–130°C. The distribution of both clay and organic maturity parameters is interpreted as a result of pre- and syn-tectonic thermal exposure of the rocks due to burial by a wedge-shaped body of thrust sheets thinning towards the Variscan foreland where only sedimentary burial was effective. The amount of uplift and denudation increases from the foreland to the Rheno-Hercynian thin-skinned thrust and fold belt.

Key words. Vitrinite reflectance; illite crystallinity; modelling; thermal history; Variscan thrusting; erosion

1 Introduction

Significant advances have been made in understanding the causes and processes of diagenesis and metamorphism related to thermal history of sedimentary basins and thrust and fold belts (Tissot and Welte, 1984; Robert, 1988; Merriman and Frey, 1999). It is generally accepted that the burial depth, geothermal gradient and geological time play important roles in these processes and that lack of one may partly be compensated by surplus of the other factor. Mathematical methods have been proposed to calculate the probable maximum palaeo-temperature and palaeo-geothermal gradients in sedimentary basins from the coal rank and slope of the diagenetic or very low-grade metamorphic trend with depth in continuous profiles (Waples, 1980; Buntebarth, 1982; Barker, 1996).

The reconstruction of the burial history and palaeogeothermal conditions is much more complex when thrusting is involved and the (meta-)sedimentary rocks are imbricated and stacked. Fast underthrusting of cold crustal surface below overriding nappe sheet causes lowering of geothermal gradient in frontal orogenic belts. In result, tectonic burial is often asociated with lower or equal but not higher thermal stress than a pure sedimentary burial of the same thickness (Angevine and Turcotte, 1983; Wygrala et al., 1990; Čermák and Bodri, 1996).

The thermal history of the Palaeozoic in the SE Bohemian Massif has been a matter of discussion by different authors (e.g. Skoček, 1976; Dvořák, 1989). The results of our studies differ from the earlier ones in the following aspects:

- regional distribution of palaeo-geothermal gradient or heat flow
- amount of eroded sedimentary strata
- extent of tectonic displacement of the units (autochthonous vs. allochthonous position).

Several computer programmes were developed to formulate mathematically the geological concept of basin evolution and to simulate subsidence, geothermics and diagenesis (Tissot and Welte, 1984; Welte and Yalçin, 1988; Issler and Beaumont, 1989; Ungerer et al., 1990; Poelchau et al., 1997; Yalçin et al., 1997). In this paper the forward modelling approach is applied to simulate the geological history as a series of stratigraphic and tectonic events under evolving thermal conditions and to describe quantitatively deposition, non-deposition, and erosion in time. The changes of thickness of the preserved and missing strata (corrected for compaction) are represented by burial history curves. Deposition and erosion of the non-preserved units are inferred from unconformities, paleogeography, tectonics, and coalification discontinuities. The thickness of the eroded units and

---

Correspondence to: E. Francu (francu@cgu.cz)

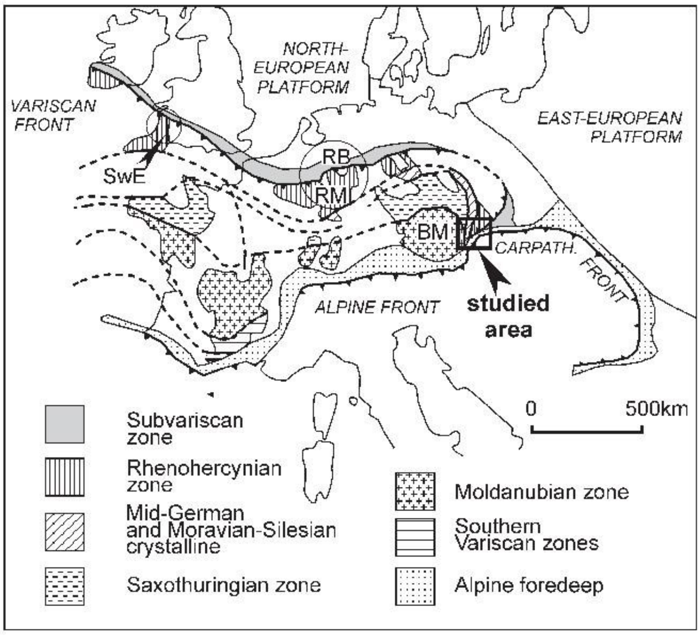

Fig. 1. Major zones of the Variscan orogenic belt and foreland in Europe (modified after Ellenberger, Tamain, 1980 and Mísař et al., 1983). Rectangle shows the studied area, and the circles represent the compared regions of the Rhenish Massif (RM), Ruhr Basin (RB), and Southwest England (SwE).

palaeo-heat flow data are iteratively estimated in the process of calibration (e.g. Poelchau et al., 1997) where the organic maturity is calculated using a kinetic approach (EASY% R_o of Sweeney and Burnham, 1990). The model is considered close to reality when the calculated vitrinite reflectance trend fits the measured data points.

2 Geological setting

The Palaeozoic in the eastern part of the Bohemian Massif (Fig. 1) is regarded as a part of the Rheno-Hercynian Zone of the Variscan orogenic belt (Franke, 1989). The Palaeozoic sequences in south-eastern Moravia are known from the outcrops in the Drahany Upland north of Brno and from deep boreholes below the Carpathian Foredeep and the overthrust of the West Carpathian Flysch Belt (Fig. 2). The crystalline basement is built by the Cadomian Brunovistulian terrane derived from the northern part of Gondwana (Finger and Steyrer, 1995) and includes the granitoids and metabasalts of the Brno Massif which are exposed at the surface in the SW. The lithostratigraphy (Fig. 3) of the studied basins starts with isolated occurrences of the Early Cambrian in the SE (Vavrdová, 1997; Jachowicz and Přichystal, 1997) and Silurian near Stínava in the NE. The main sedimentary sequences consist of a series of pre-flysch formations, Variscan flysch (“Culm”) and marginal foreland sediments (“molasse”). The transgressive basal clastics of the Lower and Middle Devonian occur in the entire area. During the Middle Devonian to Lower Carboniferous carbonates and siliciclastics were deposited in a passive margin setting with a hiatus from the Tournaisian to middle Visean within the Lišen Fm. in the SE. The carbonates crop out in a narrow belt of the Moravian Karst north of Brno (Fig. 2) while most of the surface geology of the Drahany Upland exposes the Variscan synorogenic flysch of Early Carboniferous (Visean) age. Further to the SSE the Upper Carboniferous coal-bearing molasse sediments occur below the autochthonous Mesozoic, Tertiary and the nappes of the Outer Carpathians. More details about sedimentology, paleontology and tectonics are given e.g. by Hladil et al. (1992), Kalvoda (1994), Dvořák (1995), Kumpera and Martinec (1995), Hartley and Otava (2001).

3 Earlier studies of thermal and erosion history

The published data on thermal maturity of organic matter (coalification rank) and clays in the studied area include:

1. volatile matter (V^{daf}) published mostly in technical reports and summarised by Dvořák and Skoček (1975, 1976);
2. vitrinite reflectance (R_{max} %) (see Dvořák and Wolf, 1979; Dvořák, 1989; Dvořák et al., 1997).

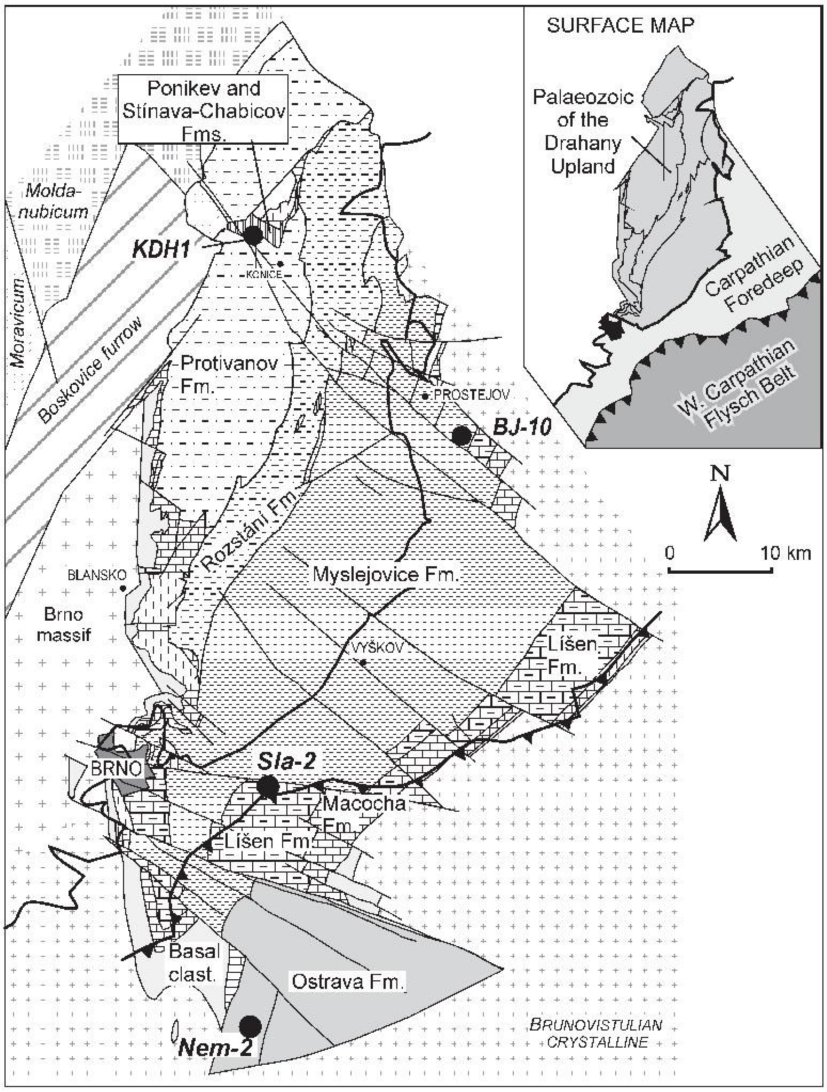

Fig. 2. Geological outcrop and subcrop map of the Palaeozoic and underlying crystalline of the SE margin of the Bohemian Massif with the locations of the modelled borehole profiles. Modified after Dvořák (1995).

3. illite crystallinity (Hb_{rel}) (see Dvořák, 1989) in the NE continuation of the Moravo-Silesian Palaeozoic outside the area shown in Fig. 2.

A general increase of thermal maturity from SE to NW has been observed in the regional distribution of R_{max} and Hb_{rel} (Dvořák and Wolf, 1979; Dvořák, 1989; Krejčí et al., 1994, 1996). Dvořák (1989) admitted that a simple extrapolation of the coalification trend to the original surface R_r values would suggest erosion of 1000 m in the foreland and "many" kilometres in the thrust-and-fold belt but rejected such a hypothesis as paleo-geographically unsustainable. He assumed that "presence of redeposited metamorphosed Devonian rocks as pebbles in the Upper Viséan flysch gave evidence against existence of thick Palaeozoic units". Dvořák (1995) hypothetised that the Variscan orogeny was associated with high temperature – low pressure conditions and possible geothermal gradients of 70–90°C/km in the foreland and over 200°C/km in the "intramontane region" (West of Drahany Upland) associated with extensive hydrothermal activity. Dvořák (1995) did not present any mathematical models to justify his palaeo-geothermal assessments.

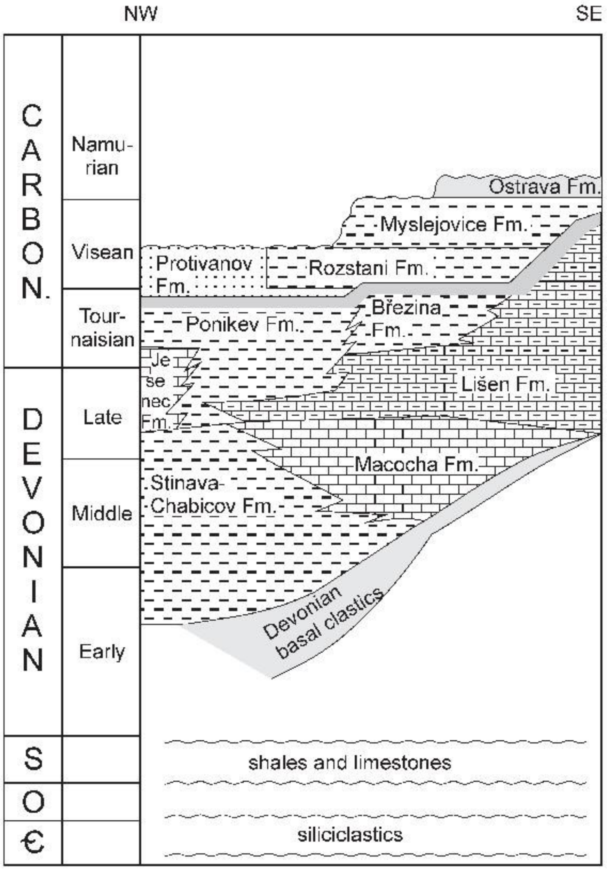

Fig. 3. Lithostratigraphy of the Palaeozoic in the Drahany Upland (modified after Dvořák, 1995). NW and SE directions related to the present geography.

Up to now, numerical models of thermal history have been applied in two adjacent areas. In the Late Palaeozoic Upper Silesian Basin, situated about 100 km NE of the studied area, the palaeo-geothermal gradient was calculated using the method of Buntebarth (1978, 1982) to be as high as 95°C/km and additional burial and erosion of 2–3 km (Šafanda et al., 1991). In the Nemcicky basin SE of the Drahany Upland forward models have recently been established by Francu et al. (1996) and Krejči et al. (1996) and suggest only mildly elevated palaeo-heat flow values. No basin modelling was applied in the Drahany Upland up to now.

4 Analytical methods

4.1 Sampling

Samples of dark shales, slates or shaly interlayers in carbonates were collected from fresh outcrops and borehole cores. Key localities are shown in Fig. 4 and often include several measured data populations. The total number of sampling sites is higher than shown.

4.2 Vitrinite reflectance

The measurement of reflectance was carried out in oil on polished surfaces using a Leitz Wetzlar MPV2 microscope-photometer, with a 50x objective and Leitz standards of 1.26 and 5.42% reflectance, in non-polarised (R_r) and plane-polarised light (R_{max} and R_{min}). In order to obtain a single parameter for the entire range of thermal maturity, the R_{max} and R_{min} values of particles with higher bireflectance were recalculated to random reflectance using the equation $R_r = (2*R_{max}+R_{min})/3$ (Teichmüller et al., 1998). The applicability of this equation was verified by a series of measurements under both conditions.

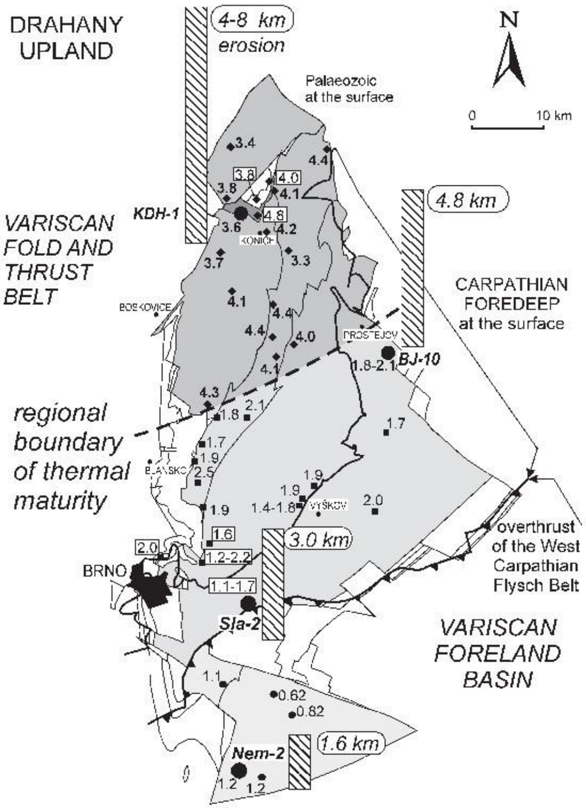

Fig. 4. Distribution of random vitrinite reflectance (R_r %) as a measure of thermal maturity in the Palaeozoic of the south-eastern Bohemian Massif (for geology see Fig. 2). The data are related to the Variscan flysch ("Culm"), those in rectangles to the pre-flysch units. Columns and values in rounded boxes show the thickness of the eroded overburden calculated using thermal modelling (relative scale).

4.3 Clay minerals

Clay-size material was separated from the rocks after removing the cements – carbonates, organic matter and iron oxides (Jackson, 1975). Two clay fractions $< 2\,\mu$m and $< 0.2\,\mu$m, were collected by centrifugation for determination of an illite crystallinity and expandability of illite-smectite respectively. Oriented slides were analysed both air-dry and after vapour glycolation (10 h. at 60°C, then 2 h. at 20°C) by X-ray diffraction: Philips diffractometer PW 1830 (generator) and PW 3020 (goniometer) with 0.02° step from 2 to 30° 2Θ. Illite crystallinity index (IC) was measured as peak width in $\Delta\,^\circ 2\Theta$ at half maximum (PWHM) of the 001 basal reflection of illite (Kübler, 1967) using background stripping and peak-fitting. The IC values were calibrated using international standards (Warr and Rice, 1994). Chlorite 002 was evaluated following Árkai et al. (1995) when illite was absent. Illite-smectite expandability was evaluated using NEWMOD program by Reynolds (1985) and diagrams by Środoń and Eberl (1984).

4.4 Thermal modelling

Burial and thermal history was simulated using the Petromod 1-D (IES) modelling software based on principles summarised by Welte and Yalçin (1988) and further explained in details by Poelchau et al. (1997) and Yalçin et al. (1997). Present steady-state or corrected subsurface temperature and heat flow data of Čermák (1977a) and Hurtig et al. (1991) were used as an input. The lower boundary conditions in the thermal model are given by evolving heat flow at the base of the sedimentary basin fill. The upper boundary conditions are controlled by palaeo-climate and temperature at the sediment/water interface. The forward modelling method takes into consideration a continuous compaction and change of the thermal field through geological time. The increase of vitrinite reflectance is calculated as a function of temperature and time using equations of chemical kinetics (Sweeney and Burnham, 1990). The model is run many times with various values of palaeo-heat-flow and palaeo-depth of burial and is considered possible when the calculated trend of vitrinite reflectance with depth fits the measured data.

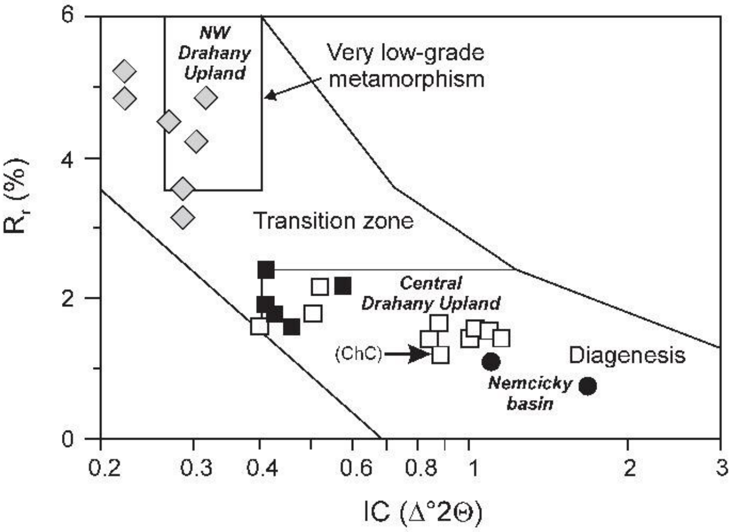

Fig. 5. Correlation of the illite crystallinity index (IC) and random vitrinite reflectance (R_r) representing partial areas of the studied region (Fig. 4). Empty boxes are calcareous shales and siltstones. The envelopes refer to the reanges of published data from other basins. The arrow indictes the equivalent illite crystallinity derived from the chlorite ChC value.

5 Results

The earlier R_{max} data from this region include 5 (Dvořák and Wolf, 1979) and 19 samples (Dvořák, 1989; Krejči et al., 1994) respectively. The newly measured 133 samples give more detailed regional distribution of the thermal maturity and are based on more measurements per sample (Fig. 4). The reliability of the thermal maturity data is verified on selected samples by parallel analyses of organic matter and clay minerals. The trend of the measured vitrinite reflectance (R_r) and illite crystallinity (IC, Fig. 5) falls within the correlation band observed in other basins (e.g. Duba and Williams-Jones, 1983; Árkai and Lelkes-Felvari, 1993; Henrichs, 1993; Underwood et al., 1993; for review see Francu et al., 1999). The applied boundaries of diagenetic through very low-grade to low-grade metamorphic zones follow the values of Robert (1988) and Merriman and Peacor (1999). These parameters indicate a wide span of palaeo-thermal stress decreasing from NW to SE (Fig. 4). Three groups of data plot together in Figs. 4 and 5. The highest maturity with R_r of 3.1–5.5% and IC = 0.22–0.38° 2Θ occurs in the northern part of the studied region. A jump to lower thermal maturity (R_r = 1.2–2.5% and IC = 0.38–0.46° 2Θ) is observed in the central part, south of a boundary going from Blansko to Prostejov and cutting across the lithostratigraphic units (dashed line in Fig. 4). Within this group a set of samples from Mokrá and Horakov (east of Brno) yield a broad range of IC values (0.40–1.15° 2Θ) while the R_r vary in a narrow range (open squares in Fig. 5). The less consistent clay parameters are related carbonate lithology where the detrital illite predominates over the newly formed illite even in the very fine grain size fraction. The lowest thermal maturity was measured in the SE in the Palaeozoic below the overhtrust of the West Carpathians.

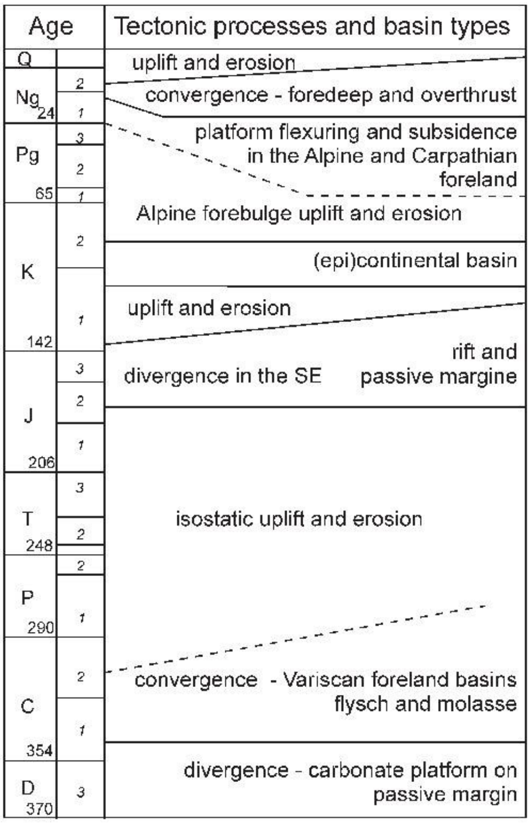

Fig. 6. Basic mechanisms controlling basin subsidence and inversions in the geological history of the SE Bohemian Massif. Ages after Gradstein and Ogg (1996).

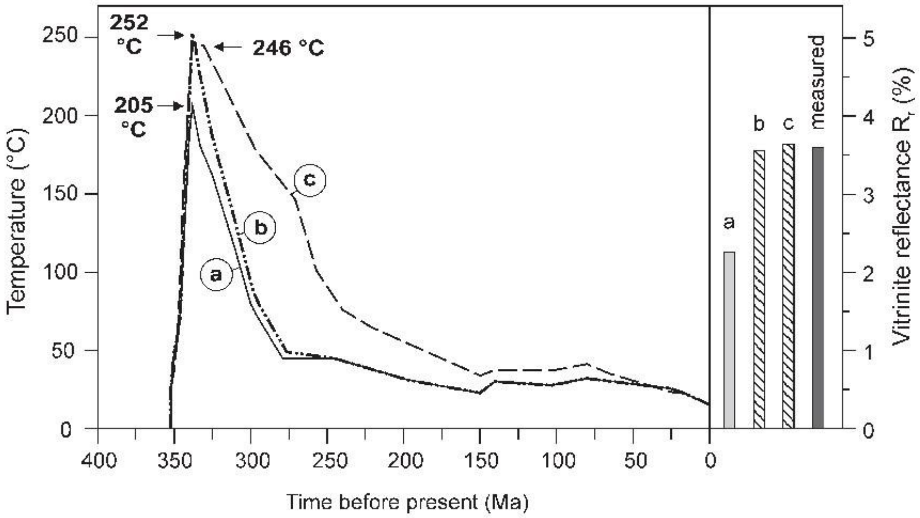

Fig. 7. Three forward models of thermal history of the deepest sample in the KDH-1 borehole profile: the calculated vitrinite reflectance using chemical kinetics (method of Sweeney and Burnham, 1990 and PetroMod 1-D program) is compared with the measured value.

Modelling was applied to quantify the thermal exposure and possible burial depth in these partial areas. It is based on the concept of the principal evolution phases with changing tectonic settings and related basin types as proposed in Fig. 6. The absolute ages are after Gradstein and Ogg (1996). The scenarios of the relative heat flow (q) changes in the model are tentatively chosen to follow the general trend in crustal extension (increase in q) and/or compression (decrease in q). Four model localities (Figs. 2 and 4) were selected to characterise the spatial relationships between the maximum burial depth within the Variscan orogeny, thermal exposure and later uplift.

5.1 The Northern sector

The N part of the Drahany Upland consists of the earliest Variscan flysch and the pre-flysch formations, i.e. Devonian to Lower Carboniferous slates and carbonates (Fig. 3). The vitrinite reflectance (Figs. 4, 5) in 75 samples from outcrops and shallow boreholes (50–250 m) suggest together with the illite crystallinity a thermal maturity equivalent to very low-grade metamorphism (Fig. 5). The differences in R_r among the samples are lower than the standard deviations of the data populations. No convincing steep maturation trend with present depth is observed either in KDH-1 or in the other 23 wells in this partial area. In the map of thermal maturity of the Visean flysch and pre-Visean units (marked separately in Fig. 4) the R_r data do not show any systematic regional trend within this sector. This is interpreted as a result of similar palaeo-thermal exposure of the rocks in the entire northern sector.

Thermal history is evaluated with alternative scenarios using a kinetic algorythm deviced for calculation of vitrinite maturation as a function of temperature and time (Sweeney and Burnham, 1990). The empirical polylines in Fig. 7 with different heating and cooling stages show the absolute temperature affecting the rocks at the base of the Protivanov Fm. (earliest Variscan flysch) in the KDH-1 borehole profile. Heating of rocks up to 205°C (Fig. 7a) yields maturity of only 2.2% R_r, i.e. by 1.5% lower than the measured vitrinite reflectance (Fig. 7 right). Both temperature-time curves (b) and (c) in Fig. 7 with maximum palaeo-temperature of 252 and 246°C respetively yield thermal maturity similar to the measured R_r data. The (c) scenario makes the same maturity as (b) with a cca. double exposure time within the top 10°C interval (236–246°C) and by 6°C lower maximum paleo-temperature (246°C). The slower cooling phase in (c) shows no visible effect on vitrinite reflectance.

The three curves in Fig. 7 represent partial outputs of 1-dimensional models of palaeo-heat flow and amount of burial and uplift (Fig. 8a, b, c). Each model yields a calculated maturity trend with depth, which is compared with the measured vitrinite reflectance. The first scenario (Fig. 8a) is conceived to get as close as possible to a shallow burial associated with extraordinary high palaeo-gradient as proposed by Dvořák (1989) or Dvořák et al. (1997). An empirical palaeo-heat flow of 140 mW*m^{-2} yields in carbonaceous siliciclastic lithologies a temperature distribution with palaeo-gradient of 123°C/km and 97°C/km at depth intervals of 0–1 and 1–2 km respectively. Such values are worldwide possible in ocean ridges, active rift and volcanic areas (Allen and Allen, 1990). The modelling results show that a burial to depth of 1.5 km and temperature of 205°C (Fig. 7a) is too shallow to produce the observed metamorphism even under such high geothermal conditions.

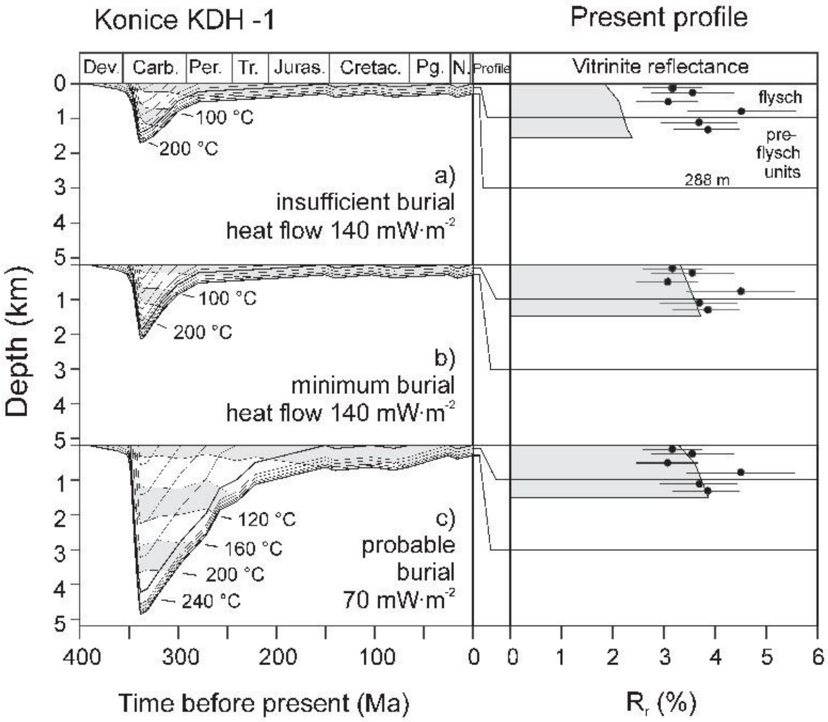

Fig. 8. Burial and thermal history scenarios of the KDH-1 borehole profile (Konice area) and their calibartion by measured vitrinite reflectance (R_r).

Table 1. Sensitivity analysis of different Carboniferous burial and thermal scenarios for the Nem-2 well

Model(Nem-2) Fig. 9	eroded units (km)	heat flow (mW/m^2)	geothermal gradient (°C/km) between 2–4 km
A (hot)	1.1	95	58
B (cold)	2.0	45	27
C (optimum)	1.6	63	37

Additional burial is simulated using the same heat flow (140 mW*m^{-2}) in the model shown in Fig. 8b. The resulting trend of calculated R_r with depth fits quite closely the measured borehole data. The interpretation is that depth of 1.9 km may be considered as the lowermost limit of the burial while the justification of such a heat flow remains open to discussion.

An alternative model (Fig. 8c) implies a palaeo-heat flow of 70 mW*m^{-2} which is slightly above the worldwide average (Allen and Allen, 1990). From the calibration it follows that burial to more than 4.5–5 km (decompacted) is necessary to match the real data. The scenario (c) may be considered rather as a mean than an upper limit and a model with burial to 9 km with 40 mW*m^{-2} produces only a slightly different result from that in Fig. 8c.

5.2 Central and SE part of the Drahany Upland

The surface geology of the central and SE parts of the Drahany Upland does not differ significantly in lithology and lithostratigraphy from the northern sector while the thermal maturity is distinctly lower and correspond to the late diagenetic alteration (wet and dry gas zones of Tissot and Welte, 1984).

Two borehole profiles are modelled in the area. The borehole Skalka BJ-10 situated S of Prostejov encountered the flysch unit (Myslejovice Fm.). The model of burial history in general is similar to that of the KDH-1 profile. The calibration by vitrinite reflectance of 1.77 a 2.09% R_r at depths of 51 and 110 m respectively suggests that erosional thickness is 4.8 km associated with palaeo-heat flow of 62 mW m^{-2} (3.5–5.7 km 65 and 50 mW m^{-2} respectively). The second modelled borehole, Slavkov-2 is situated next to the overthrust front of the West Carpathian Flysch Belt. It encounters the Devonian to Tournaisian basal clastics and carbonates (49–1320 m) and the Lower Miocene of the Carpathian Foredeep

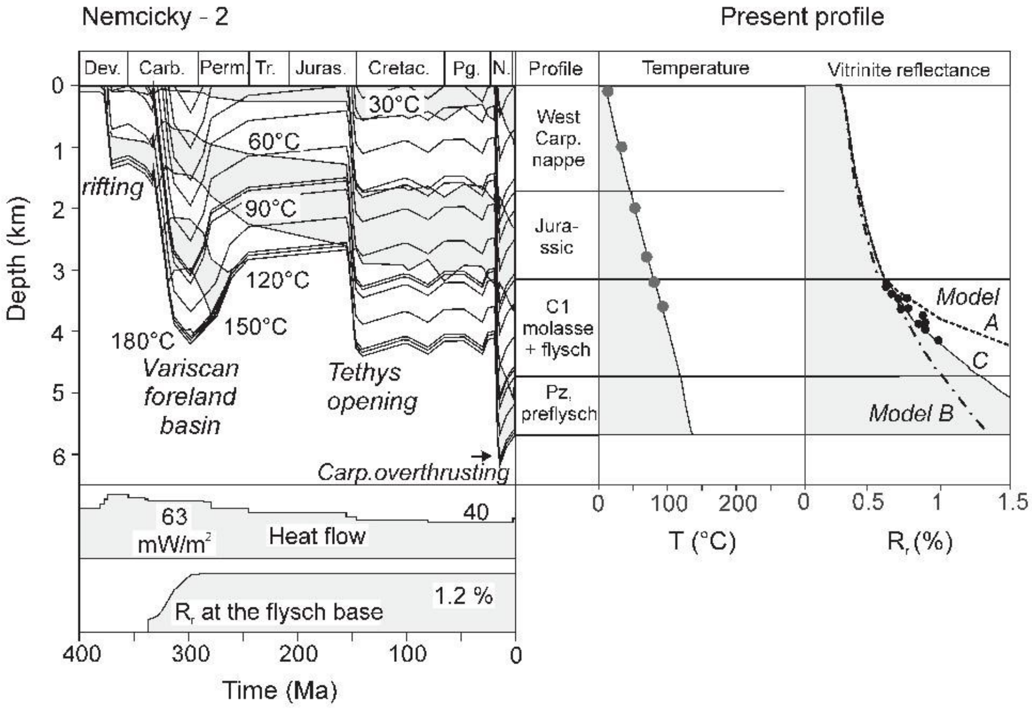

Fig. 9. Burial and thermal history of the Nem-2 borehole profile. Calibration data are depicted in the Upper Carboniferous part of the profile. Sensitivity analysis is shown by three curves of the modelled vitrinite reflectance with depth (see Table 1).

(0–49 m). The R_r data of 1.1 and 1.7% at depth of 136 and 1253 m respectively calibrate a model with 3.0 km erosion and 63 mW m^{-2}.

5.3 The Palaeozoic below the Carpathians

This part of the Palaeozoic was encountered in numerous deep boreholes below the nappes of the Outer Carpathians. Devonian and Carboniferous sediments in the S and SE in this area have diagenetic illite/smectite with 23–35% S and R_r = 0.6–1.1%. Organic matter maturity is equivalent to the oil window (Francu et al., 1996).

The borehole Nemcicky-2 with almost 5.5 km total depth is newly modelled and considered representative for this area. The sedimentary record comprises Cambrian siliciclastics (Jachowicz and Přichystal, 1997), Devonian to Carboniferous carbonates (Macocha and Lišen Fms.), relatively thin flysch (50 m of Myslejovice Fm.) and over 1000 m of Variscan molasse. Unconformities indicate erosional events within the Lower Carboniferous carbonates (Lišen Fm.) and between the Palaeozoic and the overlying autochthonous Jurassic marls.

The erosion of the uppermost Carboniferous units was followed by deposition and erosion of Mesozoic and Tertiary sediments and emplacement of West Carpathian thrust sheets (Krejčí et al., 1996). From the low coalification gradients within Jurassic, Paleogene and Neogene units in this area (Francu et al., 1996) it may be concluded that the heat flow during the Jurassic, and Tertiary did not exceed the maximum ones during the Late Carboniferous (Fig. 9). Calibration of the model by vitrinite reflectance of 0.60–0.94% at depth range of 3204–4664 (Fig. 9) suggests erossion of 1600 m and 63 mW m^{-2} during the Late Carboniferous. The sensitivity analysis was applied to evaluate the effect of different heat flow at the basin fill / basement boundary and the thickness of the eroded Palaeozoic units. The upper and lower limits (Table 1) were tested under a chosen condition that the thermal maturity at the top of the preserved Carboniferous fits the calibration data. The A and B models only fit about half of the calibration data and deviate from the data trend at greater depth. These alternatives are exagerated and probable values of deviations from the optimum input parameters may by half narrower.

6 Interpretation and discussion

The measured vitrinite reflectance in shallow boreholes in northern and central sectors of the studied area do not allow to make strict conclusions on the palaeogradient. It is, however, possible to assess the firm and weak points in the alternative concepts of geological and geothermal evolution.

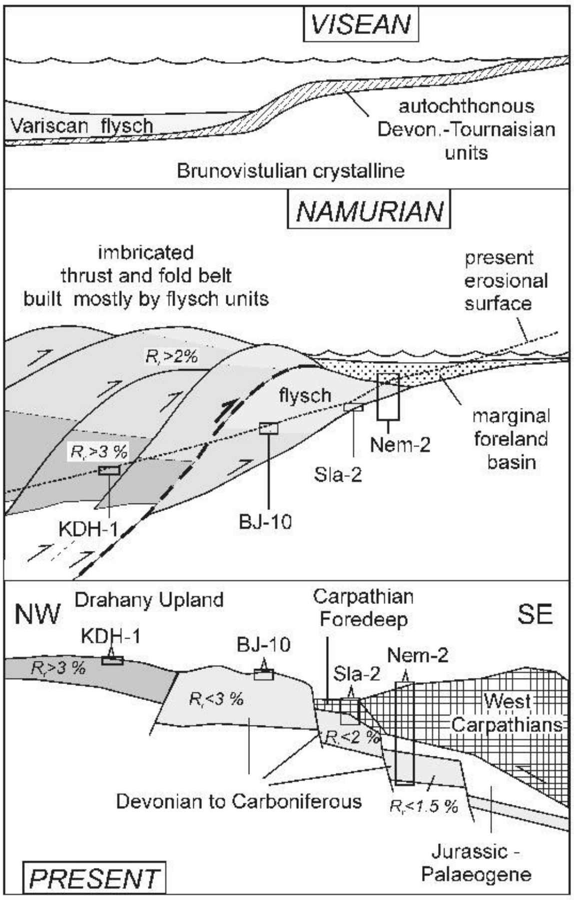

Fig. 10. Tectonic sketch (vertically not to scale) of the frontal Variscan fold and thrust belt and foreland basin in the Visean, Namurian and present. Wells with modelled burial histories are shown. The shaded areas represent thermal maturity ranges given by vitrinite reflectance (R_r %).

According to the first scenario, the Rheno-Hercynian Palaeozoic units in SE Czech Republic formed at shallow burial and under increasing palaeo-geothermal gradient from 90°C.km^{-1} in the foreland to 200°C.km^{-1} in the hinterland (e.g. Dvořák, 1989, Dvořák et al., 1997). The other concept emphasises considerable vertical movements during the last phases of the Variscan orogeny.

Mere recalculation of the vitrinite reflectance to maximum palaeo-tempearture (e.g. Fig. 7) gives values ranging from 220 to 290°C in the northern sector and from 120 to 180°C in the central area with a gap of 40°C at the Blansko-Prostejov line. Numeric simulation of continuously changing regional palaeo-heat flow does not produce such a more or less monotonous diagenetic-to-metamorphic pattern within the partial areas and such a contrast at their boundary.

The experience from other regions and calculations show that stacking of thrust sheets in frontal accretion wedges brings a relative decrease of the geothermal gradient (Angevine and Turcotte, 1983; Wygrala et al., 1990). As the extent of deformation and thrusting within this part of Rheno-Hercynian zone increases from the frontal part (S-SE) to the internal zone (N-NW), one can imply that the palaeogradients would rather decrease than increase in this direction.

In the proposed models the assumed deep burial was caused by additional deposition of a thicker flysch sedimentary pile, possibly followed by emplacement of the frontal part of the Variscan orogenic wedge from the NW during the Viséan and Late Carboniferous. The accretion mechanism with compression and shortening would first increase the burial and later cause detachment, imbrication, and exhumation of the earlier buried strata within the advancing orogenic complex (Fig. 10). It is possible to attribute the sudden jump in thermal maturity at the Blansko-Prostejov line to post-diagenetic/metamorphic movements with a more profound uplift and erosion of the northern sector in respect to the central Drahany Upland (Fig. 10). The inverted diagenetic or metamorphic zonation formed in this way with higher-grade in the rear and top and lower-grade rocks below and towards the foreland has been observed in several other orogenic systems (Houseknecht and Matthews, 1985; Fritz et al., 1996; Warr and Greiling, 1996; Merriman and Frey, 1999).

Thin-skinned overthrusting associated with Rheno-Hercynian orogenic wedge propagation in the Moravian-Silesian zone about 50–100 km NW of the Drahany Upland was characterised by Cháb et al. (1984), Čížek and Tomek (1991), Kumpera and Martinec (1995), and Hladil et al. (1999). The new data and modelling suggest that this type of tectonics could play an important role also in the Drahany area.

The amplitude of uplift and thickness of the eroded Upper Palaeozoic units decrease from 4.5–9 km in the north to about 4.6 (3.5–5.7) km in the central part, and 1.6 (1.1–2.0) km in the frontal Rheno-Hercynian zone and associated foredeep in the SE. The magnitude of erosion implies that the Palaeozoic units extended further to the south and east and also covered the crystalline of the Brno Massif (Fig. 2) which was later uplifted and exposed at the surface.

The calculation of the palaeo-geothermal gradient in Late Carboniferous Upper Silesian Basin (200 km NE of the Drahany Upland) published by Šafanda et al. (1991) using the Buntebarth method resulted in a very high gradient of 95°C/km and partly open question of the amount of erosion. Our results of the finite-element forward modelling offer a geological history with palaeo-geothermal gradients of 31–39°C / km (0–4 km) and heat flow densities of 50–65 $\mathrm{mW/m^2}$ during maximum burial. Using the relationships given by Čermák (1977b) these values would correspond to Palaeozoic crustal thickness of 30 km in the Variscan foredeep basin and 40 km in the thin-skinned orogenic wedge.

6.1 Comparison with analogous basins and thrust belts

A similar geological setting has been studied in the Ruhr area where Devonian to Upper Carboniferous formations are partly covered by the low-thermally mature Cretaceous. Littke et al. (1994), Büker et al. (1995) and Littke et al. (2000) used vitrinite reflectance, 1-D and 2-D modelling programmes and documented an increase of the palaeo-heat flow from the orogenically thickened crust in the south towards the Rheno-Hercynian foreland with relatively thinner crust. Based on vitrinite coalification trends and modelling they calculated eroded thicknesses of the Westphalian to Stephanian from 6 km in the south (Rheno-Hercynian) to 2.5 km in the more external foreland basin (Ruhr Basin) in the north. Due to erosion the present coalification rank at the surface is higher in the hinterland than in the foreland even though the palaeo-geothermal gradient decreases in the opposite direction.

A 10 km deep burial of Upper Carboniferous strata and later uplift associated with the Ouachita orogenesis (300 Ma) in Oklahoma were calculated by Houseknecht and Matthews (1985) using vitrinite reflectance as thermal maturity parameter. A close relationship of the foreland propagating thrust wedge and the decreasing metamorphic grade and diagenesis from the rear to the frontal part and autochthonous underthrust substratum was documented in the external Variscides in Southwest England (Warr et al. 1991). The above mentioned case histories and the area studied in this paper are consistent in several aspects and document a more general validity of the observed diagenetic patterns and the respective thermal models related to the Variscan orogeny.

7 Conclusions

1. Newly measured vitrinite reflectance document more densely the diagenetic to very low-grade metamorphic pattern in the SE end of the Rheno-Hercynian zone. The juxtaposed high and intermediate values of vitrinite reflectance along the boundary between Blansko (Sloup) and Prostejov in the central part of the Drahany Upland suggest a significant postdiagenetic tectonic activity and uplift. More detailed structural investigation of this line is needed.

2. A general stepwise decrease in metamorphic grade and diagenesis of the siliciclastic rocks in the Palaeozoic of the SE Bohemian Massif towards the frontal zone of the Variscan fold and thrust belt gives evidence of a close relationship of the thermal alteration and the Rheno-Hercynian thin-skinned thrust wedge propagation. The present geographic orientation of the described trends and orogenic front may be different from that during the Carboniferous.

3. The present distribution of the vitrinite reflectance and illite crystallinity can be explained by a model of a deeper, mainly tectonically driven burial with lower heat flow in the rear Rheno-Hercynian zone and relatively shallower sedimentary burial with equal or slightly higher heat flow in the foreland basin. During the orogenic wedge propagation, the subsidence and burial migrated with time towards the foreland and was probably associated with uplift of the thrust sheets in the rear.

4. The regional metamorphic and diagenetic pattern and basin modelling suggests that the diagenetic and very low-grade metamorphic grade could not be attained merely by high gradients without significant burial and erosion. The calculated values of the eroded thickness range from 4–9 km in the fold-and-thrust belt in the present north to 1.6 km in the marginal foreland basin in the south-east.

5. The presented data show similar features regarding the metamorphic and diagenetic patterns in respect to geometry of orogenic belts and their forelands observed in the Ruhr Basin, Rhenish Massif, external Variscides in Southwest England, and Ouachita Mountains. The modelling shows that the magnitude of probable erosion is similar in the mentioned segments of the Ouachita and Rheno-Hercynian zones.

Acknowledgements. This research benefited from EUROPROBE, a programme of the European Science Foundation. The authors wish to thank J. Hladil, D. H. Welte, V. Čermák, Z. Stráník, and O. Krejčí for stimulating discussions, and R. F. Sachsenhofer for reviewing and critical comments.

References

Allen, P. A. and Allen, J.: Basin Analysis: Principles and Applications, Blackwell, London, 451, 1990.

Angevine, C. L. and Turcotte D. L.: Oil generation in overthrust belts, The AAPG Bulletin, 67, 235–241, 1983.

Árkai, P. and Lelkes-Felvari, G: The effect of lithology, bulk chemistry and modal composition on illite "crystallinity" – a case study from the Bakony Mts., Hungary, Clay Min., 28, 417–433, 1993.

Árkai, P., Sassi, F. P., and Sassi, R.: Simultaneous measurements of chlorite and illite crystallinity: a more reliable tool for monitoring low-to very low grade metamorphism in metapelites. A case study from the Southern Alps (NE Italy), Eur. J. Mineral., 7, 1115–1128, 1995.

Barker, C.: Thermal modelling of petroleum generation: theory and applications, Elsevier Science B. V., Amsterdam, 1–512, 1996.

Bostick, N. H.: Microsopic measurements on the level of catagenesis of solid organic matter in sedimentary rocks to aid exploration for petroleum and to determine former burial temperatures – a review, Soc. Econ. Paleont. Miner., Spec. Publ., 26, 17–43, 1979.

Büker, C, Littke, R., and Welte, D.: 2D-modelling of thermal evolution of Carboniferous and Devonian sedimentary rocks of the eastern Ruhr basin and northern Rhenish Massif, Germany, Z. deut. geol. Ges., 146, 321–339, 1995.

Buntebarth, G.: The degree of metamorphism of organic matter in sedimentary rocks as a paleothemometer applied to the Upper Rhine Graben. – Pageo. 117, 83–91, 1978.

Buntebarth, G.: Geothermal history estimated from the coalification of organic matter, Tectonophysics, 83, 101–108, 1982.

Čermák, V.: Heat flow map of the Bohemian Massif, J. Geoph., 42, 455, 1977a.

Čermák, V. and Bodri, L.: Time-dependent crustal temperature modelling: Central Alps, Tectonophysics, 257, 7–24, 1996.

Čermák, V.: Relation between heat flow and crustal thickness, Acta Geol. Acad. Scient. Hungaricae, 21, 4, 261–263, 1977b.

Čížek, P. and Tomek, C.: Large-scale thin-skinned tectonics in the eastern boundary of the Bohemian Massif, Tectonics, 10, 2, 273–286, 1991.

Cháb, J., Fišera, M., Fediuková, E., Novotný, P., Opletal, M., and Skácelová, D.: Problems of tectonic and metamorphic evolution of the eastern part of the Hrubý Jeseník Mts., Sbor. geol. ved, Geol., 39, 27–72, 1984.

Duba, D. and Williams-Jones, A. E.: The application of illite crystallinity, organic matter reflectance, and isotopic techniques to mineral exploration: a case study in southwestern Gaspe Quebec, Econ. Geol., 78, 1350–1363, 1983.

Dvořák, J.: Anchimetamorphism in the Variscan tectogene in Central Europe – its relationship to tectogenesis, Vest. ÚÚG, 64, 1, 17–30, 1989.

Dvořák, J.: Stratigraphy, in: Dallmeyer, R. D., Franke, W., and Weber, K. (Eds.): Pre-Permian geology of Central and Eastern Europe, Springer-Verlag, Berlin - Heidelberg - New York, 479–489, 1995.

Dvořák, J., Honek, J., Pešek, J., and Valterová, P.: Deep borehole evidence for a southward extension of the Early Namurian deposits near Nemcicky, S. Moravia, Czech Republic: implication for rapid coalification, in: Gayer, R. and Pešek, J. (Eds.): European Coal Geology and Technology, Geological Society Special Publication No. 125, 179–193, 1997.

Dvořák, J. and Skoček, V.: Reconstruction of the paleo-heat flow regime in two areas of the Variscan orogene, N. Jb. Geol. Paläont. Mh. 9, 517–527, 1975.

Dvořák, J. and Wolf, M.: Thermal metamorphism in the Moravian Paleozoic (Sudeticum, ČSSR), N. Jb. Geol. Paläont. Mh., 10, 596–607, 1979.

Ellenberger, F. and Tamain, A. L. G.: Hercynian Europe, Episodes 1, 22–27, 1980.

Finger, F. and Steyrer, H. P.: A tectonic model for the eastern Variscides: Indications from a chemical study of amphibolites in the south-eastern Bohemian Massif, Geologica Carpathica, 46, 137–150, 1995.

Francu, E.: Optical properties of organic matter in Devonian and Lower Carboniferous black shales in the northern Drahany Upland, Bull. of Czech Geol. Soc., 75, 2, 115–120, 2000.

Francu, E., Francu, J., and Kalvoda, J.: Illite crystallinity and vitrinite reflectance in Paleozoic siliciclastics in the SE Bohemian massif as evidence of the thermal history, Geologica Carpatica, 50, 5, 365–372, 1999.

Francu, J., Radke, M., Schaefer, R. G., Poelchau, H. S., Čáslavský, J., and Boháček, Z.: Oil-oil and oil-source rock correlations in the northern Vienna Basin and adjacent Carpathian Flysch Zone (Czech and Slovak area), in: Wessely, G. and Liebl, W. (Eds.): Oil and gas in alpidic thrust belts and basins of Central and Eastern Europe, EAGE Spec. Publ. No. 5, 343–353, 1996.

Franke, W.: Tectonostratigraphic units in the Variscan belt of central Europe, in: Dalmeyer, R. D. (Ed.): Terranes in the circum-Atlantic Palaeozoic orogens, Geol. Soc. Am. Spec. Paper, 230, 67–90, 1989.

Fritz, H., Dallmeyer, R. D., and Neubauer, F.: Thick-skinned versus thin-skinned thrusting: Rheology controlled thrust propagation in the Variscan collisional belt (The souteastern Bohemian Massif, Czech Republic – Austria), Tectonics, 15, 6, 1389–1413, 1996.

Gradstein, F. M. and Ogg, J.: A Phanerozoic time scale, Episodes 19, 1–2, 3–5, 1996.

Hartley, A. J. and Otava, J.: Sediment provenance and dispersal in a dep marine foreland basin: the Lower Carboniferous Culm basin, Czech Republic, J. Geol. Soc., 158, 137–150, 2001.

Henrichs, C.: Sedimentographische Untersuchungen zur Hochdiagenese in der Kossen-Formation (obere Trias) der westlichen Ostalpen und angrenzender Südalpengebiete, Bochumer geol. u. geotechn. Arb., 40, 1–206, 1993.

Hladil, J., Krejčí, Z., Kalvoda, J., Ginter, M., Galle, A., and Beroušek, P.: Carbonate ramp environment of Kellwasser time interval (Lesní lom, Czechoslovakia), Bull. Soc. belg. Géol., 100, 1–2, 57–119, 1992.

Hladil, J., Melichar, R., Otava, J., Galle, A., Krs, M., Man, O., Pruner, P., Čejchan, P., and Orel, P.: The Devonian in the Easternmost Variscides, Moravia: a holistic analysis directed towards comprehension of the original context, Abh. Geol. B.-A., 54, 24–47, 1999.

Houseknecht, D. W. and Matthews, S. M.: Thermal maturity of Carboniferous strata, Ouachita Mountains, The AAPG Bulletin, 69, 3, 335–345, 1985.

Hurtig, E., Čermák, V., Haenel, R., and Zui, V. (Eds.): Geothermal atlas of Europe, Hermann Haack Verlag, Gotha, 160pp, 1991.

Issler, D. R. and Beaumont, C.: A finite element model of the subsidence and thermal evolution of extensional basins: application to the Labrador continental margin, in: Naeser, N. D. and McCulloh, T. H. (Eds.): Thermal history of sedimentary basins. Methods and case histories, Springer, New York - Berlin - Heidelberg, 239–267, 1989.

Jackson, M. L.: Soil chemical analysis. Advanced course, published by the author, Dept. Soil Sci., Univ. Wisconsin, Madison, 1–895, 1975.

Jachowicz, M. and Přichystal, A.: Lower Cambrian sediments in deep boreholes in south Moravia, J. Czech Geol. Soc., 72, 4, (in Czech) 329–332, 1997.

Kalvoda, J.: Comments on possible levels for Lower Carboniferous subdivision and results from Moravia, Geobios, 27, 5, 615–619, 1994.

Krejčí, O., Francu, J., Müller, P., Pereszlenyi, M., and Stráník, Z.: Geologic structure and hydrocarbon generation in the Carpathian flysch belt of southern Moravia, J. Czech Geol. Soc., 69, 4, 13–26, 1994.

Krejčí, O., Francu, J., Poelchau, H. S., Müller, P., and Stráník, Z.: Tectonic evolution and oil and gas generation model in the contact area of the North European Platform with the West Carpathians, in: Wessely, G. and Liebl, W. (Eds.): Oil and Gas in Alpidic Thrustbelts and Basins of Central and Eastern Europe, EAGE Spec Publ. No. 5, 177–186, 1996.

Kübler, B.: La crystallinite de l'illite et les zones tout a fait superieures du metamorphisme, in: Etages Tectoniques, Colloque de Neuchatel, 1966, A la Baconniere, Neuchatel, 105–122, 1967.

Kumpera, O. and Martinec, P.: The development of the Carboniferous accretionary wedge in the Moravian-silesian Palaeozoic Basin, J. Czech Geol. Soc., 40, 1–2, 47–64, 1995.

Littke, R., Büker, C., Lückge, A., Sachsenhofer, R. F., and Welte, D. H.: A new evaluation of palaeo-heat flows and eroded thicknesses for the Carboniferous Ruhr basin, western Germany, Int. J. Coal Geol., 26, 155–183, 1994.

Littke, R., Büker, C., Hertle, M., Karg, H., Stroetmann-Heinen, V., and Oncken, O.: Heat flow evolution, subsidence and erosion in the Rheno-Hercynian orogenic wedge of central Europe, in: Franke, W., Haak ,V., Oncken, O., Tanner, D. (Eds.): Orogenic processes: Quantification and modelling in the Variscan Belt, 231–256, 2000.

Merriman, R. J. and Frey, M.: Patterns of very low-grade metamorphism in metapelitic rocks, in: Frey, M. and Robinson, D. (Eds.): Low-grade metamorphism, Blackwell Science, Oxford, 61–107, 1999.

Merriman, R. J. and Peacor, D. R.: Very low-grade metapelites: mineralogy, microfabrics and measuring reaction progress, in: Frey, M. and Robinson, D. (Eds.): Low-grade metamorphism, Blackwel Science, Oxford, 10–60, 1999.

Mísař, Z., Dudek, A., Havlena, V., and Weiss, J. Z.: Geology of Czechoslovakia I., Bohemian Massif, SPN, Praha, 380 pp (in Czech), 1983.

Poelchau, H. S., Baker, D. R., Hantschel, Th., Horsfield, B., and Wygrala, B.: Basin simulation and the design of the conceptual basin model, in: Welte, D. H., Horsfield, B., Baker, D. R. (Eds.): Petroleum and basin evolution, Springer, Berlin - Heidelberg - New York, 5–70, 1997.

Reynolds, R. C.: NEWMOD a computer program for the calculation of one-dimensional diffraction patterns of mixed-layered clays: Reynolds, R. C. and Brook, D., Hannover, New Hamshire, 1985.

Robert, P.: Organic metamorphism and geothermal history, ELF-Aquitaine and D. Reidl, Dordrecht, 311 pp, 1988.

Šafanda, J., Honek, J., Weiss, G., and Buntebarth, G.: Paleogeothermics in the Czechoslovak part of the Upper Silesian Basin, Geophys. J. Int., 104, 625–633, 1991.

Skoček, V.: Regional and geological interpretation of organic matter coalification in the Late Palaeozoic sediments of the Bohemian Massif, J. Czech Geol. Soc., 51, 13–24 (in Czech), 1976.

Środoń, J. and Eberl, D. D.: Illite, in: Bailey, S. W. (Ed.): Micas, Reviews in Mineralogy 13, Mineralogical Society of America, 495–544, 1984.

Sweeney, J. J. and Burnham, A. K.: Evaluation of a simple model of vitrinite reflectance based on chemical kinetics, AAPG Bull., 74, 1559–1570, 1990.

Teichmüller, M., Taylor, G. H., and Littke, R.: The nature of organic matter – macerals and associated minerals, in: Taylor, G. H., Teichmüller, M., Davis, A., Diessel, C. F. K., Littke, R., Robert, P. (Eds.): Organic petrology, Gebrüder Borntraeger, Berlin, 175–274, 1998.

Tissot, B. P. and Welte, D. H.: Petroleum formation and occurrence, 2nd edn. Springer, Berlin - Heidelberg - New York, 699pp, 1984.

Underwood, M. B., Laughland, M. M., and Kang, S. M.: A comparison among organic and inorganic indicators of diagenesis and low-temperature metamorphism, Tertiary Shimanto belt, Shikoku, Japan. Geol. Soc. Amer., Spec. Paper, 273, 45–61, 1993.

Ungerer, P., Burrus, J., Doligez, B., Chénet, P. Y., and Bessis, F.: Basin evaluation by integrated two-dimensional modelling of heat transfer, fluid flow, hydrocarbon generation, and migration, AAPG Bull., 74, 3, 309–335, 1990.

Vavrdová, M.: Acritarchs of Cambrian age in the basal clastics underlying the Moravian Devonian (Nemcicky-6 borehole), Zemní plyn a nafta, 42, 1, 31–32 (in Czech), 1997.

Waples, D. W.: Time and temperature in petroleum formation: application of Lopatin's method to petroleum exploration, AAPG Bull., 64, 916–926, 1980.

Warr, L. N. and Greiling, O. R.: Thrust-related very low grade metamorphism in the marginal part of an orogenic wedge, Scandinavian Caledonides, Tectonics, 15, 6, 1213–1229, 1996.

Warr, L. N., Primmer, T. J., and Robinson, D.: Variscan very low-grade metamorphism in Southwest England: a diastathermal and thrust-related origin, J. metamorph. Geol., 9, 751–764, 1991.

Warr, L. N and Rice, H. N. A: Interlaboratory standardization and calibartion of clay mineral crystallinity and crystalite size data, J. metamorph. Geol., 12, 141–152, 1994.

Welte, D. H. and Yalçin, M. N.: Basin modelling – A new comprehensive method in petroleum geology, Adv. Organic Geochemistry, 13, 1–3: 141–151, 1988.

Wygrala, B. P, Yalçin, M. N., and Dohmen, L.: Thermal histories and overthrusting – application of numerical simulation technique. Advances in organic geochemistry 1989, Org. Geochem., 16, 267–285, 1990.

Yalçin, M. N., Littke, R., and Sachsenhofer, R. F.: Thermal history of sedimentary basins, in: Welte, D. H., Horsfield, B., Baker, D. R. (Eds.): Petroleum and basin evolution, Springer, Berlin - Heidelberg - New York, 73–167, 1997.

Příloha 2

Geršlová E., Goldbach M., Geršl M., Skupien P. (2016) Heat flow evolution, subsidence and erosion in Upper Silesian Coal Basin, Czech Republic. – International Journal of Coal Geology International Journal of Coal Geology 154-155, 30-42.

International Journal of Coal Geology 154–155 (2016) 30–42

Contents lists available at ScienceDirect

International Journal of Coal Geology

journal homepage: www.elsevier.com/locate/ijcoalgeo

Heat flow evolution, subsidence and erosion in Upper Silesian Coal Basin, Czech Republic

Eva Geršlová [a,]*, Marek Goldbach [a], Milan Geršl [b], Petr Skupien [c]

[a] Department of Geological Sciences, Faculty of Science, Masaryk University, Kotlářská 2, 611 37 Brno, Czech Republic
[b] Department of Agriculture, Food and Environmental Engineering, Mendel University, Zemědělská 1, 613 00 Brno, Czech Republic
[c] Institute of Geological Engineering, Technical University of Ostrava, 17. Listopadu 15/2172, 708 33 Ostrava, Czech Republic

ARTICLE INFO

Article history:
Received 13 August 2015
Received in revised form 10 December 2015
Accepted 15 December 2015
Available online 17 December 2015

Keywords:
Thermal maturity
Vitrinite reflectance
RE pyrolysis
Upper Silesian Coal Basin
1D basin modelling

ABSTRACT

The deep boreholes in the Upper Silesian Coal Basin provide a valuable material to evaluate thermal maturity of the present Carboniferous units. 17 boreholes were used for evaluating expected paleothicknesses of the missing units and the maximum temperatures reached via 1D modelling. The models consider the geological evolution concepts accepted for the region. The reliability of the final thermal models was calibrated with vitrinite reflectance data. Vitrinite reflectance varies between 0.46 and 2.32% R_r indicating thermally early mature to over mature organic matter for the Ostrava Fm. and Karviná Fm. The coal rank increases from the east to the west. Based on the data from RockEval pyrolysis all samples from the Ostrava and Karviná Fms. belong to type III kerogen. The RE results show that the source potential of the Carboniferous sediments was not spent in full as part of the Variscan tectogen. Burial and thermal history on the Czech side of the Upper Silesian Coal Basin was reconstructed. The set of several 1D simulations proved that the thickness of the missing Palaeozoic molasses association is 2500 to 3400 m in the foreland and 1800 to 2000 m for the platform. The maximum burial is expected at the end of the Westphalian. The consequent sedimentation of the Carpathian Foredeep and nappe thrusting did not change the Palaeozoic thermal maturity pattern within the tested area of the USCB.

1. Introduction and geological setting

The Upper Silesian Coal Basin (USCB) is one of the largest bituminous coal basins in Europe with a total area of 7000 km^2 located in Poland (78%) and the Czech Republic (22%). The first findings of bituminous coal are reported in 1763–1770 and coal mining has developed here since the 1830s with geological exploration and investigation of the technological properties of the coal. The USCB (Fig. 1) is spatially related to the Rhenohercynian and Subvariscan Zones of the Variscan orogeny (Aust et al., 1997; Kotas, 1995; Grygar and Vavro, 1995). In this respect, the USCB occupies a similar structural position to those of other European coal basins aligned in the belt stretching from the British Isles across Germany and Poland to the eastern part of Europe. The sedimentary history (Fig. 2) in the study area began with a deposition of Cambrian siliciclastics (Bula et al., 1997) on the Cadomian metamorphic and igneous rocks of the Brunovistulicum crystalline. The crystalline complex (Brunovistulicum) forming part of the Northern European shield – Baltica – lies at depths of 1–12 km below the surface and forms the basement underlying the coal-bearing sequences.

The Devonian (Givetian) transgression of basal clastics reached a broad regional extent. During the Frasnian to lower Visean, shelf carbonates and later shales were deposited in a passive margin setting. During the latest Visean and Namurian A, the Avalon plate approached Europe and created a frontal accretion wedge with slope turbidites of the Hradec-Kyjovice Fm. with sandstones, greywacke, siltstones and shales. This synorogenic foreland basin is also known as the "Culm" facies or "Variscan Flysch" in other parts of Europe. During the final phases of the continent–continent collision in the Namurian A, the marginal foreland (Subvariscan) basin formed with paralic coal-bearing Ostrava Fm. (Dopita et al., 1997; Grygar and Vavro, 1995). This formation with a maximum thickness of 3200 m represents a wide spectrum of sedimentary environments from the purely continental settings to zones of transition into marine settings. During the Namurian B–Namurian C and lowermost Westphalian, folding and thrusting in the hinterland supplied material to the foreland basin and the Karviná Fm. was deposited in a lacustrine environment. The sedimentation of Karviná Fm. (maximum thickness of 1000 m approximately) began after a short hiatus between the Namurian A and Namurian B. The preserved surface of the Palaeozoic formed an erosional truncation and there are post-Westphalian strata of an unknown thickness missing in the present USCB. The Cracow sandstone and relicts of Kwaczala arkose provide evidence that the deposition continued up to the Stephanian, at least, in the northern Polish part of the USCB (Kotas, 1995). Most of the USCB area (Fig. 1) in Poland and the Czech Republic is covered by the Lower and Middle Miocene (Karpatian and Badenian) claystones and

---

* Corresponding author.
E-mail address: gerslova.eva@gmail.com (E. Geršlová).

http://dx.doi.org/10.1016/j.coal.2015.12.007
0166-5162/

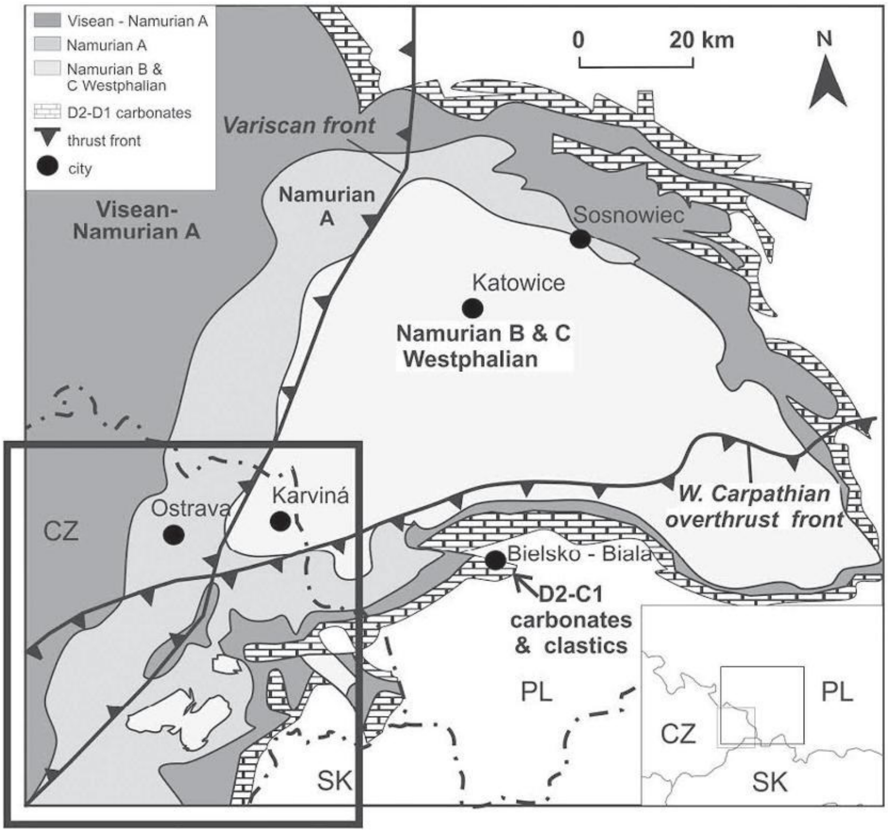

Fig. 1. Sub-crop of the pre-Tertiary map of the Czech part with the Palaeozoic units in the USCB and the Variscan and Carpathian overthrust fronts (modified from Aust et al., 1997). The study area is marked by a bold frame.

sandstones of the Carpathian Foredeep basin and the overthrust of the Western Carpathian Flysch Belt (Picha et al., 2006).

The technological coal parameters in the SW part of the USCB have been studied since the beginning of the last century (e.g. Patteisky, 1928; Stahl, 1933; Dopita and Zeman, 1960; Dopita et al., 1997; Sivek et al., 2003; Martinec et al., 2005). The newly published papers deal with the coal properties in respect to coal bed methane, CBM (Kandarachevová et al., 2009; Hemza et al., 2009). Weiss (1980) examined the coalification trend in the USCB based on a decrease to the volatile matter (V^{daf}) with a depth of several hundred well profiles. The regional coalification pattern in the USCB has been presented on several maps (Dopita and Zeman, 1960; Chudý, 1992; Pešek et al., 1998 in the Czech Republic and Kotas et al., 1983; Jurczak-Drabek, 1996 in Poland). The atlas compiled by Sivek et al. (2003) refers to the previous maps and includes coalification maps of the average value of measured vitrinite reflectance calculated from V^{daf} for each formation and member in the SW USCB. As a conclusion the coal rank is decreasing from W to E with elevated values along the Orlová Thrust. The main aim of the present paper was to demonstrate regional trends in thermal maturity and estimate the amount of the expected eroded layers from Palaeozoic units.

1.1. Tectonic setting

The structure of the USCB is the result of the Variscan orogeny. The geological structures defined in the region in terms of asymmetry involve the western region of the Variscan foredeep with a predominance of fold and thrust tectonics – determined by a considerably greater mobilisation of the brunovistulic fundamental – and the eastern unit of the "Upper Silesian Block" (Kotas, 1985) with a predominance of an extensional tectonic fault to the east. Both of these units are separated by the structure of Orlova Thrust. The basin asymmetry is most probably caused by the varying substrate stability and the migration of the Variscan orogeny processes from W to E in time. The current structure was determined by local changes in the strain field during the main phase of the Variscan orogeny and was completed by Alpine orogeny. It is not yet well defined what deformation of the USCB strata was caused by the Alpine orogeny. Very little information is available as regards the period between the most recent Carboniferous deposits and the earliest Miocene sediments in this area (Kumpera and Martinec, 1995; Ptáček et al., 2012).

2. Samples and methods

17 boreholes assessed in terms of changes in thermal maturity with depth on the Czech side of USCB. Since earlier research focused exclusively on the quality of the present coal seams, it provides a comprehensive database of parameters on coal seam maceral composition and vitrinite reflectance values (a total of 1301 archival data). The reconstruction of the temperature gradient in the past necessitates uninterrupted recording of thermal conversion within the depth interval of maximum breadth. For this reason, thermal maturity was determined

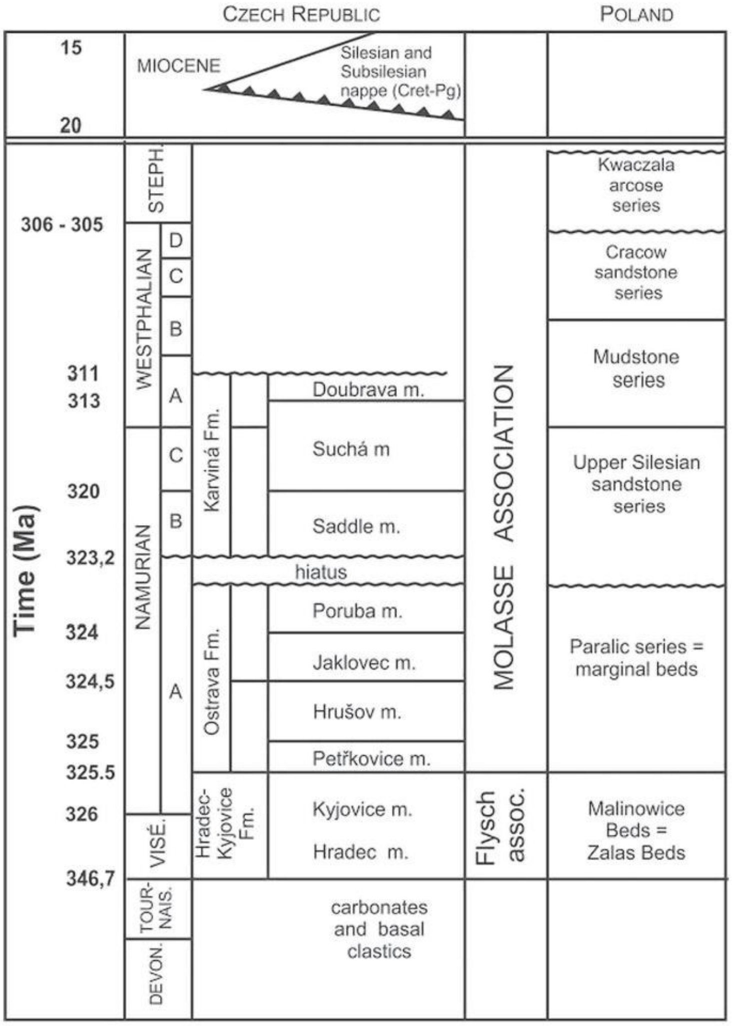

Fig. 2. Lithostratigraphy of the USCB according to Dopita et al. (1997).

by RockEval pyrolysis in 24 deep boreholes covering the entire area of interest (Fig. 3). One-dimensional (1D) models of the burial history and thermal maturity were constructed using PetroMod software 2014.2 (Schlumberger). The conceptual model for the area was reconstructed by means of the published concepts of structural evolution of the area presented in Chapter 1. Input parameters for modelling include lithology of strata, thickness, age, and heat flow (Table 1). Maturity modelling was calibrated by the measured vitrinite reflectance values (VR_r). The thickness of Carboniferous sediments eroded and thermal evolution during Variscan orogeny were subject of the sensitivity analyses.

Polished surfaces were prepared from 41 samples taken from deep boreholes and random reflectance measurements were carried out in oil under non-polarised light (R_r) using the Leitz Wetzlar MPV2 microscope-photometer with a 50× objective. The Leitz standards of 1.26 and 5.42% reflectance were used following the established procedure described by Taylor et al. (1998).

Geochemical analysis in terms of TOC measurements and Rock Eval pyrolysis covered 188 Carboniferous coals, dark black shales and slates (Table 2). The samples were dried, pulverised, homogenised and sieved through a 1 mm mesh. All samples were subjected to elemental analysis of total organic carbon (TOC) using the Eltra Metalyt CS 100/1000S apparatus and the RockEval 5 pyrolysis (Espitalie, 1986; Lafargue et al., 1998; Behar et al., 2001). The measured parameters comprise free and bound hydrocarbons (S1 and S2), and a peak temperature of pyrolysis (T_{max}).

3. Results and discussion

3.1. Organic matter characterisation

The bulk geochemical characterisation of the OM in the Ostrava and Karvina Fm. (Table 2, Fig. 4) identified a dominant kerogen type. Both of the formations revealed a maximum range in terms of total organic content within the studied series. The total organic carbon (TOC) of the Karviná Fm. varies between 0.82% and 86.4%. These coal seams and coaly siltstones are thermally mature with T_{max} of 431–471 °C. They are characterised by a decreasing evolution path of the hydrogen

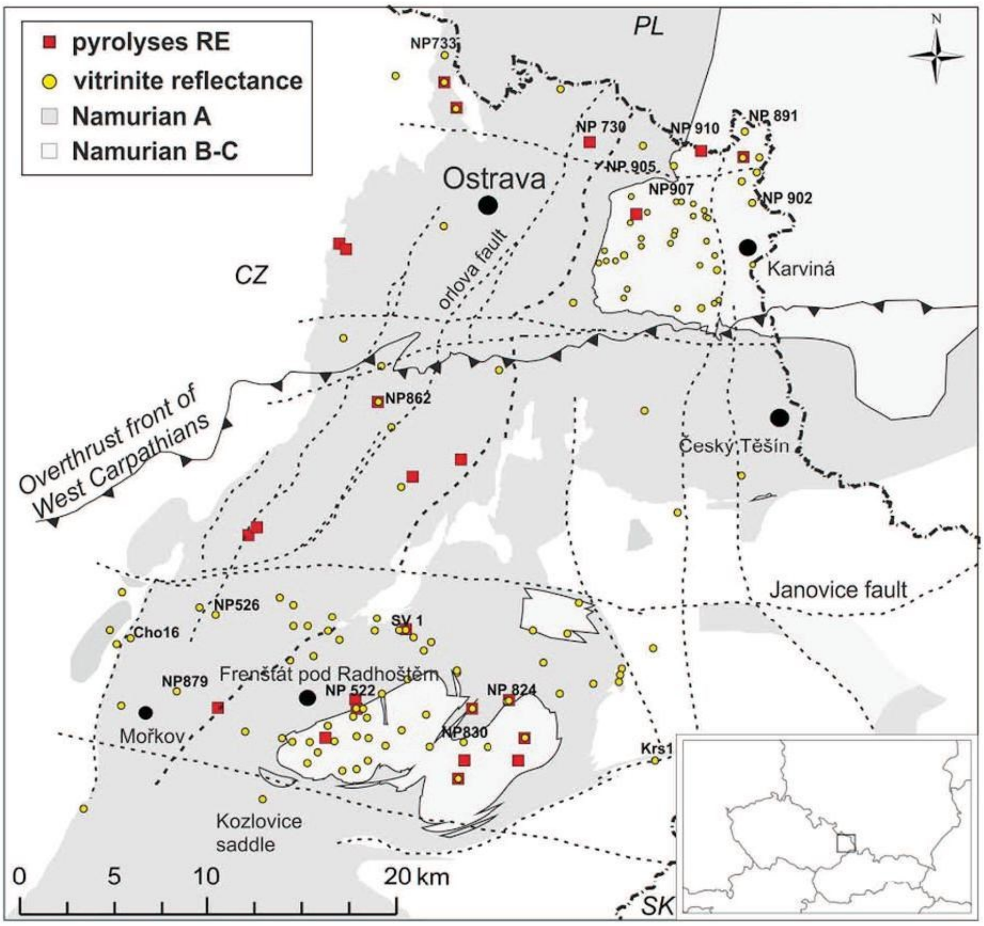

Fig. 3. Sub-crop map of the studied SW part of the USCB with boreholes with vitrinite reflectance and pyrolysis RockEval data.

index from 206 to 5 mg·g^{-1}TOC. The unusually high values of the T$_{max}$ (524–544 °C) represent oxidised samples with elevated vitrinite reflectance (1.96–2.13% R$_r$). The TOC of the Ostrava Fm. vary between 0.21% and 89.1%. These samples are thermally mature with T$_{max}$ of 423–525 °C. They are characterised by the evolution path of the hydrogen index (Fig. 4) that decreases from 237 to 1 mg·g^{-1}TOC. The very low HI values are attributed to the high thermal maturity of the coals. The HI–T$_{max}$ diagram shows that all samples from the Ostrava and Karviná Fms. are type III kerogen.

3.2. Thermal maturity

The vitrinite reflectance (VR$_r$) increases with depth (Fig. 5a, b) from 0.46 to 2.32% R$_r$ and the overall coalification trend does not show

Table 1
1D model input table of the basic geological data for the NP824 borehole.

Name	Top	Base	Thickness	Eroded thickness	Deposited from	Deposited to	Eroded from	Eroded to	Lithology
Thrust belt	−394	603	997		16.50	3.00			Sandstone + shale + conglomerate
Carpathian Foredeep	603	613	10		17.50	16.50			Sandstone + shale
Karvina Fm.	613	638	25	1800	323.20	311.00	311.00	100.00	Shale + siltsone + coal (pure)
Prokop coal	638	640	2		323.60	323.50			Coal (pure)
Poruba Mb.	640	731	91		324.00	323.60			Shale + siltsone + coal (pure)
Jaklovec Mb.	731	824	93		324.50	324.00			Shale + siltsone + coal (pure)
Hrusov Mb.	824	868	44		325.00	324.50			Shale + siltsone + coal (pure)
Petrkovice Mb.	868	1144	276		325.50	325.00			Shale + siltsone + coal (pure)
Hradec-Kyjovice Fm.	1144	1390	246		346.70	328.00			Sandstone + shale + conglomerate
Carbonates	1390	1427	37		360.00	346.70			Limestone + shale + sandstone
Carbonates	1427	1573	146		374.00	360.00			Limestone + shale + sandstone
Basal clastics	1573	1597	24		397.00	385.00			Sandstone + conglomerate
Crystalline basement	1597	1606	9		600.00	550.00			Granite (500 Ma old)

Table 2

Bulk geochemical data of Rock–Eval and TOC analysis with calculated parameters.

Borehole	Depth (m)	Formation	TOC (wt.%)	S_1 (mg/g)	S_2 (mg/g)	T_{max} (°C)	HI
NP 203	310.0	Ostrava Fm.	2.07	0.02	0.06	462	3
NP 203	349.3	Ostrava Fm.	1.20	0.02	0.08	470	7
NP 203	389.3	Ostrava Fm.	1.73	0.02	0.12	471	7
NP 203	489.0	Ostrava Fm.	1.86	0.02	0.1	470	5
NP 203	498.0	Ostrava Fm.	1.63	0.03	0.12	472	7
NP 203	532.0	Ostrava Fm.	1.44	0.04	0.06	465	4
NP 203	565.0	Ostrava Fm.	0.94	0.02	0.04	465	4
NP 203	613.4	Ostrava Fm.	15.57	0.13	1.04	473	7
NP 203	637.3	Ostrava Fm.	1.49	0.02	0.04	459	3
NP 203	680.0	Ostrava Fm.	1.50	0.02	0.04	464	3
NP 707	862.0	Ostrava Fm.	1.89	0.03	0.08	468	4
NP 707	863.7	Ostrava Fm.	2.54	0.04	0.16	472	6
NP 707	1093.0	Ostrava Fm.	1.62	0.02	0.06	461	4
NP 707	1110.2	Ostrava Fm.	5.72	0.08	0.16	467	3
NP 707	1172.0	Ostrava Fm.	2.25	0.06	0.1	463	4
NP 707	1205.0	Ostrava Fm.	1.90	0.05	0.08	459	4
NP 707	1268.8	Ostrava Fm.	1.14	0.01	0.04	463	4
NP 825	1207.8	Karvina Fm.	17.91	0.22	27.88	451	156
NP 825	1222.5	Karvina Fm.	12.94	0.14	14.7	450	114
NP 825	1265.0	Ostrava Fm.	3.61	0.07	3.02	462	84
NP 825	1273.4	Ostrava Fm.	2.15	0.06	1.24	460	58
NP 825	1292.7	Ostrava Fm.	1.16	0.03	0.48	464	41
NP 825	1350.0	Ostrava Fm.	2.81	0.21	2.36	460	84
NP 825	1363.0	Ostrava Fm.	1.75	0.09	0.84	464	48
NP 910	881.2	Karvina Fm.	3.42	0.08	2.88	450	84
NP 910	972.3	Karvina Fm.	6.73	0.11	5.78	449	86
NP 910	1038.8	Karvina Fm.	1.54	0.04	0.7	464	45
NP 910	1115.2	Karvina Fm.	1.38	0.03	0.54	464	39
NP 910	1201.2	Ostrava Fm.	3.42	0.13	3.1	466	91
NP 910	1252.7	Ostrava Fm.	3.99	0.07	2.18	466	55
NP 910	1332.3	Ostrava Fm.	7.32	0.21	5.66	469	77
NP 910	1378.0	Ostrava Fm.	3.99	0.36	2.9	469	73
NP 910	1444.9	Ostrava Fm.	0.77	0.04	0.24	463	31
NP 910	1517.0	Ostrava Fm.	25.10	0.97	17.92	468	71
NP 910	1542.7	Ostrava Fm.	1.14	0.05	0.38	469	33
NP 910	1591.0	Ostrava Fm.	2.77	0.13	0.62	467	22
NP 910	1619.3	Ostrava Fm.	1.75	0.07	0.58	471	33
NP 910	1659.6	Ostrava Fm.	1.98	0.05	0.62	471	31
NP 910	1792.0	Ostrava Fm.	1.46	0.05	0.32	471	22
NP 910	1856.5	Ostrava Fm.	1.77	0.03	0.1	470	6
NP 910	1889.6	Ostrava Fm.	2.25	0.07	0.56	471	25
SV-1	878.5	Ostrava Fm.	2.11	0.1	3.28	437	155
SV-1	903	Ostrava Fm.	1.79	0.07	2.28	438	127
SV-1	940	Ostrava Fm.	2.46	0.05	0.68	447	28
SV-1	1005.5	Ostrava Fm.	0.49	0.02	0.02	457	4
SV-1	1025.7	Ostrava Fm.	1.66	0.08	2.14	442	129
SV-1	1074.6	Ostrava Fm.	1.86	0.08	1.12	449	60
SV-1	1105.5	Ostrava Fm.	1.62	0.06	1.08	449	67
SV-1	1127.7	Ostrava Fm.	1.23	0.04	0.66	450	54
SV-1	1148	Ostrava Fm.	1.26	0.02	0.26	451	21
SV-1	1180.5	Ostrava Fm.	0.47	0.02	0.02	464	
SV-1	1200.2	Ostrava Fm.	4.65	0.23	5.42	453	117
SV-1	1278.2	Ostrava Fm.	0.38	0.02	0.2	423	53
SV-1	1341.1	Ostrava Fm.	2.03	0.08	0.72	455	35
SV-1	1355.1	Ostrava Fm.	0.79	0.02	0.48	448	61
SV-1	1379.3	Ostrava Fm.	0.90	0.05	0.3	457	33
SV-1	1405.8	Ostrava Fm.	2.26	0.12	1.26	451	56
SV-1	1425.5	Ostrava Fm.	1.14	0.05	0.44	456	39
SV-1	1448.9	Ostrava Fm.	1.42	0.05	0.56	457	39
SV-1	1470.7	Ostrava Fm.	1.46	0.05	0.38	458	26
NP 522	1006.1	Ostrava Fm.	2.22	0.07	1.06	452	48
NP 522	1025.2	Ostrava Fm.	1.34	0.1	0.66	452	49
NP 522	1045.7	Ostrava Fm.	2.25	0.1	1.26	452	56
NP 522	1102.1	Ostrava Fm.	1.38	0.04	0.46	456	33
NP 522	1125.6	Ostrava Fm.	3.97	0.15	4.76	449	120
NP 522	1150.6	Ostrava Fm.	1.38	0.11	0.68	454	49
NP 522	1175.7	Ostrava Fm.	0.40	0.02	0.12	458	30
NP 522	1259	Ostrava Fm.	1.86	0.13	2.00	458	108
NP 522	1295.9	Ostrava Fm.	1.73	0.24	0.98	460	57
NP 522	1331	Ostrava Fm.	1.43	0.14	0.88	462	62
NP 522	1352	Ostrava Fm.	1.39	0.13	0.70	461	50
NP 522	1375	Ostrava Fm.	1.61	0.14	0.78	464	48
NP 522	1395	Ostrava Fm.	2.28	0.12	0.98	465	43
NP 522	1439	Ostrava Fm.	1.18	0.05	0.48	462	41
NP 522	1458	Ostrava Fm.	23.95	2.53	21.40	463	89

Table 2 (*continued*)

Borehole	Depth (m)	Formation	TOC (wt.%)	S_1 (mg/g)	S_2 (mg/g)	T_{max} (°C)	HI
NP 522	1522	Ostrava Fm.	1.45	0.06	0.40	464	28
NP 522	1551	Ostrava Fm.	4.34	0.36	2.66	469	61
NP 522	1575	Ostrava Fm.	1.63	0.07	0.36	465	22
NP 522	1603	Ostrava Fm.	1.55	0.13	0.28	467	18
NP 522	1623	Ostrava Fm.	0.94	0.11	0.28	467	30
NP 522	1655	Ostrava Fm.	1.78	0.02	0.38	465	21
NP 522	1680	Ostrava Fm.	1.34	0.03	0.32	466	24
NP 522	1701	Ostrava Fm.	0.98	0.04	0.24	469	24
NP 522	1726	Ostrava Fm.	2.39	0.04	0.52	471	22
NP 522	1774	Ostrava Fm.	1.93	0.03	0.50	472	26
NP 522	1804	Ostrava Fm.	1.20	0.03	0.18	467	15
NP 522	1825	Ostrava Fm.	3.94	0.11	0.70	470	18
NP 534	889.3	Ostrava Fm.	1.03	0.06	0.64	458	62
NP 534	995.4	Ostrava Fm.	1.53	0.07	0.2	458	13
NP 534	1151	Ostrava Fm.	3.17	0.18	1.02	464	32
NP 534	1515.7	Ostrava Fm.	1.46	0.04	0.32	471	22
NP 534	1643.4	Ostrava Fm.	1.44	0.04	0.24	472	17
NP 534	1821.2	Ostrava Fm.	1.24	0.03	0.1	475	8
NP 730	913.6	Ostrava Fm.	1.75	0.09	0.88	464	50
NP 730	923.1	Ostrava Fm.	1.82	0.13	1.04	465	57
NP 730	1044.5	Ostrava Fm.	4.72	0.26	2.26	467	48
NP 730	1061.5	Ostrava Fm.	1.58	0.07	0.58	469	37
NP 730	1096.6	Ostrava Fm.	2.36	0.1	0.64	467	27
NP 730	1131.8	Ostrava Fm.	2.35	0.08	0.42	467	18
NP 730	1168.4	Ostrava Fm.	2.55	0.07	0.44	469	17
NP 730	1179	Ostrava Fm.	1.22	0.05	0.98	472	80
NP 730	1268	Ostrava Fm.	2.45	0.03	0.24	470	10
NP 730	1313.8	Ostrava Fm.	1.75	0.04	0.3	472	17
NP 730	1343.7	Ostrava Fm.	1.49	0.04	0.24	472	16
NP 730	1391.5	Ostrava Fm.	1.55	0.56	0.36	473	23
NP 730	1418	Ostrava Fm.	2.08	0.05	0.36	472	17
NP 730	1447.5	Ostrava Fm.	1.48	0.02	0.12	473	8
NP 730	1482.4	Ostrava Fm.	2.95	0.06	0.36	473	12
NP 730	1510.4	Ostrava Fm.	1.18	0.02	0.06	473	5
NP 730	1547	Ostrava Fm.	1.94	0.02	0.02	495	1
NP 730	1628.3	Ostrava Fm.	1.29	0.06	0.16	472	12
NP 730	1647.5	Ostrava Fm.	2.43	0.04	0.2	474	8
NP 730	1676.5	Ostrava Fm.	1.53	0.01	0.04	465	3
NP 818	1290.3	Ostrava Fm.	1.29	0.14	0.07	458	5
NP 818	1338.7	Ostrava Fm.	1.76	0.17	1.56	457	89
NP 824	1035.4	Ostrava Fm.	0.66	0.01	0.30	455	45
NP 824	1053.15	Ostrava Fm.	5.01	0.48	8.26	445	165
NP 824	1089.4	Ostrava Fm.	1.87	0.12	1.12	449	60
NP 824	1107.7	Ostrava Fm.	1.03	0.06	0.66	455	64
NP 824	1163.4	Ostrava Fm.	1.38	0.08	1.36	451	99
NP 824	1172.7	Ostrava Fm.	1.44	0.08	1.60	451	111
NP 824	1177	Ostrava Fm.	1.1	0.05	0.80	455	73
NP 824	1200.1	Ostrava Fm.	2.06	0.02	1.72	455	83
NP 824	1212.4	Ostrava Fm.	1.9	0.19	1.64	455	86
NP 824	1286.8	Ostrava Fm.	1.11	0.05	0.68	458	61
NP 824	1345.3	Ostrava Fm.	0.56	0.05	0.12	459	21
NP 824	1374	Ostrava Fm.	1.67	0.08	1.20	464	72
NP 824	1376.2	Ostrava Fm.	1.8	0.04	1.12	467	62
NP 824	1391	Ostrava Fm.	1.31	0.07	0.56	461	43
NP 824	1444	Ostrava Fm.	1.96	0.16	1.06	465	54
NP 824	1454.6	Ostrava Fm.	1.19	0.10	0.40	465	34
NP 824	1463.6	Ostrava Fm.	1.42	0.08	0.26	464	18
NP 824	1480.1	Ostrava Fm.	1.49	0.13	0.68	465	46
NP 824	1522.6	Ostrava Fm.	1.18	0.10	0.34	467	29
NP 862	770.0	Ostrava Fm.	1.09	0.07	0.2	460	18
NP 862	778.4	Ostrava Fm.	3.48	0.13	1.92	481	55
NP 862	802.7	Ostrava Fm.	32.76	0.32	27.76	476	85
NP 862	845.2	Ostrava Fm.	15.89	0.85	14.46	477	91
NP 862	875.8	Ostrava Fm.		0.09	1.62	480	
NP 862	905.4	Ostrava Fm.	15.46	0.25	12.75	477	82
NP 862	943.0	Ostrava Fm.	10.99	0.31	7.78	480	71
NP 862	978.5	Ostrava Fm.	2.42	0.07	0.92	482	38
NP 862	1004.4	Ostrava Fm.	2.54	0.08	0.86	492	34
NP 862	1022.0	Ostrava Fm.	1.6	0.02	0.46	500	29
NP 862	1051.0	Ostrava Fm.	0.92	0.01	0.14	505	15
NP 862	1127.3	Ostrava Fm.	3.98	0.1	1.64	485	41
NP 862	1156.4	Ostrava Fm.	2.08	0.04	0.6	501	29
NP 862	1193.2	Ostrava Fm.	5.65	0.14	1.58	484	28
NP 862	1220.1	Ostrava Fm.	3.18	0.05	0.96	493	30
NP 862	1220.9	Ostrava Fm.	4.6	0.05	1.9	491	41

(*continued on next page*)

Table 2 (*continued*)

Borehole	Depth (m)	Formation	TOC (wt.%)	S_1 (mg/g)	S_2 (mg/g)	T_{max} (°C)	HI
NP 862	1239.2	Ostrava Fm.	3.17	0.08	0.96	496	30
NP 862	1270.7	Ostrava Fm.	3.34	0.07	1.02	496	31
NP 862	1314.5	Ostrava Fm.	10.30	0.09	2.72	508	26
NP 862	1358.0	Ostrava Fm.	1.44	0.04	0.24	513	17
NP 862	1369.3	Ostrava Fm.	6.07	0.09	1.48	515	24
NP 862	1407.2	Ostrava Fm.	7.95	0.11	2.18	508	27
NP 862	1445.8	Ostrava Fm.	19.93	0.17	6.64	508	33
NP 862	1491.6	Ostrava Fm.	1.85	0.04	0.26	520	14
NP 862	1539.7	Ostrava Fm.	1.79	0.05	0.28	523	16
NP 862	1569.8	Ostrava Fm.	2.29	0.03	0.4	519	17
NP 862	1635.9	Ostrava Fm.	1.80	0.04	0.28	525	16
NP 862	1700.0	Ostrava Fm.	1.47	0.04	0.18	523	12
SV 6	1333.5	Karvina Fm.	1.64	0.1	0.12	526	7
SV 6	1336.3	Karvina Fm.	3.74	0.09	0.28	544	7
SV 6	1349.5	Karvina Fm.	1.32	0.08	0.1	541	8
SV 6	1359.9	Karvina Fm.	1.31	0.04	0.06	469	5
SV 6	1362.2	Karvina Fm.	1.59	0.05	0.12	457	8
SV 6	1373.1	Karvina Fm.	2.09	0.06	0.48	524	23
SV 6	1380.0	Karvina Fm.	1.68	0.1	0.72	471	43
SV 6	1380.2	Karvina Fm.	1.58	0.09	0.88	464	56
SV 6	1417.2	Karvina Fm.	1.85	0.05	0.9	461	49
SV 6	1443.5	Ostrava Fm.	3.11	0.09	1.7	466	55
SV 6	1443.6	Ostrava Fm.	2.58	0.09	1.26	466	49
SV 6	1443.7	Ostrava Fm.	2.33	0.08	1.16	468	50
SV 6	1443.7	Ostrava Fm.	2.57	0.08	1.22	467	47
SV 6	1444.0	Ostrava Fm.	2.16	0.06	1.22	460	56
SV 6	1445.8	Ostrava Fm.	3.03	0.04	1.76	468	58
SV 6	1445.9	Ostrava Fm.	3.26	0.04	2.4	465	74
SV 6	1447.3	Ostrava Fm.	1.44	0.05	0.74	468	51
SV 6	1483.8	Ostrava Fm.	5.90	0.18	4.02	457	68
SV 6	1493.7	Ostrava Fm.	1.48	0.05	0.74	460	50
SV 6	1494.2	Ostrava Fm.	1.81	0.04	0.74	464	41
SV 6	1510.2	Ostrava Fm.	1.96	0.08	1.08	464	55
SV 6	2005.0	Ostrava Fm.	2.60	0.07	0.88	494	34
SV 6	2080.0	Ostrava Fm.	2.12	0.07	0.36	497	17
SV 6	2112.0	Ostrava Fm.	1.41	0.01	0.42	501	30
SV 6	2116.0	Ostrava Fm.	1.05	0.04	0.18	504	17
SV 6	2130.0	Ostrava Fm.	1.23	0.03	0.26	504	21

TOC: total organic carbon, wt.%. S1: volatile hydrocarbon (HC) content, mg HC/g rock. S2: remaining HC generative potential, mg HC/g rock. T_{max}: temperature at maximum of S2 peak. HI: hydrogen index = S2 ∗ 100/TOC, mg HC/g TOC.

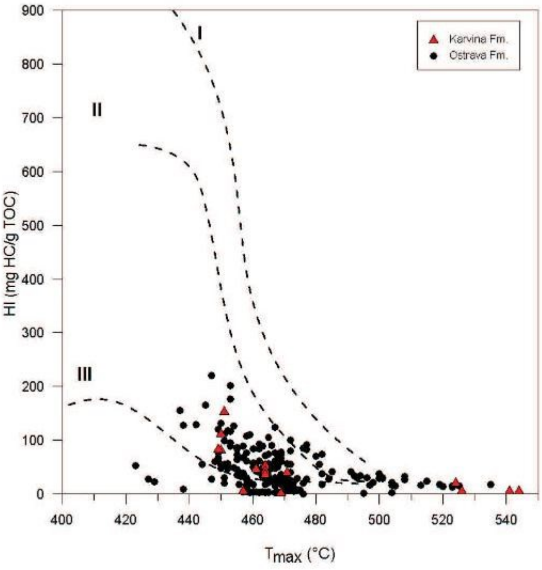

Fig. 4. Kerogen types based on the HI and T_{max} for Karviná and Ostrava Fms.

significant differences among the eastern and the western part. The current depth position of the Palaeozoic sediments is determined by the presence of the thick West Carpathian nappes that reach thickness of over 2800 m to the south.

To assign a palaeo geothermal gradient in the boreholes, where the vitrinite reflectance data were not available, the T_{max} from RE pyrolysis was used. To establish a relationship between R_r and T_{max} both parameters were measured on a set of 41 samples (Table 3). Correlation among both of the parameters demonstrated a fairly good agreement. The observed relationship of T_{max}–% R_r (Fig. 6) is in agreement with the date published from the Paris Basin (Espitalie et al., 1985) and the Polish part of the USCB (Kotarba et al., 2002).

3.3. 1D burial history reconstruction

The age of each stratigraphic unit was adjusted in agreement with the lithostratigraphic division of the Czech and Polish parts of the USCB (Kotas, 1995; Dopita et al., 1997; Sivek et al., 2003) as well as with radiometric dating according to Davydov et al. (2012) and fission track dating according to Botor (2014). The thickness of the stratigraphic units in the evaluated boreholes was taken from the borehole profiles.

The evolution of the Upper Silesian Basin from the Devonian to recent (Fig. 7) was split into the five major tectonic phases:

1. Devonian to Early Carboniferous extension with carbonate platform development on passive margin;
2. Late Carboniferous/Permian compression during the Variscan foreland basins development and the sedimentation of the flysch and molasses facies with thermal subsidence;

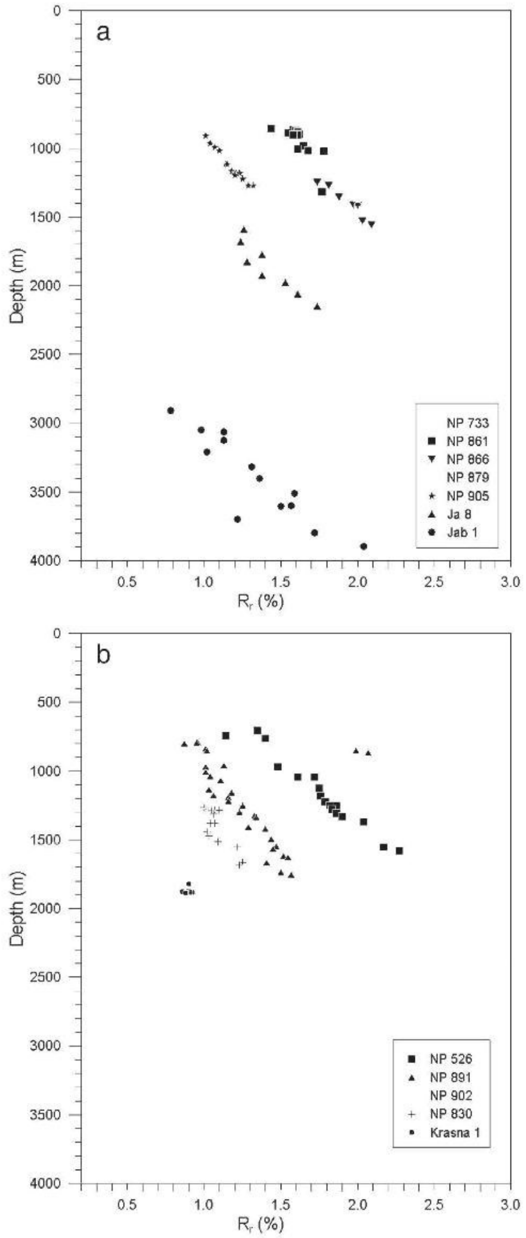

Fig. 5. Coalification trends for selected borehole profiles in the western (a) and the eastern part (b) of the USCB.

3. Permian to Jurassic period with erosion of the Palaeozoic nappes;
4. Jurassic–Cretaceous extension and passive margin development; and
5. Compression regime starting during Palaeogene platform flexuring followed by the sedimentation of the foredeep and overthrust of Carpathian nappes during the Neogene.

The expected palaeo-heat flow evolution was examined to evaluate their influence on the thermal maturity curve for the Ostrava and Karviná Fms. within the Czech part of the USCB. The HF1 represents

Table 3
Results of parallel measurement of vitrinite reflectance (R_r) and maximum pyrolyses temperature (T_{max}).

Borehole	Depth (m)	Formation	R_r (%)	T_{max} (°C)
NP 824	1035.4	Ostrava Fm.	0.98	455
NP 824	1053.15	Ostrava Fm.	0.92	445
NP 824	1089.4	Ostrava Fm.	1.00	449
NP 824	1107.7	Ostrava Fm.	0.81	455
NP 824	1163.4	Ostrava Fm.	1.04	451
NP 824	1177	Ostrava Fm.	1.03	455
NP 824	1212.4	Ostrava Fm.	1.04	455
NP 824	1286.6	Ostrava Fm.	1.09	458
NP 824	1444	Ostrava Fm.	1.11	465
NP 824	1522.6	Ostrava Fm.	1.16	467
NP 710	690	Ostrava Fm.	1.62	498
NP 818	1290.3	Ostrava Fm.	1.04	458
NP 818	1338.7	Ostrava Fm.	0.95	457
NP 534	889.3	Ostrava Fm.	0.94	458
NP 534	995.4	Ostrava Fm.	1.20	458
NP 534	1151	Ostrava Fm.	1.24	464
NP 534	1515.7	Ostrava Fm.	1.28	471
NP 534	1643.4	Ostrava Fm.	1.45	472
NP 522	1025.2	Ostrava Fm.	0.92	452
NP 522	1150.6	Ostrava Fm.	0.89	454
NP 522	1259	Ostrava Fm.	0.95	458
NP 522	1395	Ostrava Fm.	0.99	465
NP 522	1592	Ostrava Fm.	1.26	464
NP 522	1680	Ostrava Fm.	1.24	466
NP 522	1774	Ostrava Fm.	1.38	472
NP 522	1825	Ostrava Fm.	1.28	470
NP 825	1207.8	Karvina Fm.	1.05	451
NP 825	1222.5	Karvina Fm.	1.12	450
NP 825	1265	Ostrava Fm.	1.04	462
NP 825	1273.4	Ostrava Fm.	1.07	460
NP 825	1292.7	Ostrava Fm.	1.04	464
SV-6	1336.3	Karvina Fm.	1.51	544
SV-6	1373.1	Karvina Fm.	1.14	524
SV-6	1380.2	Karvina Fm.	1.12	464
SV-6	1417.2	Karvina Fm.	1.12	461
SV-6	1443.5	Ostrava Fm.	1.22	466
SV-6	1443.7	Ostrava Fm.	1.21	468
SV-6	1483.8	Ostrava Fm.	1.15	457
SV-6	1510.2	Ostrava Fm.	1.15	464
SV-6	2130	Ostrava Fm.	1.53	504
SV-1	1425.5	Ostrava Fm.	0.93	456

R_r: random vitrinite reflectance. T_{max}: temperature at maximum of S2 peak.

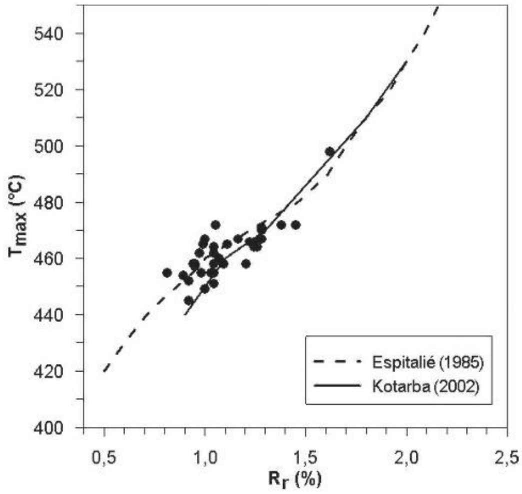

Fig. 6. Comparison of % R_r and T_{max} on 41 samples from Ostrava and Karviná Fms. Published relationship for USCB's Poland part (Kotarba et al., 2002) and the Paris basin (Espitalie et al., 1985).

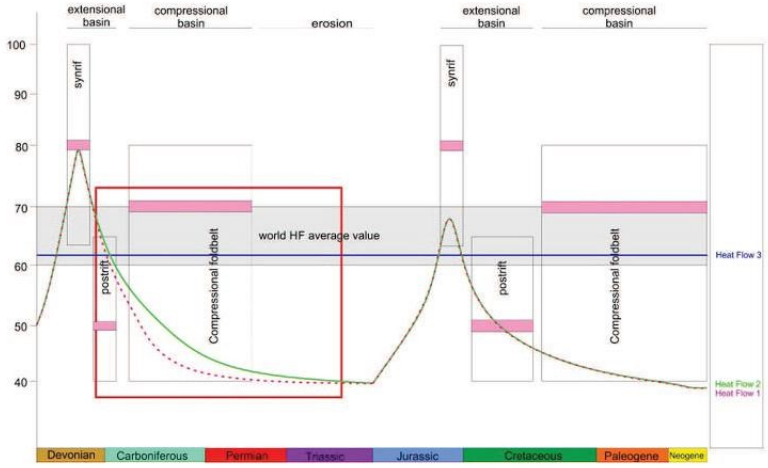

Fig. 7. The USCB evolution from the Devonian to Recent with major tectonic phases and tested palaeo-heat flow scenarios (HF1, HF2 and HF3). The red frame marks the period tested using sensitivity analysis. (For interpretation of the references to colour in this figure legend, the reader is referred to the web version of this article.)

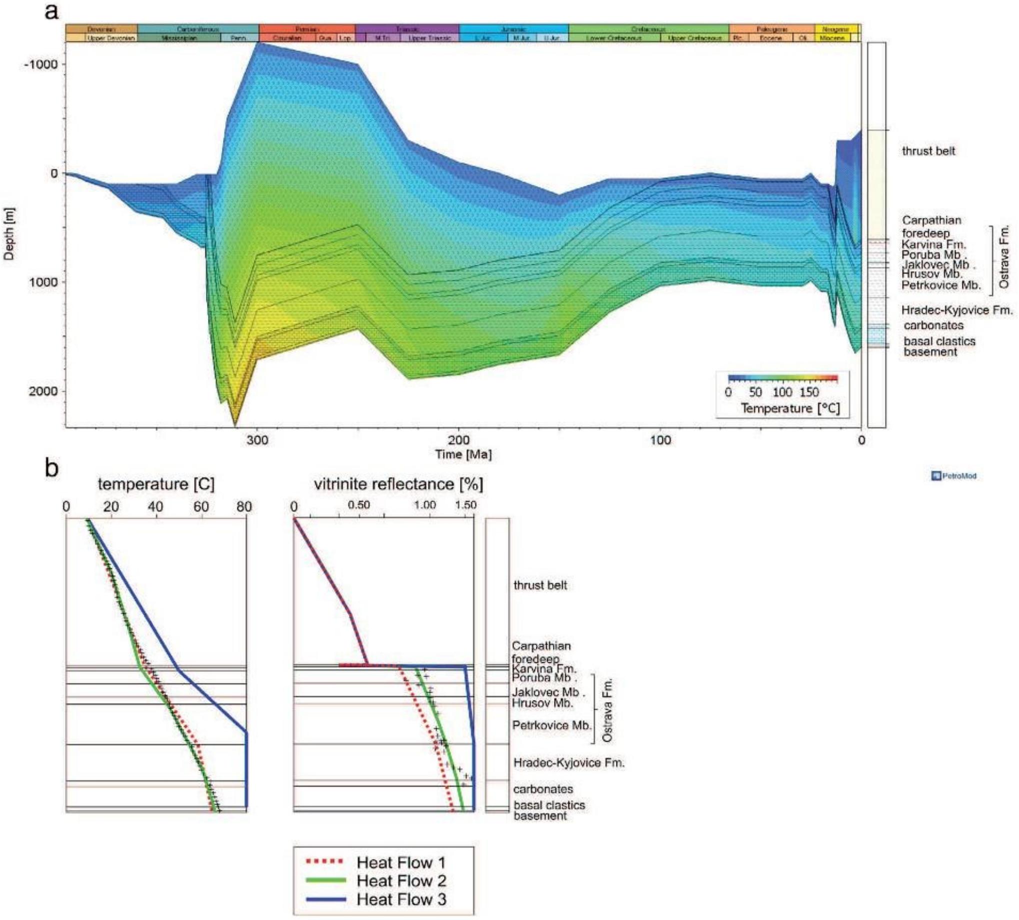

Fig. 8. Burial and thermal history of the NP 824 borehole profile (platform) and the results of sensitivity analysis with changing HF scenarios at a constant eroded thickness of 1800 m. The measured VR data used for calibration is indicated by crosses.

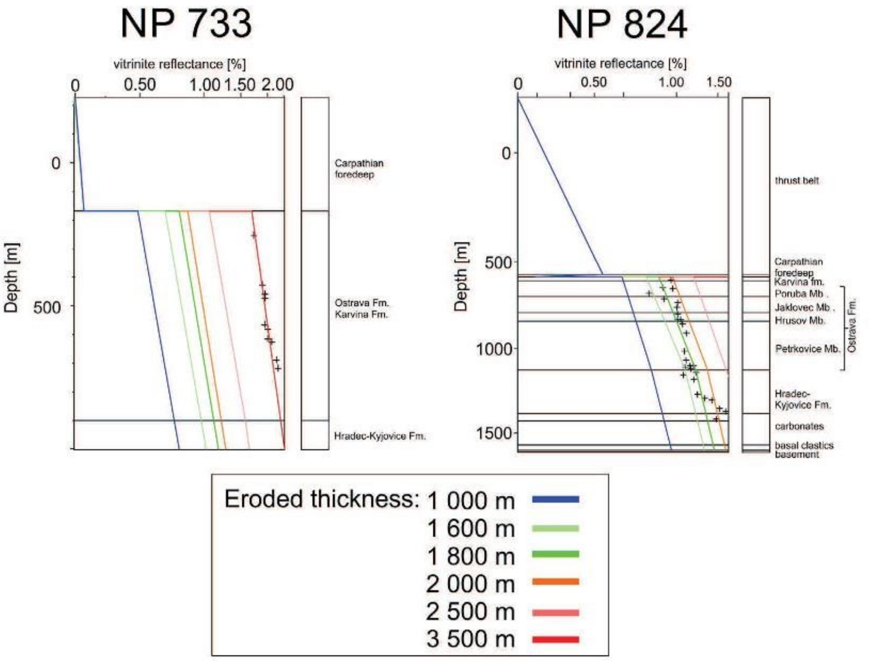

Fig. 9. Results of sensitivity analyses of the NP 733 borehole (foreland) and NP 824 (platform) with changing eroded thickness for HF1 scenario (NP 733) and changing eroded thickness for HF2 scenario (NP 824). The measured VR data used for calibration is indicated by crosses.

constant heat flow of 65 $mW \cdot m^2$ throughout the basin evolution, representing an average global heat flow value. The enhanced heat flows during the Variscan orogeny (Devonian–Late Carboniferous) were tested. The expected heat flow scenarios are based on the published geological evolution (Littke et al., 1994; Francu et al., 2002; Littke et al., 2012; Botor, 2014) and assume an increase of up to 75–80 $mW \cdot m^2$ during the Devonian (395–360 Ma) followed by cooling down to 45 $mW \cdot m^2$ in the Early Carboniferous. Another heat flow increase is assumed to have occurred during the Jurassic–Cretaceous extension (160–130 Ma). The present-day heat flow (38 $mW \cdot m^2$) was calculated from average temperature, bottom hole temperatures and modelled sediment thermal conductivities. The (1.45) beta stretching factor was used in all the palaeo-heat flows using an inverse subsidence trend (Hantschel and Kauerauf, 2009). A good agreement between the values of measured and modelled vitrinite reflectance (Sweeney and Burnham, 1990) implies that resulting 1D thermal models represent the most probable evolution in the geological past.

In total 17 1D burial and thermal models were created within the USCB. The selected wells represent deep boreholes in the USCB; two of them cover the complete sedimentary succession. The studied area is split into a western and an eastern part; they are separated by the Orlová Thrust, the boundary between the foreland and the platform of the Variscan orogeny.

The static scenario HF3 proved to be too high since we were not able to calibrate any of the evaluated wells (Fig. 8). The HF1 and HF2 scenarios represent the upper and the lower boundary of possible heat flow evolution during the Devonian and the Carboniferous according to the measured vitrinite reflectance values, indicating a possible error of ± 5 $mW \cdot m^2$. The precise heat flow scenario during the Late Jurassic could not be tested as the observed thermal maturity was achieved during the Variscan orogeny. A best-fit case was achieved using HF1 for foreland and HF2 for the platform (Figs. 8, 9). The optimum thickness for the Carboniferous erosion ranges in the Palaeozoic foreland (NP 733, NP 861 and Jablůnka 1 borehole) from 2500 to 3400 m (Fig. 9 Table 4); for the Palaeozoic platform (NP 824 and NP 891 borehole) it is 1800 to 2000 m (Fig. 9, Table 4).

The sensitivity analysis evidenced a different palaeo gradient curve in the period after the reaching of the maximum sediment thickness for the western (foreland) and the eastern (platform) part of USCB (Figs. 8 and 9). In the foreland the heat flow declined faster compared with the area on the platform.

4. Discussion

The Upper Silesian Coal Basin shows the similar geological features as sediments of the Rhenisch Massif (Rheno-hercynian fold belt) and the Ruhr basin (Subvariscan foreland). The main difference is the different azimuth of the direction of the axis of the foredeep and the platform, determined by the oblique collision during the Variscan orogeny in the Moravo-Silesian Zone (Kalvoda et al., 2008). Difference is also in the tectonic history. Compared to USCB Ruhr basin and Rhenisch Massif were affected by tectonic movements occurred during in the Late Triassic and Late Cretaceous.

Table 4
The resulting modelled thickness of the missing units for the Palaeozoic molasses association in the USCB in the Czech Republic.

Borehole	Block	Present overburden (m)	Present Pz Molasses association thickness (m)	Eroded Pz Molasses association thickness (m)
NP 733	Foreland	393	752	3400
NP 861	Foreland	855	2324	3400
NP 879	Foreland	658	1097	2500
Jablunka	Foreland	2895	1055	3100
NP 522	Platform	943	1530	1800
NP 824	Platform	1007	993	1800
SV 1	Platform	837	1789	1800

The coalification degree of sediments from Namur A to C in the USCB reach 0.46 to 2.32% R_r and as T_{max} of 423–525 °C. The comparable thermal maturity described on the Polish side is reaching $R_r = 0.65\%$ to 2.2% within the black coal to anthracite range; $T_{max} = 425–540$ °C (Kotarba et al., 2002).

The burial history of the USCB indicates rapid sedimentation during the deposition of the Ostrava Fm. and Karviná Fm. This is also demonstrated in the Polish part of the USCB where the tectonic subsidence is assumed to have occurred during the Devonian to the Carboniferous period (Narkiewicz, 2007). The main tectonic feature, the Orlová Thrust, marks the boundary between the foreland and the platform of the Variscan orogeny in the USCB during the Carboniferous. Observed in the USCB territory was regional growth of layer thickness from the east to the west towards the Variscan orogeny zone (Kotas, 1995;

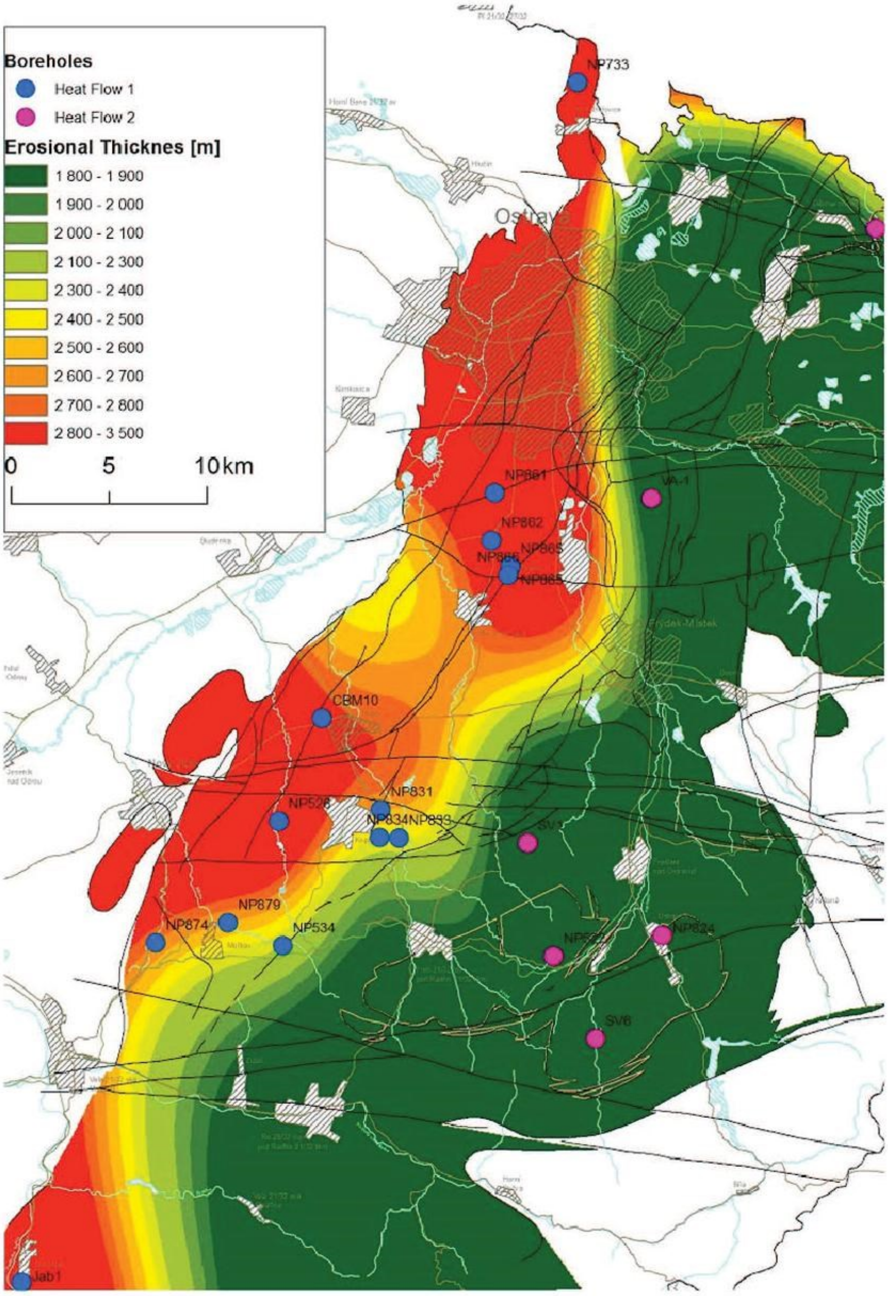

Fig. 10. Map of the eroded Palaeozoic molasses association units.

Kumpera and Martinec, 1995; Narkiewicz, 2007). The estimated thickness of the equivalent of Ostrava and Karviná Fms. in Poland is 3000 to 4000 m approximately based on the extrapolation of the present sediment thicknesses from the east (Narkiewicz, 2007). For the central and eastern parts, the erosion is estimated to be 1200 to 3000 m in Poland (Belka, 1993). The model is assuming that the eroded Carboniferous layers were removed during the Carboniferous (Table 1; Fig. 8). We assumed the eroded thickness of the Palaeozoic units to range from 2500 to 3400 m in the western part and from 1800 to 2000 m in the east. These values may be regarded as a maximum scenario for the USCB.

The map of the eroded Palaeozoic molasses association units (Fig. 10) was created using spline interpolation method in ArcGIS, using the result of the seventeen 1D models as input data. The total thickness was calculated beginning at the top of the Petřkovice Member. The platform and the foreland parts were modelled using heat flow scenarios 1 and 2.

The observed westward increase in eroded thicknesses is caused by an uplift of the studied area, which decreased eastwards at the end of the Variscan folding. The much greater values of thickness in the foreland basin can be correlated with the presence of Variscan nappes and one can assume a greater expansion of Palaeozoic sediments to the west.

A gradual increase is described in the degree of thermal conversion in the NW to SE direction in the Rhenish Massif (Teichmüller et al., 1979). This trend is also reflected in the subsidence history when one assumes the thickness of the eroded units in the Westphalian/Stephanian period to be 6000 m to SE and 2500 m to NW (Littke et al., 1994; Büker et al., 1995, 1996; Karg, 1998; Littke et al., 2012). The subsequent erosion of the thick overlying units is attributed to the shortening of the sedimentation area and folding of the orogenic belt (Oncken, 1991; Oncken et al., 1995). The different directional orientation of the distribution of thermal maturity in USCB is determined by the arc ending of the Variscan orogenic belt in the territory of the Czech Republic, giving the evidence for the emergence of the present degree of coalification during the Palaeozoic.

The best fit paleo-heat flow scenario for the time of maximum burial in the late Carboniferous ranges from 75 to 80 $\mathrm{mW \cdot m^{-2}}$. This HF evolution described does not match the results published by Šafanda et al. (1991) who expected a heat flow of 190 $\mathrm{mW \cdot m^{-2}}$ during Namurian A, and a heat flow of 115 to 130 $\mathrm{mW \cdot m^{-2}}$ for Namurian B and Namurian C. Based on the sensitivity analysis with constant erosion, slightly higher HF values are expected on the platform during the cooling phase. The new results, however, are consistent with the heat flow data published by Littke et al., 2000 although the USCB territory is not expected to be significantly different from the Rhenish Massif and the Ruhr Basin in terms of the thickness of the earth's crust.

Tested was also the influence of the increased thermal flow during the Jurassic to the Cretaceous period, one that is estimated by some authors (Picha et al., 2006). The fact is impossible to either disprove or confirm since the maximum temperature reached at the Jurassic to the Cretaceous borderline is comparable, or even lower. This has also been documented by the results of the study of apatite fission tracks (Botor, 2014) on the Polish side of USCB.

5. Conclusion

New RockEval data supplemented by vitrinite reflectance data provide important information on thermal maturity of the USCB. The stage of thermal transformation of organic matter seen on the Czech side of USCB ranges from 0.46 to 2.32% R_r; this matches the subbituminous to semi anthracite coal rank. The coal rank increases from the east (Variscan platform) towards the west (Variscan foreland). The hydrogen index (HI) = 1–164 and S2 = 0.02–27.8 mg/g. The results document that the source potential of the Carboniferous sediments was not spent in full as part of the Variscan tectogen. In the southeastern portion, southern to Příbor region, the paleo-thickness approximates the current figures of depth. It can be deduced from the former fact that the process of organic matter transformation is underway even in the current period in the segments placed deeper under the nappes.

The analysed depth trends of the thermal maturity for 135 boreholes varies slightly and reflect minor changes within the Upper Silesian basin in the amount of the eroded strata. The organic matter thermal maturity reflects the geological setting during the end of the Westphalian and is related to different thickness of the Palaeozoic units rather than to different thermal regimes. The expected thickness of the molasses association varies between 1800 and 3400 m towards the west and east.

The best fit heat flow scenario was used in 1D models starting from 75 to 80 $\mathrm{mW \cdot m^{-2}}$ during the Palaeozoic followed by a continuous decrease in the heat flow until the recent period. There is no difference in the palaeogeothermal regime in the USCB during the sedimentation period. Based on the sensitivity analysis the following stage of uplift and erosion is characterised with a different thermal regime depending on the molasses association thickness — the platform (1800 to 2000 m) and the foreland (2500 to 3400 m).

The consequent sedimentation of the Carpathian Foredeep and nappe thrusting did not change the Palaeozoic thermal maturity pattern within the tested area of the USCB.

Acknowledgements

This study benefitted from the Masaryk University project MUNI/M/0081/2013. The authors wish to thank Doc. Pavel Muller for his helpful comments and recommendations related to thermal maturity.

References

Aust J., Čechová, Š., Hozza, L., Kaštovský, V., Krůl, M., Raszyková, L., Šmitová, Š., 1997. Subcrop Map of the Upper Silesian Coal Basin, 1:100 000, Czech Republic MŽP ČR.

Behar, F.V., Beaumont, B.D., Penteado, H.L., 2001. Rock–Eval 6 technology: performances and developments, Oil & Gas Science and Technology Rev. IFP. vol. 56 pp. 111–134.

Belka, Z., 1993. Thermal and burial history of the Cracow-Silesian region (southern Poland) assessed by conodont CAI analysis. Tectonophysics 227, 161–190.

Botor, D., 2014. Timing of coalification of the Upper Carboniferous sediments in the Upper Silesia Coal Basin on the basis of apatite fission track and helium dating. Miner. Resour. Manag. 30 (1), 85–103 (in Polish with English abstract).

Büker, C., Littke, R., Welte, D., 1995. 2D-modelling of thermal evolution of Carboniferous and Devonian sedimentary rocks of the eastern Ruhr basin and northern Rhenish Massif, Germany. Z. Dtsch. Geol. Ges. 146, 321–339.

Büker, C., Carpitella, F., Littke, R., Welte, D., 1996. Burial and thermal history of Carboniferous sediments in well Floverich 2E-1 (Aachen-Erkelenz coal district: Germany). Zbl. Geol. Paläontol. 1 (11/12), 1261–1273.

Bula, Z., Jachowicz, M., Prichystal, A., 1997. Lower Palaeozoic deposits of the Brunovistulicum. In: Negendank, J.F.W., McCann-, T. (Eds.), Trans-European suture zone; EUROPROBE TESZ meeting. Terra Nostra Bonn 97–11, pp. 32–38.

Chudý, J., 1992. Maceral Composition and Coalification of Bitumenous Coals from Karviná Basin. MS VŠB Ostrava (135 pp. (in Czech)).

Davydov, V.I., Korn, D., Schmitz, M.D., 2012. The Carboniferous Period. In: Gradstein, F.M., Ogg, J.G., Schmitz, M.D., Ogg, G.M. (Eds.), The Geologic Time Scale. Elsevier, Amsterdam, pp. 603–651.

Dopita, M., Zeman, J., 1960. Uwęglenie pokladów w Górnośląskim Zaglębiu Węglowym. Kwartalnik Geol. 3, 565–575.

Dopita, M., Aust, J., Brieda, J., Černý, I., Dvořák, P., Fialová, V., Foldyna, J., Grmela, A., Grygar, R., Hoch, I., Honěk, J., Kaštovský, V., Konečný, P., Kožušníková, A., Krejčí, B., Kumpera, O., Martinec, P., Merenda, M., Müller, K., Novotná, E., Ptáček, J., Purkyňová, E., Řehoř, F., Strakoš, Z., Tomis, L., Tomšík, J., Valterová, P., Vašíček, Z., Vend, J., Žídková, S., 1997. Geology of the Czech Part of the Upper Silesian Basin. Ministerstvo životního prostředí České republiky, Praha (in Czech with English abstract).

Espitalie, J., 1986. Use of T_{max} as a maturation index for different types of organic matter. Comparison with vitrinite reflectance. In: Burrus, J. (Ed.), Thermal Modeling in Sedimentary Basins: Paris, Editions Technip, pp. 475–496.

Espitalie, J., Deroo, G., Marquis, F., 1985. Rock–Eval pyrolysis and its applications (part two). Oil Gas Sci. Technol. Rev. IFP 40 (6), 755–784.

Francu, E., Francu, J., Kalvoda, J., Poelchau, H.S., Otava, J., 2002. Burial and uplift history of the Palaeozoic Flysch in the Variscan foreland basin (SE Bohemian Massif, Czech Republic). In: Bertotti, G., Schulmann, K., Cloetingh, S. (Eds.), Continental Collision and the Tectono-sedimentary Evolution of Forelands. European Geophysical Society — Stephan Mueller Special Publication Series vol. 1, pp. 259–278.

Grygar, R., Vavro, M., 1995. Evolution of Lugosilesian orocline (north-eastern periphery of the Bohemian Massif): kinematics of Variscan deformation. J. Czech Geol. Soc. 40 (1–2), 65–90.

Hantschel, T., Kauerauf, A.I., 2009. Fundamentals of Basin and Petroleum Systems Modelling. Springer (476 pp.).

Hemza, P., Sivek, M., Jirásek, P., 2009. Factors influencing the methane content of coal beds of the Czech part of the Upper Silesian Coal Basin, Czech Republic. Int. J. Coal Geol. 79, 29–39.

Jurczak-Drabek, A., 1996. Petrographical Atlas of Coal Deposits, Upper Silesian Coal Basin 1:300 000. PIG, Warszawa.

Kalvoda, J., Bábek, O., Fatka, O., Leichmann, J., Melichar, R., Nehyba, S., Špaček, P., 2008. Brunovistulian terrane (Bohemian Massif, Central Europe) from late Proterozoic to late Paleozoic: a review. Int. J. Earth Sci. 497–517 (2008, roč. 97, č. 3, s).

Kandarachevová, J., Sedláčková, L., Hýlová, L., Jirásek, J., Sivek, M., 2009. Lateral development of coalification in the Czech part of the Upper Silesian Basin and its connection with gas deposits. Int. J. Coal Geol. 78, 225–232.

Karg, H., 1998. Numerische Simulation der thermischen Geschichte, Subsidenz und Erosion des westlichen Rechtsrheinischen Schiefergebirges, des Ruhrbeckens und Paläozoikums der Niederrheinischen Bucht. MS, Berichte des Forschunszentrum Jülich 3618, 455 s.

Kotarba, M.J., Clayton, J.L., Rice, D.D., Wagner, M., 2002. Assessment of hydrocarbon source rock potential of Polish bituminous coals and carbonaceous shales. Chem. Geol. 184, 11–35.

Kotas, A., 1985. Structural evolution of the Upper Silesian Coal Basin (Poland), X. Congr.Int.Strat.Coal Carb., Madrid 1983, C.R.3, pp. 459–469.

Kotas, A., 1995. Lithostratigraphy and sedimentologic–paleogeographic development of the Upper Silesian Coal Basin. In: Zdanowski, A., Zakowa, H. (Eds.), The Carboniferous System in Poland. Prace Państwowego Instytutu Geologicznego Warszawa, pp. 124–134.

Kotas, A., Bula, Z., Gadek, S., Kwarcinski, J., Malicki, R., 1983. Geological atlas of the Upper Silesian Coal Basin. Part II Coal Quality Maps 1:100 000. Wydawnictwa Geologiczne, Warszawa.

Kumpera, O., Martinec, P., 1995. The development of the Carboniferous accretionary wedge in the Moravian–Silesian Paleozoic Basin. J. Czech Geol. Soc. 40, 47–64.

Lafargue, E., Marquis, F., Pillot, D., 1998. Rock–Eval 6 applications in hydrocarbon exploration, production, and soil contamination studies. Oil Gas Sci. Technol. Rev. IFP 53, 421–437.

Littke, R., Büker, C., Lückge, A., Sachsenhofer, R.F., Welte, D.H., 1994. A new evaluation of palaeo-heat flows and eroded thicknesses for the Carboniferous Ruhr basin, western Germany. Int. J. Coal Geol. 26, 155–183.

Littke, R., Hertle, M., Karg, H., Stroetmann-Heinen, V., Oncken, O., 2000. Heat flow evolution, subsidence and erosion in the Rhenohercynian orogenic wedge of central Europe. Geol. Soc. Spec. Publ. 179, 231–255.

Littke, R., Urai, J.L., Uffmann, A.K., Risvanis, F., 2012. Reflectance of dispersed vitrinite in Palaeozoic rocks with and without cleavage: implications for burial and thermal history modeling in the Devonian of Rursee area, northern Rhenish Massif, Germany. Int. J. Coal Geol. 89, 41–50.

Martinec, P., Kožušníková, A., Jirásek, J., Sivek, M., 2005. Atlas of Coal of the Upper Silesian basin. 67. Anagram, Ostrava.

Narkiewicz, M., 2007. Development and inversion of Devonian and Carboniferous basins in the eastern part of the Variscan foreland (Poland). Geol. Q. 51, 231–256.

Oncken, O., 1991. Aspects of the structural and paleogeothermal evolution of the Rhenish Massif. Ann. Soc Géol. Belg. 113, 139–159.

Oncken, O., Massonne, H.J., Schwab, M., 1995. Metamorphic evolution. In: Dallmeyer, R.D., Franke, W., Weber, K. (Eds.), Pre-Permian Geology of Central and Eastern Europe. Springer, Berlin-Heidelberg-New York, pp. 82–86.

Patteisky, K., 1928. Chemical properties of coal in the Ostrava and Karvina districts. Bituminous Coal Mines in the Ostrava–Karviná district, I, Ostrava.

Pešek, J., Kumpera, O., Holub, V., Skoček, V., 1998. Paleogeographic Atlas: Late Paleozoic and Triassic Formations, Czech Republic. Český geologický ústav, Praha.

Picha, F.J., Stranik, Z., Krejci, O., 2006. Geology and hydrocarbon resources of the Outer Western Carpathians and their foreland, Czech Republic. In: Golonka, J., Picha, F.J. (Eds.), The Carpathians and Their Foreland. Geology and Hydrocarbon Resources: AAPG Memoir 84, pp. 49–175.

Ptáček, J., Grygar, R., Koníček, P., Waclawik, P., 2012. The impact of Outer Western Carpathian nappe tectonics on the recent stress–strain state in the Upper Silesian Coal Basin (Moravosilesian Zone, Bohemian Massif). Geol. Carpath. 63 (1), 3–11.

Šafanda, J., Honěk, J., Weiss, G., Buntebarth, G., 1991. Paleogeothermics in the Czechoslovak part of the Upper Silesian Basin. Geophys. J. Int. 104, 625–633.

Sivek, M., Dopita, M., Krul, M., Caslavsky, M., Jirasek, J., 2003. Atlas of Chemical-Technological Properties of Coals in the Czech Part of the Upper Silesian Basin. Vysoká škola báňská, Technical University, Ostrava.

Stahl, A., 1933. Inkohlung und Flözlagerung in ostsudetischen Steinkohlen. Jahrbuch der reussischen geol. Landesanstalt, LIV.

Sweeney, J.J., Burnham, A.K., 1990. Evaluation of a simple model of vitrinite reflectance based on chemical kinetics. AAPG Bull. 74, 1559–1570.

Taylor, G.H., Teichmüller, M., Davis, A., Diessel, C.F.K., Littke, R., Robert, P., 1998. Organic Petrology. Gebrüder Borntraeger, Berlin.

Teichmüller, M., Teichmüller, R., Weber, K., 1979. Inkohlung und Illit-Kristalinitat Vergleichende Untersuchungen im Mesozoikum und Paleozoikum von Westfalen. Fortschr. Geol. Rheinld. U. Westf. 27, 201–276.

Weiss, G., 1980. Coalification with depth in the Czechoslovak part of the Upper Silesian Basin. Sborník GPO 22, 24–36 (in Czech).

Příloha 3

Francu E., Francu J., Kalvoda J. (1999) Illite crystallinity and vitrinite reflectance in Paleozoic siliciclastics in the SE Bohemian Massif. Geologica Carpathica. 50, 5, 365-372.

GEOLOGICA CARPATHICA, 50, 5, BRATISLAVA, OCTOBER 1999
365–372

ILLITE CRYSTALLINITY AND VITRINITE REFLECTANCE IN PALEOZOIC SILICICLASTICS IN THE SE BOHEMIAN MASSIF AS EVIDENCE OF THERMAL HISTORY

EVA FRANCŮ[1], JURAJ FRANCŮ[1] and JIŘÍ KALVODA[2]

[1]Czech Geological Survey, Leitnerova 22, 658 69 Brno, Czech Republic; francu@cgu.cz
[2]Department of Geology, Masaryk University, Kotlářská 2, 611 37 Brno, Czech Republic; dino@sci.muni.cz

(Manuscript received December 9, 1998; accepted in revised form June 22, 1999)

Abstract: The thermal maturity of Paleozoic rocks in the SE part of the Bohemian Massif is characterized by clay minerals and organic matter. The expandability of illite-smectite (S in I-S), illite crystallinity index (IC) and reflectance of (R_r) were measured and their regional distribution was evaluated. The mutual correlation of IC and R_r from diagenesis to very low-grade metamorphism is compared with the published data and used to distinguish data with more reliable paleogeothermal information from those affected by other factors. In the SE part the Paleozoic units have illite-smectites with an expandable component of 15–35 % S. The reflectance values (R_r of 0.55–1.1 %) are in good agreement with the expandability and suggest the oil window range of catagenesis with paleotemperature close to 100 °C. In the NNW part of the area the clays contain no expandable layers in illite. The illite crystallinity (IC of 0.36–0.24 Δ°2Θ) and vitrinite reflectance (R_r from 3.17 to 5.23 %) indicate very low-grade metamorphic conditions with probable maximum paleotemperatures of 240–300 °C. The systematic change in both clay and organic parameters shows the gradual decrease in thermal exposure towards the front of the Variscan orogenic zone in the S and SE and suggest extensive erosion in the NNW.

Key words: Paleozoic, thermal history, vitrinite reflectance, expandability, illite crystallinity, I-S.

Introduction

The illite crystallinity index (IC), expandability of illite-smectite (S in I-S) and vitrinite reflectance (R_r) are widely used parameters of thermal alteration of sedimentary rocks. Smectite to illite evolution is a typical diagenetic reaction with a gradual decrease of expandable layers (% S), increase of illite layers in I-S, and progressive ordering ("reichweite" R0 and R > 0) followed by growth of illite crystals (Środoń & Eberl 1984). The Al-Si substitution in the tetrahedral sheet, the increase of the layer charge and irreversible potassium fixation in the interlayer play the decisive role in illitization (Moore & Reynolds 1997). These processes occur in temperature range from 50 to 300 °C covering diagenesis and very low-grade metamorphism. The understanding of the structural changes during smectite to illite conversion benefited from computer simulation of X-ray diffraction profiles (Reynolds & Hower 1970).

The illite crystallinity index characterizes the structural evolution of illite, mainly the increasing size of coherently diffracting domains and decreasing lattice distortion. It is based on the shape of the first (001) peak of illite (Weaver 1960; Kübler 1964; Weber 1972). The full width at half maximum (FWHM) expressed in Δ°2Θ is used by most authors as "IC" — the illite crystallinity index (Kübler 1967; Árkai & Lelkes-Felvári 1993). A similar parameter is evaluated for chlorite using 001 and 002 peaks (Árkai et al. 1995). The correlation of the IC of illite and chlorite shows an earlier narrowing of the chlorite peaks than that of illite during late diagenesis and very low grade metamorphism (Árkai 1991).

Organic matter in sedimentary rocks (kerogen) is a sensitive indicator of thermal stress in the range of 50–300 °C (Bostick 1979; Robert 1988). Coalification (thermal maturity) depends on the total thermal history of the host rocks, that is both temperature and exposure time (Waples 1985). Vitrinite reflectance (R_r) is the best established parameter of organic matter which can be measured in most black shales and slates. Its application is limited by the absence of terrestrial plant debris in pre-Devonian or purely marine rocks.

Many authors applied analytical data of clay minerals and organic matter in regional studies and related them to paleotemperatures in sedimentary basins and orogenic belts (Pearson & Small 1988; Robert 1988; Franců et al. 1990; Pollastro 1990 and 1993; Underwood et al. 1993; Środoń 1995). Thermal alteration of both rock components is irreversible during uplift and temperature drop. During weathering, however, the clay minerals undergo illite-to-smectite breakdown which erases the paleo-thermal signature.

Regional setting

The surface geology of the studied area consists of the Paleozoic of the Drahany and Zábřeh Uplands (Drahanská and Zábřežská vrchovina), Lower Miocene and Pliocene of the

Carpathian Foredeep, and the Tertiary of the Carpathian Flysch Belt. The outcrop and subcrop map of the Paleozoic with simplified names of regional units and overlain boundaries of the surface units is in Fig. 2. The sample location numbers refer to Table 1 where more detailed lithostratigraphy is given.

The Paleozoic units of the eastern Bohemian Massif are regarded as a part of the Rhenohercynian and Subvariscan Zone (Franke in Dallmeyer et al. 1995) of the Variscan orogenic belt (Fig. 1). The Bruno-Vistulian crystalline basement consolidated during the Cadomian orogeny is overlain in some places by Lower Cambrian siliciclastics (Vavrdová 1997), one occurrence of Silurian shales and limestones, and widespread Middle Devonian "basal clastics". The stratigraphic profile continues upwards with Devonian to Lower Carboniferous carbonates (Macocha, Jesenec, and Líšeň Fms.) and pre-flysch siliciclastics (Stinava-Chabičov and Ponikev Fms.). The Variscan synorogenic flysch (Culm) of Lower Carboniferous (Viséan) age (Protivanov, Rozstání, and Myslejovice Fms.) covers most of the outcrop and subcrop surface of the Paleozoic in this region. The Upper Carboniferous molasse sediments in the east (Ostrava and Karviná (?) Fms.) are the uppermost units of the Paleozoic and represent the Subvariscan Zone (Dvořák 1995).

The Mírov Unit (Otava & Sulovský 1997) is a separate tectonic block adjacent to the NW of the Drahany Upland and includes mostly siliciclastics, probably of Devonian age (Mohelnice Fm.).

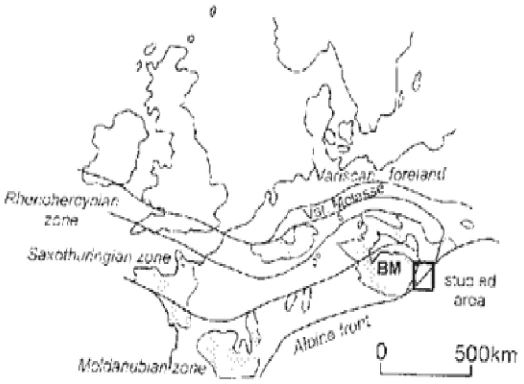

Fig. 1. The Bohemian Massif (BM) and its position in the Variscan orogenic zones of central and NW Europe (modified after Chaloupský 1989). The grey areas are Variscan massifs. The position of the studied area is indicated by the rectangle.

Table 1: Geological and analytical characteristics of the studied samples.

Location in map	Locality	Depth (m)	Age	Formation	Tectonic unit	Fraction µm	FWHM IC (°2Θ)	% EXP mean	R_r (%)	R_{max} (%)	R_{min} (%)
1	Mezihoří	0	D2.3	Mohelnice	Mírov unit	< 2	0.36	0	3.89*	5.41	0.85
1	Mezihoří	0	D2.3	Mohelnice	Mírov unit	< 0.2	0.53	0	3.89*	5.41	0.85
2	KDH 8A	125.5	D3-C1	Macocha	carbonates	< 2	0.24	0	4.84*	5.78	2.97
2	KDH 8A	171.6	D3-C1	Macocha	carbonates	< 2	0.24	0	5.23*	5.95	3.79
3	KDH 5	158.5	D3-C1	Ponikev	Pre-flysch Paleozoic	< 2	0.34	0	4.24*	5.51	1.69
3	KDH 5	229.4	D3-C1	Ponikev	Pre-flysch Paleozoic	< 2	0.36	0	4.86*	6.00	2.58
4	KDH 1	11	C1	Protivanov	Variscan flysch belt	< 2	0.32	0	3.17*	4.09	1.32
4	KDH 1	24.5	C1	Protivanov	Variscan flysch belt	< 2	0.32	0	3.56*	4.46	1.75
4	KDH 1	76.2	C1	Protivanov	Variscan flysch belt	< 2	0.30	0	4.51*	5.03	2.26
5	Sloup-Šošůvka	0	D2-C1	paleokarst	carbonates	< 2	0.52	< 4	-		-
6	Ostrov u Macochy	0	C1v	Rozstání	Variscan flysch belt	< 2	0.44	< 4	1.79	-	-
7	Jedovnice	0	C1v	Rozstání	Variscan flysch belt	< 2	0.55	< 4	1.61		-
8	Kiriny	0	C1v	Rozstání	Variscan flysch belt	< 2	0.48	< 4	2.42	-	-
9	Ochoz, Nové Dvory	0	C1v	Rozstání	Variscan flysch belt	< 2	0.48	< 4	1.92		-
10	Mokrá - LV 10	44.7	C1v	Myslejovice	Variscan flysch belt	< 0.2	0.709 (ChC)	< 1	-	-	-
10	Mokrá - LV 10	44.7	C1v	Myslejovice	Variscan flysch belt	< 2	0.637 (CIC)	< 4	-		-
11	Mokrá - LV 9	125.6	C1v	Myslejovice	Variscan flysch belt	< 0.2	1.21	< 4	1.57	-	-
11	Mokrá - LV 9	125.6	C1v	Myslejovice	Variscan flysch belt	< 2	1.23	< 4	1.57	-	
12	Mokrá - LV 5	68.7	D2-C1	Líšeň	carbonates	< 0.2	1.09	< 4	1.38	-	-
12	Mokrá - LV 6	68.7	D2-C1	Líšeň	carbonates	< 2	1.46	< 4	1.28	-	
13	Mokrá - LV 11	41.8	D2-C1	Líšeň	carbonates	< 0.2	1.30	< 4	1.55	-	-
14	Hády (Džungle)	0	D2-C1	Líšeň	carbonates	< 2	0.44	< 4	2.01	-	
15	Uhr-13	2553	C1	Myslejovice	Variscan flysch belt	< 0.2	1.65**	13	0.55	-	-
15	Dam-1	2791	C2-1	Ostrava	Variscan Foredeep	< 0.2	1.98**	32	0.62	-	
16	Dam-1	3021	C2-1	Ostrava	Variscan Foredeep	< 0.2	1.42**	35	0.68		
16	Dam-1	3021	C2-1	Ostrava	Variscan Foredeep	< 2	1.91**	-	0.68		
16	Dam-1	3592	C1v	Myslejovice	Variscan flysch belt	< 0.2	2.28**	24	0.75	-	-
16	Dam-1	3592	C1v	Myslejovice	Variscan flysch belt	< 2	1.68**	-	0.75	-	
16	Dam-1	4877	D2-C1	Macocha	carbonates	< 0.2	2.26**	19	0.80	-	-
17	Něm-2	3796	C2-1	Ostrava	Variscan Foredeep	< 0.2	1.98**	23	0.80	-	-
17	Něm-2	3964	C2-1	Ostrava	Variscan Foredeep	< 0.2	2.16**	25	0.85	-	-
17	Něm-2	4243	C2-1	Ostrava	Variscan Foredeep	< 0.2	1.92**	23	0.95	-	-
17	Něm-2	5338	D2-C1	Macocha	carbonates	< 0.2	2.14**	-	1.10	-	-
17	Něm-2	5338	D2-C1	Macocha	carbonates	< 2	1.11**	-	1.10	-	-

* recalculated R_r from R_{max} and R_{min} ** IC values have just approximate meaning

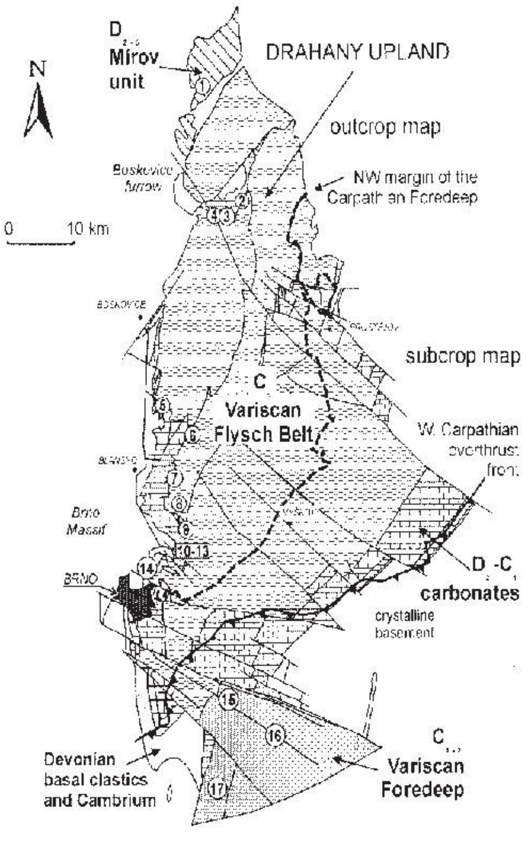

Fig. 2. Outcrop and subcrop map of the SE part of Moravo Silesian Paleozoic (modified after Dvořák 1995 with supplements of Otava, personal com.). The geological subdivision is simplified and each unit includes several formations. Sample numbers refer to the more detailed description in Table 1.

Samples

Surface and borehole core samples of Devonian and Carboniferous sedimentary rocks were collected to characterize the regional trend of thermal maturity from N to S (Fig. 2 and Table 1). Lithologically they are mostly siltstones, shales or slates (occasionally quartzified), and shale interlayers in limestones.

Methods

Clay mineral analysis

The clay fraction was separated from the powdered rocks after elimination of cements such as carbonates, organic matter and iron-manganese oxyhydroxides (Jackson 1975). Grain size fractions < 2 μm and < 0.2 μm were obtained by sedimentation and centrifugation. Oriented slides were analysed by X-ray diffraction both air dry and glycolated (EG, 10 hrs. at 60 °C, then 2 hrs. at 20 °C). Philips diffractometer PW 1830 (generator) and PW 3020 (goniometer) were used with 0.02° step from 2 to 30 $\Delta°2\Theta$. Peak fitting was applied to substract the ramp background and determine the individual peak positions in the composite peaks and to evaluate the full width at half maximum (FWHM). The Ir index (Środoń & Eberl 1984) defined as the ratio (001/003 air-dry)/(001/003 EG) was measured and calculated to characterize trace amounts of expandable layers in highly illitic materials. Expandability of illite-smectite was evaluated from peak positions using the plots of Środoń & Eberl (1984) and NewMod simulations (Reynolds 1985). The illite crystallinity index (IC) was measured as FWHM of the 001 basal reflection (Kübler 1967) or the chlorite (002) crystallinity index (ChC) when illite was absent (Weaver et al. 1984; Árkai 1991).

Organic matter

The measurements of reflectance were carried out in oil on polished surfaces of rocks using Leitz Wetzlar MPV2 microscope-photometer, objective 50× and Leitz standards of 1.26 and 5.42 %. The reflectance was measured in non-polarized and plane-polarized light (R_r, R_{max} and R_{min}). In order to obtain a single parameter for the entire range of thermal maturity, the R_{max} and R_{min} values of particles with higher bireflectance were recalculated to random reflectance using the equation $R_r = (2{*}R_{max}+R_{min})/3$ (Teichmüller et al. 1998). The measured organic particles (macerals) were petrographically identified as vitrinite, liptinite, inertinite or redeposited material following Teichmüller et al. (1998) and only the data of indigenous vitrinite or vitrinite-like macerals were used in further evaluation of the thermal history.

Results

The clay fraction of the studied series of rocks includes illite, chlorite, kaolinite and mixed-layer minerals. Illite smectite (I-S) has expandability of 0–35 % S and illite crystallinity index (IC) ranges from 0.24 to 2.28 $\Delta°2\Theta$. Vitrinite reflectance (R_r) increases from 0.55 to 5.23 %. These values (Table 1) cover thermal alteration from burial diagenesis to very low-grade metamorphism. The data are divided into four groups of samples characterized by typical features in the XRD patterns which represent subsequent phases of the shale-to-slate evolution (Figs. 3–7 and 10).

The first group of data comprises Paleozoic sediments with the lowest thermal alteration. It is documented by the XRD patterns (Fig. 3) of an air dry and glycolated clay (fraction < 2 μm) of an Upper Carboniferous shaly limestone with a low amount of detrital silt and clay. The IC index of 1.68 $\Delta°2\Theta$ is too high to be used as a measure of illite crystal size. The shape and position of I-S peaks change significantly after glycolation and indicate a mixture of detrital, that is inherited illite and newly formed expandable I-S.

The expandable component is better characterized by an analysis of the very fine clay fraction (< 0.2 μm) of the same

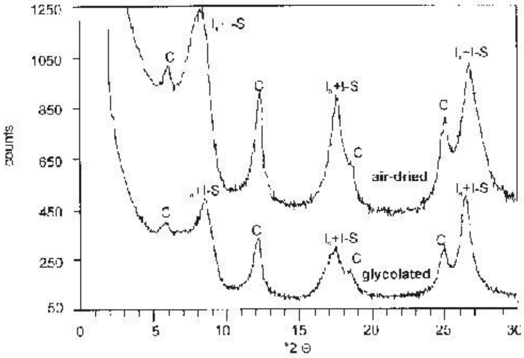

Fig. 3. The XRD pattern of coarser clay fraction (< 2 μm) of a shaly limestone, Dambořice-1 (3592 m). The sample is enriched in detrital illite (Id) and chlorite (C) which are associated with illite-smectite (I S).

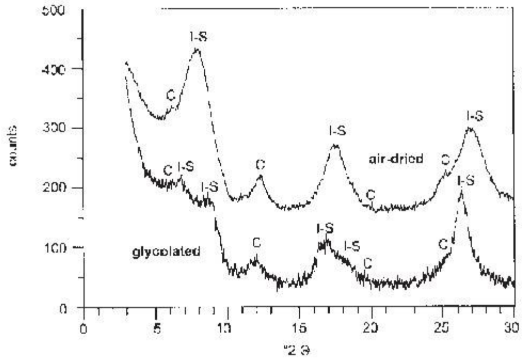

Fig. 4. The XRD pattern of the fine clay fraction (< 0.2 μm) of a shaly limestone, Dambořice-1 (3592 m). Detrital illite is eliminated.

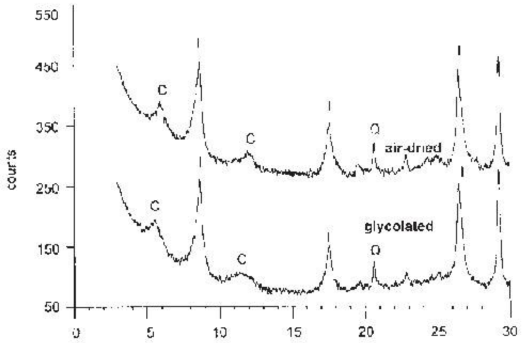

Fig. 5. The XRD pattern of the Hády outcrop sample (V Džungli Quarry), fraction < 2 μm. I — illite, C chlorite, Q — quartz.

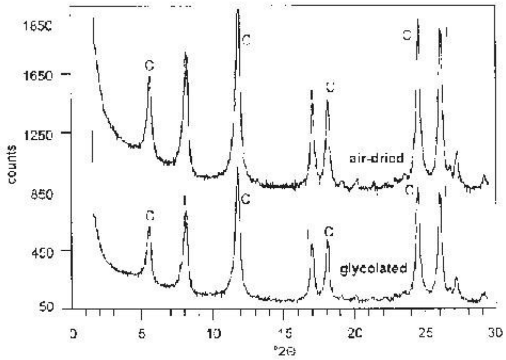

Fig. 6. The XRD pattern from the Mohelnice outcrop, fraction < 2 μm.

sample where the detrital illite is eliminated. Glycolation results in a split of broad 001 and 002 illitic peaks into pairs of rectorite-type peaks with expandability of 24 % S and R1 ordering (Fig. 4). Such clay parameters and vitrinite reflectance of 0.55 1.1 % are typical of the burial diagenetic phase of thermal alteration. Regionally these rocks occur in the S and SE where boreholes encountered the Devonian and Carboniferous below the nappes of the Western Carpathians at depths of 2.8–5.4 km.

The second and third groups of samples (Fig. 5) represent highly illitic material with illite peaks slightly changing their shape after glycolation. Chlorite is common and sometimes even more abundant than illite (Fig. 6). In some samples a shift of the chlorite peak after glycolation suggests the presence of an expandable component in the chlorite. Little or no material of the < 0.2 μm grain size can be separated from the samples in a non-destructive way, most probably due to crystal growth. The estimated amount of smectite layers in illite is < 4 % and the illite crystallinity index is 1.46–0.44 Δ°2Θ. The chlorite crystallinity index (ChC) is 0.7–0.6 Δ°2Θ. The clay parameters and vitrinite reflectance of 1.4–2.4 % found in different stratigraphic

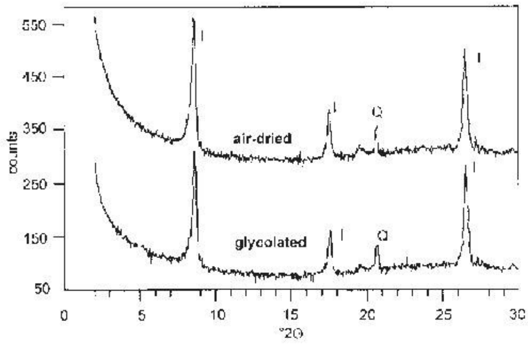

Fig. 7. The XRD pattern of KDH-8A borehole, 171.6 m, fraction < 2 μm.

units of the Drahany Upland and Mirov Unit correspond to thermal alteration of the late diagenetic phase.

The last group of samples is characterized by almost non expanding illitic mineral (Fig. 7) with narrow and sharp peaks and IC values of 0.24–0.36 Δ°2Θ. This type of minerals occurs in the Konice area and is associated with high vitrinite reflectance (R_{max} = 4–6, R_r = 3.17–5.23 %) and bireflectance (R_{max} – R_{min} = 2.16–3.82 %) equivalent to the metaanthracite rank. Both parameters suggest that these rocks experienced very low-grade metamorphic conditions.

Correlation between illite crystallinity and vitrinite reflectance

The illitization stage and coal rank are primarily controlled by thermal history (Środoń & Eberl 1984; Robert 1988). Examination of their mutual correlation is an important step in the data reliability assessment. The cross-plot of the illite crystallinity index (IC) and mean random vitrinite reflectance (R_r) shown in Fig. 8 reviews the earlier published data (Duba & Williams-Jones 1983; Underwood et al. 1991, 1993; Todorov et al. 1992; Henrichs 1993).

Other authors characterize the illite crystalinity and coalification rank by Hb_{rel} and R_{max}. To convert Hb_{rel} to IC readers need to know the value of peak width at half maximum (FWHM) of the quartz standard (Hb_{rel} = [Hb (001) illite/Hb (100) quartz]*100). Conversion of R_{max} to R_r requires R_{min} values (see methods above). The published data where the FWHM of quartz and R_{min} are missing or the R_r and IC values are given only as ranges (Wolf 1975; Kish 1987; Teichmüller et al. 1979) are, therefore, not included as references in Fig. 8.

The diagram in Fig. 9 summarizes the diagenetic and metamorphic zones with their boundary values (Teichmüller et al. 1979; Robert 1988; Kish 1983, 1991). The general trend shows decrease of vitrinite reflectance (R_r) with increasing IC index. The data below this trend (Todorov et al. 1992) represent measurements of authigenic vitrinite and redeposited detrital illite. The data which would plot above this trend (Figs. 8 and 9, upper right corner) do not represent consistent evidence of thermal history. Such a combination of the R_r and IC values may occur when the following materials are measured:

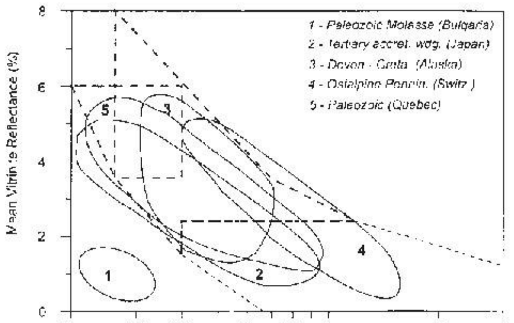

Fig. 8. Review of the published data on diagenesis/metamorphism (1 — Todorov et al. 1992; 2 — Underwood et al. 1993; 3 — Underwood et al. 1991; 4 — Henrichs 1993; 5 — Duba & Williams-Jones 1983). Our data plot within the dashed line envelope.

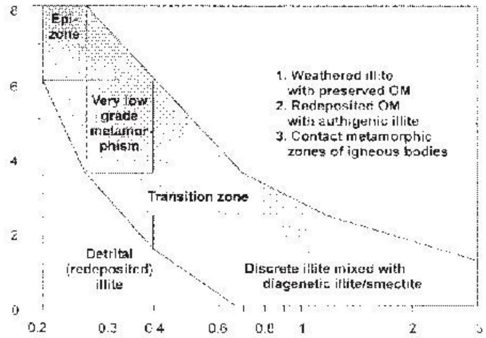

Fig. 9. Generalized relationships between illite crystallinity (IC) and random vitrinite reflectance (R_r). The boundaries of the metamorphic zones are given according to Teichmüller et al. (1979), Robert (1988), Kisch (1983).

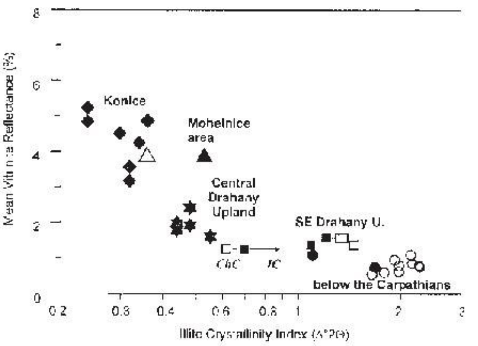

Fig. 10. Cross plot of two paleothermal indicators in Paleozoic samples from the southeastern part of the Bohemian Massif. Different symbols represent the partial areas. The open symbols (fraction < 0.2 μm) linked with black symbols (< 2 μm) belong to the same raw samples. The arrow indicates the estimated equivalent illite crystallinity derived from the chlorite crystallinity index (ChC).

1. redeposited organic matter from more metamorphosed rocks associated with authigenic illite-smectite;

2. preserved organic matter and disaggregated illite in secondary illite-smectite in weathered black slates;

3. graphitized organic matter (or metaanthracite) associated with poorly aggraded illite in rocks from the contact metamorphic zones of igneous bodies (Árkai, personal communication 1999).

All our measured samples (Fig. 10) plot within the shaded belt of "good" correlation in Fig. 9.

Regional distribution of the paleothermal signature

The distribution of the diagenetic-to-metamorphic alteration based on the illite crystallinity index is shown in the outcrop and subcrop map of the studied Paleozoic (Fig. 11).

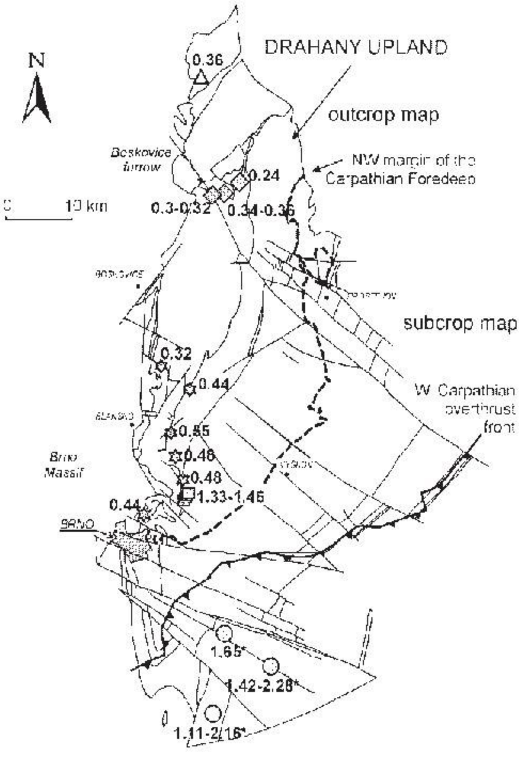

Fig. 11. Regional distribution of the illite crystallinity index (IC, Δ°2Θ) in Paleozoic shales and shaly limestones of the SE Bohemian Massif. The symbols are identical to those in Fig. 10.

The Carboniferous strata below the West Carpathian overthrust have diagenetic expandable illite-smectite and organic maturity equivalent to the oil generation zone of diagenesis (c.f. Franců et al. 1989; Pollastro 1990; Pereszlényi et al. 1993, 1997; Milička et al. 1994; Masaryk et al. 1995). The present results of clay analysis support the earlier conclusions based only on vitrinite reflectance (Dvořák & Wolf 1979; Dvořák 1989; Krejčí et al. 1994). The expandability values correspond to the maximum burial temperatures of 80–130 °C observed in other basins (Franců et al. 1990) which is also well constrained by the vitrinite reflectance of R_r = 0.55-1.1 %.

In the SE part of the Drahany Upland (e.g. Mokrá quarry) the clay and organic data (ChC of 0.64, R_r of 1.38–1.57 %) suggest a late diagenetic phase (dry gas zone) with an estimated paleotemperature of 130–170 °C.

In the central Drahany Upland the illitic material in the < 2 µm fraction has an expandable component of < 4 % S. The IC ranges from 0.32 to 0.55 Δ°2Θ and vitrinite reflectance (R_r) from 1.9 to 2.4 %. These data are typical of late diagenetic conditions with temperatures of 170–200 °C (Bostick 1979; Underwood et al. 1991, 1993).

Even higher thermal maturity is observed in the Mírov Unit (Mohelnice Fm.) NW of the Drahany Upland (Table 1, Figs. 10 and 11).

In the Konice window the vitrinite reflectance is of the metaanthracite rank and the illite crystallinity is in the very low-grade metamorphic range. From comparison with similar data (Milička et al. 1991; Šucha et al. 1994) or supported also by fluid inclusions (e.g. Robert 1988; Frey et al. 1980; Frey 1986) it may be estimated that the evaluated Variscan flysch and pre-flysch sediments were buried at a temperature of 240–300 °C.

Conclusions

Illite crystallinity and vitrinite reflectance in the Paleozoic sedimentary rocks of the SE Bohemian Massif show a rather broad but clear correlation belt. The data suggest a close link between the maximum paleotemperature and position within the Variscan orogen. High temperature exposure, deep burial and significant erosion probably occurred in the inner part of the Variscan thrust and fold belt which is now situated in the NW part of the Drahany Upland.

Intermediate paleo-thermal signature is observed in the central and SE part of the Drahany Upland and in the Mírov Unit (Zábřeh Upland).

Low thermal maturity gives evidence of shallower burial in the frontal Rhenohercynian and Subvariscan zones now buried under the nappes of the Outer Carpathians.

Acknowledgements: The authors wish to express their many thanks to J. Otava, J. Dvořák, P. Müller, and J. Środoń for helpful suggestions and to V. Šucha and P. Árkai for the revision of the manuscript.

References

Árkai P., 1991: Chlorite crystallinity and empirical approach and correlation with illite crystallinity, coal rank and mineral facies as exemplified by Paleozoic and Mesozoic rocks of northeast Hungary. *J. Metamorphic Geol.*, 9, 723–734.

Árkai P. & Lelkes-Felvári G., 1993: The effect of lithology, bulk chemistry and modal composition on illite "crystallinity" — a case study from the Bakony Mts., Hungary. *Clay Miner.* 28, 417–433.

Árkai P., Sassi F.P. & Sassi R., 1995: Simultaneous measurements of chlorite and illite crystallinity: a more reliable tool for monitoring low-to very low grade metamorphism in metapelites. A case study from the Southern Alps (NE Italy). *Eur. J. Mineralogy.* 7, 1115–1128.

Bostick N.H., 1979: Microscopic measurements of the level of catagenesis of solid organic matter in sedimentary rocks to aid exploration for petroleum and to determine former burial temperatures — a review. *SEPM*, 26, 17–43.

Chaloupský J., 1989: Major tectonostratigraphic units of the Bohemian Massif. *Geol. Soc. Amer., Spec. Pap.*, 230, 101–114.

Dallmeyer R.D., Franke W. & Weber K. (Eds.), 1995: Pre-Permian geology of Central and Eastern Europe. *Springer-Verlag*, Berlin, 1–604.

Duba D. & Williams Jones A.E., 1983: The application of illite crystallinity, organic matter reflectance, and isotopic techniques to mineral exploration: a case study in south-western Gaspe Quebec. *Econ. Geol.*, 78, 1350–1363.

Dvořák J. & Wolf M., 1979: Thermal metamorphism in the Moravian Paleozoic (Sudeticum, Č.S.S.R.). *Neu. Jb. Geol. Paläont. Abh., Mh.*, 10, 597–607.

Dvořák J., 1989: Anchimetamorphism in the Variscan tectogene in Central Europe its relationship to tectogenesis. *Věst. ÚÚG*, 64, 1, 17–30 (in Czech).

Dvořák J., 1995: Stratigraphy. In: Dallmeyer R.D., Franke W. & Weber K. (Eds.): *Pre-Permian geology of Central and Eastern Europe. Springer-Verlag*, Berlin, 479–489.

Franců J., Rudinec R. & Šimánek V., 1989: Hydrocarbon generation zone in the East Slovak Neogene basin: model and geochemical evidence. *Geol. Zbor. Geol. Carpath.*, 40, 3, 355–384.

Franců J., Müller P., Šucha V. & Zatkalíková V., 1990: Organic matter and clay minerals as indicators of thermal history in the Transcarpathian depression (East Slovak Neogene Basin) and the Vienna basin. *Geol. Zbor. Geol. Carpath.*, 41, 5, 535–546.

Frey M., 1986: Very low-grade metamorphism of clastic sedimentary rocks. In: Frey M. (Ed.): Low-temperature metamorphism. *Blackie*, Glasgow, 9–58.

Frey M., Teichmüller M., Teichmüller R., Mullis J., Künzi B., Breitschmid A., Gruner U. & Swizer B., 1980: Very low-grade metamorphism in external parts of the Central Alps: Illite crystallinity, coal rank and fluid inclusion data. *Eclogae Geol. Helv.*, 73, 1, 173–203.

Henrichs C., 1993: Sedimentographische Untersuchungen zur Hochdiagenese in der Kossen-Formation (obere Trias) der westlichen Ostalpen und angrenzender Südalpengebiete. *Bochumer Geol. Geotechn., Arb.*, 40, 206.

Jackson M.L., 1975: Soil chemical analysis-advanced cours. *Madison*, Wisconsin, 1–386.

Kisch H.J., 1987: Correlation between indicators of very low grade metamorphism. In: Frey M. (Ed.): *Low temperature metamorphism. Blackie*, Glasgow, 227–301.

Kisch H.J., 1983: Mineralogy and petrology of burial diagenesis (burial metamorphism) and incipient metamorphism in clastic rocks. In: Larsen G. & Chilingar G.V. (Eds.): *Diagenesis in Sediment and Sedimentary Rocks 2. Elsevier*, Amsterdam, 289–493, 513–541.

Kisch H.J., 1991: Illite crystallinity: Recommendations on sample preparation, X-ray diffraction, settings, and interlaboratory samples. *J. Metamorphic Geol.*, 9, 665–670.

Krejčí O., Francû J., Müller P., Pereszlényi M. & Stránik Z., 1994: Geologic structure and hydrocarbons generation in the Carpathian flysh belt of southern Moravia. *Věst. ČGÚ*, 69, 4, 13–26.

Kübler B., 1964: Les argiles, indicateurs de métamorphisme. *Rev. Inst. Franç. Petrole*, 19, 1093–1112.

Kübler B., 1967: La crystallinitede l'illite et les zones tout a fait superieures du metamorphisme. In: *Etages Tectoniques, Colloque de Neuchatel, 1966, A la Baconniere*, Neuchatel, 105–122.

Masaryk P., Milička J., Pereszlényi M. & Pagáč I., 1995: Geophysics, geochemistry and lithofacies in the Paleogene of the Levoča Mts. In: Kaličiak M. (Ed.): *Proceedings of the 3rd Conference in mem. J. Slávik. GÚDŠ*, Bratislava, 47–54 (in Slovak).

Milička J., Francû J., Horváth I. & Toman B., 1991: Optical, structural and thermal characterization of meta-anthracite from Zemplinicum. *Geol. Carpathica*, 42, 1, 53–58.

Milička J., Pereszlényi M., Šefara J. & Vass D., 1994: Organic geochemical study of the junction zone of the Danube Basin and Inner West Carpathians, Slovakia. *First Break*, 12, 11, 571–574.

Moore D.M. & Reynolds R.C., 1997: X-ray diffraction and the identification and analysis of clay minerals. *Oxford University Press*, Oxford, New York, 1–378.

Otava J. & Sulovský P., 1997: Material comparison of the Mohelnice Formation (Mírov development) and Moravosilesian Culm. *Geol. výzk. Morav. Slez. v r. 1996*, Brno, 28–30 (in Czech).

Pearson M.J. & Small J.S., 1988: Illite smetite diagenesis and paleotemperatures in northern north sea Quaternary to Mesozoic shale sequences. *Clay Miner.*, 23, 109–132.

Pereszlényi M., Milička J. & Vass D., 1993: Geochemistry and modelling of oil generation window in the Danube Basin. In: Rakús M. & Vozár J. (Eds.): *Geodynamic model and deep structure of the West Carpathians. GÚDŠ*, Bratislava, 201–206 (in Slovak).

Pereszlényi M., Vitáloš R., Milička J., Jankû J. & Slávik M., 1997: Oil and gas potential of the accretionary wedge of the West Carpathians. Proceedings of the 3rd International Conference on Oil and Gas Bussiness Activities. *Moravian Oil Company*, Hodonín, 197–199 (in Slovak).

Pollastro R.M., 1990: The illite/smectie geothermometer — concepts methodology, and application to basin history and hydrocarbon generation. In: Nuccio F. & Barker C.E. (Eds.): *Application of thermal maturity studies to energy exploration RMS-SEPM*, 1–18.

Pollastro R.M., 1993: Considerations and applications of the illite-smectite geothermometer in hydrocarbon-bearing rocks of Miocene to Mississipian age. *Clays and Clays Miner.*, 41, 119–133.

Reynolds R.C. Jr., 1985: NEWMOD, a computer program for the calculation of one-dimensional diffraction patterns of mixed layered clays. R.C.Reynolds Jr., 8 Brook Rd., Hanover, N.H.

Reynolds R.C. & Hower J., 1970: The nature of interlayering in mixed layer illite-montmorillonite. *Clays and Clay Miner.*, 18, 25–36.

Robert P., 1988: Organic metamorphism and geothermal history. *Elf-Aquitaine and D. Reidel publishing company*, Dordrecht, 1–311.

Środoń J. & Eberl D.D., 1984: Illite. In: Bailey S.W. (Ed.): *Micas*, 13, *Miner. Soc. Amer.*, 495–544.

Środoń J., 1995: Reconstruction of maximum paleotemperatures at present erosional surface of the Upper Silesia Basin, based on the composition of illite-smectite in shales. *Stud. Geol. Pol.*, 108, 9–20.

Šucha V., Kraus I. & Madejová J., 1994: Ammonium illite from anchimetamorphic shales associated with anthracite in the Zemplinicum of the Western Carpathians. *Clay Miner.*, 29, 369–377.

Teichmüller M., Taylor G.H. & Littke R., 1998. The nature of organic matter — macerals and associeted minerals. In: Taylor G.H., Teichmüller M., Davis A., Diessel C.F.K., Littke R. & Robert P. (Eds.): *Organic petrology. Gebrüder Borntraeger*, Berlin, 175–274.

Teichmüller M., Teichmüller R. & Weber K., 1979: Inkohlung und Illit-Kristalinitat Vergleichende Untersuchungen im Mesozoikum und Paleozoikum von Westfalen. *Fortschr. Geol. Rheinl. Westf.*, 27, 201–276

Todorov I., Schegg R. & Chochov S., 1992: Maturity studies in the Carboniferous Dobroudja coal basin (northeastern Bulgaria) — coalification, clay diagenesis and thermal modelling. *Int. J. Coal Geol.*, 21, 161–185.

Underwood M.B., Brocculeri T., Bergfeld D., Howell D.G. & Pawlewicz M., 1991: Statistical comparison between illite crystallinity and vitrinite reflectance, Kandik region of east-central Alaska. In: Bradley D.C. & Dusel-Bacon C. (Eds.): *Geologic studies in Alaska by the U.S. Geological Survey*, *1991. USGS Bull.*, 2041, 222–237.

Underwood M.B., Laughland M.M. & Kang S.M., 1993: A comparison among organic and inorganic indicators of diagenesis and low-temperature metamorphism, Tertiary Shimanto belt, Shikoku, Japan. *Geol. Soc. Amer., Spec. Pap.*, 273, 45–61.

Vavrdová M., 1997: Acritarchs of Cambrian age in the basal clastics underlying the Moravian Devonian (Němčičky-6 bore hole). *Zem. Plyn Nafta*, 42, 1, 31–32 (in Czech).

Waples D.W., 1985: Geochemistry in petroleum exploration. *REIDEL*, Boston, 1–232.

Weaver C.E., 1960: Possible use of clay minerals in the search for oil. *Bull. Amer. Assoc. Petrol. Geologists*, 44, 1505–1518.

Weaver C.E., Highsmith P.B. & Wampler J.M., 1984: Chlorite (Chapter 5). In: Weaver C.E. & Associates (Eds.): *Shale-slate metamorphism in southern Appalachians. Developments in Petrology, 10, Elsevier*, Amsterdam, 99–140.

Weber K., 1972: Notes on determinatin of illite crystallinity. *Neu. Jb. Mineral Abh., Mh.*, 267–276.

Wolf M., 1975: Relationship of illite crystallinity and coalification *Neu. Jb. Geol. Paläont. Abh., Mh.*, 437–447 (in German).

Příloha 4

Abrams, M.A. , Dahdah, N.F. , Franců, E. (2009) Development of methods to collect and analyze gasoline range (C5–C12) hydrocarbons from seabed sediments as indicators of subsurface hydrocarbon generation and entrapment. Applied Geochemistry 24, 10, 1951-1970.

Applied Geochemistry 24 (2009) 1951–1970

Contents lists available at ScienceDirect

Applied Geochemistry

journal homepage: www.elsevier.com/locate/apgeochem

Development of methods to collect and analyze gasoline range (C_5–C_{12}) hydrocarbons from seabed sediments as indicators of subsurface hydrocarbon generation and entrapment

Michael A. Abrams [a,*], Nicola F. Dahdah [a], Eva Francu [b]

[a] *Energy & Geoscience Institute, University of Utah, Salt Lake City, Utah, USA*
[b] *Czech Geological Survey, Leitnerova 22, 65869 Brno, Czech Republic*

A R T I C L E I N F O

Article history:
Received 3 December 2008
Accepted 17 July 2009
Available online 26 July 2009

Editorial handling by R. Fuge

A B S T R A C T

Gasoline range hydrocarbons (C_5–C_{12}) are usually associated with petroleum generation, yet few surface geochemical surveys have attempted to evaluate the gasoline range hydrocarbons in near-surface marine sediments. This is due to the difficulty in capturing and analyzing this volatile range of hydrocarbons with minimum loss and evaporative fractionation. In this study, a Headspace Solid Phase Microextraction (HSPME) method was developed and evaluated for the purpose of capturing the gasoline range of hydrocarbons within unconsolidated sediment using a solventless protocol.

The sediment SPME extraction method is based on the condition that phase/composition equilibrium is reached between sediment/water mix, container headspace, and SPME fiber coated with sorbent. In the experiments, the effectiveness of SPME to detect and measure low concentrations of migrated crude oil in marine sediments was evaluated. The following optimum laboratory procedure for SPME gasoline monitoring was established: collect the sample in sealed disrupter chamber (sealed sediment storage container which breaks apart sediment and releases interstitial volatile hydrocarbons), use a water bath to keep a stable laboratory temperature, use an NaCl saturated solution to help aromatic compounds move out of the solution to vapor phase, and wait a sufficient time to reach equilibrium. The results show that HSPME is very sensitive with sub ppm detection limits. SPME proved to be suitable to reveal the natural background and micro-seepage level of gasoline hydrocarbons in marine sediments.

1. Introduction

The gasoline range petroleum hydrocarbons comprise molecules with 5–12 carbons (C_5–C_{12}) arranged in linear, branched and cyclic aliphatic structures along with monoaromatic hydrocarbons such as benzene, toluene and o-, m- and p-xylenes. This group of hydrocarbons is normally derived from thermogenic processes associated with a working petroleum system (mature source rock generating sufficient volume of petroleum for entrapment), unlike the hydrocarbon gases (C_1–C_4) which may be from thermogenic or microbial processes (note C_2–C_4 microbial production is very limited, see Whiticar, 1999). The gasoline plus range hydrocarbons are volatile and will migrate within key oil migration avenues in petroleum bearing basins often reaching the sediment surface as near-surface petroleum seepage (Leythaeuser et al., 1983; and Kross and Leythaesser, 1996; Conant et al., 1996).

To date, few surface geochemical surveys have attempted to evaluate the gasoline plus range hydrocarbons in near-surface marine sediments. Most marine surface geochemical surveys evaluate the sediment interstitial light hydrocarbons C_1–C_5 using headspace gas analysis and high molecular weight hydrocarbons (C_{15+}) using solvent extraction, gas chromatography, and total scanning fluorescence (TSF) (Abrams, 1996, 2005). Conventional headspace light hydrocarbon analysis is not an effective method to evaluate the C_8–C_{12} hydrocarbons due to higher boiling points and low vapor pressures relative to the hydrocarbon gases (C_1–C_5) (Abrams and Dahdah, in press).

The purpose of this paper is to report on a relatively inexpensive method to screen near-surface marine sediments collected as part of regional surface geochemical surveys for the purpose of detecting migrated gasoline range hydrocarbons. *Solid Phase Microextraction* (SPME) is a method currently used in environmental surveys which has the potential to be used in surface geochemical surveys as a quick, inexpensive gasoline plus range screening tool (Potter and Pawliszyn, 1994; Steffan and Pawliszyn, 1996). SPME was initially developed for the analysis of volatile aromatic hydrocarbons (BTEX) using fused silica fiber coated with PDMS (polydimethylsiloxane,

---

* Corresponding author. Present address: Apache Corporation, 2000 Post Oak Blvd Suite 100, Houston, TX 77056-4400, USA. Tel.: +1 713 296 6742; fax: +1 713 296 6288.
E-mail address: michael.abrams@apachecorp.com (M.A. Abrams).

0883-2927/$ - see front matter © 2009 Elsevier Ltd. All rights reserved.
doi:10.1016/j.apgeochem.2009.07.009

adsorbent polymer) immersed to aqueous phase (Zhang and Pawliszyn, 1993a,b).

The Energy & Geoscience Institute at the University of Utah organized a research project to evaluate SPME as well as other surface geochemistry methods in a controlled laboratory experiment as well as in the field over known areas of leakage. The industry funded multi year *Surface Geochemistry Calibration* (SGC) study provided a platform to test existing and newly developed surface geochemistry methods (Abrams et al. 2004). The SGC study designed a series of laboratory experiments to test the effectiveness of SPME with varying concentration of gasoline range hydrocarbons mixed with cleansed shallow marine sediments. This paper reviews the SGC experimental results to determine the effectiveness of SPME as an inexpensive method to screen marine sediments for the presence of migrated gasoline range hydrocarbons.

2. Review of gasoline range sampling methods

Sampling the full gasoline plus range hydrocarbons in near-surface sediments requires a method which can capture and analyze the entire boiling point range with minimum fractionation. Standard solvent extraction methods will not work as the normal solvents used are within the same boiling point range as the hydrocarbons one is trying to capture.

The most common method used to examine the gasoline range hydrocarbons (C_6–C_8) in unconsolidated shallow marine sediments is the canned headspace analysis (Abrams, 1996, 2005). The non-mechanical headspace method utilizes a high speed shaking process to remove the interstitial sediment gases within a metal press lid container. The extracted interstitial sediment gases are sampled through a silicone septum on the top of a modified paint can container and then analyzed using conventional gas chromatography – flame ionization detection (GC-FID). The sample is prepared in the field by adding a designated aliquot of sediment, processed distilled or filtered water, and air or inert gas (He or N_2).

Headspace gas chromatograms from an offshore Gulf of Mexico survey, with large scale macroseepage (high concentrations with total sediment interstitial hydrocarbon gases in excess of 200,000 ppm; Abrams, 2005) display hydrocarbons up to C_{10} that include monoaromatic compounds such as benzene (Fig. 1). Note the systematic decrease in peak heights with increasing C number after pentane (C_5). This is partially related to the distribution of gasoline range hydrocarbons in the original crude oil but also related to limitations of the headspace sampling method for evaluating higher molecular weight hydrocarbons (above C_{5+}). The headspace method would be less effective in areas of passive micro-seepage (low concentrations with total sediment interstitial hydrocarbon gases greater than of 10,000 ppm but less than 50,000 ppm; Abrams, 2005).

The GORE-SORBER® module utilizes ePTFE (polytetrafluoroethylene) and sorbent filled collectors to collect and evaluate near-surface gasoline plus range hydrocarbons. ePTFE is a chemically inert microporous hydrophobic structure that allows the vapor transfer of hydrocarbons up C_{20+} but not water (Gore and Associates, 1997). The land based method places the sorber in the near-surface soil for an extended period of time (2–4 weeks) to collect a passive sample. The passive sampling method had to be modified to work in a marine survey because the GORE-SORBER® could not be placed on the ocean bottom for several weeks. The modified marine sampling GORE-SORBER® protocol places the sorber in a special glass container with a designated volume of sediment sub-sampled from a gravity core sample. The sorber is examined for a full range of hydrocarbons from C_2–C_{20+} via thermal desorption coupled with mass spectroscopy. Note that the hydrocarbons must be in a vapor phase to pass through the ePTFE material and adsorb onto the sorbent material.

The University of Victoria and Geological Survey of Canada (GSC) examined gasoline range hydrocarbons from crude oil samples (Harris et al., 1999) using Solid Phase Microextraction or SPME. The method works very well capturing the complete gasoline range hydrocarbons in pure oils but had not been tested with sediments containing low levels of migrated hydrocarbons (Harris et al., 1999).

The SGC study used a modified SPME method called Headspace Solid Phase Microextraction or HSPME. The headspace SPME method relies on an "equilibrium" between liquid sample, headspace and fiber in the vial providing a representation of the sediment gasoline plus the range hydrocarbon relative concentrations. The time needed to reach equilibrium will depend on the partition coefficients of all compounds between the three phases, but

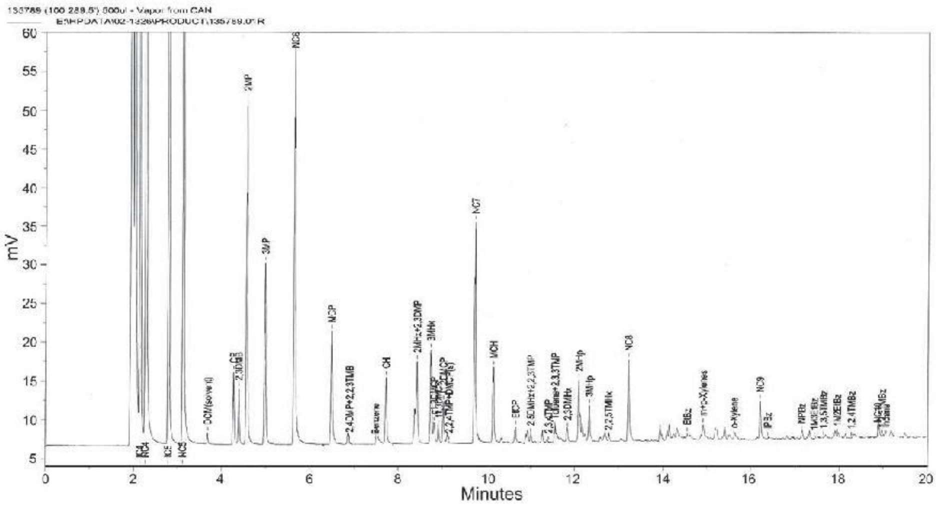

Fig. 1. Conventional headspace gas chromatography C_1–C_{10+} analysis.

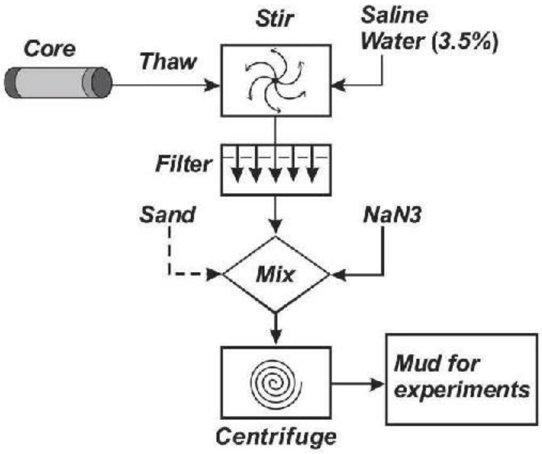

Fig. 2. Batch procedure for the preparation of sediment mixtures.

especially between the liquid (solute) and headspace (vapor). Harris et al. (1999) used a simplified concept of the Dias and Freeman early work (1997); equilibrium is achieved when the amount of analyte extracted remains constant regardless of increasing exposure time between fiber and sample. The liquid–vapor equilibrium is reached for gasoline range hydrocarbons within 10–15 min according to Harris et al. (1999). Harris et al. (1999) found 5 min was insufficient because the C_{8+} hydrocarbons have higher partition coefficients and need a longer time to equilibrate with the SPME fiber. The most significant factor affecting the magnitude of the partition coefficient is the affinity of an analyte for the fiber

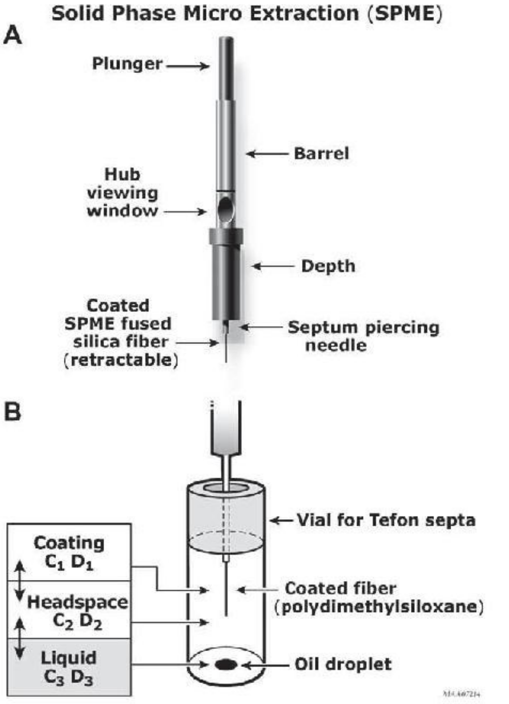

Fig. 4. Conventional SPME practice by transferring an aliquot of oil-spiked mud (oil drop shown) to a 15 mL vial with a Teflon lined silicone rubber septum (adapted from Harris et al., 1999).

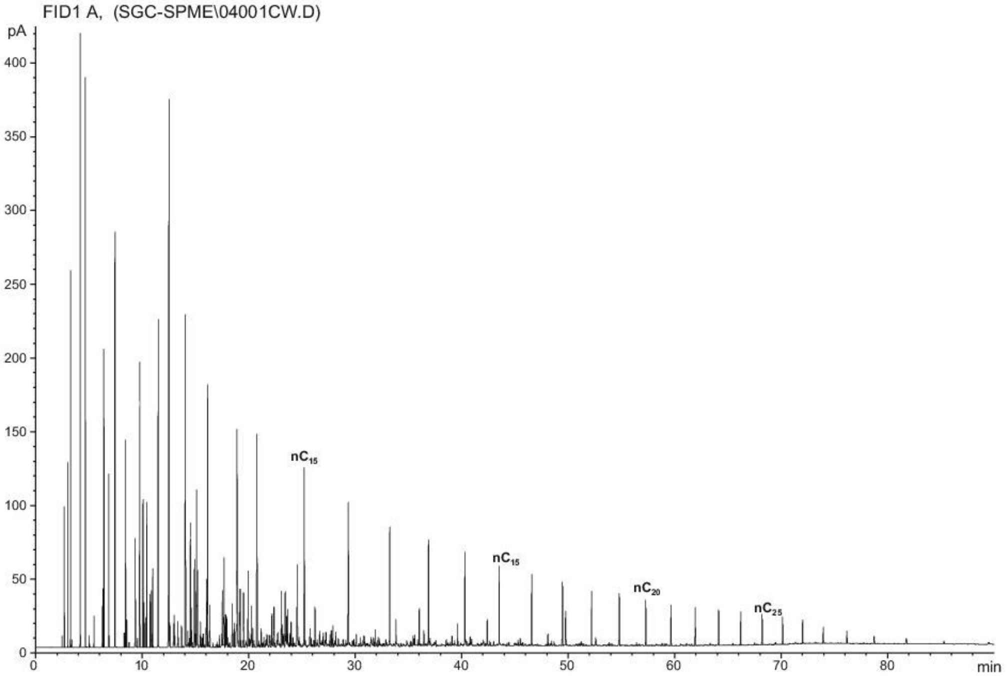

Fig. 3. Gas chromatogram of oil used in gasoline range HSPME experiments.

a

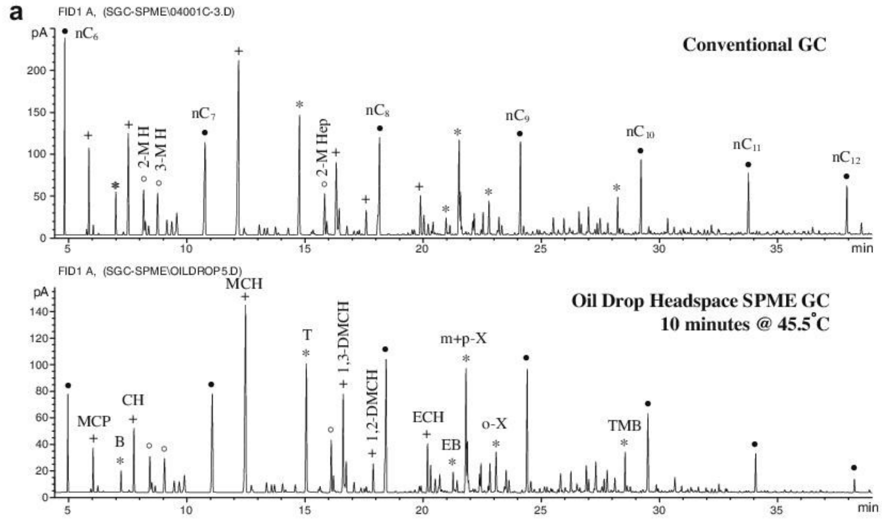

Key to Labels

normal alkanes

- ● $nC_6 - nC_{12}$: hexane, heptane, octane, nonane, decane, undecane, & dodecane

branched alkanes

° 2-MH	2-methylhexane
° 3-MH	3-methylhexane
° 2-MHep	2-methylheptane

cyclic alkanes

+ MCP	methylcyclopentane
+ CH	cyclohexane
+ MCH	methylcyclohexane
+ 1,3-DMCH	cis 1,3-dimethylcyclohexane
+ 1,2-DMCH	trans 1,2-dimethylcyclohexane
+ ECH	ethylcyclohexane

aromatics

* B	benzene
* T	toluene
* EB	ethylbenzene
* m+p-X	meta + para xylene (co-elution)
* o-X	ortho xylene
* TMB	1,2,4-trimethylbenzene

b

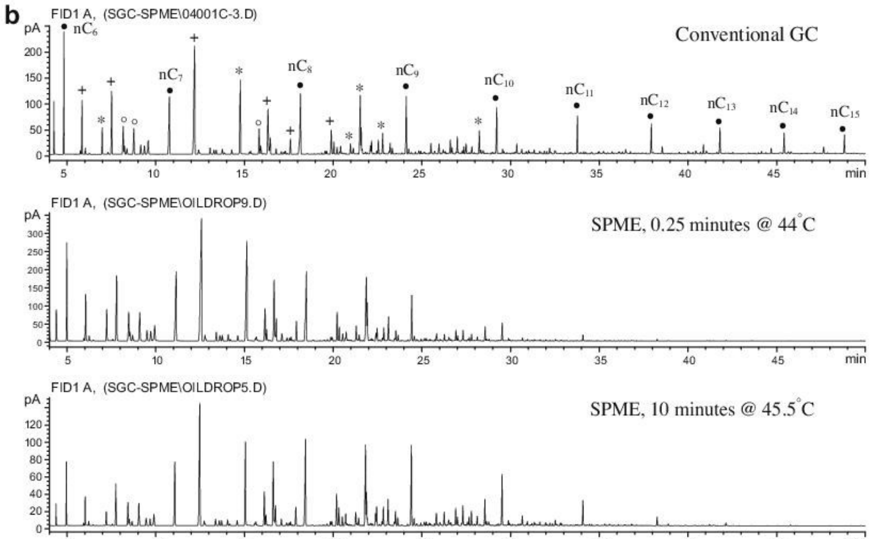

Fig. 5. (a) Comparison of conventional WO (whole oil) GC for test oil (top) and test oil drop headspace SPME analysis for 10 min exposure at 45.5 °C using 100 μm PDMS SPME fiber (bottom). (b) Comparison of conventional WO (whole oil) GC for test oil (top) to oil drop HSPME GC for variable exposure times 0.25 (middle) and 10 min (bottom) using 100 μm PDMS SPME fiber at 45.5 °C.

coating. The choice of an appropriate stationary phase is extremely important.

The SGC laboratory experiments further examined HSPME optimal conditions for marine sediment sampling by testing different fibers and varying the boundary conditions such as temperature, solution salinity, matrix and exposure times to determine optimal extraction conditions. The results of these experiments will be discussed in later sections.

3. Laboratory experiments

3.1. Sediment preparation

The petroleum charge experiments require uniform sediments representing typical deep sea and slope marine sediments. The sediment must have the same properties within the entire volume (homogenous), no interstitial hydrocarbon gases or microbes as a potential source of gas, and free of clumps. In addition, the sediment preparation process should not change the natural behavior of the sediment such as clay sorption. Thus no acids were used to remove potential sorbed or bound hydrocarbons or in situ high molecular weight hydrocarbons.

Table 1
SPME Stage I mixing parameters.

	5 ppm mix (wt/wt)	50 ppm mix (wt/wt)	500 ppm mix (wt/wt)
Processed mud (g)	151.8	151.5	151.8
Processed mud (g/cc)	1.44	1.44	1.44
Processed mud (cc)	105.4	105.2	105.4
Crude oil (g)	0.0008	0.0076	0.0759
Crude oil (g/cc)	0.771	0.771	0.771
Crude oil (cc)	0.0010	0.0098	0.0985
Deionized water (cc)	210.9	210.5	210.8

The deep sea marine sediment samples were kindly provided by TDI-Brooks International, from two seabed geochemical surveys; offshore deep water Angola and offshore deep water Gulf of Mexico. The sediment core samples provided were extra core material, unused in the original survey and located in areas with no anomalous sediment hydrocarbons or seismic indications of near-surface leakage. The sediments provided were in 18–25 cm (7–10 in.) segment, capped plastic core liners. All cores were kept frozen until processed. To reach the above mentioned criteria, the following batch procedure for the preparation of sediment mixtures was developed (Fig. 2); six segments of core for each batch were thawed overnight in a 19 L container, 3 L NaCl solution (35 g/L in deionized water) was added to the mud sample, the mud suspension was stirred and homogenized using a high speed industrial drill and a thin set mixer blade, the coarse grains and clumps were separated from the suspension using a sieve (opening 3.96 mm), fine grained sand (30–100 mesh Ottawa sand) was added to every other batch (1:7 or 14.3% sand by volume) and the mixture homogenized (sand added to provide similar sediment properties as near-surface shelf break sediments), 0.3 mL of 5% wt/v solution sodium azide (NaN_3) bactericide was added per batch and the mixture stirred (The amount of NaN_3 required to eliminate in situ bacteria was unknown. A few surface geochemical contractor laboratories currently using NaN_3 were contacted. None could provide in-house laboratory studies or published studies which examined the amount required to prevent bacterial activity. A 0.1 mL NaN_3 solution per 1 L of added water was used in this study based on the protocols currently used by many of the surface geochemical contractors), the suspension was allowed to settle in the container overnight, water was removed from sediment suspension using vented 1 L bucket centrifuge system (3000 rpm for 15 min), and finally the sediment batch was refrigerated in a 5 L plastic container.

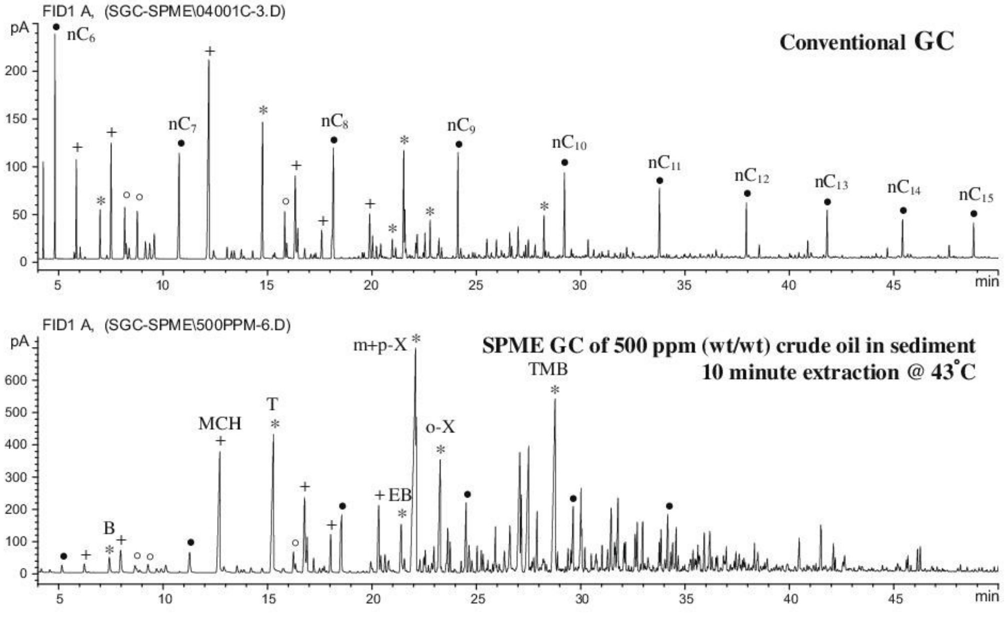

Fig. 6a. Comparison of conventional WO (whole oil) GC for test oil (top) and HSPME analysis of 500 ppm (wt/wt) oil in mud using 100 μm PDMS SPME fiber with a 10 min extraction at 43.0 °C (bottom).

3.2. Gasoline range plus experiment protocols

The HSPME gasoline range laboratory experiments were conducted in three stages:

1. pure crude oil in the sampling 15 mL vial,
2. crude oil and water–mud slurry in the sampling 15 mL vial, and
3. composite standard mixture of gasoline range hydrocarbons in a closed 480 mL disrupter container (see details below).

The disrupter container was designed for the SGC study as a field collection and storage device to provide optimal sediment preservation and removal of interstitial light hydrocarbons with minimal fractionation and/or alteration (Abrams and Dahdah, in

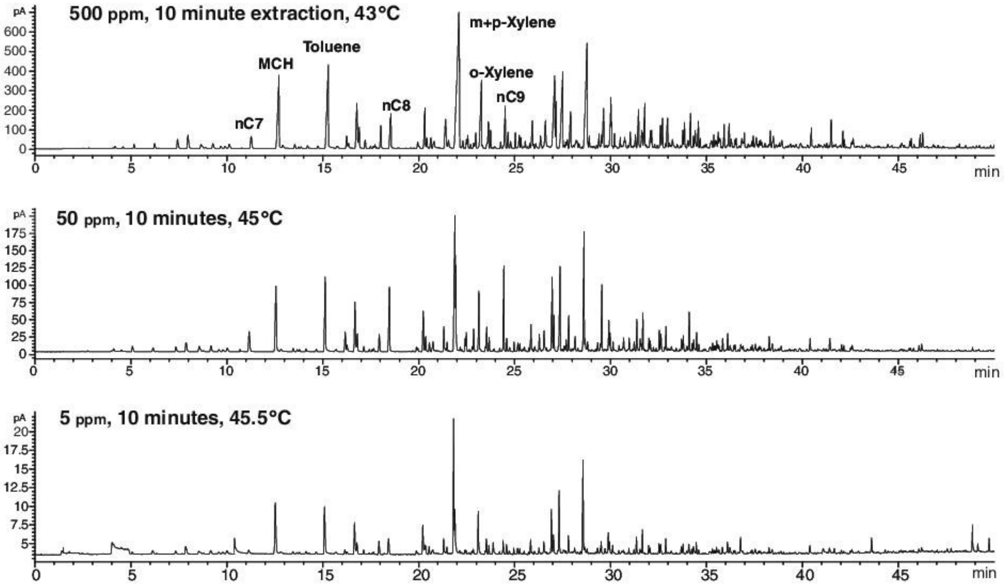

Fig. 6b. HSPME GC response for oil-mud mix at varying concentrations (500–5 ppm) with exposure time (10 min) and temperature constant (approximately 45 °C).

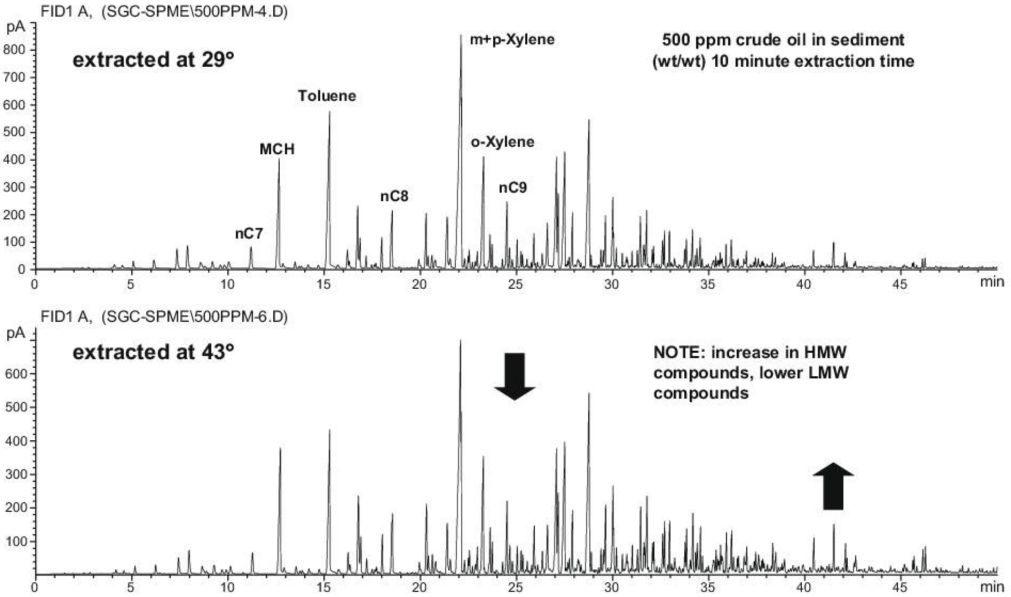

Fig. 6c. HSPME GC response for oil-mud mix at varying temperatures (29 °C and 45 °C) for 500 ppm concentration level and 10 min extraction time. GC displays elevated response of higher carbon numbers and decreased response of lower carbon numbers with higher temperatures.

press). The sealed disrupter container with sampling septum contains an internal fixed blade which does not rotate. The sediment moves at an elevated rate of motion using a high speed unidirectional paint shaker. The sediment sample passes through the disrupter blades quickly breaking apart the sediment and releasing the interstitial light hydrocarbons without the problems noted in the conventional blender and ball mill methods (Abrams and Dahdah, in press).

The purpose of these series of experiments was to evaluate the effectiveness of HSPME to detect and measure low concentrations of migrated crude oil in marine sediments. Key issues to be address in these experiments included; lowest level of hydrocarbon

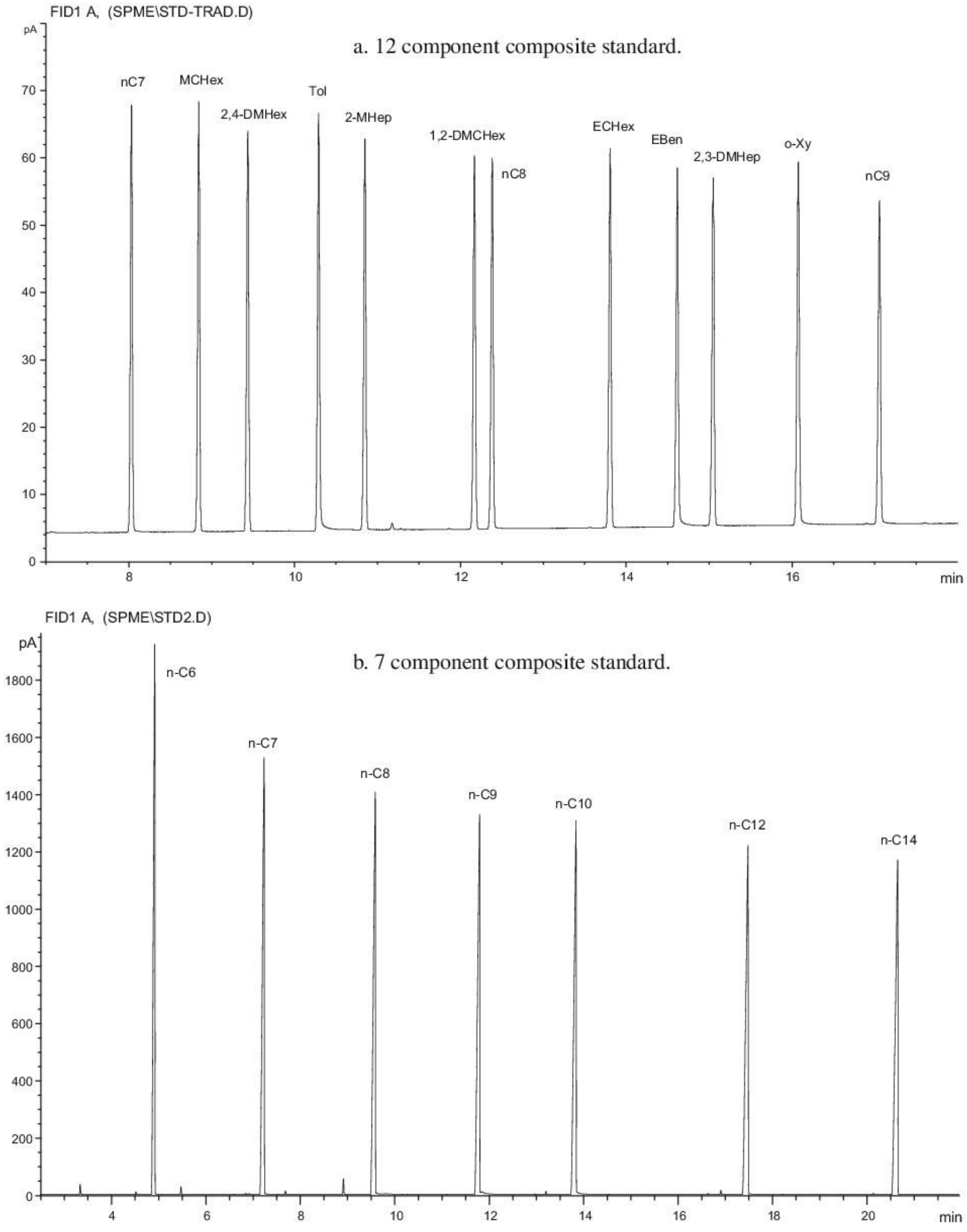

Fig. 7. Composite standards used for HSPME experiments.

seepage that could be detected with HSPME, optimal laboratory conditions for maximum recovery (temperature, water–sediment mix, water salinity, exposure time and fiber type), evaluation of HSPME fiber compound selectivity, and sediment migrated oil interaction (sorption).

The HSPME experiments were conducted using a Wyoming crude oil provided by the Flying J oil refinery with an API gravity of 51°. The Wyoming oil has a full range of gasoline range plus hydrocarbons with no volatile loss or bacterial alteration (Fig. 3). It should be noted that a 51° light oil with a full range of gasoline range plus hydrocarbons with no volatile loss or bacterial alteration does not represent a "typical" marine hydrocarbon seep but provides a baseline to evaluate the HSPME effectiveness (Abrams, 2005).

4. Results

4.1. Pure crude oil only

The first set of experiments was designed to reproduce the Harris et al. (1999) experiments and evaluate the effectiveness of HSPME as a gasoline range plus detection tool as well as to examine different fiber and exposure time issues. A similar HSPME set up used by Harris et al. (1999) was used, placing the oil droplet in a vial with a Teflon lined silicone rubber septum. The vial was placed on a heating/stir plate to facilitate temperature control. To evaluate fibers, exposure time, temperature and concentration with a pure crude oil, a 100 μm PDMS (polydimethylsiloxane) SPME fiber was inserted into the vial headspace above a crude oil droplet using Supelco's manual SPME apparatus shown in Fig. 4 at two temperatures (30 °C and 45 °C) and variable time intervals (0.25–30 min).

Comparison of conventional whole oil gas chromatography (WOGC) (Fig. 5a top) to oil drop HSPME gas chromatography at 10 min exposure and 45.5 °C temperature using the 100 μm PDMS fiber (Fig. 5a bottom) indicates no selectivity by compound class, but the comparison does show inefficiency of the SPME 100 μm PDMS fiber in the n-C_{7-} and n-C_{10+} range.

Fig. 5b compares conventional whole oil gas chromatography to oil drop HSPME gas chromatography for variable exposure times (0.25 and 10 min) using the 100 μm PDMS SPME fiber. Note the elevated response of higher C numbers and decreased response of lower C numbers with longer extraction time, 0.25 min (middle) to 10 min (bottom). The differences are related to the fiber response and compound volatility.

4.2. Crude oil and mud slurry mix

In the second set of experiments, small amounts of oil were mixed with processed marine sediments. The processed Angola mud was spiked with a Wyoming pipeline crude oil (51° API) at 5, 50 and 500 ppm concentrations. Deionized (DI) water was added at a 2:1 volume (Table 1). The mud, water and oil were mixed in a disrupter container using an unidirectional paint can shaker. After shaking for 5 min, 3.5 mL of the homogenized slurry was transferred to 15 mL vials with a small magnetic stir bar. The vials were placed on a heating/stir plate to facilitate mixing for headspace analysis.

Comparing conventional gas chromatography analysis of the crude oil to oil drop in the headspace using HSPME (Fig. 5a) displayed no compound class selectivity. However, when extracting headspace using HSPME above the oil–spiked mud slurry, the results indicated an enhancement of aromatic compounds over saturate compounds (Fig. 6a bottom). This result may be an artifact of the sediment oil mix preparation procedures. By opening the container in which the mud sample was spiked and homogenized; the

Table 2
Standard mixture No. 1 used for calibration of the SPME method.

Compound name	Compound class	Carbon number	Amount (g)	wt.% of mix
Heptane	Alkane	7	0.2085	8.48
Methylcyclohexane	Napthene	7	0.2066	8.41
2,4-Dimethylhexane	Alkane	8	0.2060	8.38
Toluene (methylbenzene)	Aromatic	7	0.2045	8.32
2-Methylheptane	Alkane	8	0.2059	8.38
trans 1,2-dimethylcyclohexane	Napthene	8	0.2013	8.19
Octane	Alkane	8	0.2066	8.41
Ethylcyclohexane	Napthene	8	0.2080	8.46
Ethylbenzene	Aromatic	8	0.2009	8.17
2,3-Dimethylheptane	Alkane	9	0.2045	8.32
o-xylene (1,2-dimethylbenzene)	Aromatic	8	0.2041	8.30
Nonane	Alkane	9	0.2009	8.17
Total amount (g)			2.4578	100.00

Table 3
Standard mixture No. 2 used for calibration of the SPME method.

Compound name	Compound class	Carbon number	Amount (g)	wt.% of mix
Hexane	Alkane	6	0.2101	11.45
Heptane	Alkane	7	0.2054	11.19
Octane	Alkane	8	0.2078	11.32
Nonane	Alkane	9	0.2018	10.99
Decane	Alkane	10	0.2029	11.05
Dodecane	Alkane	12	0.2078	11.32
Tetradecane	Alkane	14	0.2037	11.10
Pentadecane	Alkane	15	0.0800	4.36
Hexadecane	Alkane	16	0.1592	8.67
Heptadecane	Alkane	17	0.1570	8.55
Total amount (g)			1.8357	100.00

original vapor phase quickly escapes when the mud is transferred to the vial preferentially retaining the aromatic compounds due to their higher solubility in water. Thus the new headspace in the vial is not representative of the original spiked sample.

The HSPME gas chromatogram response was evaluated for oil and mud mixes at varying concentrations; 500–5 ppm (Fig. 6b). The exposure time was kept constant at 10 min and temperature kept constant at approximately 45 °C. Although the response was significantly lower at the 5 ppm concentration, the key oil related gasoline range compounds could be detected and identified. Based on these results, it is believed that the HSPME method can be used to detect very small concentrations of migrated gasoline range hydrocarbons in sediments.

HSPME gas chromatogram response was evaluated for varying extraction temperatures, 29 °C and 45 °C; while extraction time was kept constant at 10 min for a 500 ppm concentration sample (Fig. 6c). The higher temperatures will drive more analyte from the liquid phase into headspace vapor, but the increased temperature also reduces the efficiency of SPME fiber absorption. Fig. 6c displays elevated response of higher C numbers and decreased response of lower C numbers with higher temperatures.

4.3. Multi-component hydrocarbon mix

In the third and last set of HSPME experiments, a simpler system (limited number of compounds) was tested under a more controlled laboratory setting to avoid volatile loss problems experienced in the second set of HSPME experiments. The processed Angola mud was spiked with two multi-component hydrocarbon mixes, one containing a 12 component composite with four major compound groups: normal alkanes, cycloalkanes, iso-alkanes and aromatics (Fig. 7a and Table 2), and a second containing seven component composite with one compound group: normal alkanes (Fig. 7b and Table 3). The second mixture actually has 10 alkanes, but the weight percent of n-C_{15}, n-C_{16}, and n-C_{17} are not equal to the first seven in the mix and were ignored.

The composite standards and mud were mixed in a sealed disrupter container to prevent volatile loss. The SPME fiber was exposed to disrupter container headspace via a septum on the upper disrupter cap.

The goal during this final stage of SPME experiments was to evaluate the effect of temperature and water salinity on the equilibrium between mud and headspace during hydrocarbon

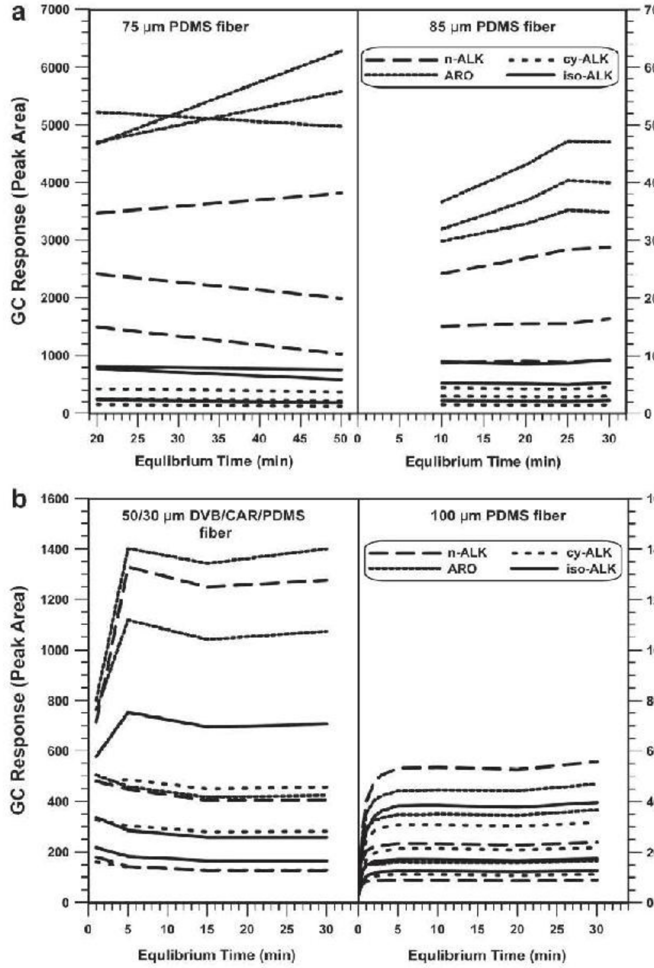

Fig. 8. Standard No. 1 in dry disrupter using different SPME fibers at ambient temperatures (23.0 °C). (a) 75 PDMS and 85 PDMS fibers. (b) 50/30 DVB/CAR/PDMS and 100 PDMS.

desorption from slurry to overlying vapor; and headspace and fiber during sorption of hydrocarbons from ambient vapor to SPME fiber. The HSPME experimental conditions examined in these last set of experiments included sampling temperature (22–23 °C, ambient conditions and elevated temperatures of approximately 34 °C), equilibrium time (1–50 min), pore water salinity (deionized water and saturated NaCl solution), and four different commercially produced Supelco SPME fibers of fused silicon coated with specific absorptive phase(*s*) of different thicknesses; 100 μm polydimethylsiloxane-PDMS, 85 μm carboxen/polydimethylsiloxane-CAR/PDMS, 75 μm carboxen/polydimethylsiloxane-CAR/PDMS, and 50/30 μm divinylbenzene/carboxen/polydimethylsiloxane-DVB/CAR/PDMS.

The experiments started with the simple system of standard vapor and fiber with sorbent and gradually increased in complexity. In each experiment, only one parameter was changed to evaluate its specific effect on measured data. The experiments were carried out with the following settings; standard in a closed disrupter container (dry), standard and water solution in a closed disrupter container, and standard and brine solution plus mud in a closed disrupter container.

Based on the experience gained from each step, each experiment was a stepwise progression to optimize the analytical procedure.

4.3.1. Standard in a closed disrupter container

One microliter of pure Standard No. 1 was injected by syringe into the closed disrupter container without any other components via the disrupter lid septum. The effect of exposure time on absorbed quantity of the hydrocarbons mixed together in standards was evaluated for all SPME fibers. The exposure time ranged from 15 s to 50 min and two different temperatures (approximately 23 °C and 34 °C) were used. Thus the peak areas in each analysis reflected specific absorption efficiency along with the detector re-

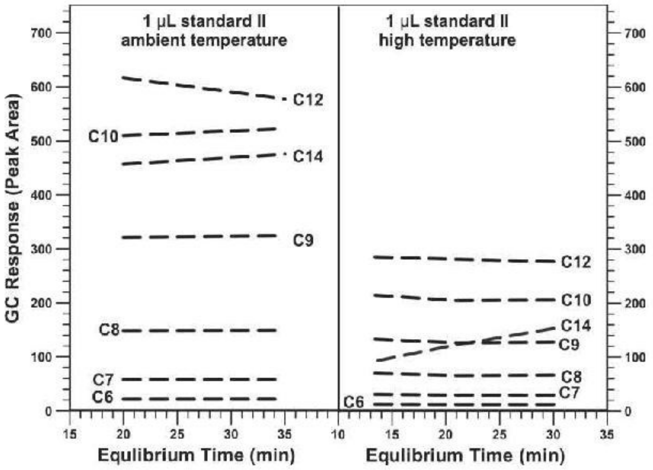

Fig. 9a. Standard No. 2 (7 component, normal alkanes) in dry disrupter using different temperatures for 100 PDMS fiber with ambient temperature (23 °C) and elevated temperature (34 °C).

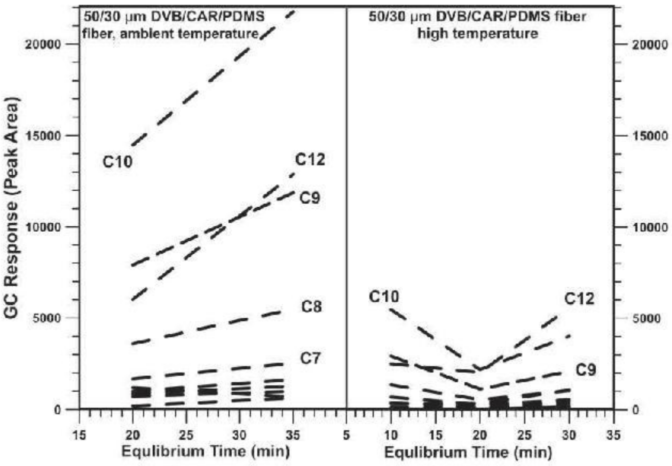

Fig. 9b. Standard No. 2 (7 component, normal alkanes) in dry disrupter using different temperatures for 50/30 DVB/CAR/PDMS fiber with ambient temperature (23 °C) and elevated temperature (34 °C).

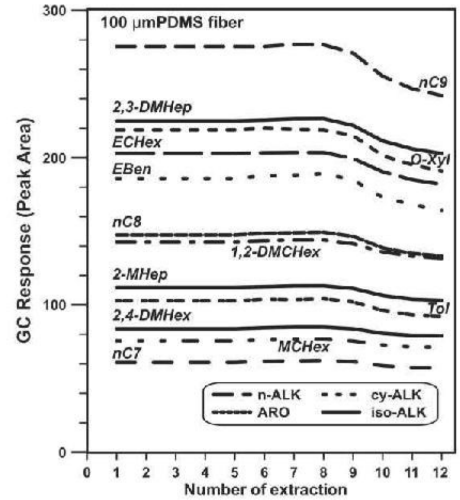

Fig. 10. Standard number 2 (7 component normal alkanes) within closed chamber with replicate headspace samplings using 100 µm PDMS fiber.

sponse factor of the injected, absorbed, and analyzed compounds from the composite Standard No. 1.

The 75 and 85 µm CAR/PDMS fibers displayed very strong preferential selectivity to aromatic hydrocarbons (Fig. 8a) resulting in the aromatic compounds having concentrations significantly higher than the cylco- and iso-alkanes. The 100 PDMS and 50/30 DVB/CAR/PDMS fibers provided needed sensitivity to small concentrations with less compound group selectivity problems (Fig. 8b). The 100 PDMS and 50/30 DVB/CAR/PDMS fibers also reached near equilibrium within 5–10 min whereas the 75 and 85 µm CAR/PDMS fibers required 25 or more minutes to reach equilibrium and stabilize (Fig. 8a and b).

Based on the above results, the 100 PDMS and 50/30 DVB/CAR/PDMS SPME fibers were chosen for the next series of calibration evaluations. Standard No. 2 (7 component alkanes only) was examined using the 100 µm PDMS and 50/30 µm DVB/CAR/PDMS fibers at two temperatures, (approximately 23 °C and 34 °C) to examine the SPME fiber temperature sensitivities. The higher temperatures drive more analyte from the liquid into headspace vapor but the increased temperature also reduces the efficiency of SPME fiber absorption. Thus increased temperatures (above ambient) do not provide a more “efficient” result (Figs. 9a and 9b). The SPME fibers are highly sensitive to small variations in room temperature. From repeated measurements the experiments indicated that reproducible hydrocarbon results require temperature differences less than 1 °C. Temperature variations greater than 1 °C may result in differences unrelated to hydrocarbons present in the sample.

In the next experiment, reproducibility of repeated headspace sampling using the 100 µm PDMS fiber was evaluated. The results showed that after eight repeated samplings of headspace vapor, the GC response (peak area) starts to decrease (Fig. 10). Similar observations were noted by Bernard (1978) with his headspace gas experiments undertaken during his PhD studies. The lower GC response signal is related to the decrease in total volatile hydrocarbon available after repeated removal of equilibrated headspace light hydrocarbons.

4.3.2. Standard and water solution in closed disrupter container

The 100 µm PDMS and 50/30 µm DVB/CAR/PDMS fibers were selected for the next set of experiments, testing the influence of water salinity. The disrupter container was filled with 320 mL solution (deionized or NaCl saturated water), the lid closed, 1 µL of standard added to the disrupter through the septum using a syringe, and then shaken for 5 min. Exposure time was 1–20 min at room temperature (approximately 23 °C). The preferred solubility of aromatic hydrocarbons in water was suppressed by using brine as the liquid phase in the experimental setting. It should be noted that the time required for equilibrium was longer in NaCl saturated solution relative to deionized water (Fig. 11).

Comparison of two different SPME fibers using the Standard No. 1 (12 components) with 2/3 volume NaCl saturated solution and disrupter container, indicated that the total amount of absorbed hydrocarbons on the 50/30 µm DVB/CAR/PDMS fiber was higher than that on the 100 µm PDMS fiber (Fig. 12). Therefore the 50/30 µm DVB/CAR/PDMS fiber is more efficient than the 100 µm PDMS fiber. When saturating the solution with salt, heat is no longer required to drive analytes into the headspace as a vapor. Theoretically the gasoline range plus hydrocarbons were less soluble in

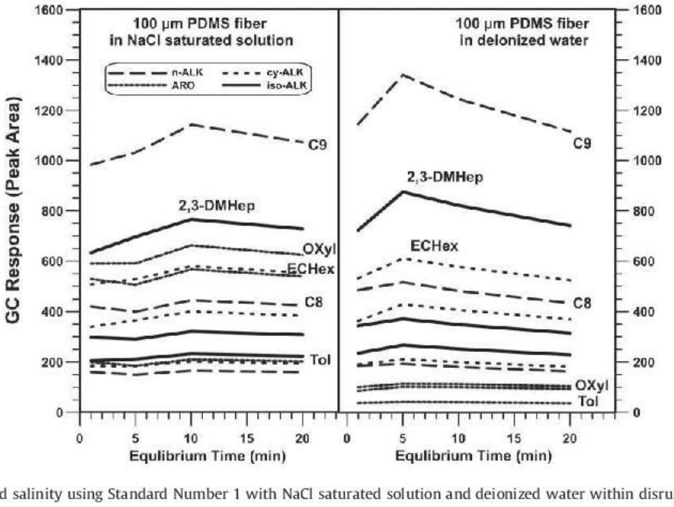

Fig. 11. Influence of increased salinity using Standard Number 1 with NaCl saturated solution and deionized water within disrupter and 100 µm PDMS fiber.

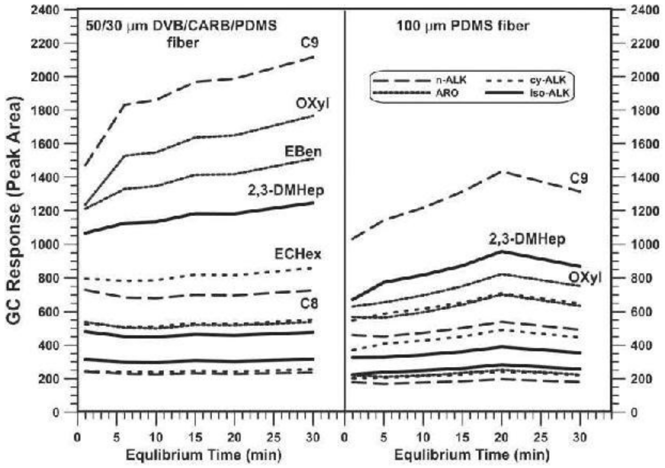

Fig. 12. Results for 100 PDMS and 50/30 DVB/CAR/PDMS fibers with same system (standard number 1 with 2/3 NaCl saturated solution in disrupter).

the saturated brine solution, but the mud may have had other sorption properties unrelated to the water solubility. It should be noted that once the saturated brine has been added to a marine sediment naturally exposed to seepage, the bulk of the partitioning will be within the water phase and the sorption capabilities of the sediment is beyond the survey control.

4.3.3. Standard, brine solution, and mud in disrupter container

The 100 µm PDMS and 50/30 µm DVB/CAR/PDMS SPME fibers were tested using Standard No. 1, brine solution, and mud slurry mix in the closed 480 mL disrupter canister. The disrupter container was filled with 160 mL of processed Angola mud, 160 mL saturated NaCl solution, the lid sealed, and 1 µL of Standard No. 1 added to the disrupter through the septum using syringe injection. The mixture was shaken for 10 min using the paint shaker. Key observations from the standard in brine solution versus the standard in mud/brine slurry in disrupter container (Fig. 13); different order and level of absorbed compounds when compared to composite standard and liquid system, increased time required to reach equilibrium, decreased amount of SPME extracted hydrocarbons relative to the composite standard and liquid system, and differences in hydrocarbon retention by sediments with different composition.

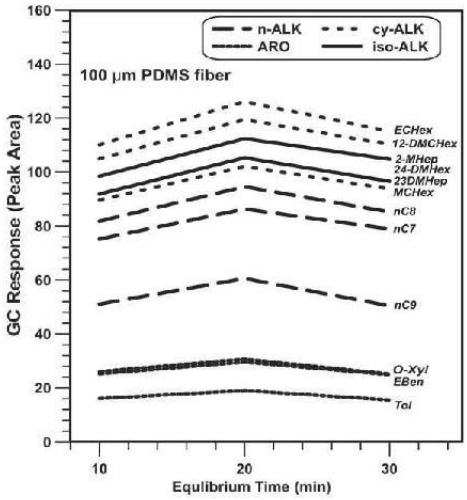

Fig. 13. Results from 1 µL Standard Number 1 in the Angola mud, NaCl saturated solution mixture using 100 µm PDMS fiber indicating an increase time required to reach equilibrium.

The addition of mud increased the experimental system complexity and provided additional evidence that organic matter sorption by unconsolidated sediments is an important factor which could modify the extracted gasoline range hydrocarbon composition. This is well recognized in the environmental literature, but generally ignored in surface geochemical studies. These experiments not only demonstrated that sediment adsorption is a factor, but provided new data on changes in distribution of compounds in the original migrated fluid. This will be an important factor when using gasoline range interpretation concepts developed for reservoir fluids with marine sediment extracted gasoline range hydrocarbons.

4.4. Evaluating optimal sampling protocols

Closed vessel experiments using the pure Flying J whole oil mixed with the Angola mud were used to further evaluate optimal extraction time and sediment–oil interactions. The 100 µm PDMS and 50/30 DVB/CAR/PDMS fibers were both used with 1 µL drop of crude oil placed into the dry glass vial. The minimum sufficient extraction time was 60 min for the 100 µm PDMS and 40 min for 50/30 DVB/CAR/PDMS fibers (Figs. 14a and 14b). The 100 µm PDMS fiber had better sorption efficiency for C_7–C_{14} hydrocarbons and the C_{7-} and C_{14+} the amount of absorbed hydrocarbons decreases. The 50/30 DVB/CAR/PDMS fiber was more efficient in sorption of aromatic hydrocarbons (T – toluene, p + mXy – para and meta xylene) and included a slightly broader molecular range of hydrocarbons when compared with the 100 µm PDMS.

Next, the disrupter container with internal blades to break apart the sediment and provide a more uniform distribution of charge hydrocarbon, was filled with 160 mL processed Angola mud, 160 mL saturated NaCl brine solution, and one tablespoon of excess NaCl. The lid was closed and 1 µL oil added to the disrupter through the septum using a syringe. The disrupter container with the mud, oil and saline water was placed in the paint shaker for 10 min. The 100 PDMS fiber was used. The closed disrupter container with the crude oil and mud/brine slurry was sampled multiple times (10). The results varied during the first day of sampling and analysis. The oil/brine solution/mud mixture required two days to reach equilibrium and provide constant relative amounts of HSPME compounds (Fig. 15a). The HSPME showed similar results after 20 and 30 min of exposure to the vapor above the

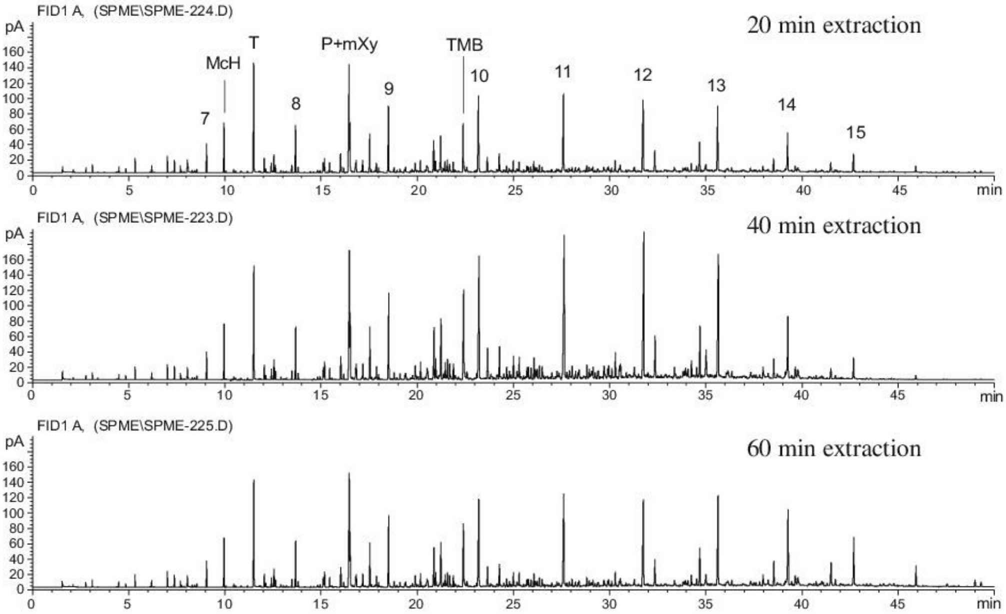

Fig. 14a. Evaluation of optimal extraction time using oil drop in vial analyzed with 100 µm PDMS at ambient temp 22 °C. The 100 µm PDMS fiber has better sorption efficiency for C_7–C_{14} hydrocarbons while C_7 minus and C_{14} plus decreases.

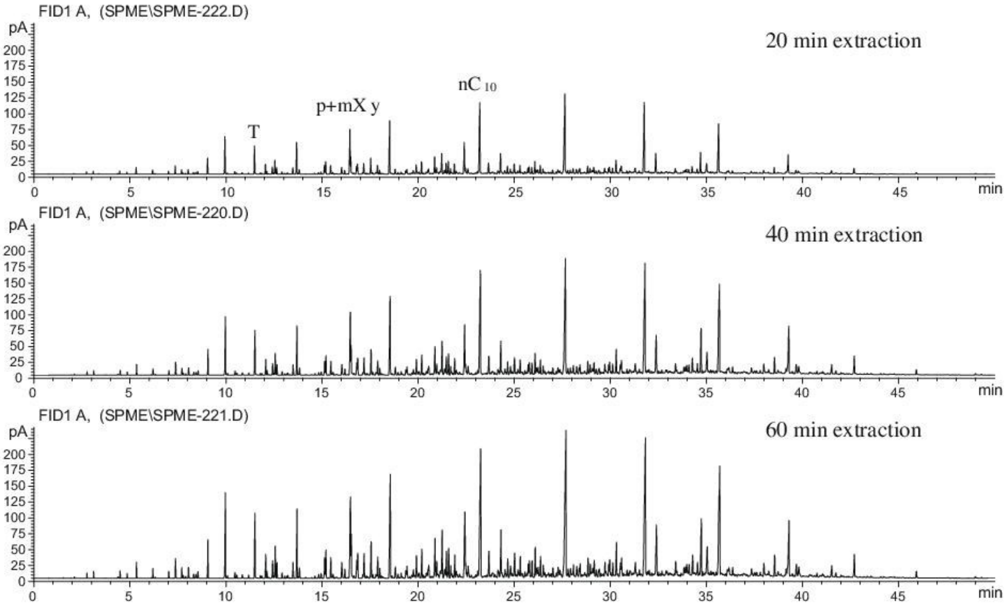

Fig. 14b. Evaluation of optimal extraction time using oil drop in vial analyzed with 50/30 µm DVB/CAR/PDMS at ambient temp 22 °C. 50/30 µm DVB/CAR/PDMS fiber is more efficient in sorption of aromatic hydrocarbons (T – toluene, p + mXy – para and meta xylene) and includes a slightly broader molecular range.

mud and liquid in the chamber (Fig. 15b). Twenty minutes were sufficient for constant results. The 100 μm PDMS preferentially adsorbed methcyclohexane (MCH) with respect to *n*-alkanes and aromatic compounds. The 50/30 DVB/CAR/PDMS fiber provided a lower amount of MCH and higher aromatic hydrocarbons (Fig. 15c).

4.5. Field trials of HSPME method

Approximately 70 piston cores with three sub-samples were collected as part of a seabed geochemical exploration program. A 160 mL sub-sample was provided to conduct disrupter container headspace gases (C_1–C_5) and gasoline range plus (C_5–C_{12+}) HSPME

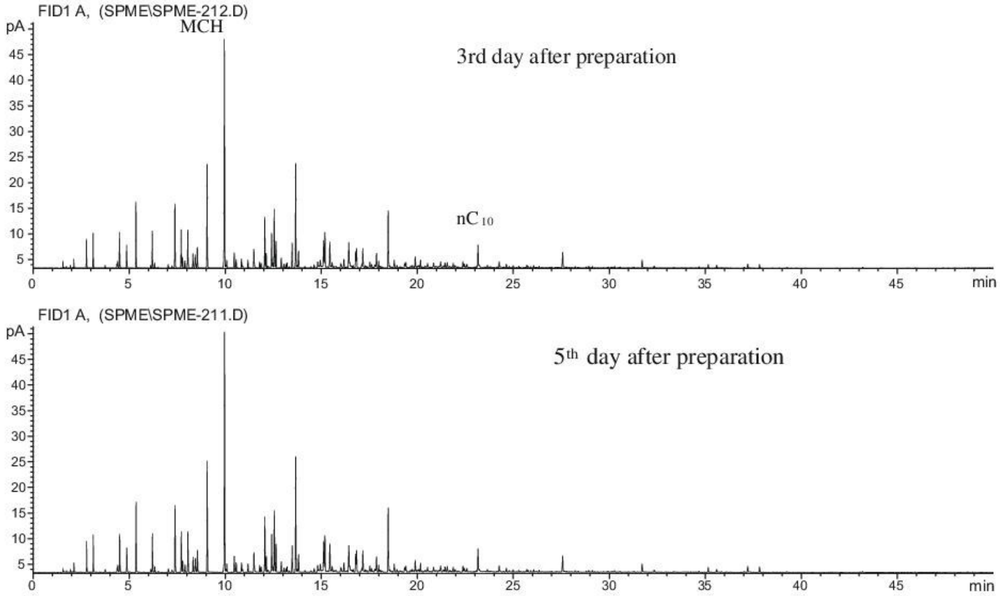

Fig. 15a. Crude oil and mud in disrupter 30 min extraction analyzed with 100 μm PDMS at ambient temp 22 °C. The oil/brine solution/mud mixture required two days to reach equilibrium and provide constant relative amounts of HSPME compounds.

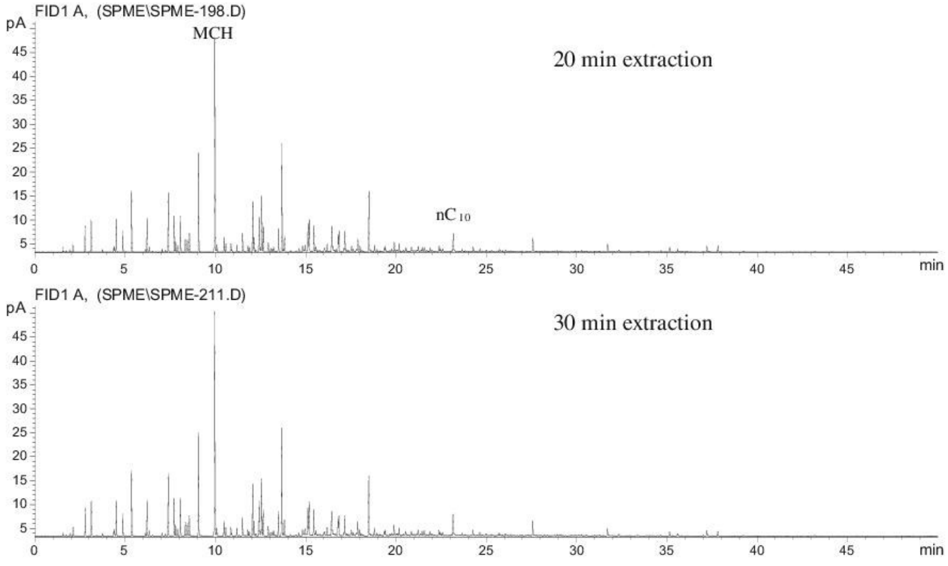

Fig. 15b. Oil drop and mud in disrupter analyzed 5th day after preparation with 100 μm PDMS at ambient temp 22 °C. The HSPME shows similar results after 20 and 30 min of exposure to the vapor above the mud and liquid in the chamber.

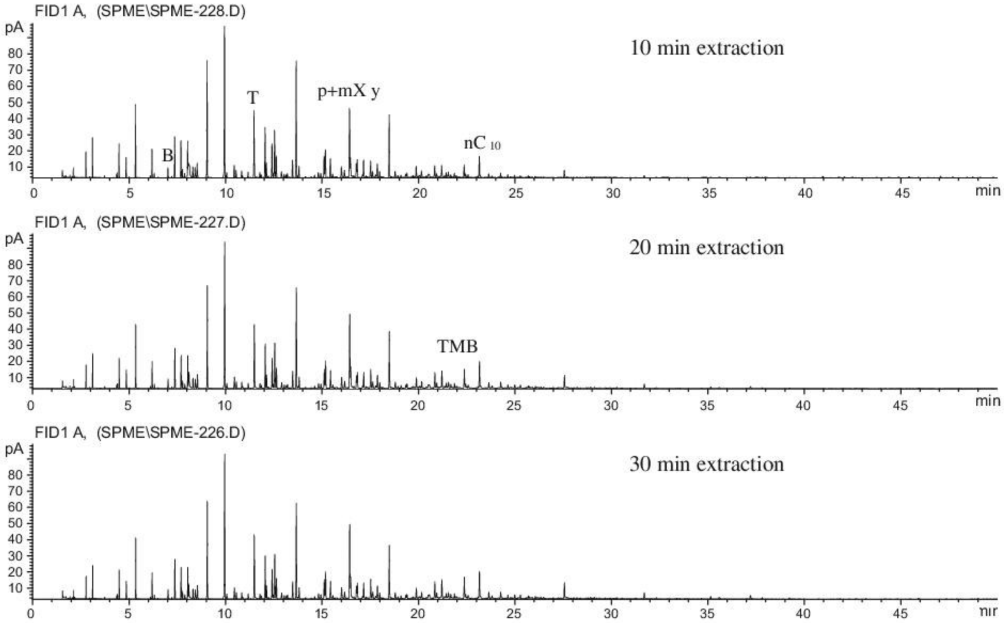

Fig. 15c. Oil drop and mud in disrupter analyzed 9th day after preparation with 50/30 μm DVB/CAR/PDMS fiber at ambient temp 22 °C. The 50/30 DVB/CAR/PDMS fiber provides a lower amount of MCH and higher aromatic hydrocarbons.

analysis. The samples were kept frozen until analysis in the University of Utah Energy & Geoscience Institute Geochemistry Research Laboratories. The frozen core samples were analyzed as follows; thawed disrupters with sediment sample were placed in a 45 °C water bath for 1 h (bath temperature drops initially), the thawed sample disrupters were shaken for 10 min using a commercial unidirectional paint mixer, a gastight syringe was used to sample the disrupter headspace through the septum, and the sample manually injected onto the split/splitless GC inlet for hydrocarbon gas (C_1–C_5) analysis. After headspace analysis was successfully completed, an SPME fiber assembly was inserted into the disrupter container headspace for 20 min extraction, then injected onto a split/splitless GC inlet for 5 min desorption.

4.5.1. HSPME quantification procedure

The samples could not be spiked with a standard due to the very small concentrations found in marine sediments and SPME fiber response. In an attempt to relate SPME fiber response to the amount of oil in mud, the average response at different times for uncharged muds spiked with the oil standard was calculated. The curves represented a 2 point calibration for GC response of 1 and 10 μL of oil added to mud with three time slices and sum. GC area was translated into μL of oil in disrupter equivalence, 1 μL of oil in 160 mL of mud represented 6.25 ppm v/v (total oil components). The HSPME data was reported as a sum of all resolvable areas within the main boiling point range detected with the SPME fiber plus the UCM (unresolved complex mixture).

4.5.2. HSPME results

Most of the 200 plus marine sediment samples analyzed contained very low concentrations of interstitial gas (C_1–C_5) and low HSPME total area (unresolved area). The disrupter HSPME gas chromatograms displayed two major signatures, background (Fig. 16) and anomalous (Fig. 17).

The background HSPME gas chromatograms (GCs) contained very low overall signal response (less than 10 total GC area). The chromatograms were dominated by peaks from the SPME fiber (Fig. 16) which were desorbed during the standard thermal extraction GC analysis. This is relatively normal for SPME fibers based on previous studies undertaken by the authors. The background SPME fiber contributed response will vary between analyses and with fiber condition thus the calculation of a standard background is not possible. Several factors contribute to the noisy SPME fiber background; it was operated at it's upper limit desorption temperature; and it was exposed to harsh extraction conditions (needle passes through mud slurry film before headspace exposure and high salinity). These conditions accelerate breakdown of the fiber phase causing shorter life and premature mechanical failures.

The anomalous HSPME gas chromatograms had a high overall signal response, which increased with depth, depleted in the light end, and had an unconsolidated complex mixture (UCM) "baseline hump" (Fig. 17 shows a depth profile of three sections from within a single core). Examination of the compound distributions indicated that the anomalous HSPME gas chromatograms were very different than for a "normal" oil signature. The GCs displayed severe depletion of the normal alkanes, monomethyl alkanes and the monoaromatics such as benzene (B), toluene (T) and the xylenes. Also depleted, but not as severely, were the cycloalkanes and single methyl cycloalkanes. However, compounds that are normally minor constituents of crude oil, such as the iso-alkanes and cycloalkanes with more than one methyl group, were elevated.

To demonstrate the key differences, three whole oil gas chromatograms (WOGC) are compared in Figs. 18 and 19; standard oil conventional split injection analysis (top chromatogram), disrupter HSPME analysis of mud mixed with the standard oil (middle chromatogram), and disrupter HSPME analysis of anomalous field sample (bottom chromatogram). Fig. 19 is the C_5–C_8 detail of Fig. 18.

The standard oil conventional WOGC shown in Figs. 18 and 19 (top chromatogram) contains normal distributions of the *n*-alkanes (*n*-C_5 to *n*-C_{12}), the monomethyl alkanes [2- and 3-methylpentane (2-MP and 3-MP); 2- and 3-methylhexane (2-MH and 3-MH); 2-, 3-, and 4-methylheptane (2-MHep, 3-MHep, and 4-MHep)]; aromatics (benzene, toluene, and m + p- and o-xylenes); cycloalkanes [such as cyclopentane (CP) and cyclohexane (CH)]; and the monomethylcycloalkanes methyl-cyclopentane (MCP) and methyl-

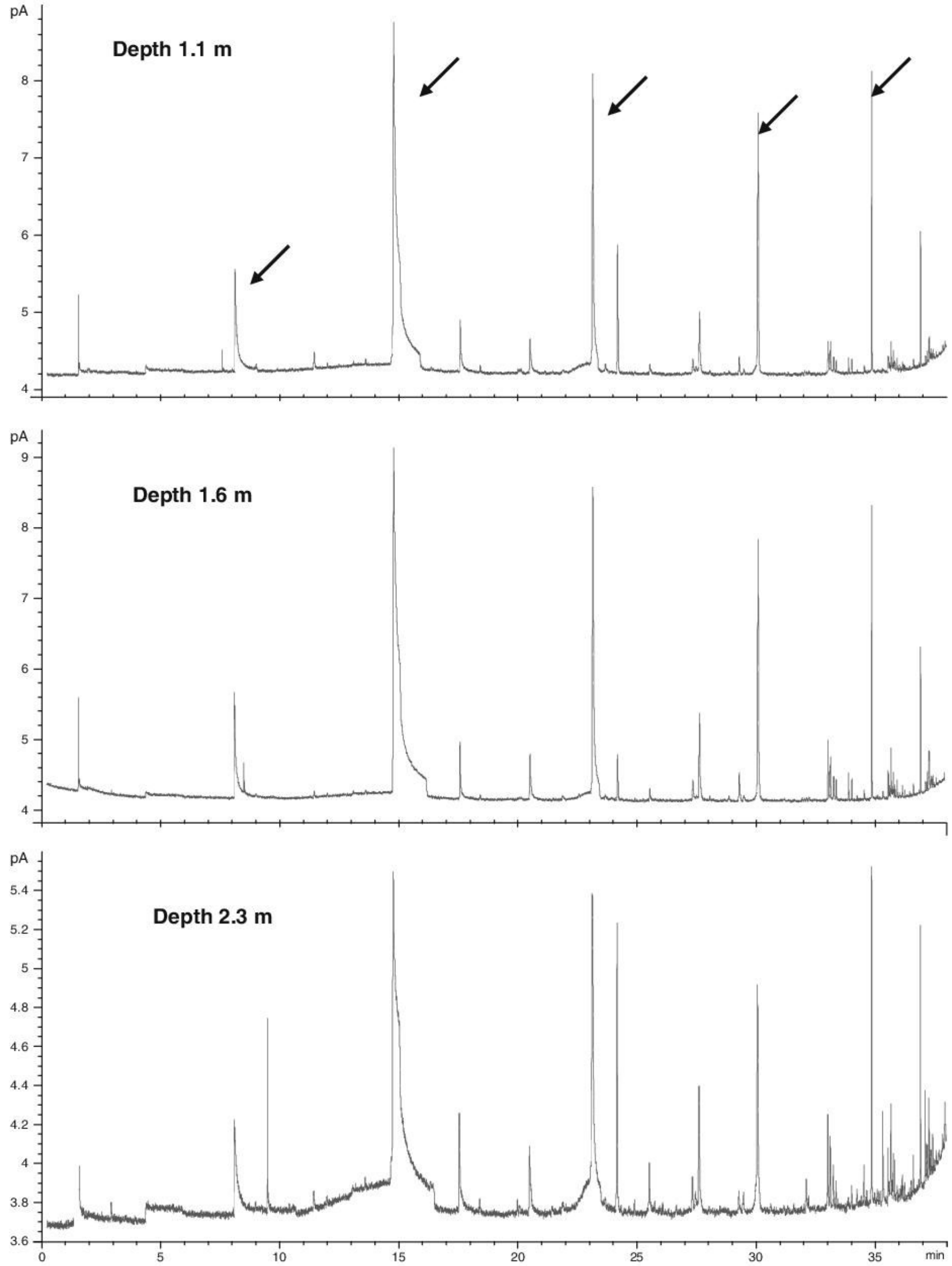

Fig. 16. Disrupter HSPME gas chromatogram signatures for depth profile within background core. Note the very low signal response. Peaks identified by arrow are normal fiber contributed signals.

cyclohexane (MCH). The iso-alkanes and cycloalkanes with more than one methyl group such as 2,3-dimethylbutane (2,3-DMB), 2,2,3-trimethylbutane (2,2,3-TMB), 2,3-dimethylpentane (2,3-DMP), 1,1,3-trimethylcyclopentane (1,1,3-TMCP) are much lower in abundance and are minor peaks; also typical of a normal distribution for crude oil.

The middle WOGC shown in Figs. 18 and 19 are from disrupter HSPME extraction of a mud sample mixed with the standard oil. The chromatograms contain similar characteristics as the standard oil conventional gas chromatogram except a relative reduction of the monoaromatics is seen due to water solubility. There is also a distinctive loss of signal for hydrocarbons less than n-C$_7$ and

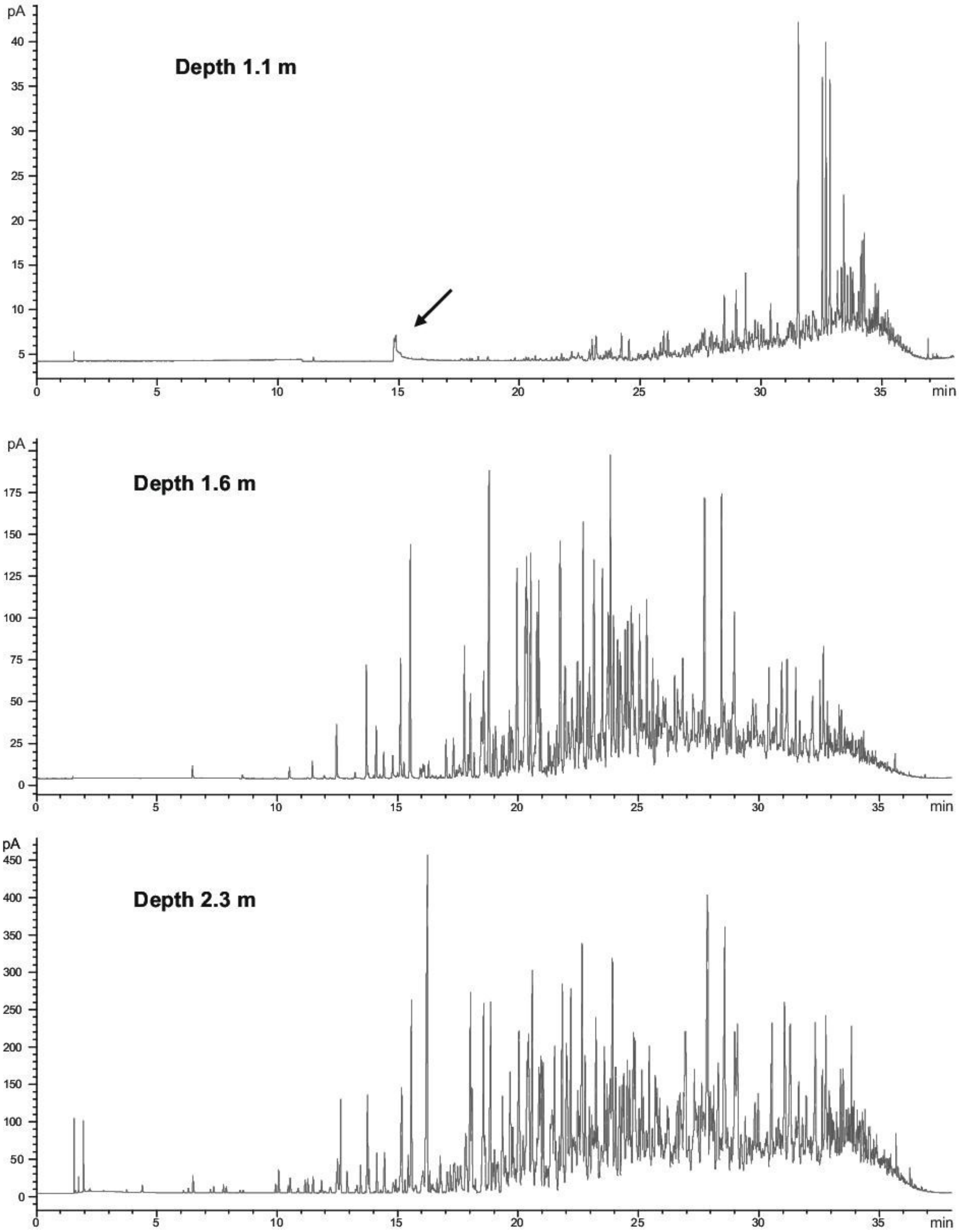

Fig. 17. Disrupter HSPME gas chromatogram signatures for depth profile within anomalous core. Note the elevated signal response which is also increasing with depth. The peak identified by the arrow is one of the larger fiber response peaks, note how small it is relative to the anomalous peaks.

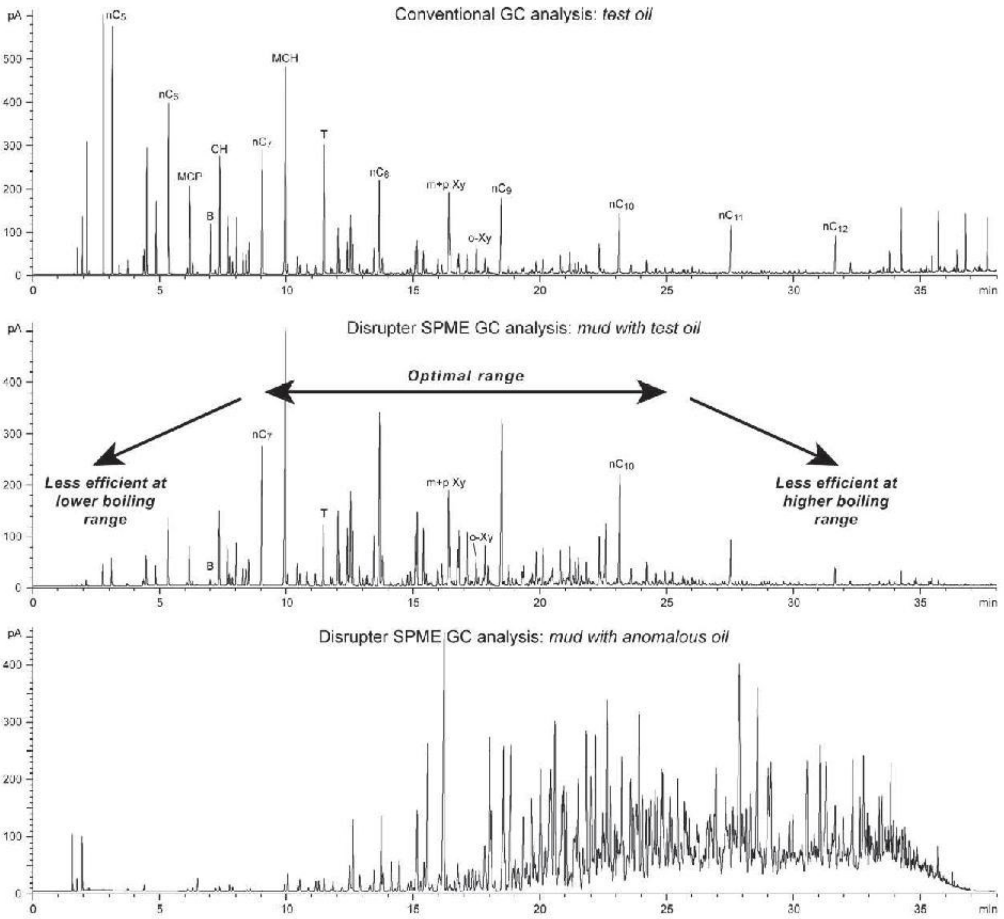

Fig. 18. Comparison of conventional whole oil gas chromatogram (WOGC) from standard oil (top) versus WOGC from disrupter HSPME of mud mixed with standard oil (middle) versus WOGC from disrupter HSPME of anomalous sample (bottom).

beyond n-C_{10} which demonstrates the optimum boiling range of the particular SPME fiber used for these experiments. The effective range is C_5–C_{12}, with the ability to detect high concentrations up to approximately C_{16}.

In stark contrast, the bottom WOGC chromatograms shown in Figs. 18 and 19 are from disrupter HSPME extraction for one of the anomalous core samples. The WOGC has a very different compound distribution relative to the two previous WOGC chromatograms. The anomalous sediment core sample contains very low to absent n-alkanes (n-C_5, n-C_6, n-C_7, and n-C_8) and aromatics (benzene, toluene, and xylenes). The single methyl alkanes (2-MP, 3-MP, 2-MH, 3-MH, 2-MHep, 3-MHep and 4-MHep), the cyclo-alkanes (CP and CH), and the single methyl cyclo-alkanes (MCP and MCH) are depleted. However, the iso-alkanes and cyclo-alkanes with more than one methyl group such as 2,3-DMB, 2,2,3-TMB, 2,3-MP, and 1,1,3-TMCP are elevated and prominent. Beyond n-C_8 the complexity of the increasing number of isomers and co-elutions makes it difficult to unravel, but the observed trend extends throughout the C_5–C_{12} gasoline range.

This unique compound distribution is commonly found in biodegraded reservoir oils. George et al. (2002) examined the gasoline range plus hydrocarbons with varying levels of biodegradation. George et al. (2002) observed the more soluble components such as benzene and toluene were removed by water washing; and the main controls on susceptibility to biodegradation include C skeleton, degree of alkylation, and position of alkylation. The biodegradation preference noted by George et al. (2002) includes; ring preference where iso-alkanes are retained over alkycyclohexanes; to some extent alkycyclopentanes and dimethylpentanes are more resistant than most dimethylcyclopentanes; methylhexanes depleted faster than methylpentanes and dimethylcyclopentanes; and alkylcyclohexanes are more resistant than linear alkanes. In addition, George et al. (2002) observed lower susceptibility to biodegradation with greater alkyl substitution for iso-alkanes, alkycyclohexanes, alkycyclopentanes and alkybenzenes; and position of alkylation such that adjacent methyl groups reduce susceptibility of an isomer to biodegradation.

These observations made by George et al. (2002) regarding biodegradation of reservoir oils appear to match the compound distributions noted in the seabed geochemical survey samples. The good news is that migrated petroleum can be identified in seabed geochemical samples using the disrupter container HSPME method. The bad news is the gasoline range plus compounds are readily altered in near-surface marine sediments making conventional

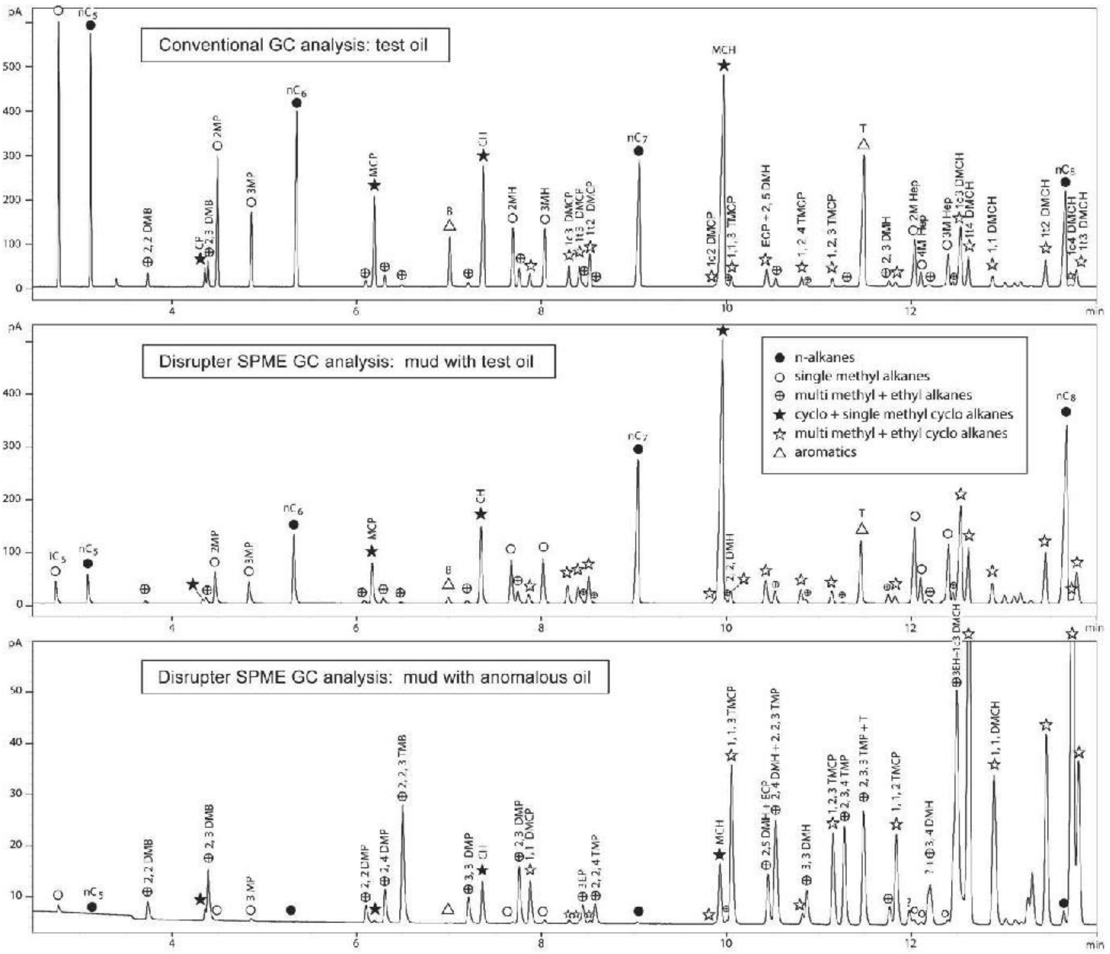

Fig. 19. Comparison of conventional whole oil gas chromatogram (WOGC) from standard oil (top) versus WOGC from disrupter HSPME of mud mixed with standard oil (middle) versus WOGC from disrupter HSPME of anomalous sample (bottom).

organic matter typing and determination of organic maturity relatively difficult. One will need to look at the higher molecular weight compounds (C_{12+}) using the more resistant biomarker range compounds to undertake a more rigorous source organic facies and maturation interpretation.

5. Discussion

The laboratory experiments using oil only, oil with processed marine sediment, and simple standards mixed with processed marine sediments demonstrated that HSPME has a very high sensitivity with detection of 1 μL, or less, of light crude oil in 160 mL of wet sediment. This amounts to approximately 6 ppm of total crude oil.

The laboratory protocols for optimal detection of gasoline range hydrocarbons in marine sediments using HSPME include; the use of a water bath to keep a stable laboratory temperature since the HSPME method is highly sensitive to small temperature fluctuations; use of a NaCl saturated solution to help aromatic compound partition from solution to vapor phase; and allowing 20 min for the SPME fiber to reach equilibrium with headspace vapors.

Supelco recommends the 100 μm PDMS fiber but the experimental results indicated that the 50/30 μm DVB/CAR/PDMS is a more efficient sorbent for aromatic and saturated hydrocarbons from a broader molecular range (C_7–C_{15}). It should be noted that there is a higher aromatic selectivity. More testing of real systems is necessary to better assess which fiber, 100 μm PDMS or 50/30 μm DVB/CAR/PDMS, is more efficient. The 100 PDMS was chosen because it was not selective by compound class.

HSPME experiments suggest that hydrocarbons within the gasoline range interact with the sediment by sorption. Potential fractionation by preferential sorption may occur and further study will be required to better understand the effects of sorption on selected gasoline range compounds.

The field testing of HSPME in a seabed geochemical survey confirmed that HSPME can be an effective tool to detect both micro and macro seepage. Examination of HSPME extract gas chromatograms from the anomalous sediment samples displayed a very different compound distribution than normally found in conventional undegraded oils; very low normal alkanes, aromatics, cycloalkanes and cycloalkanes with one methyl group but elevated iso-alkanes and cycloalkanes with more than one methyl group. This compound distribution is commonly found in biodegraded and water washed reservoir oils indicating the gasoline range hydrocarbons are subject to severe alteration effects in marine sediments even below the zone of maximum disturbance (Abrams, 1996). The addition of NaCl to the sample at high saturation levels appears to prevent post sampling bacterial alteration but most of the bacterial alteration and water washing most likely has occurred in situ prior to sampling (Abrams and Dahdah, in press) and appears to occur rapidly.

6. Conclusions

Headspace Solid Phase Microextraction, or HSPME, can be used as an effective tool to identify hydrocarbon seepage in marine sediments by examining the gasoline range hydrocarbons (C_5–C_{12+}) based on both laboratory experiments and field trials. The gasoline range hydrocarbons are volatile and most likely the first to leak from petroleum accumulations to the near-surface. This would make the gasoline range hydrocarbons (C_5–C_{12}) a very important target in surface geochemical surveys. This study identified a cost effective screening protocol using selected HSPME fibers, field collection in a tight sealing container (disrupter) which can break apart the sediment and release sediment volatile hydrocarbons, and specific laboratory procedures to most effectively capture the gasoline plus range hydrocarbons in near-surface unconsolidated marine sediments. It appears that in many or most cases the gasoline range hydrocarbons will be highly altered and not resemble the reservoired oil it came from. Nonetheless recognizing and detecting the gasoline range hydrocarbons even if extremely altered is an important advance in surface geochemistry surveys.

Acknowledgements

Many thanks to the Surface Geochemistry Calibration (SGC) research project industry supporters and Energy & Geoscience Institute (EGI) at the University of Utah. Drs. Harry Dembicki (Anadarko), Graham Logan (Geoscience Australia), Ger van Graas (StatoilHydro), Dennis Miller (Petrobras), Neil Frewin (Shell), Andy Bishop (Shell), Brad Huizinga (ConocoPhillips), Angelo Riva (ENI), and Peter Eisenach (Wintershall) who have all been extremely helpful during the various phases of the multi year industry funded research project. Special thanks to Dr. Kim Manzano-Kareah who was with EGI at the time of this study and a big help in completing the SGC report. Special thanks to the reviews by Drs. Harry Dembicki and Neil Frewin who provided excellent suggestions. The figures were drafted by Jeffrey Massara of Apache Corporation and Doug Jensen of Energy & Geoscience Institute.

References

Abrams, M.A., 1996. Distribution of subsurface hydrocarbon seepage in near surface marine sediments. In: Schumacher, D., Abrams, M.A. (Eds), Hydrocarbon Migration and Its Near Surface Effects. Am. Assoc. Petrol. Geol. Mem. 66, 1–14.

Abrams, M.A., 2005. Significance of hydrocarbon seepage relative to sub-surface petroleum generation and entrapment. Mar. Petrol. Geol. Bull. 22, 457–478.

Abrams, M.A., Dahdah, N.F., in press. Surface sediment gases as indicators of subsurface hydrocarbons – examining the record in laboratory and field studies. Mar. Petrol. Geol. Bull.

Abrams, M.A., Dahdah, N.F., Francu, E., 2004. Evaluating petroleum systems elements and processes in frontier exploration areas using seabed geochemistry. World Oil 225 (6), 53–60.

Bernard, B.D., 1978. Light hydrocarbons in marine sediments. Ph.D. thesis, Texas A&M Univ., College Station, Texas.

Conant, B.H., Gillham, R.W., Mendoza, C.A., 1996. Vapor transport of trichloroethylene in the unsaturated zone: field and numerical modeling investigations. Water Resour. Res. 32, 9–22.

Dias, R.F., Freeman, K.H., 1997. Carbon isotope analyses of semivolatile organic compounds in aqueous media using solid phase microextraction and isotope ratio monitoring GC/MS. Anal. Chem. 69, 944–950.

George, S., Boreham, C.J., Minifie, S.A., Teerman, S.C., 2002. The effect of minor to moderate biodegradation on C_5 to C_9 hydrocarbons in crude oils. Org. Geochem. 33, 1293–1317.

Gore and Associates, 1997. Surface Geochemical Exploration. W.L. Gore and Associates.

Harris, S.A., Whiticar, M., Eek, M.K., 1999. Molecular and isotopic analysis of oils by solid phase microextraction of gasoline range hydrocarbons. Org. Geochem. 30, 721–737.

Kross, B.M., Leythaesser, D., 1996. Molecular diffusion of light hydrocarbons in sedimentary rocks and its role in the migration and dissipation of natural gas. In: Schumacher, D., Abrams, M.A. (Eds), Hydrocarbon Migration and Its Near Surface Effects. Am. Assoc. Petrol. Geol. Mem. 66, 173–184.

Leythaeuser, D., Schaefer, R.G., Pooch, H., 1983. Diffusion of light hydrocarbons in subsurface sedimentary rocks. Am. Assoc. Petrol. Geol. Mem. Bull. 67, 889–895.

Potter, D.W., Pawliszyn, J., 1994. Rapid determination of polyaromatic hydrocarbons and polychlorinated biphenyls in water using solid-phase microextraction and GC/MS. Environ. Sci. Technol. 28, 298–305.

Steffan, A., Pawliszyn, J., 1996. Analysis of flavor volatiles using headspace solid phase microextraction. J. Agric. Food Chem. 44, 2187–2193.

Whiticar, M.J., 1999. Carbon and hydrogen isotope systematics of bacterial formation and oxidation of methane. Chem. Geol. 161, 291–314.

Zhang, Z., Pawliszyn, J., 1993a. Headspace solid-phase microextraction. Anal. Chem. 65, 1843–1852.

Zhang, Z., Pawliszyn, J., 1993b. Analysis of organic compounds in environmental samples by headspace solid phase microextraction. J. High Resolut. Chromatogr. 16, 689–692.

Příloha 5

Čopjaková R., Franců E., Novák M. (2011) Formation of authigenic monazite-(Ce) to monazite-(Nd) from Upper Carboniferous graywackes of the Drahany Upland: Roles of the chemical composition of host rock and burial temperature. Lithos 127, november, 373-385.

Lithos 127 (2011) 373–385

Contents lists available at SciVerse ScienceDirect

Lithos

journal homepage: www.elsevier.com/locate/lithos

Formation of authigenic monazite-(Ce) to monazite-(Nd) from Upper Carboniferous graywackes of the Drahany Upland: Roles of the chemical composition of host rock and burial temperature

Renata Čopjaková [a,b,*], Milan Novák [b], Eva Franců [a]

[a] Czech Geological Survey, Leitnerova 22, 658 69 Brno, Czech Republic
[b] Institute of Geological Sciences, Faculty of Science, Masaryk University, Kotlárská 2, 611 37 Brno, Czech Republic

ARTICLE INFO

Article history:
Received 6 January 2011
Accepted 2 August 2011
Available online 8 August 2011

Keywords:
Authigenic monazite
Diagenesis
Very-low grade metamorphism
Graywackes
Lower Carboniferous Culm basin
Bohemian Massif

ABSTRACT

Irregular aggregates of monazite-(Ce) to monazite-(Nd), up to 150 μm in diameter, have been found in graywackes from the Protivanov Formation, Drahany Upland, Czech Republic. Monazite aggregates enclose a variety of detrital and authigenic minerals. Textural evidences suggest that they are of authigenic origin and grew during very low-grade metamorphism at a maximum temperature ~200–300 °C in relation to a deep burial. Rarely, they enclose relics of detrital monazite with a chemical composition typical for high-grade monazite. Intensive fluid-related REE-remobilization occurred in relation to this very low-grade metamorphism. Authigenic monazite appears to form only in Ca-poor rocks. In Ca-rich graywackes, which underwent the same low-temperature metamorphic overprint, authigenic synchysite-(Ce) or parisite-(Ce) are common instead. In the overlaying Rozstání and Myslejovice Formations (T~150–200 °C), remobilization of REEs was low and authigenic monazite did not form even in the Ca-poor graywackes. Authigenic monazite shows low concentrations of Th, U, Ca, Y + HREE, and a low Eu anomaly. The central parts of the aggregates are enriched in Nd + MREE, whereas the outer parts are enriched in La and Ce. Zoning pattern suggests an evolution in fluid chemistry during diagenesis/very low-grade metamorphism or it relates to different solubility of the individual REE-phosphates. The major source of REEs in the pore fluids are probably detrital minerals mainly monazite. Other minor sources of REEs probably include Fe-oxide/hydroxide and/or clay minerals, which could have contributed to the Nd + MREE-rich cores in the authigenic monazite.

1. Introduction

Monazite (monoclinic $LREEPO_4$) is a common accessory mineral in medium- to high-grade metamorphic rocks (e.g. Ferry, 2000; Foster and Parrish, 2003; Foster et al., 2002; Kingsbury et al., 1993; Krenn et al., 2008; Lanzirotti and Hanson, 1996; Smith and Barreiro, 1990; Spear and Pyle, 2002), however, studies dealing with formation of monazite at diagenetic to low-grade metamorphic conditions are sporadical. Nodular low-grade monazite representing burial-related stage has been reported from black shales (Donnot et al., 1973; Evans and Zalasiewicz, 1996; Evans et al., 2002; Lev et al., 1998; Milodowski and Zalasiewicz, 1991). Low-grade metamorphic monazite-(Ce) has been described in metapelites and sandstones equilibrated under greenschist and blueschist conditions at T~300–400 °C, P~3–10 kbar (e.g. Burnotte et al., 1989; Cabella et al., 2001; Franz et al., 1996; Janots et al., 2006; Ohr et al., 1994; Rasmussen and Muhling, 2007, 2009; Rasmussen et al., 2001, 2005, 2007; Wan et al., 2007; Wing et al., 2003).

There is uncertainty regarding the metamorphic or diagenetic temperatures at which low-T monazite grows in (meta)sediments. Monazite formation in low-temperature metasediments is controlled by several others factors such as the whole-rock composition, composition of diagenetic/metamorphic fluids and/or tectonic processes (González-Álvarez et al., 2006; Rasmussen and Muhling, 2009; Wilby et al., 2007). In this paper we present evidences for the monazite formation in graywackes during a deep burial. We describe in detail the occurrence, textural characteristics, REE geochemistry and REE source of authigenic monazite. The effects of graywacke whole-rock chemical composition and burial temperature also are discussed.

2. Geological setting

The Drahany Upland is exposed on the easternmost part of the Bohemian Massif (Fig. 1a). This is a foreland basin related to the Variscan Orogen and belongs to the Moravian–Silesian Culm Basin. The Drahany Upland represents deep-marine sediments, widespread graywackes, less abundant shales and minor conglomerates, deposited as an axial turbidite

---

* Corresponding author at: Czech Geological Survey, Leitnerova 22, 658 69 Brno, Czech Republic.
E-mail addresses: copjakova@sci.muni.cz (R. Čopjaková), mnovak@sci.muni.cz (M. Novák), eva.francu@geology.cz (E. Franců).

0024-4937/$ – see front matter © 2011 Elsevier B.V. All rights reserved.
doi:10.1016/j.lithos.2011.08.001

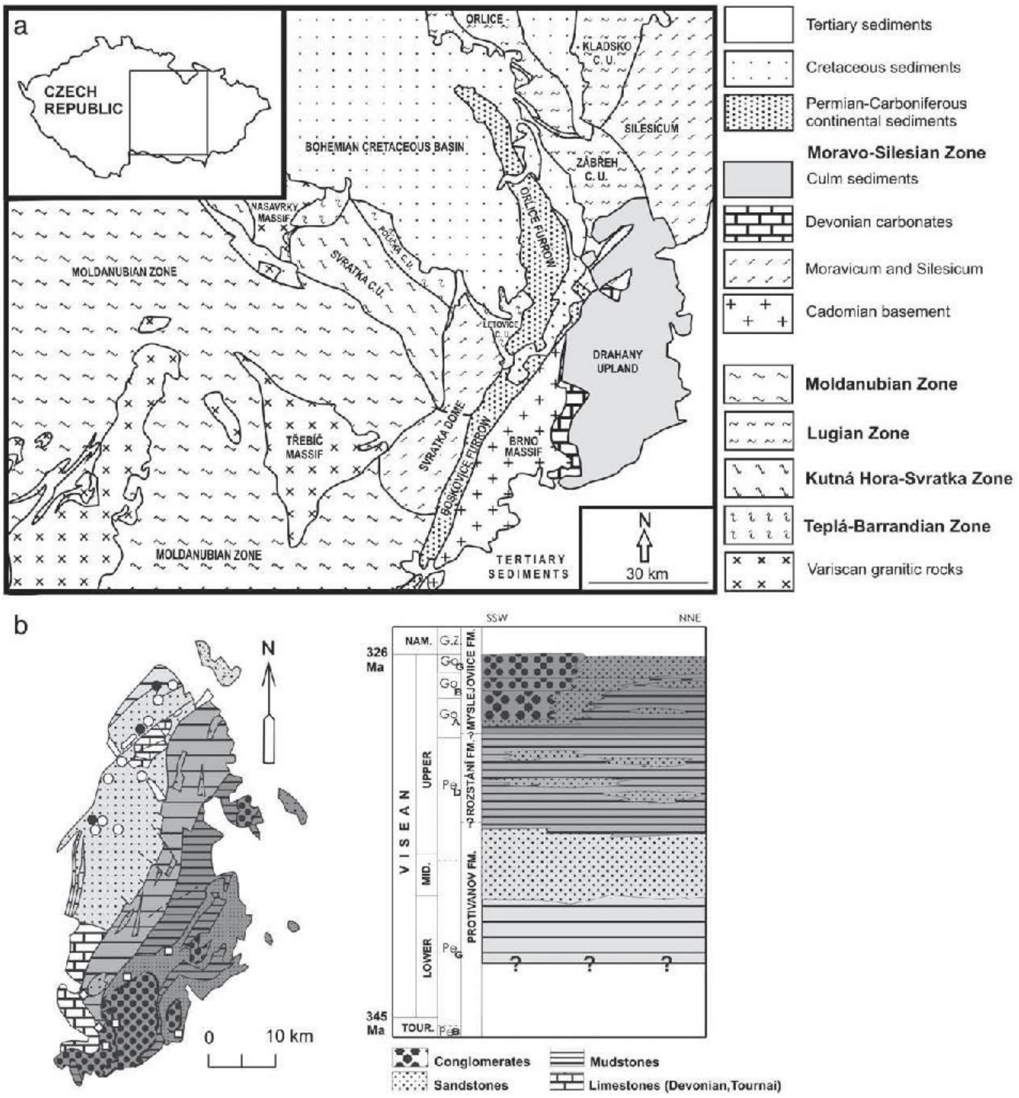

Fig. 1. Geological setting; a) position of Drahany Upland along the eastern margin of the Bohemian Massif; b) schematic geological map and stratigraphic scheme of the Culm sediments of the Drahany Upland (modified from Hartley and Otava, 2001) showing localities from the Protivanov Formation with common authigenic monazite (full circle) and with common authigenic synchysite or parisite (open circle). Note that relicts of altered detrital monazites were found in each of them. Furthermore, there are displayed other localities from the Rozstání (diamond) and Myslejovice (square) Formation with unaltered detrital monazite.

system (Hartley and Otava, 2001). Based on the lithostratigraphic studies, Dvořák (1973) divided the sediments of the Drahany Upland from older to younger into the Protivanov, Rozstání and Myslejovice Formations, respectively (Fig. 1b). Synorogenic Carboniferous flysch sedimentation records the uplift and unroofing history of the adjacent mountain fold–thrust belt in this foreland basin (Schulmann and Gayer, 2000). Flysch basin sedimentation commenced probably in the Mid–Early Visean, ~340 Ma (Hartley and Otava, 2001). The youngest member of the Drahany Upland was deposited at ~325 Ma ago (Gradstein et al., 2005; Kotková et al., 2007). These sediments were later deformed by the Mid-Late Carboniferous Variscan Orogeny (Kumpera and Martinec, 1995).

The graywackes are poorly sorted and mostly contain detrital quartz, K-feldspar, plagioclase, muscovite, chlorite, chloritized biotite, and rock fragments. Mainly silt-size basal graywacke matrix is composed of sericite, chlorite, quartz, and plagioclase, recrystallized clay minerals with minor Ti-oxide, Fe-oxide/hydroxide, and rare calcite. Heavy minerals include dominant garnet, apatite and zircon. Monazite, epidote, ilmenite, rutile, titanite, tourmaline, and chromite are present in minor amounts (Čopjaková, 2007; Hartley and Otava, 2001).

3. Analytical methods

3.1. Sampling

Samples of fresh medium-grained graywackes and interbedded shales were collected over the region of the Drahany Upland (Fig. 1b). About 7 kg of graywacke from each locality was crushed for heavy mineral separation and whole-rock chemical analysis. Heavy minerals (63–

250 μm) were separated from the sieved samples using tetrabromethane (2.95 g/cm^3). REE-minerals from heavy mineral concentrates and thin sections of host rocks were examined.

3.2. Electron microprobe and whole-rock chemical analyses

The compositions of monazite and associated rhabdophane were investigated using a combination of quantitative electron microprobe (EMP) analyses and X-ray element mapping. They were done using with a CAMECA SX100 electron microprobe in the wavelength-dispersion mode in the Joint Laboratory of Electron Microscopy and Microanalysis of the Masaryk University and Czech Geological Survey (Brno, Czech Republic). Operating conditions included an accelerating voltage of 15 kV, a beam current of 160 nA for monazite and 20 nA for rhabdophane, and a beam diameter of 2 μm for monazite and 5 μm for rhabdophane. Peak counting times vary from 20 to 240 s in order to optimize detection limits. Uranium was determined on the U Mβ line (counting time 60 s, detection limit 270 ppm), Th on the Th Mα line (counting time 40 s, detection limit 250 ppm) and Pb on the Pb Mα line (counting time 240 s, detection limit 130 ppm). Synthetic and natural phases (U — metallic U, Pb — PbSe, Th — $CaTh(PO_4)_2$, P — $LaPO_4$, Y — YAG, La — $LaPO_4$, Ce — $CePO_4$, Pr — $PrPO_4$, Nd — $NdPO_4$, Sm — $SmPO_4$, Eu — $EuPO_4$, Gd — $GdPO_4$, Dy — $DyPO_4$, Er — YErAG, Al — sanidine, Si — sanidine, Ca — $CaTh(PO_4)_2$, Fe — andradite, S — $BaSO_4$, Sr — $SrSO_4$, F — topaz) were used as standards. Data were reduced using the PAP matrix correction routine (Pouchou and Pichoir, 1985). Overlapping of peaks and background positions were carefully tested and chosen using detailed WDS angle scans on natural and synthetic REE-phases. The background model on PbMα according to Jercinovic and Williams (2005) using exponential interpolation was chosen. Concentrations of Pb were additionally manually corrected for $YL\gamma_2$, $ThM\zeta_1$ and $ThM\zeta_2$ overlap on PbMα and concentrations of U were corrected for overlapping with ThMγ. The concentration of F (Si and Eu) was calculated by empirical correction for the interference of Ce (Nd and Dy respectively) on FKα (SiKα and EuLβ respectively). The monazite age was calculated using the method of Montel et al. (1996). Element maps were acquired at a resolution of 0.5–1 μm using a focused electron beam, an accelerating voltage of 15 kV, probe current of 120 nA, and 400–600 ms/pixel dwell time.

Whole-rock chemical analyses of graywackes were performed on approximately 5 kg of crushed and pulverized sample rock. Whole-rock chemical compositions measured at Acme Analytical Laboratories (Vancouver, Canada). Major oxides were determined using ICP-ES. Loss on ignition (LOI) was calculated by weight difference after ignition at 1000 °C. Trace elements were analyzed using ICP-MS.

3.3. Vitrinite reflectance

Samples of shales closely associated with the graywackes were taken for the vitrinite reflectance measurements. Careful sample selection was needed to omit the effect of tectonics or younger fluid influx. The polished surfaces were prepared and reflectance measurement was carried out at oil in non-polarized light (R_o) using a Leitz Wetzlar MPV2 microscope-photometer with a 50× objective. The Leitz standards of 1.26 and 5.42% reflectance were used following an established procedure described by Taylor et al. (1998). The thermal history of the samples was evaluated in agreement with the thermal maturity data summarized in Kish (1987) and Merriman and Frey (1999) and with the most probable scenario for the region proposed by Franců et al. (2002).

4. Results

4.1. Occurrence of authigenic monazite and textural relations

Authigenic monazite is a common mineral in some graywackes from the Protivanov Formation (see Fig. 1b), where it represents a major carrier of REEs. It forms aggregates irregular in shape, up to 150 μm large, in the graywacke matrix. It is commonly in association with authigenic quartz, chlorite, sericite, Ti-oxide and Fe-oxide/hydroxide. Authigenic monazite encloses abundant inclusions of (i) authigenic (oval and/or anhedral inclusions of quartz, Ti-oxide, Fe-oxide/hydroxide, chlorite, illite) and (ii) detrital minerals (quartz and K-feldspar, up to ~20 μm in size) identical to those of the graywacke matrix (Fig. 2a–d).

Authigenic monazite frequently does not show any textural relationship to other REE-bearing minerals, neither authigenic nor detrital. In some cases, authigenic monazite may be overgrown by rhabdophane (hexagonal $LREEPO_4.H_2O$) (Fig. 2e,f). Authigenic xenotime-(Y) (YPO_4) and florencite ($LREEAl_3(PO_4)_2(OH)_6$) associated with authigenic monazite were sporadically observed (see Fig. 2f,g). Some authigenic monazite grains (<5% of authigenic monazite) contain inherited, inclusions-free monazite core (<30 μm) with different chemical composition (Fig. 2a,b), which is interpreted to be detrital. They also occur in association with authigenic thorite replacing detrital monazite (Fig. 2h). In places, aggregates of authigenic minerals (fine-grained mixture of monazite ± sericite ± chlorite ± quartz) define the shape of original REE-bearing detrital grain, which was completely replaced (Fig. 2i). Textural relationships suggest that authigenic monazite formed after sediment deposition at the same time as other authigenic minerals in the graywacke matrix.

Authigenic REE-minerals are common in all samples of graywackes from the Protivanov Formation. Where authigenic monazite is absent, Ca-bearing minerals synchysite-(Ce) ($Ca(Ce,La)(CO_3)_2F$) and parisite-(Ce) ($Ca(Ce,La)_2(CO_3)_3F_2$) were found. Note that the amounts of authigenic REE-bearing minerals strongly decrease from the Protivanov to the Myslejovice Formation although the whole-rock REE content and mineral composition are rather uniform. It seems that the REEs in the Myslejovice Formation are contained predominantly in unaltered detrital minerals.

Detrital monazite is a common accessory mineral in the sediments. Rounded or euhedral to subhedral grains of detrital monazite (5–150 μm in diameter) are common mainly in the upper sedimentary successions (Rozstání and Myslejovice Formations) and they do not exhibit any evidence of post-depositional alteration. Toward the base (Protivanov Formation), its abundance significantly decreases and shows a variety of replacement reactions, replacement of detrital monazite by apatite + rhabdophane + thorite, replacement of detrital monazite by allanite + apatite + rhabdophane + thorite and detrital monazite dissolution and reprecipitation of low-T monazite and thorite (Čopjaková and Škoda, 2006; Čopjaková et al., 2008).

4.2. Chemical composition, compositional zoning and CHIME dating in monazite

Authigenic monazite has a heterogeneous chemical composition (monazite-(Ce) to monazite-(Nd)) with some specific characteristics (Table 1). The larger monazite grains (>~20 μm) often shows typical core-rim chemical zoning, whereas, small grains of monazite do not exhibit any systematic chemical zoning, but significant chemical variation does exist among the individual grains. The contents of major REEs (La–Gd; except Pr) are highly variable (Ce = 0.281–0.527 apfu, Nd = 0.086–0.375 apfu, La = 0.056–0.292 apfu), but rather constant contents of Pr (0.036–0.067 apfu) are typical. Relatively high concentration of Eu (up 1.35 wt.% Eu_2O_3) is a characteristic feature, whereas HREEs are very low and frequently below the detection limit. The Y, Th, and U contents are commonly low, i.e. (0.07–1.27 wt.% Y_2O_3; 0.05–4.28 wt.% ThO_2; average 0.63 wt.% ThO_2 and ≤0.18 wt.% UO_2). Minor amounts of Sr (≤0.56 wt.% SrO) typically enter authigenic monazite. The $\sum Ca + Si$ significantly predominate over $\sum Th + U + Pb$, whereas the ratio of $Ca/(Th + U + Pb)$ is close to 1 (see Fig. 3a,b). In general, the chemical compositions of authigenic monazite are close to the ABO_4 formula.

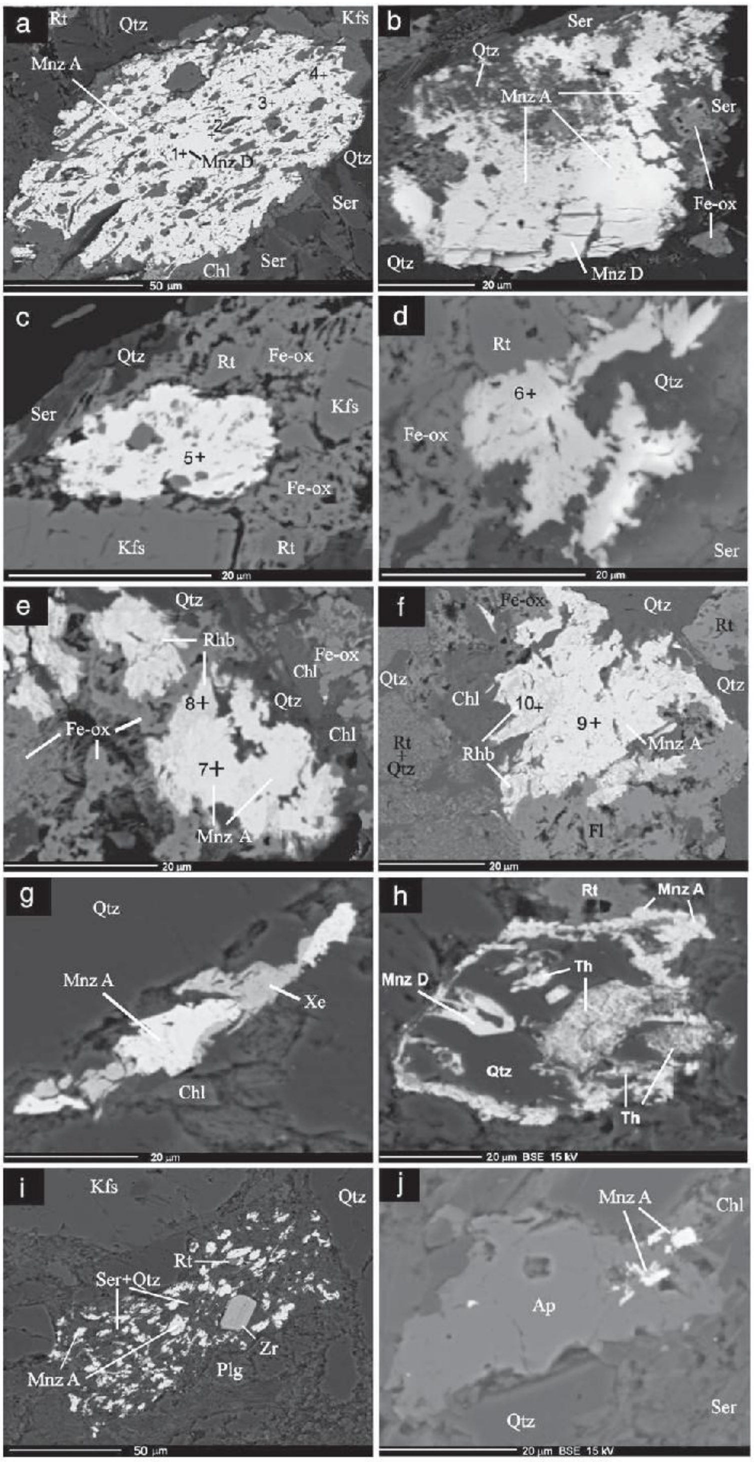
a
Rt
Qtz
Kfs
Mnz A
4+
3+
2
1+
Mnz D
Qtz
Ser
Chl
Ser
50 µm
b
Ser
Qtz
Mnz A
Ser
Fe-ox
Qtz
Mnz D
20 µm
c
Qtz
Rt
Fe-ox
Ser
Kfs
5+
Fe-ox
Kfs
Rt
20 µm
d
Rt
6+
Qtz
Fe-ox
Ser
20 µm
e
Qtz
Rhb
Fe-ox
Chl
8+
Qtz
Chl
Fe-ox
7+
Mnz A
20 µm
f
Fe-ox
Qtz
Rt
Qtz
Qtz
Chl
10+
9+
Mnz A
Rt
Qtz
Rhb
Fl
20 µm
g
Qtz
Mnz A
Xe
Chl
20 µm
h
Rt
Mnz A
Mnz D
Th
Qtz
Th
20 µm BSE 15 kV
i
Kfs
Qtz
Rt
Ser+Qtz
Zr
Mnz A
Plg
50 µm
j
Mnz A
Chl
Ap
Qtz
Ser
20 µm BSE 15 kV

Table 1
Representative microprobe analyses of monazite and rhabdophane.

	Mnz 1	Mnz 2	Mnz 3	Mnz 4	Mnz 5	Mnz 6	Mnz 7	Rhb 8	Mnz 9	Rhb 10
SO_3	<0.01	<0.01	<0.01	<0.01	<0.01	<0.01	<0.01	0.35	<0.01	0.17
P_2O_5	30.53	30.48	30.51	30.54	30.15	29.60	29.60	27.82	29.25	27.22
SiO_2	0.12	0.02	0.66	0.48	0.11	0.92	3.11	1.10	0.49	2.38
UO_2	0.99	0.07	0.02	<0.02	0.05	0.02	0.04	0.16	0.03	0.07
ThO_2	4.47	0.13	0.33	0.09	0.62	1.06	1.81	6.13	3.64	5.75
La_2O_3	12.56	3.90	8.81	17.24	12.07	16.47	13.75	12.55	20.05	15.96
Ce_2O_3	27.34	19.64	29.72	33.35	28.27	32.62	30.95	26.29	35.28	27.99
Pr_2O_3	3.15	4.35	4.31	3.49	3.75	3.29	3.38	2.84	2.50	2.42
Nd_2O_3	12.02	26.86	17.41	11.56	16.50	10.82	11.64	9.37	6.12	7.07
Sm_2O_3	2.50	9.05	3.79	1.56	4.03	1.82	2.00	1.68	0.71	1.00
Eu_2O_3	<0.09	1.35	0.56	<0.09	0.34	<0.09	<0.09	<0.12	<0.09	<0.12
Gd_2O_3	1.87	3.20	1.77	0.52	2.27	0.99	1.14	1.04	0.16	0.66
Dy_2O_3	0.78	0.44	0.37	0.17	0.51	0.26	0.20	0.32	<0.06	0.16
Er_2O_3	0.15	0.05	0.05	<0.04	0.07	<0.04	0.05	<0.04	<0.04	0.05
Y_2O_3	2.63	0.59	0.58	0.31	0.89	0.67	0.59	0.95	0.07	0.82
Al_2O_3	<0.02	<0.02	0.18	0.24	0.02	0.07	0.23	0.40	0.13	1.15
FeO	<0.03	<0.03	<0.03	0.07	0.50	0.35	1.42	1.28	0.44	1.12
PbO	0.14	<0.01	<0.01	<0.01	<0.01	0.01	0.03	0.08	0.05	0.15
CaO	1.08	0.13	0.20	0.06	0.16	0.26	0.30	3.44	0.75	2.38
SrO	<0.03	0.05	0.12	0.04	0.16	0.13	0.13	1.39	0.57	1.13
BaO	<0.03	<0.03	<0.03	<0.03	<0.03	<0.03	<0.03	0.38	<0.03	0.22
F	<0.05	<0.05	<0.05	<0.05	<0.05	<0.05	<0.05	0.34	0.16	0.19
−O═F	0.00	0.00	0.00	0.00	0.00	0.00	0.00	−0.14	−0.07	−0.08
Total	100.35	100.30	99.39	99.73	100.48	99.45	100.37	97.41	100.35	97.78
S^{6+}	0.000	0.000	0.000	0.000	0.000	0.000	0.000	0.010	0.000	0.005
P^{5+}	1.000	1.010	1.000	0.999	0.996	0.977	0.939	0.925	0.967	0.896
Si^{4+}	0.005	0.001	0.026	0.019	0.004	0.038	0.101	0.043	0.019	0.093
Subtotal	1.005	1.011	1.026	1.018	1.000	1.015	1.040	0.978	0.986	0.994
U^{4+}	0.009	0.001	0.000	0.000	0.000	0.000	0.000	0.001	0.000	0.001
Th^{4+}	0.039	0.001	0.003	0.001	0.006	0.009	0.015	0.055	0.033	0.051
La^{3+}	0.179	0.056	0.126	0.246	0.174	0.237	0.196	0.182	0.291	0.229
Ce^{3+}	0.387	0.281	0.421	0.472	0.404	0.466	0.433	0.378	0.506	0.398
Pr^{3+}	0.044	0.062	0.061	0.049	0.053	0.047	0.048	0.041	0.034	0.034
Nd^{3+}	0.166	0.375	0.241	0.159	0.230	0.151	0.155	0.134	0.084	0.098
Sm^{3+}	0.033	0.122	0.051	0.021	0.054	0.025	0.026	0.023	0.010	0.013
Eu^{3+}	0.000	0.018	0.007	0.000	0.005	0.000	0.000	0.000	0.000	0.000
Gd^{3+}	0.024	0.042	0.023	0.007	0.029	0.013	0.014	0.014	0.002	0.008
Dy^{3+}	0.010	0.006	0.005	0.002	0.006	0.003	0.002	0.004	0.000	0.002
Er^{3+}	0.002	0.001	0.001	0.000	0.001	0.000	0.001	0.000	0.000	0.001
Y^{3+}	0.054	0.012	0.012	0.006	0.018	0.014	0.012	0.020	0.001	0.017
Al^{3+}	0.000	0.000	0.008	0.011	0.001	0.003	0.010	0.018	0.006	0.053
Fe^{2+}	0.000	0.000	0.000	0.002	0.016	0.012	0.044	0.042	0.014	0.037
Pb^{2+}	0.001	0.000	0.000	0.000	0.000	0.000	0.000	0.001	0.001	0.002
Ca^{2+}	0.045	0.006	0.008	0.003	0.006	0.011	0.012	0.145	0.032	0.099
Sr^{2+}	0.000	0.001	0.003	0.001	0.004	0.003	0.003	0.032	0.013	0.026
Ba^{2+}	0.000	0.000	0.000	0.000	0.000	0.000	0.000	0.006	0.000	0.003
Subtotal	0.993	0.984	0.970	0.980	1.007	0.994	0.971	1.130	1.027	1.093
$\sum$ cat.	1.998	1.995	1.994	1.996	2.007	2.008	2.010	2.065	2.020	2.063
O^{2-}	4.000	4.000	4.000	4.000	4.000	4.000	4.000	3.957	3.980	3.976
F^-	0.000	0.000	0.000	0.000	0.000	0.000	0.000	0.043	0.020	0.024
Σ an.	4.000	4.000	4.000	4.000	4.000	4.000	4.000	4.000	4.000	4.000

Structural formulae of monazite and rhabdophane were calculated on the basis of 4 anions pfu. The analytical points are marked in Fig. 2; 1 – Detrital monazite relic enclosed in authigenic monazite (Fig. 2a); 2–4 – Analyses of authigenic monazite from central part to the rim (Fig. 2a); 5,6 – Small irregular grains of authigenic monazite from the Fig. 2c,d; 7,8 – Authigenic monazite and surrounding rhabdophane from the Fig. 2e; 9–10 – Authigenic monazite and surrounding rhabdophane from the Fig. 2f.

The zoned texture in authigenic monazite is characterized by an increase in La and Ce and decrease in REE smaller than Pr (most significantly Nd, Sm and Gd) along with a deepening negative Eu anomaly from the core to the outer rim. This zoning is well-documented in the chondrite-normalized REE-patterns, which changes from a concave pattern with a maximum in Sm and indistinct Eu anomaly in the central part of the grain to a steep slope pattern with a decrease from La to Er and a pronounced negative Eu anomaly in the outer rim (Fig. 4). High variability in the REE patterns correlates well with La/Gd ratio = 1.3 to 146.

Small detrital cores (<30 μm) from the central part of the authigenic monazite yielded elevated Th (~2–8 wt.% ThO_2), U (0.2–1.9 wt.% UO_2) and Y (0.7–3.0 wt.% Y_2O_3) concentrations, which are generally higher than those in the adjacent authigenic monazite. The detrital cores are also enriched in other HREEs and show Eu contents below the detection limit. The X-ray maps (Fig. 5) illustrate a Th–U–Y-enriched inherited

Fig. 2. BSE images of authigenic monazite; a) large monazite grain with abundant inclusions of authigenic and detrital minerals. Detrital relic of monazite is seen in the center; b) authigenic monazite rich in small inclusions replacing detrital monazite; c,d) small irregular authigenic monazite with abundant inclusions; e) authigenic monazite overgrown by rhabdophane (darker in BSE image); f) authigenic monazite overgrown by rhabdophane (darker in BSE image) and florencite; g) authigenic monazite associated with authigenic xenotime; h) relict of altered detrital monazite replaced by thorite, quartz and authigenic monazite; i) former detrital REE-bearing mineral (monazite?) totally replaced by authigenic monazite, sericite, and quartz; j) detrital apatite showing signs of a marginal dissolution associated with authigenic monazite. Abbreviations: Mnz A – authigenic monazite; Mnz D – detrital monazite; Rhb – rhabdophane; Fl – florencite; Qtz – quartz; Kfs – K-feldspar; Ser – sericite; Chl – chlorite; Rt – Ti-oxide (probably rutile); Fe-ox – Fe-oxides/hydroxides; Ap – fluorapatite; Xe – xenotime-(Y); Th – Thorite; Zr – zircon. Numbers correspond to analytical point locations used in Table 1.

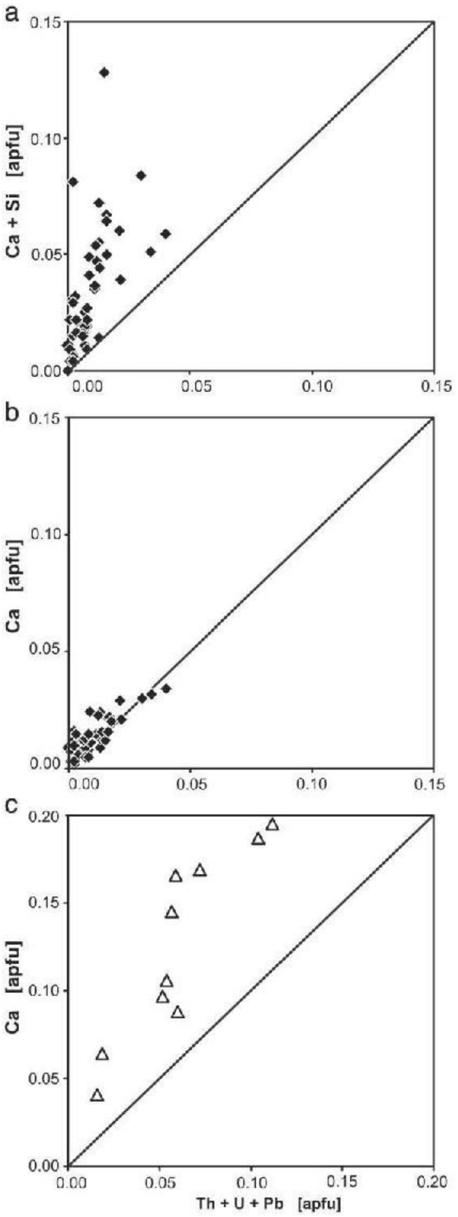

Fig. 3. Binary graphs showing some substitution trends in monazite and rhabdophane discussed in the text; a) Ca + Si vs. total Th + U + Pb in authigenic monazite; b) Ca vs. total Th + U + Pb in authigenic monazite; c) Ca vs. total Th + U + Pb in rhabdophane overgrowing authigenic monazite.

detrital core with a sharp contact between the core and adjacent authigenic monazite, and a gradual evolution in chemical composition of the authigenic monazite from the core to the rim.

The CHIME (chemical Th–U-total Pb isochron method) dating of authigenic monazite yields a well-defined isochrone with a weighted average age of 324 ± 28 Ma (Fig. 6a). Low contents of Th and U, and, consequently, low concentrations of Pb, are responsible for the high age uncertainty in spite of a large number of electron microprobe analyses (n = 48).

4.3. Chemical composition of rhabdophane

Rhabdophane is hardly distinguishable from authigenic monazite using BSE images and EDS-spectra; nevertheless, some chemical differences are specific. Rhabdophane-(Ce) has lower analytical totals $\sum = 94.85–97.78$ wt.% and normalization on 4 anions indicate a weak surplus of cations in the REE position (1.04–1.17 apfu). It typically has elevated contents of Ca (1.48–4.45 wt.% CaO) and Th (1.69–11.71 wt.% ThO_2) but low U (0.07–0.16 wt.% UO_2). The Ca content significantly predominates over $\sum$Th + U + Pb (compare Fig. 3b and c). Rhabdophane has slightly lower LREE and higher Y + HREE contents relative to authigenic monazite and Eu contents below the detection limit. Elevated contents of Fe (0.93–4.50 Fe_2O_3), Al (0.39–1.14 wt.% Al_2O_3), Sr (0.55–1.63 wt.% SrO), Ba (≤0.47 wt.% BaO), S (≤1.01 wt.% SO_3) and F (≤0.34 wt.% F) also are typical. Chemical differences between rhabdophane and authigenic monazite are documented in the X-ray distribution maps (Fig. 7) and in Table 1. A weak patchy zoning is typical for rhabdophane, where Th and Ca vary on a very small scale.

4.4. Vitrinite reflectance and palaeo-temperature

The thermal maturity (R_o ~ 1.9–2.10%) is low in the samples from the Myslejovice Formation, where no authigenic monazite and no detrital monazite alterations were observed. A jump to higher thermal maturity with R_o from 4.05 to 4.49% was observed in the samples from the Protivanov Formation. For localities with authigenic monazite, the measured R_o values are 4.05% to 4.44% respectively. This data set of the vitrinite reflectance is in good agreement with those obtained by Franců et al. (1999, 2002) from rocks in the vicinity of the sample localities: R_o = 1.2–2.2% in the Myslejovice Formation, and 3.3–4.5% in the Protivanov Formation and with a general increase of thermal maturity from SSE to NNW of the Drahany Upland (Dvořák, 1989; Dvořák and Wolf, 1979).

The vitrinite reflectance suggests that the thermal maturity of the Protivanov Formation sediments is equivalent to very low-grade metamorphism (anchizone) with a maximum palaeo-temperature 250–300 °C. Moreover, the R_o data do not show any systematic regional trend within the Protivanov Formation, which is interpreted as having experienced a similar palaeo-thermal exposure (Franců et al., 2002). The reliability of the thermal maturity data based on the vitrinite reflectance is supported by the illite crystallinity data (Franců et al., 1999), which suggest palaeo-temperatures of 220–260 °C for the Protivanov Formation. The thermal maturity equivalent to the late diagenetic zone with a maximum palaeo-temperature of ~150–200 °C is typical for sediments from the south-eastern part of the Drahany Upland (Myslejovice Formation), where neither authigenic monazite, nor alteration of detrital monazite was observed.

4.5. Whole-rock chemical composition of graywackes

Whole rock chemistry of graywackes from 14 localities (Protivanov and Myslejovice Formations) show an uniform chemical composition in both the major and trace elements except for the Ca content, which varies from 0.36 to 2.45 wt.% CaO (Table 2; Fig. 8a). Low Ca contents (0.36–0.54 wt.% CaO) are typical for graywackes containing authigenic monazite in the Protivanov Formation and for the graywackes from the Myslejovice Formation (0.40–0.46 wt.% CaO). Other graywacke samples from the Protivanov Formation, where authigenic monazite has not been found, show higher Ca contents (1.12–2.45 wt.% CaO). The $\sum$REE + Y concentrations in graywackes are uniform in all samples (133–160 ppm) as well as the chondrite-normalized REE distribution patterns. These show a steep LREE (La–Eu) distribution, and nearly flat

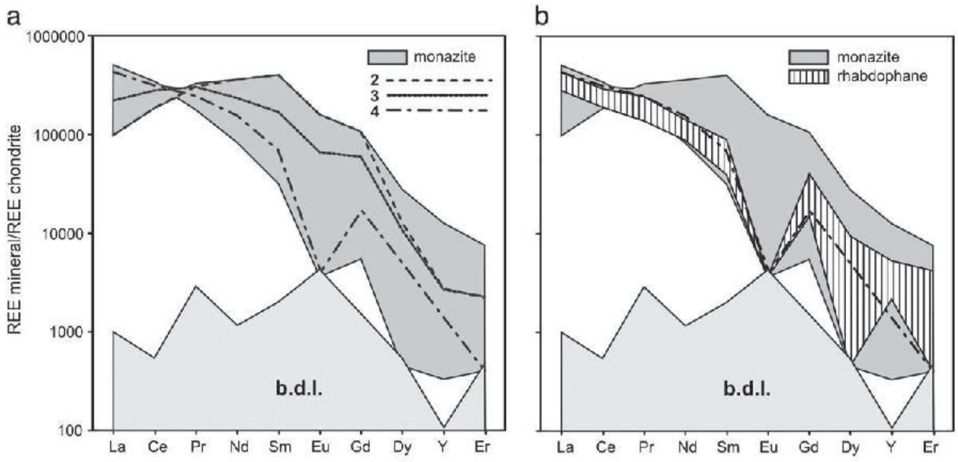

Fig. 4. Chondrite normalized patterns (Taylor and McLennan, 1985) of REE in authigenic monazite and overgrowing rhabdophane. Area labeled by b.d.l. stands values below the EMP detection limit; a) gray area — authigenic monazite; three representative REE-patterns for the analyses 2, 3 and 4 from Fig. 2a and Table 1 showing the zoning trend in monazite; b) dashed area — rhabdophane; area for authigenic monazite (gray) and representative REE-pattern for monazite rim overgrown by rhabdophane are shown for comparison.

HREE pattern ($La_N/Yb_N = 6.7–9.4$ and $Gd_N/Yb_N = 1.6–1.8$) with a slight Eu ($Eu/Eu^* = 0.63–0.78$) and Ho negative anomaly (Fig. 8b). Similar REE contents and REE patterns are common from recent and/or Phanerozoic turbidites of passive continental margins (Bhatia, 1985; McLennan et al., 1990; Nathan, 1976). The whole rock chemical composition of the graywackes reflect a provenance consisting of a terrain built from recycled sedimentary rocks along with plutonic, and metamorphic rocks. Higher contents of Ca along with less pronounced

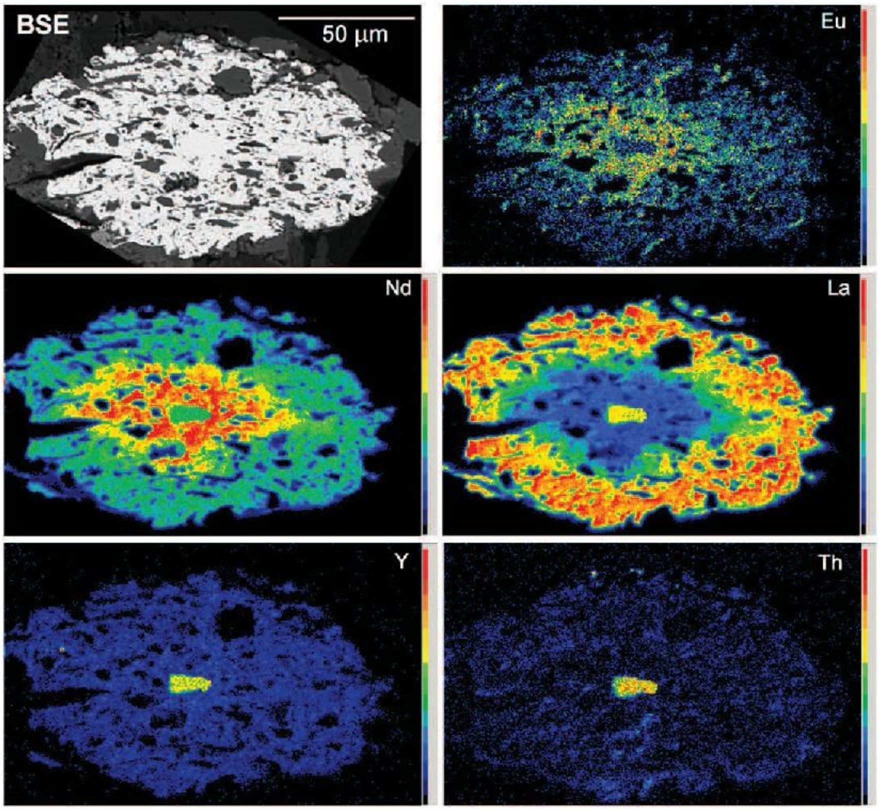

Fig. 5. Wavelength-dispersive X-ray maps of representative elements for zoned authigenic monazite enclosing a small relic of detrital monazite.

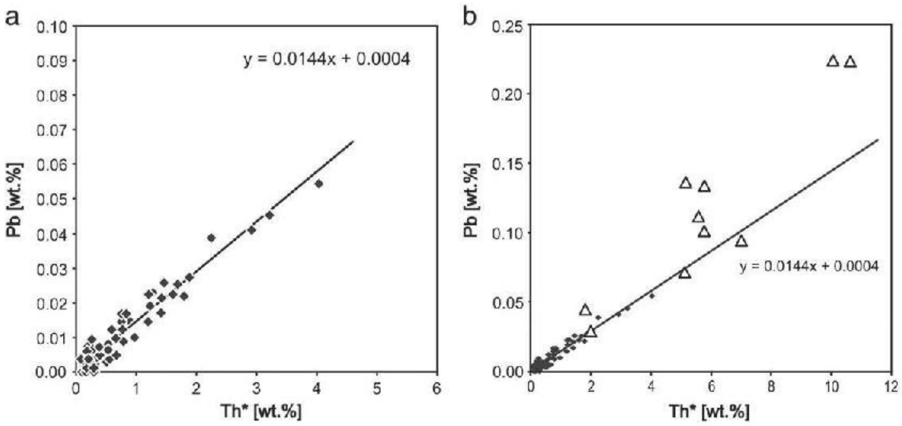

Fig. 6. a) Th*–Pb plot for authigenic monazite (full diamonds) with the isochrone and equation of regression line; b) Th*–Pb plot for rhabdophane overgrowing authigenic monazite (open triangles); isochrone, equation of regression line and points for authigenic monazite (small full diamonds) are shown for comparison. Th* equals to the theoretical Th content, which would produce the measured Pb for the relevant calculated age.

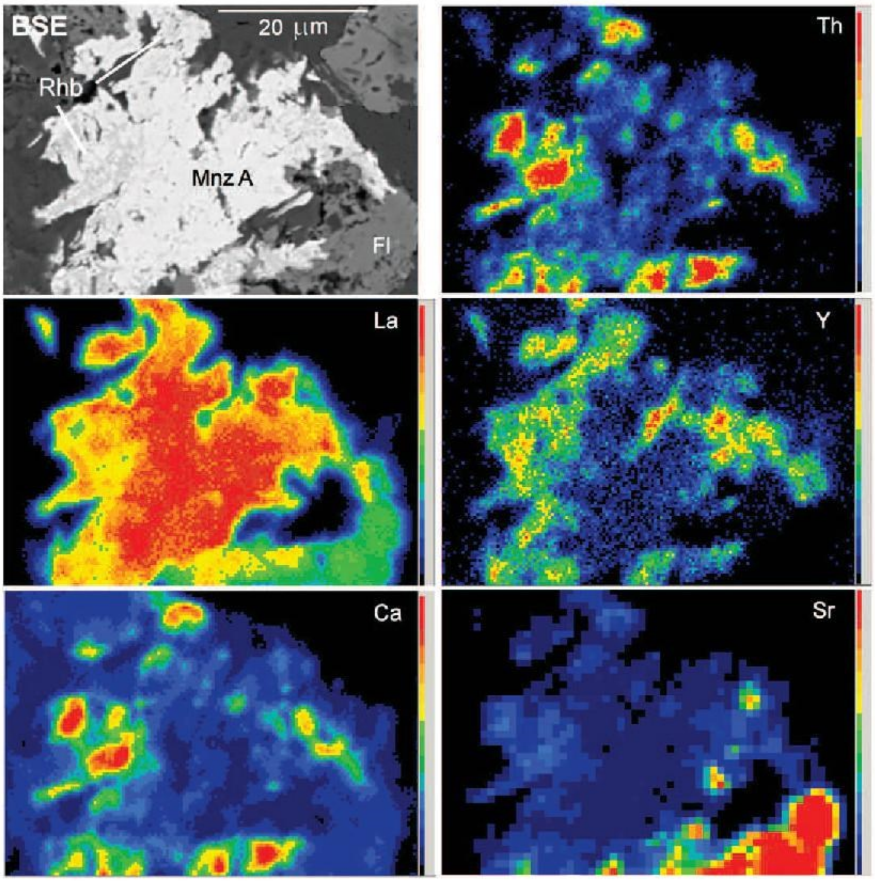

Fig. 7. Wavelength-dispersive X-ray maps of representative elements for authigenic monazite overgrown by rhabdophane-(Ce).

Table 2
Representative whole-rock chemical composition of graywackes (major and trace elements).

Wt.%	1	2	3	ppm	1	2	3
P_2O_5	0.19	0.13	0.15	Ba	607	610	767
SiO_2	68.96	69.86	71.40	Be	2.0	2.0	2.0
TiO_2	0.73	0.61	0.55	Co	9.0	9.1	8.7
Al_2O_3	13.84	12.77	12.86	Cs	5.9	4.9	4.6
Fe_2O_3	5.24	4.69	4.30	Ga	15.2	14.0	15.4
Cr_2O_3	0.01	0.01	0.009	Hf	6.6	5.0	4.4
MnO	0.06	0.08	0.06	Nb	10.7	9.3	9.6
MgO	1.97	1.93	1.80	Rb	111	95.4	126
CaO	0.36	1.65	0.40	Sn	4.0	2.0	3.0
Na_2O	2.53	2.46	2.67	Sr	112	211	175
K_2O	2.81	2.60	3.21	Ta	0.9	0.9	0.8
LOI	3.10	3.00	2.4	Th	13.1	10.0	10.9
Total	99.83	99.85	99.83	U	4.8	2.5	3.0
TOC	0.09	0.21	0.09	V	88	77	68
ppm				W	1.9	1.5	2.0
Y	23.1	19.8	19.6	Zr	230	168	140
La	24.6	22.6	25.8	Mo	0.10	0.10	0.10
Ce	52.6	44.5	51.1	Cu	11.3	10.6	10.5
Pr	6.43	5.61	6.38	Pb	17.0	10.2	20.0
Nd	25.4	22.5	24.7	Zn	57.0	53.0	59.0
Sm	5.24	4.29	4.54	Ni	24.1	25.8	25.6
Eu	0.99	1.00	0.98	As	26.6	6.6	4.2
Gd	4.46	3.66	3.93	Cd	<0.1	<0.1	<0.1
Tb	0.71	0.62	0.65	Sb	0.40	0.30	0.20
Dy	4.05	3.49	3.47	Bi	0.20	0.10	0.20
Ho	0.81	0.69	0.68	Ag	<0.1	<0.1	<0.1
Er	2.23	1.92	1.97	Au	<0.5	0.80	<0.5
Tm	0.37	0.32	0.31	Hg	0.06	0.01	0.03
Yb	2.24	1.95	1.82	Tl	0.1	<0.1	<0.1
Lu	0.33	0.31	0.29	Se	<0.5	<0.5	<0.5
REE + Y	154	133	146				

1 – Graywacke with authigenic monazite, Protivanov Formation; 2 – Graywacke without authigenic monazite, Protivanov Formation; 3 – Graywacke, Myslejovice Formation.

Eu anomalies in some samples from the Protivanov Formation likely correspond to higher amounts of the I-type arc volcanic component.

5. Discussion

5.1. Evidences for authigenic origin of monazite

There are several lines of textural and chemical evidence indicating that inclusion-rich monazite grains from graywackes are authigenic. Irregular shape of monazite and presence of small angular inclusions of detrital minerals preclude its detrital origin. Highly irregular in shape, inclusion-rich grains are typical for diagenetic and low-grade metamorphic monazite (Burnotte et al., 1989; Evans et al., 2002; Milodowski and Zalasiewicz, 1991; Rasmussen and Muhling, 2007, 2009; Rasmussen et al., 2007; Wing et al., 2003). No microtextures suggesting syntectonic monazite formation linked to deformation of basin sediments similarly as Wilby et al. (2007) were observed. Monazite petrography supports its main growth together with metamorphic chlorite and abundant Ti-oxides, which are likely related to chloritization of biotite. Petrographic observations along with vitrinite reflectance and illite crystallinity data suggest a monazite growth during very low-grade metamorphism in relation to a deep burial, which was caused by the additional deposition of a thicker flysch sedimentary pile. The CHIME monazite age (324 ± 28 Ma) is coincident with the ending of sedimentation in the Drahany basin (Gradstein et al., 2005; Kotková et al., 2007). Chemical composition (low Th, U, Y and HREE contents and elevated Eu concentrations) and zoning in REEs observed in authigenic monazite from the Protivanov Formation resemble other sub-amphibolite-facies monazites of different origin – diagenetic, low-grade metamorphic or syntectonic (Burnotte et al., 1989; Evans et al., 2002; Janots et al., 2008; Milodowski and Zalasiewicz, 1991; Rasmussen and Muhling, 2007, 2009; Wing et al., 2003). Monazite represents a potentially important geochronometer to determine the age of diagenesis, burial metamorphism, and/or later low-grade metamorphic and/or tectonic events and hydrothermal processes (Evans et al., 2002; Rasmussen et al., 2001, 2005, 2007; Wilby et al., 2007). Therefore, careful petrographic study of monazite is important to reliably establish its origin before an interpretation of the radiometric age is performed.

5.2. Monazite formation and source of REE

The sources of REEs and reactions which produced monazite under conditions of diagenesis to very low-grade metamorphism are not well understood. The presence of authigenic monazite suggests mobilization of REEs from the host (meta)sedimentary rocks. Source of REEs for low-T monazite is usually related to: (i) desorption of REEs adsorbed on the surface of clay minerals during their diagenetic transformations (Burnotte et al., 1989; Milodowski and Zalasiewicz, 1991; Rosenblum and Mosier, 1983); (ii) desorption of REEs during early diagenetic reductions of Fe oxides/hydroxides (Lev et al., 1998; Milodowski and Zalasiewicz, 1991); (iii) degradation of organic matter (REE adsorbed on the surface coatings or incorporated into biogenic

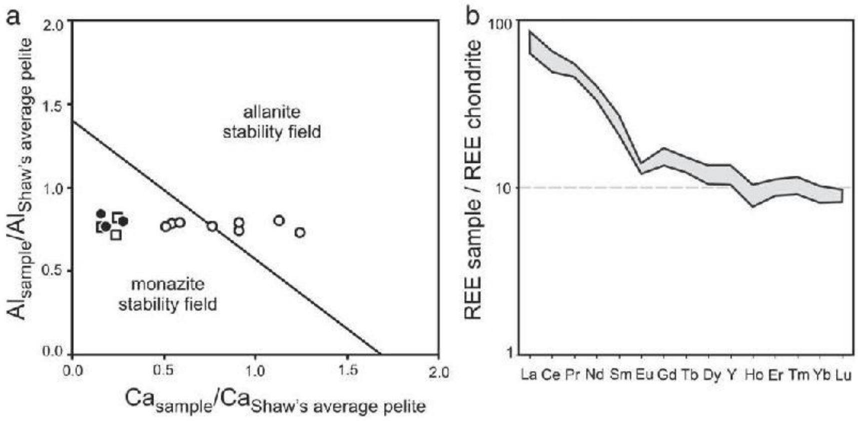

Fig. 8. Whole-rock composition of graywackes; a) Ca and Al contents of the samples referenced to Shaw's data for average pelite (Shaw, 1956). For symbols see Fig. 1. The discrimination line illustrates the relationship between whole-rock composition and the stability of low-temperature monazite and metamorphic allanite from the biotite and garnet zones of Buchan and Barrovian metapelites according to Wing et al. (2003); b) field of chondrite-normalized patterns of REE and Y (chondrite data for normalization from Taylor and McLennan, 1985).

material) in response to an early burial compaction (Evans and Zalasiewicz, 1996; Lev et al., 1998); (iv) dissolution of detrital REE-minerals including monazite as was described from greenschist-facies metasediments in the Witwatersrand basin (Rasmussen and Muhling, 2009) and from the central Alps (Janots et al., 2008).

The presence of complexly zoned monazite grains with rare detrital cores and authigenic overgrowths along with altered detrital monazite relics in the same rock suggest that authigenic monazite in the Protivanov Formation may be a product of fluid-assisted dissolution of detrital monazite and precipitation of authigenic monazite during very low-grade metamorphism. Both options of monazite formation, in situ monazite dissolution–reprecipitation (Putnis, 2002, 2009) and precipitation from passing fluids without immediate spatial affinity to altered detrital monazite are possible.

There are no direct textural evidences indicating participation of other less stable REE-bearing detrital minerals (allanite, apatite, xenotime, titanite) in the formation of authigenic monazite. However, allanite is quite rare; one to two orders of magnitude less abundant than detrital monazite, and its replacement by synchysite and rhabdophane was observed across the whole region of the Drahany Upland. Detrital apatite shows signs of a marginal dissolution on one of the localities with authigenic monazite, and only exceptionally authigenic monazite formed close to such altered apatite (Fig. 2j). Replacement of detrital titanite by mixture of TiO_2 phase + chlorite was observed in the samples with common authigenic monazite. In graywackes with higher activity of CO_2 in fluids, alteration of titanite led to the formation of TiO_2 phase + calcite + quartz, and in some cases small amounts of synchysite was identified. Detrital xenotime is rather exceptional. Theoretically, a portion of the REEs, especially HREE and Y, may have originated from detrital garnet (locally with up to 0.3 wt.% of Y_2O_3), which is partly corroded in the Protivanov Formation (Čopjaková et al., 2005).

Low contents of organic matter in graywackes (0.05–0.09 wt.% organic C) and missing spatial correlation with monazite crystallization preclude organic matter to be important REE and P source. Leaching of adsorbed REEs from clay minerals, and/or Fe oxide/hydroxide surfaces during early to late diagenesis, can be an additional minor source of REEs. Evidence for this includes recrystallized clay minerals and authigenic pyrite present in the samples.

There is no textural evidence to consider rhabdophane as a precursor of authigenic monazite in the Drahany basin, as was suggested for diagenetic monazite by Donnot et al. (1973) and Milodowski and Zalasiewicz (1991). Rhabdophane overgrowing authigenic monazite likely formed from REE-bearing pore fluids during decreasing temperature compared with authigenic monazite. Rhabdophane is stable only at low $T < \sim 200$ °C (at P_{H2O} 50–200 MPa; Akers et al., 1993).

5.3. Monazite chemistry

5.3.1. REE distribution in monazite

The reason for the zoning observed in low-T monazite is not fully elucidated up to date. Rasmussen et al. (2007) attributed a Pr, Nd, Sm, Eu-enriched monazite core and a La, Ce-enriched rim to different stages of formation. Nevertheless, gradual evolution of the chemical composition in the authigenic monazite from the Drahany Upland and the results of the CHIME monazite dating imply growth during a single event rather than an episodic growth. Milodowski and Zalasiewicz (1991) suggest the REE migration as organic and bicarbonate complexes during diagenesis, and increasing stability of these complexes with increasing REE atomic number is responsible for zoning in the monazite nodules. Solution complexation reactions involving organic and/or the most common inorganic (carbonate, phosphate, hydroxide) ligands, leading to the general increase of solubility of REE from La to Lu in waters (Lee and Byrne, 1992, 1993; Sonke and Salters, 2006; Wood, 1990), cannot fully explain observed zoning pattern (core–rim increase in La and Ce together with decrease in Nd + MREE and Y + HREE). In contrary, Pourret et al. (2007) discussed the ability of organic acids to preferentially complex MREE.

Burnotte et al. (1989) suggest that this zoning pattern can be explained by differences in the solubility of the individual REE phosphates. $REEPO_4$ solubility in aqueous solutions is poorly understood and some of them give conflicting results. Moreover the most comprehensive studies were carried out on REE-phosphates with the rhabdophane structure. The general trends can be summarized as follows: minimal solubility is observed for LREE between Ce and Sm; $LaPO_4$ solubility is substantially larger than neighboring LREE and for HREE solubility increases with increasing atomic number (Carron et al., 1958; Firsching and Brune, 1991; Jonasson et al., 1985; Liu and Byrne, 1997; Wood and Williams-Jones, 1994).

Another possible reason responsible for monazite zoning is evolution in pore fluid chemistry from early diagenesis to very low-grade metamorphism during increasing burial. There are several lines of evidence in the published literature, which may rather indicate this process. A concave MREE-rich REE pattern was observed in early diagenetic fluids (Haley et al., 2004; Takebe and Yamamoto, 2007). Intensive LREE and MREE (mainly from Ce to Gd) liberation into the sediment pore waters and REE redistribution over long distances attributed to early diagenetic processes, was described from turbidite sequences (Bock et al., 1994; Milodowski and Zalasiewicz, 1991). Fe-oxides/hydroxides precipitating in the water column provide an efficient scavenger of REE (especially Ce and MREE) from seawater with an inverted seawater REE pattern (Bau, 1999; De Carlo and McMurtry, 1992; Elderfield et al., 1981; Haley et al., 2004; Koeppenkastrop and De Carlo, 1992; Pattan et al., 2001). During early diagenesis of clastic sediments with typical shale-like REE patterns, abundant REEs with a “MREE bulge” type pattern are released into water by reduction of Fe-oxides/hydroxides (Haley et al., 2004; Johannesson and Zhou, 1999). In a similar way, preferential dissolution of authigenic or biogenic MREE-rich phosphates during early diagenesis may yield waters with MREE enrichment as well (Hannigan and Sholkovitz, 2001; Takebe and Yamamoto, 2007). With increasing depth of burial, when very low-grade conditions are achieved, detrital REE-bearing minerals (mainly monazite) are intensively dissolved, and represent a major source of REE (mainly LREE) for low-T monazite. Therefore volumetrically dominant Ce- and La-rich parts of low-T monazite with deep Eu anomalies are probably derived from a detrital source. It is likely that all processes operate together, though it is difficult to determinate which of these processes is dominant.

5.3.2. Other compositional features of authigenic monazite

Authigenic monazite is characterized by low contents of Th and U. The $Ca/(Th + U + Pb)$ ratio close to 1 (Fig. 3b) indicates that the cheralite substitution $ThCaREE_{-2}$ predominates over the huttonite substitution $ThSiREE_{-1}P_{-1}$. The higher Si contents in authigenic monazite (Fig. 3a), which is not compensated by Th + U contents, indicate the presence of very fine inclusions of quartz or silicates below the resolution of EMP. This is supported by elevated contents of Al or Fe in the relevant EMP analyses (see Table 1) and WDS line scans, where Si contents mirror those of major monazite forming elements (P, LREE).

We suggest chemically distinct inherited monazite cores to be relics of a detrital monazite. Chemical composition of monazite cores is similar to some detrital monazite grains found in graywackes (Čopjaková and Škoda, 2006). Differences in the chemical composition between authigenic (low PT) and detrital monazite (high PT) reflect different PT conditions and fluid chemistry. Hence, dissolution of detrital monazite and precipitation of authigenic monazite was not a simple isochemical process. Some elements were removed (Th, U, Y + HREE, Pb) from and some were added (Sr, Eu) into the system via pore fluids mainly owing to the dissolution of other detrital minerals. The source of Sr and Ba entering authigenic REE-minerals (rhabdophane > monazite) is probably altered detrital plagioclase (up to 0.5 wt.% SrO in plagioclase from clasts of I-type granites; Čopjaková, 2007). No Sr or Ba was detected in detrital monazite (Čopjaková, 2007; Čopjaková and Škoda, 2006).

Rhabdophane overgrowing authigenic monazite also may incorporate some elements removed from detrital monazite such as Th, Y + HREE, Pb. Relatively high Pb content in rhabdophane, in contrast with the Th and U content and diagenetic age, implies its preferential incorporation (Fig. 6b). Incorporation of Pb into rhabdophane has also been observed in graywackes where rhabdophane is not associated with authigenic monazite (Škoda and Čopjaková, 2006) or where rhabdophane forms at the expense of allanite (Krenn and Finger, 2007).

5.4. Monazite formation as a function of temperature

The temperatures, at which the first monazite appears during a prograde metamorphism (diagenesis) of siliciclastic sediments, are still rather controversial. Based on synthesis of the published data, low-T monazite in siliciclastic (meta)sediments can form during burial diagenesis to low-grade metamorphism in the wide range of T ~ 100–400 °C. Starting from the lowest T, nodular monazite crystallization during diagenesis of black shales was proposed by Evans and Zalasiewicz (1996) and Milodowski and Zalasiewicz (1991). Evans et al. (2002) specified monazite formation during burial at the conditions coincident with the oil window (T ~ 100–150 °C). Donnot et al. (1973) described low-T monazite formed between 200 and 300 °C (anchizone) in Paleozoic schists. Similar T ~ 200–300 °C was suggested for monazite formation in phyllites (Rosenblum and Mosier, 1983), but the process responsible for the monazite formation is contact metamorphism rather than regional metamorphism. Low-T monazite is more common in low-grade epizonal metamorphic conditions at temperatures of ~ 300–400 °C in diverse metapelite terrains (e.g., Burnotte et al., 1989; Franz et al., 1996; Janots et al., 2006; Ohr et al., 1994; Rasmussen et al., 2001, 2005, 2007; Wan et al., 2007; Wing et al., 2003) and in metasandstones (Rasmussen and Muhling, 2007, 2009). In contrast, in many metamorphic terrains, the first monazite does not form until amphibolite facie conditions were achieved and usually in close relation to the prograde allanite breakdown (Ferry, 2000; Foster and Parrish, 2003; Kingsbury et al., 1993; Smith and Barreiro, 1990). Low-T monazite usually disappears during prograde metamorphism and is replaced by metamorphic allanite at T ~ 400–450 °C coincident with biotite or chloritoid isograd (Janots et al., 2006, 2008; Wing et al., 2003).

Temperatures of ~ 200–300 °C were estimated for monazite formation during diagenesis in graywackes of the Drahany Upland. Monazite precipitation can relate to decreasing monazite solubility in aqueous solutions with increasing temperature in the temperature range 200–300 °C (Poitrasson et al., 2004; Wood and Williams-Jones, 1994). Although intensive remobilization of REEs occurred in all samples from the Protivanov Formation, and the whole area underwent equal palaeo-thermal evolution, authigenic monazite formed only in some of them. Hence, the palaeo-temperature is likely not the only factor controlling formation of authigenic monazite.

5.5. Monazite formation as a function of whole-rock chemistry

The presence of authigenic monazite does not show any apparent relationship to the whole-rock $\sum$ REE + Y and REE patterns (see Fig. 8b and Table 2). Authigenic monazite appears only in Ca-poor rocks, which underwent a temperature overprint corresponding to very low-grade metamorphism in the presence of REE-remobilization. In Ca-rich graywackes, which underwent the same low-temperature metamorphic overprint and REE remobilization, authigenic synchysite-(Ce) or parisite-(Ce) are common instead. Decreasing the thermal overprint of the graywackes to T ~ 150–200 °C also decreases remobilization of REEs. For example authigenic monazite did not precipitate even in the Ca-poor graywackes. These observations suggest that differences in the Ca content in the host rock, along with temperatures, probably exert a major control on low-T monazite growth. The role of Ca and/or Al whole-rock contents on monazite stability has been revealed in amphibolite-facies metapelites as well; in metapelites with low Ca and Al contents monazite is formed, whereas higher Ca and Al contents stabilize allanite (Ferry, 2000; Foster and Parrish, 2003; Janots et al., 2008; Krenn and Finger, 2007; Wing et al., 2003). Nevertheless, the expected effect of the Al content on the formation of low-grade monazite in the Protivanov Formation cannot be confirmed, due to its limited variability.

Low-T monazite formation seems to be usually tied to low-Ca siliciclastic sedimentary rocks, though whole-rock data from these rocks containing diagenetic/low-grade metamorphic monazite are quite rare. Low-T metamorphic monazite occurs exclusively in sandstones with low Ca contents under slightly higher greenschist-facies conditions (T ~ 350 °C) (Rasmussen and Muhling, 2009). Common diagenetic monazite nodules occur in low-Ca turbidite mudstones and anoxic hemipelagites (<0.2 wt.% CaO) from central Wales (Milodowski and Zalasiewicz, 1991). Franz et al. (1996) and Wan et al. (2007) reported metamorphic monazite from low-Ca (<0.37 wt.% CaO and 0.15 wt.% CaO respectively) greenschist facies rocks. Wing et al. (2003) described low-T metamorphic monazite from chlorite zone metapelites independent of Ca content. In metapelites with average or above-average Ca and/or Al contents, low-T monazite is replaced by metamorphic allanite precisely at the biotite isograd (see Fig. 8a). Rare, low-T monazite is able to survive in rocks with below-average Ca and/or Al contents at higher metamorphic grades (Ky zone of the Barrovian terrain and And and Sil zones of the Buchan terrain). Consequently, the Ca (and Al) contents in the host rock probably control the upper stability limit for low-T monazite.

The results from this study along with other published data discussed above indicate that monazite formation in sub-amphibolite-facies metasediments is stabilized by a low whole-rock Ca content and low Ca contents probably extend the low-T monazite stability field into lower and higher metamorphic grades. Nevertheless, temperature, fluid activity and REE and P source are also crucial regarding the formation and general stability of low-T monazite. Further comprehensive studies focusing on low-T monazite, which include understanding its formation in relation to the accompanying mineral assemblage, the whole rock chemistry and temperature, are essential to maximize its petrographic potential.

Acknowledgments

The authors express gratitude to the constructive reviews of D. Harlov and F. Finger which significantly improved the original manuscript. We are grateful to R. Škoda and J. Toman for technical assistance. Financial supports from the grant GAČR (grant no. 205/07/474) to RČ, grant FRVŠ (grant no. 0528/02) to RČ and the long term Research Plan of the Ministry of Education of the Czech Republic MSM0021622412 (INCHEMBIOL) to MN are gratefully acknowledged.

References

Akers, W.T., Grove, M., Harrison, T.M., Ryerson, F.J., 1993. The instability of rhadbophane and its unimportance in monazite paragenesis. Chemical Geology 110, 169–176.

Bau, M., 1999. Scavenging of dissolved yttrium and rare earths by precipitating iron oxyhydroxide; experimental evidence for Ce oxidation, Y–Ho fractionation and lanthanide tetrad effect. Geochimica et Cosmochimica Acta 63, 67–77.

Bhatia, M.R., 1985. Rare earth element geochemistry of Australian Paleozoic graywackes and mudrocks: provenance and tectonic control. Sedimentary Geology 45, 97–113.

Bock, B., McLennan, S.M., Hanson, G.N., 1994. Rare earth element redistribution and its effects on the neodymium isotope system in the austin Glen Member of the Normanskill Formation, New York, USA. Geochimica et Cosmochimica Acta 58 (23), 5245–5253.

Burnotte, E., Pirard, E., Michel, G., 1989. Genesis of gray monazites: evidence from the Paleozoic of Belgium. Economic Geology 84, 1417–1429.

Cabella, R., Lucchetti, G., Marescotti, P., 2001. Authigenic monazite and xenotime from pelitic metacherts in pumpellyite–actinolite-facies conditions, Sestri-Voltaggio Zone, Central Liguria, Italy. The Canadian Mineralogist 39, 717–727.

Carron, M.K., Naeser, C.R., Rose Jr., H.J., Hildebrand, F.A., 1958. Fractional precipitation of rare earths with phosphoric acid. U.S. Geological Survey Bulletin 1036, 253–275.

Čopjaková, R., 2007. The reflection of provenance changes in the psefitic and psammitic fraction sedimentary fraction of the Myslejovice Formation (heavy mineral analysis). MS. PhD.- thesis, Masaryk University, Brno, Czech Republic, p. 137. (In Czech).

Čopjaková, R., Škoda, R., 2006. Detrital and authigenic REE-minerals in the Culm sediments of Drahany Uplands, their significance for provenance study of clastic material and diagenetic processes. Acta Musei Moraviae — Scientiae Geologicae 91, 105–127 (In Czech).

Čopjaková, R., Sulovský, P., Paterson, B.A., 2005. Major and trace elements in pyrope-almandine garnets as sediment provenance indicators of the Lower Carboniferous Culm sediments, Drahany Uplands, Bohemian Massif. Lithos 82, 51–70.

Čopjaková, R., Škoda, R., Novák, M., 2008. Altered Monazite from the Lower Carboniferous Culm Sediments of the Drahany Uplands (Bohemian Massif) — A Result of High-Temperature Diagenesis? — Proceedings from MIMET 2008 Workshop, pp. 26–31.

De Carlo, E.H., McMurtry, G.M., 1992. Rare-earth element geochemistry of ferromanganese crusts from the Hawaiian Archipelago, central Pacific. Chemical Geology 95, 235–250.

Donnot, M., Guigues, J., Lulzac, Y., Magnien, A., Parfenoff, A., Picot, P., 1973. Un nouveau type de gisement d'europium: la monazite grise à europium en nodules dans les schistes paleozoiques de Bretagne. Mineralium Deposita 8, 7–18.

Dvořák, J., 1973. Synsedimentary tectonics of the Paleozoic of the Drahany Upland (Sudeticum, Moravia, Czechoslovakia). Tectonophysics 17, 359–391.

Dvořák, J., 1989. Anchimetamorphism in the Variscan tectogene in Central Europe — its relationship to tectogenesis. Věstník Ústředního Ústavu Geologického 64 (1), 17–30.

Dvořák, J., Wolf, M., 1979. Thermal metamorphism in the Moravian Paleozoic (Sudeticum, ČSSR). Neues Jahrbuch fur Geologie und Palaontologie Monatshefte 10, 596–607.

Elderfield, H., Hawkesworth, C.J., Greaves, M.J., Calvert, S.E., 1981. Rare earth element geochemistry of oceanic ferromanganese nodules and associated sediments. Geochimica et Cosmochimica Acta 45, 1231–1234.

Evans, J., Zalasiewicz, J.A., 1996. U–Pb, Pb–Pb and Sm–Nd dating of authigenic monazite: implications for the diagenetic evolution of the Welsh Basin. Earth and Planetary Science Letters 144, 421–433.

Evans, J.A., Zalasiewicz, J.A., Fletcher, I., Rasmussen, B., Pearce, N.J.G., 2002. Dating diagenetic monazite in mudrocks: constraining the oil window? Journal of the Geological Society 159 (6), 619–622.

Ferry, J.M., 2000. Patterns of mineral occurrence in metamorphic rocks. American Mineralogist 85 (11–12), 1573–1588.

Firsching, F.H., Brune, S.N., 1991. Solubility products of the trivalent rare-earth phosphates. Journal of Chemical & Engineering Data 36, 93–95.

Foster, G.L., Parrish, R.R., 2003. Metamorphic monazite and the generation of P–T-t paths. In: Vance, D., Muller, W., Villa, I.M. (Eds.), Geochronology: Linking the Isotopic Record with Petrology and Textures: Geological Society, London, Special Publications, 220, pp. 25–47.

Foster, G., Gibson, D., Horstwood, M., Fraser, J., Tindle, A., 2002. Textural, chemical and isotopic insights into the nature and behaviour of metamorphic monazite. Chemical Geology 191, 181–205.

Francú, E., Francú, J., Kalvoda, J., 1999. Illite crystalinity and vitrinite reflectance in Paleozoic siliciclastics in the Bohemian Massif as evidence of thermal history. Geologica Carpathica 50 (5), 65–71.

Francú, E., Francú, J., Kalvoda, J., Poelchau, H.S., Otava, J., 2002. Burial and uplift history of the Palaeozoic Flysch in the Variscan foreland basin (SE Bohemian Massif, Czech Republic): EGU Stephan Mueller Special Publication Series, 1, pp. 167–179.

Franz, G., Andrehs, G., Rhede, D., 1996. Crystal chemistry of monazite and xenotime from Saxothuringian–Moldanubian metapelites, NE Bavaria, Germany. European Journal of Mineralogy 8, 1097–1118.

González-Álvarez, I., Kusiak, M.A., Kerrich, R., 2006. A trace element and chemical Th–U total Pb dating study in the lower Belt-Purcell Supergroup, Western North America: provenance and diagenetic implications. Chemical Geology 230, 140–160.

Gradstein, F.M., Ogg, J.G., Smith, A.G., 2005. A Geologic Time Scale 2004, p. 610.

Haley, B.A., Klinkhammer, G.P., McManus, J., 2004. Rare earth elements in pore waters of marine sediments. Geochimica et Cosmochimica Acta 68, 1265–1279.

Hannigan, R.E., Sholkovitz, E.R., 2001. The development of middle rare earth elements enrichments in freshwaters: weathering of phosphate minerals. Chemical Geology 175, 495–508.

Hartley, A.J., Otava, J., 2001. Sediment provenance and dispersal in a deep marine foreland basin: the Lower Carboniferous Culm Basin, Czech Republic. Journal of the Geological Society 158, 137–150.

Janots, E., Negro, F., Brunet, F., Goffe, B., Engi, M., Bouybaouène, M.L., 2006. Evolution of the REE mineralogy in HP-LT metapelites of the Sebtide complex, Rif, Morocco: monazite stability and geochronology. Lithos 87, 214–234.

Janots, E., Engi, M., Berger, A., Allaz, J., Schwarz, J.O., Spandler, C., 2008. Prograde metamorphic sequence of REE minerals in pelitic rocks of the Central Alps: implications for allanite–monazite–xenotime phase relations from 250 to 600 °C. Journal of Metamorphic Geology 26, 509–526.

Jercinovic, M.J., Williams, M.L., 2005. Analytical perils (and progress) in electron microprobe trace element analysis applied to geochronology: background acquisition, interferences, and beam irradiation effects. American Mineralogist 90, 526–546.

Johannesson, K.H., Zhou, X., 1999. Origin of middle rare earth element enrichments in acid waters of a Canadian High Arctic lake. Geochimica et Cosmachimica Acta 63, 153–165.

Jonasson, R.G., Bancoft, G.M., Nesbit, H.W., 1985. Solubilities of some hydrous REE phosphates with implications for diagenesis and seawater concentrations. Geochimica et Cosmachimica Acta 49, 2133–2139.

Kingsbury, J.A., Miller, C.F., Wooden, J.L., Harrison, T.M., 1993. Monazite paragenesis and U–Pb systematics in rocks of the eastern Mojave Desert, California, U.S.A.: implications for thermochronometry. Chemical Geology 110, 147–167.

Kish, H.J., 1987. Correlation between indicators of very low-grade metamorphism. In: Frey, M. (Ed.), Low Temperature Metamorphism. Blackie, Glasgow, pp. 227–299.

Koeppenkastrop, D., De Carlo, E.H., 1992. Sorption of rare-earth elements from seawater onto synthetic mineral particles: an experimental approach. Chemical Geology 95 (3–4), 251–263.

Kotková, J., Gerdes, A., Parrish, R.R., Novák, M., 2007. Clasts of Variscan high-grade rocks within Upper Visean conglomerates — a missing link in the late Variscan evolution of Central Europe: constraints from U–Pb chronology. Journal of Metamorphic Geology 25 (8), 781–801.

Krenn, E., Finger, F., 2007. Formation of monazite and rhabdophane at the expense of allanite during Alpine low temperature retrogression of metapelitic basement rocks from Crete, Greece: microprobe data and geochronological implications. Lithos 95, 130–147.

Krenn, E., Ustaszewski, K., Finger, F., 2008. Detrital and newly formed metamorphic monazite in amphibolite-facies metapelites from the Motajica Massif, Bosnia. Chemical Geology 254, 164–174.

Kumpera, O., Martinec, P., 1995. The development of the Carboniferous accretionary wedge in the Moravian–Silesian Paleozoic basin. Journal of the Czech Geological Society 40 (1–2), 47–64.

Lanzirotti, A., Hanson, G.N., 1996. Geochronology and geochemistry of multiple generations of monazite from the Wepawaug Schist, Connecticut, USA: implications for monazite stability in metamorphic rocks. Contributions to Mineralogy and Petrology 125, 332–340.

Lee, J.H., Byrne, R.H., 1992. Examination of comparative rare earth element complexation behavior using linear free-energy relationships. Geochimica et Cosmochimica Acta 56, 1127–1137.

Lee, J.H., Byrne, R.H., 1993. Complexation of trivalent rare earth elements (Ce, Eu, Gd, Tb, Yb) by carbonate ions. Geochimica et Cosmochimica Acta 57, 295–302.

Lev, S.M., McLennan, S.M., Meyers, W.J., Hanson, G.N., 1998. A petrographic approach for evaluating trace-element mobility in a black shale. Journal of Sedimentary Research 68 (5), 970–980.

Liu, X., Byrne, R.H., 1997. Rare earth and yttrium phosphate solubilities in aqueous solution. Geochimica et Cosmochimica Acta 61 (8), 1625–1633.

McLennan, S.M., Taylor, S.R., McCulloch, M.T., Maynard, J.B., 1990. Geochemical and Nd–Sr isotopic composition of deep sea turbidites. Part I: implications for crustal evolution. Geochimica et Cosmochimica Acta 2015–2050.

Merriman, R.J., Frey, M., 1999. Patterns of very low-grade metamorphism in metapelitic rocks. In: Frey, M., Robinson, D. (Eds.), Low-Grade Metamorphism. Blackwell Science, Oxford, pp. 12–87.

Milodowski, A.E., Zalasiewicz, J.A., 1991. Redistribution of rare earth elements during diagenesis of turbidite/hemipelagite mudrock sequences of Llandovery age from central Wales: Geological Society, London, Special Publications, 57, pp. 101–124.

Montel, J.M., Foret, S., Veschambre, M., Nicollet, C., Provost, A., 1996. Electron microprobe dating of monazite. Chemical Geology 131, 37–53.

Nathan, S., 1976. Geochemistry of the Greenland Group (Early Ordovician), New Zealand. New Zealand Journal of Geology and Geophysics 19, 683–706.

Ohr, M., Halliday, A.N., Peacor, D.R., 1994. Mobility and fractionation of rare earth elements in argillaceous sediments: implications for dating diagenesis and low-grade metamorphism. Geochimica et Cosmachimica Acta 58, 289–312.

Pattan, J.N., Rao, Ch.M., Migdisiov, A.A., Colley, S., Higgs, N.C., Demidenko, L., 2001. Ferromanganese nodules and their associated sediments from the Central Indian Ocean Basin: rare earth element geochemistry. Marine Georesources and Geotechnology 19, 155–165.

Poitrasson, F., Oelkers, E., Schott, J., Montel, J.M., 2004. Experimental determination of synthetic $NdPO_4$ monazite solubility in water from 21 °C to 300 °C: implications for rare earth element mobility in crustal fluids. Geochimica et Cosmochimica Acta 68, 2207–2221.

Pouchou, J.L., Pichoir, F., 1985. PAP procedure for improved quantitative microanalysis. Microbeam Analysis 20, 104–105.

Pourret, O., Davranche, M., Gruau, G., Dia, A., 2007. Rare earth elements complexation with humic acid. Chemical Geology 243 (1–2), 128–141.

Putnis, A., 2002. Mineral replacement reactions: from macroscopic observations to microscopic mechanisms. Mineralogical Magazine 66, 689–708.

Putnis, A., 2009. Mineral replacement reactions. In: Oelkers, E.H., Schott, J. (Eds.), Thermodynamics and Kinetics of Water–Rock Interactions. : Reviews in Mineralogy and Geochemistry, 70. Mineralogical Society of America, Chantilly, Virginia, pp. 87–124.

Rasmussen, B., Muhling, J.R., 2007. Monazite begets monazite: evidence for the dissolution of detrital monazite and reprecipitation of syntectonic monazite during low-grade regional metamorphism. Contributions to Mineralogy and Petrology 154, 675–689.

Rasmussen, B., Muhling, J.R., 2009. Reactions destroying detrital monazite in greenschist-facies sandstones from the Witwatersrand basin, South Africa. Chemical Geology 264, 311–327.

Rasmussen, B., Fletcher, I.R., McNaughton, N.J., 2001. Dating low-grade metamorphic events by SHRIMP U–Pb analysis of monazite in shales. Geology 29 (10), 963–966.

Rasmussen, B., Fletcher, I.R., Sheppard, S., 2005. Isotopic dating of the migration of a low-grade metamorphic front during orogenesis. Geology 33 (10), 773–776.

Rasmussen, B., Fletcher, I.R., Muhling, J.R., 2007. In situ U–Pb dating and element mapping of three generations of monazite: unravelling cryptic tectonothermal events in low-grade terranes. Geochimica et Cosmochimica Acta 71, 670–690.

Rosenblum, S., Mosier, E.L., 1983. Mineralogy and occurrence of europium-rich dark monazite. U.S. Geological Survey Professional Paper 1181 67 pp.

Schulmann, K., Gayer, R., 2000. A model for a continental accretionary wedge developed by oblique collision: the NE Bohemian Massif. Journal of the Geological Society of London 157, 401–406.

Shaw, D.M., 1956. Geochemistry of pelitic rocks. Part III: major elements and general geochemistry. Geological Society of American Bulletin 67, 919–934.

Škoda, R., Čopjaková, R., 2006. Authigenic REE minerals from greywackes of the Drahany Uplands, Czech Republic and their significance for diagenetic processes. Mineralogia Polonica 28, 208–210.

Smith, H.A., Barreiro, B., 1990. Monazite U–Pb dating of staurolite grade metamorphism in pelitic schists. Contributions to Mineralogy and Petrology 105, 602–615.

Sonke, J.E., Salters, V.J.M., 2006. Lanthanide-humic substances complexation. I. Experimental evidence for a lanthanide contraction effect. Geochimica et Cosmochimica Acta 70, 1495–1506.

Spear, F.S., Pyle, J.M., 2002. Apatite, monazite, and xenotime in metamorphic rocks. In: Kohn, M.J., Rakovan, J., Hughes, J.M. (Eds.), Phosphates: Geochemical, Geobiological and Materials Importance: Reviews in Mineralogy and Geochemistry, 48. Mineralogical Society of America, USA, pp. 293–335.

Takebe, M., Yamamoto, K., 2007. Relative REE abundances of porewater in Pacific pelagic sediments: estimation by equilibrium calculations based on REE composition of Mn-oxide and apatite components. Bulletin of the Nagoya University Museum 23, 1–12.

Taylor, S.R., McLennan, S.M., 1985. The Continental Crust: Its Composition and Evolution. Blackwell Scientific Publications, Oxford, p. 321.

Taylor, G.H., Teichmüller, M., Davis, A., Diessel, C.F.K., Littke, R., Robert, P., 1998. Organic Petrology. Gebrüder Borntraeger, Berlin, p. 704.

Wan, Y., Song, T., Liu, D., Yang, T., Yin, X., Chen, Z., Zhang, Q., 2007. Mesozoic monazite in Neoproterozoic metasediments: evidence for low-grade metamorphism of Sinian sediments during Triassic continental collision, Liaodong Peninsula, NE China. Geochemical Journal 41, 47–55.

Wilby, P.R., Page, A.A., Zalasiewicz, J.A., Milodowski, A.E., Williams, M., Evans, J.A., 2007. Syntectonic monazite in low-grade mudrocks: a potential geochronometer for cleavage formation? Journal of the Geological Society 164 (1), 53–56.

Wing, B.A., Ferry, J.M., Harrison, T.M., 2003. Prograde destruction and formation of monazite and allanite during contact and regional metamorphism of pelites: petrology and geochronology. Contributions to Mineralogy and Petrology 145, 228–250.

Wood, S.A., 1990. The aqueous geochemistry of the rare-earth elements and yttrium. 1. Review of available low-temperature data for inorganic complexes and the inorganic REE speciation of natural waters. Chemical Geology 82, 159–186.

Wood, S.A., Williams-Jones, A.E., 1994. The aqueous geochemistry of the rare-earth elements and yttrium: 4. Monazite solubility and REE mobility in exhalative massive sulfide-depositing environments. Chemical Geology 115, 47–60.

Příloha 6

Bábek O., Franců E., Kalvoda J., Neubauer F. (2008) A digital image analysis approach to measurement of the conodont colour alteration index (CAI): a case study from the Moravo-Silesian Zone, Czech Republic. - N. Jb. Geol. Paläont., 249/2: 185-201;

N. Jb. Geol. Paläont. Abh.
2008, vol. 249/2, p. 185–201, Stuttgart, August 2008, published online 2008

A digital image analysis approach to measurement of the conodont colour alteration index (CAI): a case study from the Moravo-Silesian Zone, Czech Republic

Ondřej Bábek, Brno and Olomouc, **Eva Franců,** Brno, **Jiří Kalvoda,** Brno and
Franz Neubauer, Salzburg

With 9 figures and 2 tables

Bábek, O., Franců, E., Kalvoda, J. & Neubauer, F. (2008): A digital image analysis approach to measurement of the conodont colour alteration index (CAI): a case study from the Moravo-Silesian Zone, Czech Republic. – N. Jb. Geol. Paläont. Abh., **249**: 185–201; Stuttgart.

Abstract: Presented is a simple non-destructive method for quantifying conodont colour based on digital processing of conodont images taken by a digital camera attached to a binocular microscope operating under incident light, using the RGB colour space. The digital colour data was calibrated to a spectral reflectance of the standard colour background. The results from the Moravo-Silesian Zone (MSZ) of the Bohemian Massif, Czech Republic, demonstrate an excellent relationship existing between the digital intensities of the red (R), green (G) and blue (B) colours and CAI in the range from CAI 3 to CAI 6. The R/B colour ratio proved the best proxy of CAI. The R/B ratio decreases with increasing CAI from values >1.6 (CAI 3) to ~1.0 (CAI5) and then slightly increases to 1.15 (mean for CAI 5.5) and 1.26 (mean for CAI 6). It is closely related to CAI ($R^2 = 0.8974$) within CAI 3 to CAI 5 interval. The R/B ratio is similar in concept to the slope of the reflectance curve obtained from the spectral reflectance of conodonts by previous authors, as well as to the shift from yellow and brown colours towards greyscale conodont colours with increasing thermal maturation according to the original definition of CAI. Regional distribution of the CAI and R/B ratio from the MSZ suggests that the digital conodont colour data is closely related to vitrinite reflectance and illite crystallinity data.

Keywords: RGB colour space, conodonts, colour calibration, spectral reflectance, thermal maturation, Devonian, Carboniferous, Variscides.

Introduction

Colour is an important property of geological materials. Since it is related to mineral and chemical composition and texture of minerals, organic matter, rocks and soils, its measurement has broad applications in earth sciences. Numerous techniques for measuring colour and numerous colour systems are used, including the Munsell hue, value, and chroma (HVC) colour system, spectral reflectance curves, CIE (Commission Internationale de l'Eclairage) L* a*b* (lightness, redness/greenness, yellowness/ blueness) colour space with rectangular coordinates, CIE L*C*H* (lightness, chroma (saturation) and hue) colour space with polar coordinates, Helmholtz chromaticity coordinates, and the RGB (digital intensities of red, green and blue components) colour system (Levin et al. 2005; Mathieu et al. 1998; Torrent et

DOI: 10.1127/0077-7749/2008/0249-0185

0077-7749/08/0249-0185 $ 4.25

al. 1983; Viscarra-Rossel et al. 2006). Each of the colour systems and measuring techniques has its benefits and drawbacks. The Munsell system is semi-quantitative and subjective, and may be subject to considerable error due to operator fatigue or illumination conditions (Mathieu et al. 1998; Viscarra-Rossel et al. 2006). Measurement of spectral reflectance curves usually requires the use of expensive spectrometers or chromameters, may be limited in the field conditions or under microscope, and the results are less convenient for statistical processing and prediction in comparison with the coordinated colour models (Deaton et al. 1996; Levin et al. 2005). Digital colour image analysis, on the other hand, meets with increasingly higher application in the earth sciences. Among the coordinated colour spaces used in image analysis, the RGB colour model is most popular due to quick data acquisition, easy statistical processing and high precision even when compared to the use of spectrophotometers (Levin et al. 2005). The RGB colour model has been successfully applied in many case studies in sedimentary petrology (Götte & Ricchter 2005 2006; Obara 2005), coal petrology (Simons et al. 1997; Van Geet et al. 2001), stratigraphy (Kashiyama et al. 2004), soil science (Levin et al. 2005; van Huyssteen et al. 2006), hydrology (Goddijn & White 2006), and thermal maturation studies (van de Laar & David 1998).

Colour changes of microfossils such as conodonts, chitinozoans, graptolites, acritarchs and plant spores are often used as a semi quantitative measure of the thermal maturity of sediments. Of these methods, the conodont colour alteration index (CAI, Epstein et al. 1977; Rejebian et al. 1987), in particular, proved useful as a rapid, inexpensive technique for assessing thermal maturity. The CAI technique is especially advantageous where quantitative methods of thermal maturation, such as the coal rank, vitrinite reflectance, illite and chlorite crystallinity, fluid inclusions homogenization temperature and apatite fission track (Franců et al. 1990; Pollastro 1993; Pearson & Small 1988; Robert 1988; Srodon 1995; Underwood et al. 1993) fail due to unfavourable lithology or due to their effective temperature range.

The aim of this paper is to describe a new method for quantifying conodont colour based on RGB colour image analysis of whole conodont elements using a digital camera attached to a binocular microscope and routine image-analysis software. The data set selected for this study includes conodont collections from the Moravo-Silesian Zone, Czech Republic. The quantitative representation of conodont colour will be compared with the subjective CAI determination and vitrinite reflectance data on a regional scale.

Conodont Colour Alteration Index (CAI)

Conodonts are the tiny (0.2 to 5 mm) remains of the feeding apparatuses of an extinct group of primitive chordates, which were common from the Cambrian to the late Triassic (Briggs et al. 1983; Lindström 1964; Sweet 1988). The conodonts are made up of calcium phosphate (apatite, francolite) organised in thin, concentric lamellae. When heated, the colour of the conodont elements changes from white, pale yellow to dense black (Ellison 1944; Epstein et al. 1977). Epstein et al. (1977) combined field conodont collections with artificially heated samples in order to establish a semi-quantitative scale of five colour intervals from 1 to 5, the conodont colour alteration index (CAI), which they demonstrated as changing with increasing temperature from 50 °C to 300 °C. Rejebian et al. (1987) defined CAI 6, 7 and 8 (grey, opaque white and crystal clear) expanding the working range of the technique to more than 600 °C. The temperature-controlled colour change is related to the transformation of organic matter between the phosphate lamellae of conodonts (Königshof 2003). During the artificial maturation of conodonts, the progressive removal of carboxyl, alcohol, ether and carbonyl functional groups, the elimination of C-O bonds and nitrogen compounds and the development of highly ordered graphitic-like carbon was observed (Marshall et al. 2001). Apart from temperature, however, the CAI may by influenced by the passage of hydrothermal fluids (Königshof 1992, 2003), element size variation (Garcia-Lopez et al. 1997), taxonomic variations at the generic level (Marshall et al. 2001) and the lithology of the host rock (Legall et al. 1981). The CAI has been successfully applied in a number of thermal-maturation case studies worldwide (Garcia-Lopez et al. 1997; Gawlick et al. 1994; Helsen 1995; Helsen & Königshof 1994; Königshof 1991; 1992; Kovács et al. 2006; Nicoll 1981; Nicoll & Gorter 1984; Nowlan & Barnes 1987; Sudar & Kovács 2006; Wiederer et al. 2002).

The CAI is determined microscopically under incident light from the thin edges or lighter parts of the conodonts by comparing them with a set of laboratory produced standards, field-assembled conodonts, and/or the conodont colour or the Munsell soil colour chart (Epstein et al. 1977). Such determination is based on

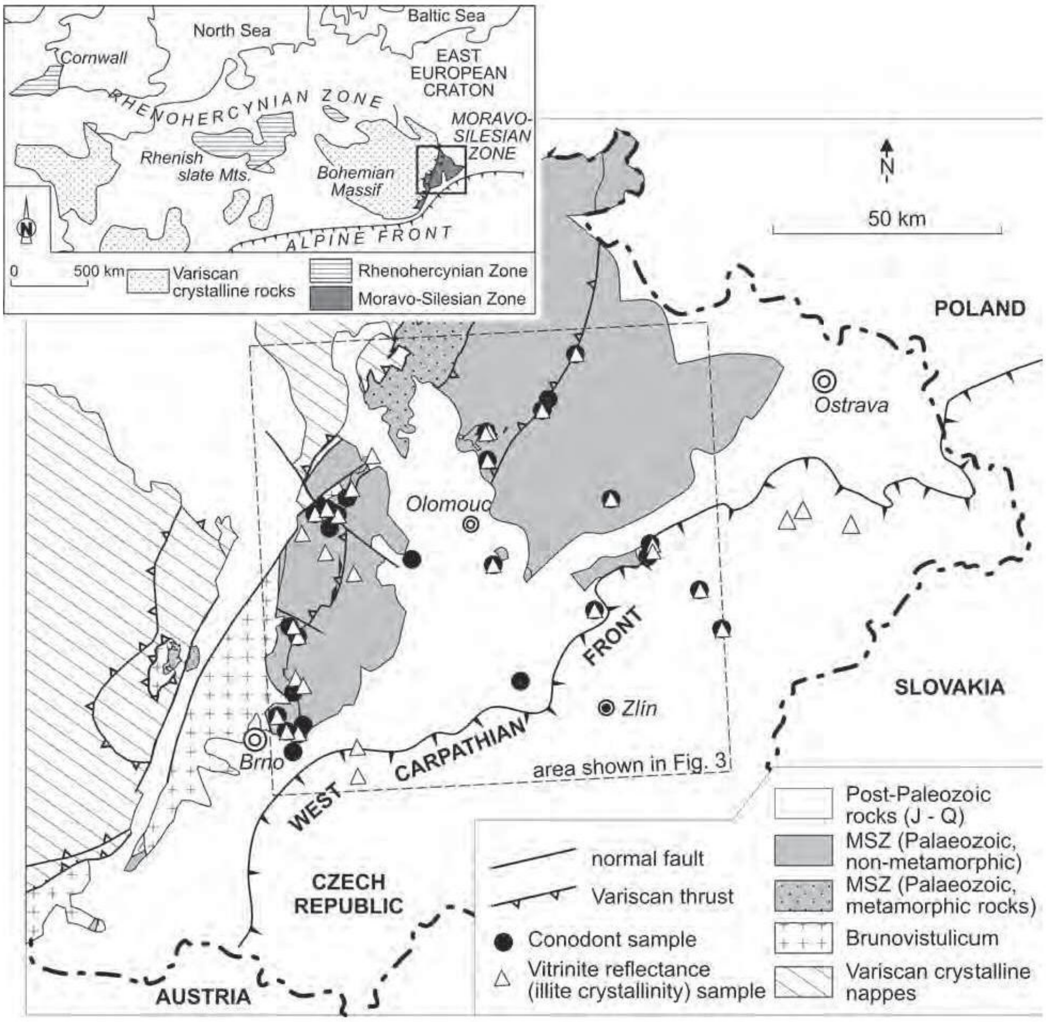

Fig. 1. Simplified geological map of Moravo-Silesian Zone, with location of CAI and thermal maturity samples.

the human eye's perception of light reflected from the conodont in the visible spectrum of electromagnetic radiation, which is a subjective measure (Deaton et al. 1996). In an attempt to quantify the conodont colour alteration, several authors used infrared spectroscopy (Nöth & Richter 1992), fluorescence spectrometry (Mastalerz et al. 1992), gas chromatography-mass spectrometry (Bustin et al. 1992), electron spin resonance (Belka et al. 1987), organic geochemistry (Marshall et al. 1999), spectral reflectance (Deaton et al. 1996), and colour image analysis (Helsen et al. 1995). The latest two methods are most closely related to the primary meaning of the CAI as expressed by Epstein et al. (1977), i. e. the conodont colour perceived by the human eye. Helsen et al. (1995) measured the intensities of the red, green and blue colour components of reflected light (RGB mode) from selected small areas (10 x 20 μm) on polished conodonts. The method proved successful in relating the RGB intensities to CAI, but was destructive and time consuming (polishing) as well as partly subjective (the selection of the area for measurement). The spectral reflectance technique of DEATON et al. (1996) proved highly accurate, nonsubjective and reproducible in quantifying conodont colour, but required a large number of conodont elements per sample (30 large elements), and the use of expensive equipment.

Geological setting

The Moravo-Silesian Zone (MSZ) is located in the eastern part of the Czech Republic and southern Poland, at the eastern margin of the Bohemian Massif (Fig. 1). It is considered the eastward extension of the Rhenohercynian and Subvariscan zones of the European Variscides (DVOŘÁK & PAPROTH 1969; FRANKE 1995). To the W, the MSZ is bordered by Variscan crystalline nappes along the Moravo-Silesian Fault Zone (SCHULMANN et al. 1991). To the E, it is covered by Mesozoic and Tertiary sediments of the Outer Western Carpathians. In the N, the MSZ extends to the Hamburg – Cracow Fault Zone in southern Poland (KALVODA et al. 2003). The MSZ is composed of sheared, unmetamorphosed to slightly metamorphosed sediments and volcanics of the Cambrian, the Ordovician and the Early Devonian (Pragian) to the Late Carboniferous (Namurian) age. These rocks rest unconformably upon Upper Proterozoic crystalline rocks of the Brunovistulicum (DUDEK 1980; KALVODA et al. 2007).

The Palaeozoic rock successions of the MSZ are comprised of Lower to Middle Devonian shallow-marine siliciclastics ("basal clastics"), Middle- to Upper Devonian to shallow-water platform carbonates (Macocha Formation), Upper Devonian to Lower Carboniferous deep-water carbonates and shales (Líšeň Formation) and, in places, Devonian to Tournaisian alkali- to subalkali basalts. These facies were deposited during the extensional phase of the MSZ (CHLUPÁČ 1988; HLADIL 1994; ZIEGLER 1988) and were soon replaced by deep-water Variscan synorogenic siliciclastics (so-called "Culm" facies) of the Viséan to the Early Namurian age (HARTLEY & OTAVA 2001; KUMPERA & MARTINEC 1995). The Culm siliciclastics are in places overlain by Namurian to Westphalian paralic and continental coal-bearing cyclothems of the Upper Silesian Coal Basin representing the final depositional phase in the evolution of the Moravo-Silesian Basin. Most of the conodont samples discussed in this paper were obtained from carbonates of the Macocha and Líšeň formations.

Structure and thermal alteration of the MSZ

The MSZ is considered to represent a Palaeozoic accretionary wedge, which developed between the overriding nappe stack of the Moldanubian and Teplá-Barrandian units, and the subducted Brunovistulian crystalline basement (CHADIMA et al. 2006; DALLMEYER et al. 1992; FRITZ & NEUBAUER 1995). The structure of the MSZ is interpreted as an imbricate stack of NW-dipping tectonic slices (BÁBEK et al. 2006; CHÁB 1986; ČÍŽEK & TOMEK 1991). The intensity of the deformation (ductile vs. brittle deformation, magnetic fabric) decreases in the W-E to NW-SE orogen-perpendicular direction (CHADIMA et al. 2006; RAJLICH 1990). The main folding and thrusting events took place in the Late Carboniferous, in all probability close to the Westphalian/Stephanian boundary ("Asturian phase").

The published thermal alteration data reveals a general SE–to-NW regional trend of increasing thermal maturation. In the Cracow-Silesia foreland of the MSZ, southern Poland, the thermal overprint is relatively low reaching the dry-gas/oil-window zone, related mainly to intrusions of small intrusive bodies (BELKA 1993). In the western hinterland of the MSZ in Moravia, the thermal maturity is much higher reaching up to the anchimetamorphic grade. The published thermal-maturity data from the Moravian part of the MSZ is based on random vitrinite reflectance (Rr)(DVOŘÁK 1989; DVOŘÁK & WOLF 1979; FRANCŮ et al. 1999 2002) and illite crystallinity (IC) (DVOŘÁK 1989; FRANCŮ et al. 1999). In the S to SE part of the MSZ, values of IC range from 0.44 to 1.46 $\Delta\ 2^{o}\Theta$ and R_r from 1.1 to 2.2 %, corresponding to the maximum burial temperatures ~100 to ~200 °C. In the central part of MSZ, values of IC range from 0.44 to 0.55 $\Delta\ 2^{o}\Theta$ and R_r from 1.7 to 2.5 %. In the W part, values of IC range from 0.24 to 0.36 $\Delta\ 2^{o}\Theta$ and R_r from 3.17 to 5.23 %, which corresponds to the maximum burial temperatures of ~330 °C (FRANCŮ et al. 1999). Most of the published IC and R_r data was measured from the synorogenic "Culm" facies of the Myslejovice and Rozstání formations. Only a limited number of samples were measured from limestones of the Macocha and Líšeň formations. With the exception of scarce, unpublished comments by KREJČÍ (1991), no data on the conodont colour alteration has been published as yet from the Moravian part of the MSZ. The distribution of the R_r and illite crystallinity was explained in the model of a deep, mainly tectonically driven, burial with lower heat flow in the western hinterland and a relatively shallower sedimentary burial with equal or slightly higher heat flow in the eastern foreland part of the basin (FRANCŮ et al. 1999, 2002).

Material and methods

A total of 25 core samples and 48 outcrop samples of carbonate rocks were taken for the CAI analysis. Most of the samples (45) were obtained from the existing conodont collections deposited at Masaryk University, Brno, and the Czech Geological Survey, Brno, Czech Republic. These samples, weighing 1 to 1.5 kg, were digested in 12 to 15% vol. water solution of acetic acid for 3 to 5 weeks (KREJČÍ 1991). New outcrop conodont samples (27) with 1.5 to 3 kg weight were digested in 12% vol. water solution of acetic acid for 4 to 5 weeks. Conodonts were picked from the insoluble residues under a binocular microscope in order to minimize artificial fragmentation of elements.

CAI and quantitative conodont colour measurements

Subjective determination of CAI was carried out using the comparative charts of EPSTEIN et al. (1977). Other CAI charts are available that are more recent (KÖNIGSHOF 2003), but since there are distinct colour shifts between different charts, we kept to the original one by EPSTEIN et al. (1977). The preparation of a regional CAI standard by laboratory heating as recommended by EPSTEIN et al. (1977) was not possible due to the absence of thermally unaltered conodonts in the study area. The lightest, best-preserved conodont elements (two to six per sample), with minimum impurities and coatings, were mounted on a glazed white porcelain slide with 20 x 40 mm dimensions. The conodonts were observed under a Leica binocular microscope with a Leica CLS 150X illuminator, 150 W/21 V halogen bulb, at 2850 K light colour temperature. A circular illumination stage attached to the microscope lens was used in order to provide omnidirectional light incidence and avoid shaded areas on the conodont surfaces. The samples were photographed by a Leica DFC 48 digital camera with an automated microscope tube positioning system with 12 μm step width, and IM 1000 image processing software in order to provide deep focus throughout the element surface. All samples were photographed with x65 to x80 magnification. The images (4 915 200 pixels each) were then exported to a regular desktop PC and processed in the RGB colour mode using Olympus analySIS FIVE image-analysis software and a routine bitmap editor (Corel PhotoPaint 12). The whole area of each conodont element in a sample (approximately from 0.3 to 1.3×10^6 pixels) was analysed. We have analysed 275 conodont elements from 73 samples of Middle Devonian (Givetian) to Early Carboniferous (Tournaisian) age. Conodonts of the genus *Palmatolepis* and *Polygnathus* were most frequent; *Ancyrodella, Bispathodus, Branmehla, Gnathodus, Icriodus, Protognathodus, Pseudopolygnathus, Spathognathodus*, unidentifiable platform elements and ramiform elements were less frequent. The analytical results included the total area in pixels, a sample histogram, the median and standard deviation value in the red, green and blue colour channel of the image.

Colour calibration

Colour sensed by charge couple device (CCD) sensors used in digital cameras can be affected by illumination conditions, contrasts within the image scene, brightness fall-off towards the margins of the image, and adjacency effects that smooth the boundaries between objects. Several of these effects may occur due to variation in exposure, magnification, or light contamination from external sources during photography. In order to overcome these negative effects, the images can be calibrated by the use of colour reference chips photographed along with the objects ("in-flight" calibration) (DEAN et al. 2000; LEVIN et al. 2005; WEBSTER & MOLLON 1997). Colour calibration of the conodont sample images was performed in two ways, internal calibration and external calibration based on spectrophotometry of the reference white standard (cf. LEVIN et al. 2005). The "in-flight" (relative) calibration was based on region of interest (ROI), which was a rectangular area of about 2000 x 2000 to 2000 x 3500 pixels, located in the white porcelain standard, in the upper right part of each image. Mean red, green and blue intensities were measured in the ROI of each image. Within the set of 73 samples measured, the obtained range of mean RGB values in the ROI was 210 to 237 for R (mean 228), 213 to 238 for G (mean 228), and 214 to 242 for B (mean 231). A strong linear correlation (Fig. 2)

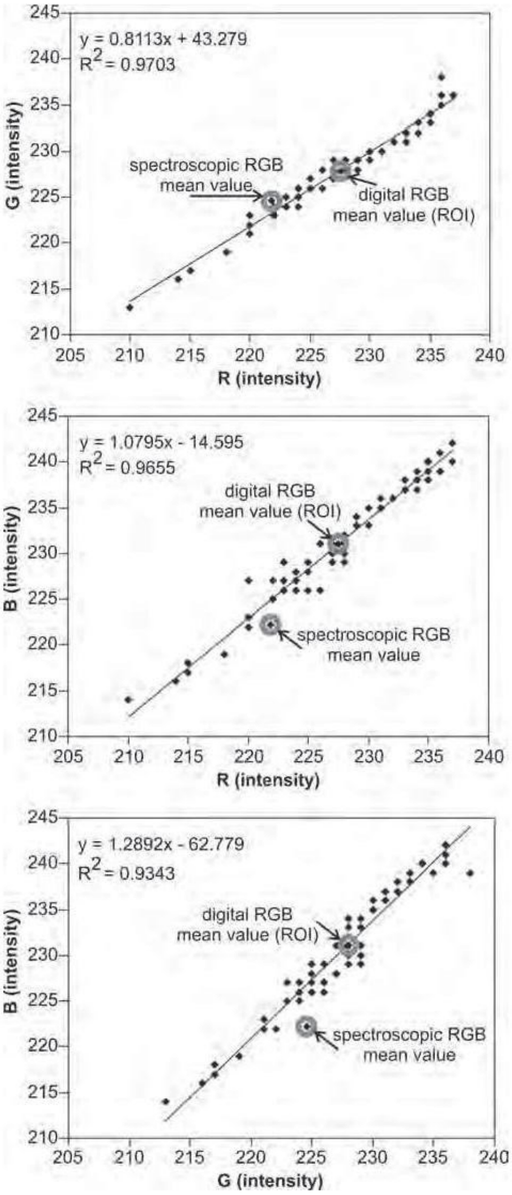

Fig. 2. Results of "in-flight" calibration of RGB data. Correlation between R, G and B colours of region of interest (ROI) located in white porcelain standard. Note shift of RGB data point derived from spectroscopic measurement of white standard (grey circle) from linear correlation line.

exists between the mean R/G, R/B and G/B intensities of the ROI (correlation coefficient R^2 is 0.97 for R/G; 0.97 for R/B; and 0.94 for G/B). Due to the fact that the RGB values of the white standard are extremely well correlated, one can assume that no significant shifts towards the red, green or blue colour occurred due to negative CCD sensor effects during photography. The obtained variation within the ROI only reflects shifts towards the black (a proportional increase of RGB intensities) or white (a proportional decrease of RGB intensities) colours, which is related to the brightness (illumination) of the scene. Mean intensities of R (228), G (228) and B (231) were used as the digital standard RGB values of the white standard (ROI). The external (absolute) colour calibration was based on the spectrophotometry measurement of the white standard. The colour of the white standard was measured by a X-Rite SP62 spectrophotometer (X-Rite Inc.) with an 8 mm aperture, operating in CIEL*a*b* colour space, in the D65/10° Illuminant/Observer mode. Mean L*, a* and b* values from ten measurements of the white standard were converted to RGB values using a free EasyRGB Color Calculator by Logicol S.r.l., Italy, which is available at http://www.easyrgb.com. The resultant spectrophotometric standard RGB values of the white standard are 222 for R, 225 for G, and 222 for B. Compared to the spectrophotometric RGB values of the white standard, the digital standard RGB values of the ROI (R: 228, G: 228, B: 231) are shifted from the RGB space greyscale diagonal, most notably towards the blue (positive B shift) and magenta (negative G shift) component of reflected light (Fig. 2). These shifts are interpreted so as to reflect the characteristic features of the instrument (light source, optical path, CCD sensor) and the local conditions of illumination. The calibrated red intensities of each conodont element were obtained from the raw digital data red according to the formula $R_{(c)} = R_{(s)} - (R_{ROI(s)} - R_{(ws)})$, where $R_{(c)}$ = the calibrated median red intensity of the conodont element; $R_{(s)}$ = the raw-data median red intensity of the conodont element in sample; $R_{ROI(s)}$ = the median red intensity in the sample ROI; $R_{(ws)}$ = the mean spectrophotometric red intensity of the white standard (R: 222, G: 225, B: 222).

Vitrinite reflectance and the illite crystallinity measurement

In order to cross-correlate the conodont colour data directly to thermal maturation, 24 conodont samples were analysed for vitrinite reflectance (VR) and illite crystallinity (IC). The number of samples was limited due to the lack of comparative core material for borrowed conodont collections and/or due to unfavourable lithology. For VR analysis, polished rock slabs mounted in epoxy resin were measured under Leitz Wetzlar MPV2 microscope-photometer and Leitz standards of 1.26 and 5.42% reflectance and recalculated to random reflectance (Teichmüller et al. 1998). Clay minerals for IC analysis were separated from sediments and conodont insoluble residues by centrifugation. Oriented clay fraction slides were analyzed air-dry and after vapour ethylene-glycol solvatation by Philips PW 1830 X-ray diffractometer with attached Phillips PW 3020 goniometer. The IC values were measured according to Kübler (1967), calibrated using the international standards (Warr & Rice 1994) and converted to VR values.

Results and discussion

Thermal maturation and CAI

CAI was subjectively determined from 68 out of the 73 samples using the published comparative chart of Epstein et al. (1977). The results indicate that the conodonts from the MSZ correspond to the CAI range from 3 to 6, with most samples being matured to CAI 5. We have not found any conodonts matured to lower and higher CAI values (CAI 1-2, CAI 6.5-8) in the study area. The regional distribution of the CAI data closely follows the N-to-S trend of decreasing thermal maturation as revealed from vitrinite reflectance (Rr) and illite crystallinity (IC) data. The conodont samples from the S part of the MSZ showing CAI values from 3 to 4 correspond to Rr values from 1.41 to 2.1% (Fig. 3) and published IC values from 0.44 to 1.46 Δ 2°Θ, which indicate maximum burial temperatures from ~100 to ~200 °C (Franců et al. 1999). The conodonts from the central and northern part of the MSZ showing CAI 5 to CAI 6 values correspond to a very broad range of Rr values (Rr from 2.5 to 5.75%, Fig. 3) and published IC values (from 0.24 to 0.55 Δ 2°Θ, Franců et al. 1999), which correspond to maximum burial temperatures up to

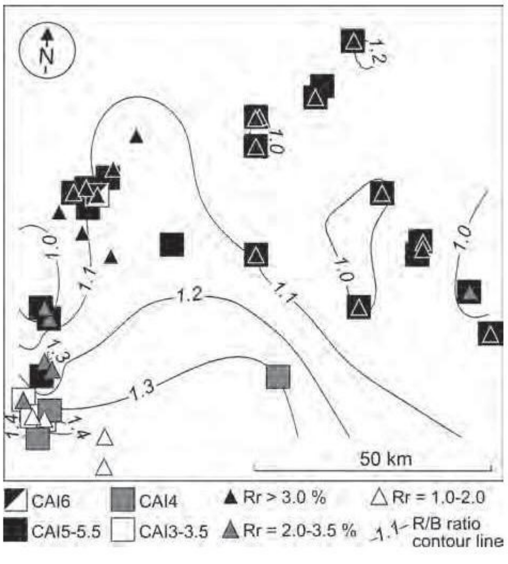

Fig. 3. Regional distribution of CAI, R/B, and vitrinite reflectance data. For area location see Fig. 1.

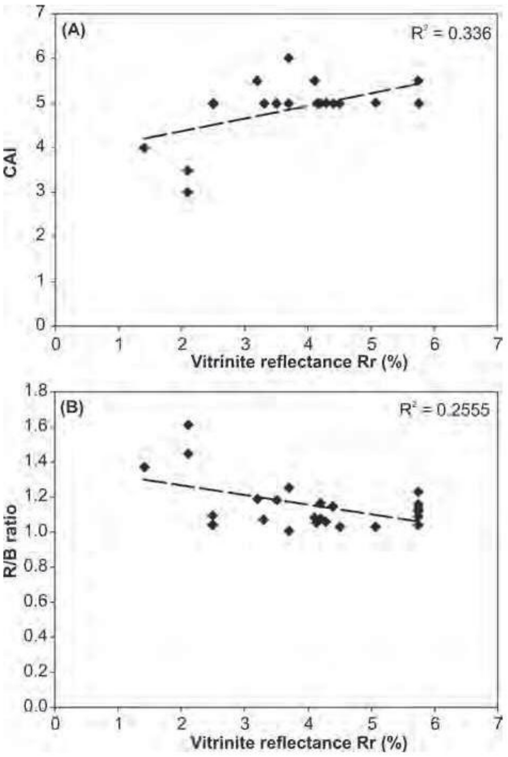

Fig. 4. For 24 data points from MSZ (**A**) relationship between vitrinite reflectance and CAI, and (**B**) vitrinite reflectance and R/B ratio. Note the CAI 5.5-6 samples, which correspond to relatively low Rr values in (A).

Table 1. Statistics of RGB data from MSZ.

	Range		Arithmetic mean		Median		Mode		Standard deviation		Skewness	
	R.D.*	C.D. **	R.D.	C.D.	R.D.	C.D.	R.D.	C.D.	R.D.	C.D.	R.D.	C.D.
CAI3, 9 measurements												
R	94-135	90-129	114.44	109.33	114	110	-	-	12.46	12.21	-0.02	0.00
G	78-112	77-108	93.33	90.67	93	90	-	-	10.67	10.28	0.28	0.37
B	63-87	55-80	72.67	66.44	69	63	-	-	8.68	8.35	0.57	0.61
R/B	1.46-1.78	1.50-1.92	1.58	1.65	1.55	1.63	-	-	0.10	0.12	0.83	1.01
CAI3.5, 22 measurements												
R	79-117	76-121	95.32	92.68	93	89.5	89	78	10.82	12.49	0.36	0.52
G	68-106	67-104	83.59	83.50	82	83	81	80	10.48	9.97	0.30	0.27
B	53-83	45-79	67.14	62.09	66	61	60	56	7.44	8.04	0.15	0.22
R/B	1.18-1.67	1.28-1.71	1.42	1.50	1.43	1.47	-	1.47	0.10	0.10	0.05	0.54
CAI4, 16 measurements												
R	57-114	51-110	80.94	75.44	79	70	57	70	17.16	17.70	0.52	0.55
G	49-96	45-90	70.19	66.44	68.5	63	66	63	12.6	12.98	0.32	0.31
B	43-77	36-66	59.19	51.94	59	51	56	49	8.26	8.47	0.07	-0.03
R/B	1.18-1.64	1.24-1.76	1.36	1.44	1.31	1.40	-	-	0.15	0.16	0.70	0.60
CAI5, 135 measurements												
R	34-109	28-99	57.55	51.16	56	50	48	44	13.08	12.83	0.81	0.70
G	37-114	30-108	61.96	58.33	62	56	46	55	14.42	13.70	0.73	0.77
B	36-91	26-82	56.77	46.70	56	47	51	47	10.92	10.49	0.72	0.65
R/B	0.83-1.20	0.90-1.33	1.01	1.09	1.00	1.09	1.00	1.00	0.07	0.08	0.24	0.11
CAI5.5, 72 measurements												
R	43-124	41-113	75.17	69.13	72.5	67	58	56	15.64	15.3	0.81	0.70
G	43-130	42-124	80.33	77.17	78	73.5	78	73	16.59	15.83	0.73	0.77
B	42-105	37-91	70.47	60.19	69	58	72	54	12.66	11.85	0.72	0.65
R/B	0.89-1.24	0.93-1.34	1.07	1.15	1.05	1.14	1.00	1.14	0.07	0.08	0.33	0.09
CAI6, 3 measurements												
R	123-138	120-135	129	126	126	123	-	-	6.48	6.48	1.46	1.46
G	115-126	113-124	120	118	119	117	-	-	4.55	4.55	0.78	0.78
B	101-113	95-107	106.33	100	105	99	-	-	4.99	4.99	0.94	0.94
R/B	1.20-1.22	1.24-1.26	1.21	1.26	1.22	1.26	-	-	0.01	0.01	-1.56	-1.70
CAI not determined, 18 measurements												
R	47-133	45-138	100.44	98.50	102	99.5	117	-	21.43	24.38	-0.69	-0.31
G	48-119	48-127	95.17	95.50	97	97	119	110	18.42	19.58	-0.92	-0.57
B	47-103	43-106	83.17	78.39	85	78	85	67	14.84	17.10	-0.77	-0.14
R/B	1.00-1.44	1.05-1.49	1.20	1.25	1.22	1.25	-	-	0.11	0.10	-0.04	0.26
Total, 275 measurements												
R	34-138	28-138	71.99	66.41	67	60	48	56	22.60	23.65	0.76	0.86
G	37-130	30-127	72.81	69.89	70	67	68	59	19.27	19.53	0.49	0.59
B	36-113	26-107	64.12	55.07	62	53	60	47	14.52	15.16	0.71	0.90
R/B	0.83-1.78	0.90-1.92	1.11	1.19	1.05	1.13	1.00	1.00	0.18	0.18	1.42	1.38

* R.D.: Raw data

** C.D. Data calibrated to spectrophotometric white standard

~330°C (Franců et al. 1999). Samples showing CAI 6 do not correspond to the higher thermal maturation indicated by the Rr and IC data. The CAI, Rr and IC data from the MSZ indicates similar burial temperature intervals (cf. Jones 1992), but due to the narrow spread, the CAI data seem to be much less sensitive to burial temperature changes than the vitrinite reflectance data with a large spread. When cross-correlated with vitrinite reflectance data (Fig. 4a), the CAI data show only a poor correlation ($R^2 = 0.336$). This is considered a result of a scarcity of the reflectance data available for low CAI values, and the fact that other influences than thermal alteration (dolomitization, activity of hydrothermal fluids, etc.) may have affected the conodont colour.

RGB representation of the conodont colour

The obtained range of the raw-data median intensities from 257 single conodonts of the MSZ ranging from CAI 3 to CAI 6 were 34 to 138 for the red component, 37 to 130 for the green component and 36 to 113 for the blue component. After absolute calibration, the range was 28 to 138 for the R component, 30 to 127 for the G component and 26 to 107 for the B component (Tab. 1). The highest intensities of the R, G and B components are typical for brown conodonts assigned to CAI 3 (R:109.33, G:90.67, B:66.44; see Tab. 1). The intensities gradually decrease towards higher CAI values. Brown to dark brown conodonts, assigned to CAI 3.5, have mean RGB values of 92.68

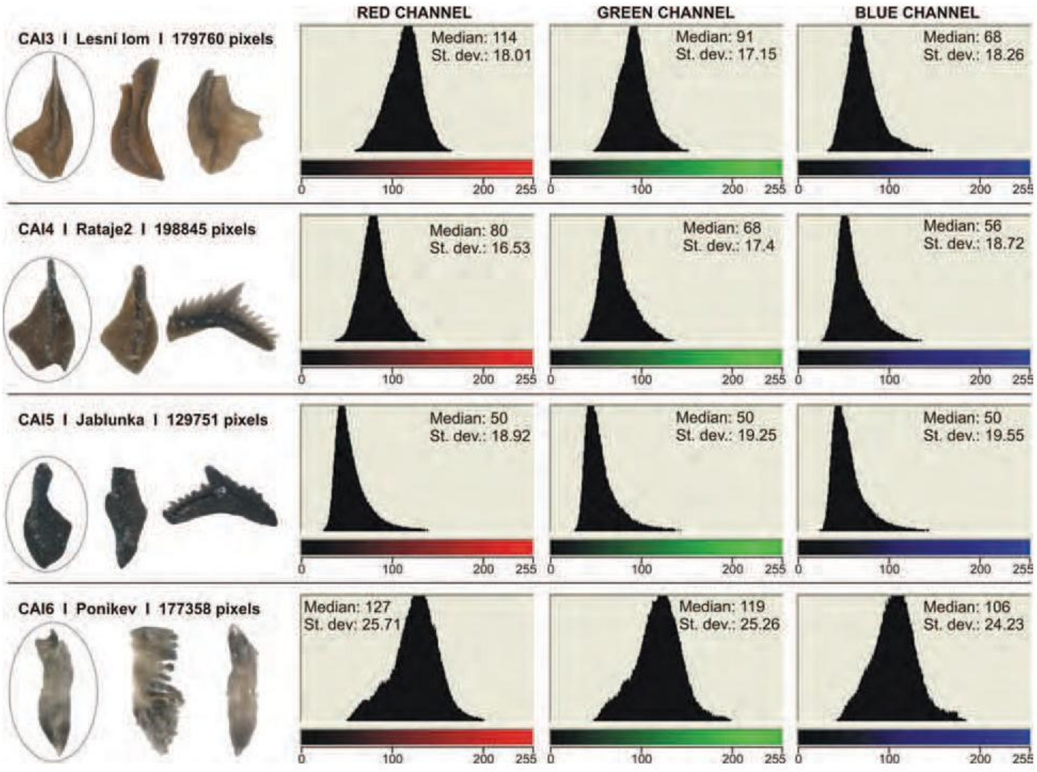

Fig. 5. Representative samples of CAI from MSZ and sample histograms of reflected light intensities (circled conodonts) in red, green and blue colour channel generated by Corel PhotoPaint 12.0 bitmap editor.

for R, 83.50 for G, 62.09 for B, and conodonts of CAI 4 have mean RGB values of 75.44 for R, 66.44 for G, and 51.94 for B. Black conodonts of CAI 5 have the lowest mean intensities of 51.16 for R, 58.33 for G, and 46.70 for B. The intensities of the RGB components then increase towards CAI 5.5 and CAI 6. The mean RGB values in grey to black-grey conodonts of CAI 5.5 are 69.13 for R, 77.17 for G, and 60.19 for B. The mean RGB values of grey conodonts of CAI 6 are 126 for R, 118 for G, and 110 for B.

Representative examples of conodonts corresponding to CAI 3 to CAI 6 are shown in Fig. 5. The samples corresponding to CAI 3 and CAI 6 show a relatively wide spread of intensities in all the three colour channels. The CAI 6 colour data are negatively skewed and show a tendency to bimodal (or polymodal) distribution, which is considered to reflect patchy whitening related to the release of organic substances from the conodont tissue at the passage from CAI 5 to CAI 6 (cf. MARSHALL et al. 2001). Sample histograms of conodont colour corresponding to CAI 4 and CAI 5 are typically narrow, unimodal and may be positively skewed, which is considered to reflect small lighter impurities on the generally dark conodont surface. The sample of the CAI 3 typically show much higher intensities in the red channel (median 114) than in the blue channel (median 68), but the difference between the red and blue intensity gradually decreases with the passage through to CAI 4 and CAI 5 to end up in the same, low median values in both the colour channels (Fig. 5). The histogram shapes are similar to those of HELSEN et al. (1995) obtained from polished conodont surfaces.

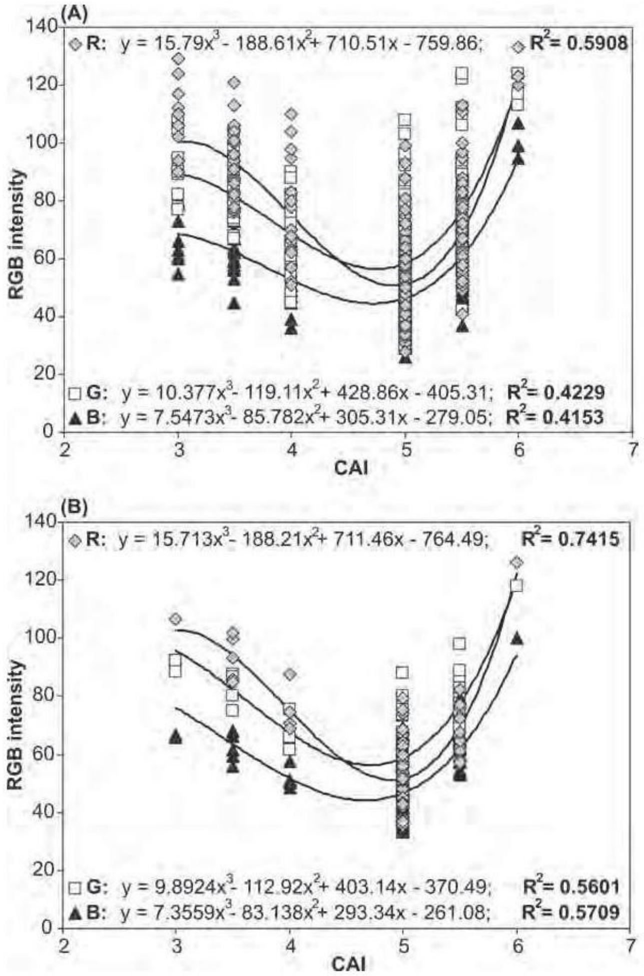

Fig. 6. Relationship between sample CAI and sample mean RGB intensities of reflected light from conodont surface. (**A**) Single conodont data, 257 measurements; (**B**) sample-averaged data, 68 measurements.

The patterns of RGB intensity decrease within the CAI 3 to CAI 5 interval followed by a rapid increase in the CAI 5 to CAI 6 interval (Fig. 6a) and are consistent with the results of Helsen et al. (1995) obtained from image analysis of polished conodont sections (their Fig. 5). When plotted against CAI, the calibrated RGB values show approximately cubic polynomic distribution in a scatter plot, with correlation coefficients for the R ($R^2 = 0.5908$), G ($R^2 = 0.4229$) and B ($R^2 = 0.4153$) component. For a better representation of the sample CAI, the single conodont RGB data was aggregated to average sample RGB (the mean value from RGB data from all conodonts in a sample). The averaged RGB data also show cubic polynomic distribution when plotted against CAI from 3 to 6, with even better correlation coefficients for the R ($R^2 = 0.7415$), G ($R^2 = 0.5601$) and B ($R^2 = 0.5709$) component (Fig. 6b). The better correlation is obviously achieved due to less scattered data, but this approach is consistent with the original methodology of the CAI measurement, which is usually measured from several conodonts per sample (cf. Deaton et al. 1996; Epstein et al. 1977). The RGB intensities seem to provide a good proxy of CAI, although there is a risk of confusion between CAI 4 and CAI 5.5, which, at a first glance, have similar RGB characteristics (Fig. 6a, b). The conodonts matured to CAI 4, however, show a tendency toward brown coloration

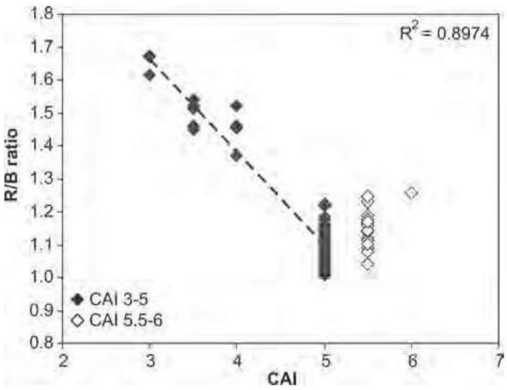

Fig. 7. Relationship between sample CAI and sample mean red to blue (R/B) intensity ratio. Regression line and correlation coefficient refer to CAI 3 to CAI 5 data only.

whereas those of CAI 5.5 are grey under visual inspection. In the RGB space, the brown colour in CAI 4 is represented by a shift towards the red colour component and higher values of R compared to G and B, as opposed to rather equilibrated R, G and B values in the greyscale corresponding to CAI 5.5. In the RGB colour space, represented by orthogonal RGB Cartesian coordinates, the grey colours are present in the main diagonal from black (R = G = B = 0) to white (R = G = B = 255) (VISCARRA ROSSEL et al. 2006, p. 322).

R/B colour ratio

Besides the total RGB intensity, the internal relationship between the red, green and blue channels should also be considered. In most samples, the mean intensity is highest in the red component, intermediate in the green and lowest in the blue component. This maximum variance can therefore be expressed as the R/B intensity ratio. The R/B ratio varies from 0.83 to 1.92 for calibrated, single conodont data (Tab. 1) and from 1.01 to 1.67 for calibrated, sample-averaged data. The R/B ratio was found to quickly decrease from CAI 3 (mean 1.65) through CAI 4 (mean 1.44) to CAI 5 (mean 1.09) and then remain approximately the same or slightly increase to CAI 5.5 (mean 1.15) and CAI 6 (mean 1.26) (Tab. 1, Fig. 7). The CAI: R/B ratio plots show a very good negative correlation (R^2 = 0.8974) with CAI within CAI 3 to CAI 5 interval. R/G and G/B ratios were also tested as possible proxies of CAI, but they show a lower correlation with CAI (R^2 = 0.6623 for R/G and 0.1050 for G/B, Tab. 2).

The R/B ratio of the whole conodont surface thus qualifies as a very good proxy of CAI in the interval from CAI 3 to CAI 5. The model of R/B ratio is very much consistent with the published data on conodont spectral reflectance (DEATON et al. 1996). This reflectance data obtained from the conodont surface indicates that the slope of the total reflectance curve within the 500 - 850 nm wavelength range is correlated with CAI. The monochromatic primary stimuli of the red, green and blue colours in the RGB system occur at 700, 546 and 436 nm, respectively, of the visible light spectrum (VISCARRA ROSSEL et al. 2006, p. 322). The high slope values of the reflectance curve therefore imply higher reflectance at the red end of the spectrum, higher values of R in the RGB system and lower reflectance in its violet end and lower B values. Low reflectance curve slope values are typical for conodonts of CAI 5, 5.5 and 6, which show similar values of reflectance in the red and violet end of the spectrum (DEATON et al. 1996, p. 1000), consistent with the R/B ratios approaching unity in the conodonts of CAI 5, 5.5 and 6 from the MSZ. The slope of a hypothetic linear reflectance curve located between the 700 and 436 nm wavelength stimuli for the R and B colour, respectively, was calculated from the calibrated RGB data from the MSZ. The slope values

Table 2. Linear correlation coefficients for data from CAI 3 to CAI 5 interval.

	R		G		B		R/B		R/G		G/B	
	R.D. *	C.D. **	R.D.	C.D.	R.D.	C.D.	R.D.	C.D.	R.D.	C.D.	R.D.	C.D.
CAI	0.6903	0.7022	0.3217	0.3786	0.1628	0.2968	**0.9141**	**0.8974**	0.7648	0.6623	0.5830	0.1050
Rr	0.0517	0.1469	0.0144	0.0021	0.0597	0.0278	0.3527	0.3339	0.5523	0.5697	0.0229	0.1029

* R.D.: Raw data

** C.D.: Data calibrated to spectrophotometric white standard

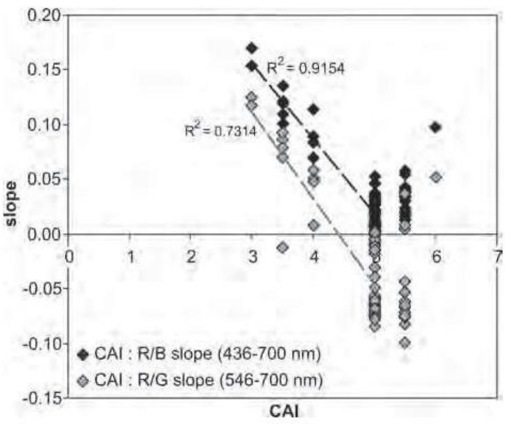

Fig. 8. Relationship between sample CAI and slope of hypothetical reflectance line calculated from RGB data from MSZ, converted to monochromatic reflectance stimuli at 700 (R), 546 (G) and 436 (B) nm wavelength. Regression lines and correlation coefficients refer to CAI 3 to CAI 5 data only. Note generally lower slope between R and G (higher wavelengths) than between R and B (lower wavelengths).

ranged from 0.0009 (CAI 5) to 0.1697 (CAI 3). The results show a very good negative linear correlation to exist between the slope and CAI within the interval from CAI 3 to CAI 5 ($R^2 = 0.9154$, 50 data points) (Fig. 8). We also calculated the slope for the R and G colour at the 700 and 546 nm wavelength, respectively, yielding a range from -0.10006 (CAI 5.5) to 0.1247 (CAI 3) and CAI to the slope correlation coefficient $R^2 = 0.7314$ for the CAI 3 to CAI 5 interval (Fig. 8). The absolute values of the slope calculated from RGB data differ from those obtained by Deaton et al. (1996), which, in our opinion, is caused by the different wavelength intervals used for the calculation, and general inconsistency between the RGB colour space model and the spectral reflectance data.

In our view, the intensities of the R, G and B colours in the RGB system and, in particular, the R/B ratio provide a good proxy of CAI. This relationship is clearly visible in the R:B scatter plot (Fig. 9), where samples of the same CAI values plot within distinct fields delimited by the absolute intensity of the R and B colour and the slope of the R/B ratio line. With increasing colour alteration, within the interval from CAI 3 to 5, the CAI is defined primarily by the R/B ratio, which decreases from ~1.6 to ~1.0. With further progression from CAI 5 to CAI 5.5 and 6, the R/B ratio remains approximately stable or slightly increases to ~1.2 to ~1.3. The absolute intensities of the R and B colours, however, increase to even higher values than those characteristic for CAI 3. Due to the thermal maturation limits of the study area, we were unable to investigate the RGB patterns for CAI 1-2 and CAI 6.5-8 values. From the published trends of the RGB intensities and the slope of spectral reflectance curves in the CAI 1-2 interval (Deaton et al. 1996; Helsen el at. 1995) it is envisaged that the total R, G and B intensities and the R/B ratio will further increase towards CAI 2 and CAI 1. For the CAI 6.5-8 interval with further shifts towards light grey, white and crystal clear colours (Rejebian et al. 1987), we can expect a similar trend as for the CAI 5 to CAI 6 interval that is, even increasing RGB intensities with the R/B ratio approaching unity. Further study is needed to cover the whole spectrum of CAI values.

The R/B ratio shows similar regional distribution patterns as the CAI and the vitrinite reflectance (Fig. 3). The R/B ratio data, however, from the MSZ are only poorly correlated to vitrinite reflectance data ($R^2 = 0.2555$, Fig. 4b). The distribution of the data points on the R/B: Rr scatter plot is similar to CAI: Rr plot (Fig. 4a). The poor correlation may be caused by the scarcity of the available vitrinite reflectance data and the fact that influences other than thermal maturation, including hydrothermal fluids, dolomitization, contact metamorphism and lithology of the host rock, may have affected the colour of the conodonts. The degree of dolomitization of the MSZ is generally low, with most dolomitization confined to conodont-barren Middle to Upper Devonian platform carbonates. Until now, no contact-metamorphosed sediments have been reported from the MSZ. However, most of the area was affected by Late Varsican thrust-and-fold tectonics associated with hydrothermal activity, which potentially led to significant conodont deformation and discoloration (Bábek & Novotný 1999; Slobodnik et al. 2006). This is supported by the colour alteration of most conodonts from the tectonically affected areas, which corresponds to CAI 5.5-6 but whose thermal alteration verified by VR values (Rr: 3.2 to 4.2%) corresponds only to CAI 5 (Fig. 4). It should be stressed that, compared to the semi quantitative CAI, the R/B ratio and the absolute RGB intensities only provide better, quantitative representation of conodont colour regardless on what factors it is influenced by. Further studies comprising large num-

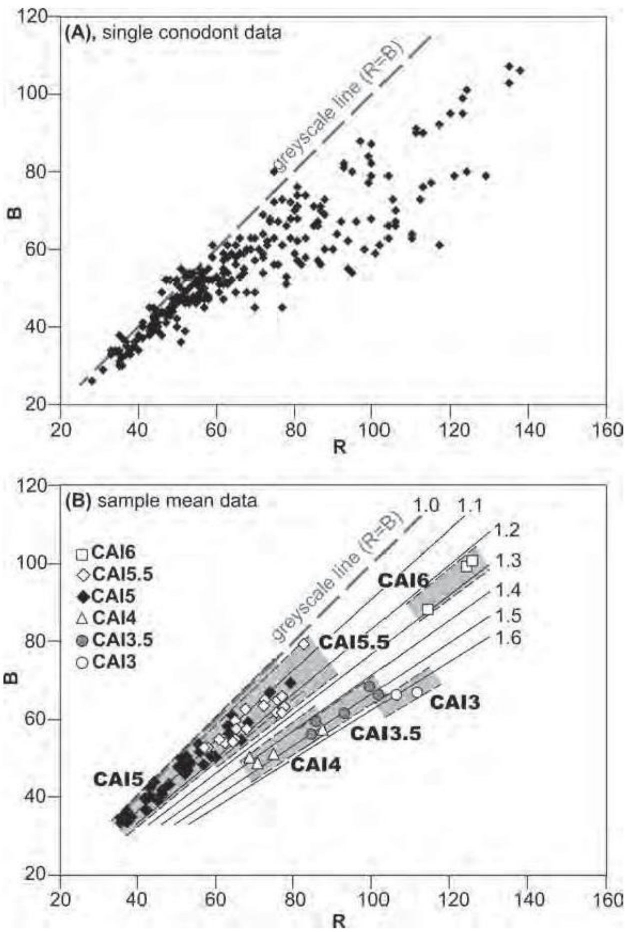

Fig. 9. (A) R/B scatter plot of calibrated single conodont and (B) sample-averaged data. Samples assigned to distinct CAI plot within distinct fields delimited by R/B ratio and absolute intensities of R and B colour compound.

bers of conodont colour and vitrinite reflectance data are needed in order to make this relationship clearer.

The use of calibrated versus non-calibrated RGB data

The difference between raw RGB data and those calibrated using the spectrophotometry measurement of the white standard is low. The basic statistical characteristics of the whole RGB data set as well as the data sets assigned to the individual CAI values, such as range, mean, median, mode, standard deviation and skewness, are very similar for both the raw and calibrated data (Tab. 1). For example, errors between the raw and calibrated data calculated from the arithmetic means of the CAI 3 to CAI 6 data sets range within 2.4 to 12.5% for R, 0.1 to 6.2% for G, 6.3 to 21.6% for B, and 4.0 to 7.3% for the R/B ratio. The error values are well within acceptable limits, especially for the R/B ratio. The calibrated R/B ratios, when correlated to CAI in the CAI 3 to CAI 5 interval, show approximately the same correlation coefficient ($R^2 = 0.8974$) as do the R/B ratios derived from raw data ($R^2 = 0.9141$), although the differences between correlation coefficients for the individual colours are relatively high (Tabs. 1, 2). Ratio indices are successfully used to emphasize the colour content of RGB data, as they effectively compensate for the brightness/illumination variation of the scene (LEVIN et al. 2005). Our results suggest that the use of the R/B ratio as a proxy of CAI is therefore beneficial even though data not standardized to spectroscopic calibration is used.

Conclusions

Quantification of conodont colour using a digital camera and the RGB colour space was demonstrated in order to provide a good representation of the conodont colour alteration index (CAI). The technique utilizes routine observation of conodonts in incident light under binocular microscope, is non-destructive and does not require high investment costs. The mean intensities of the R, G and B colours from single conodonts and from the sample average data decrease within CAI 3 to CAI 5 interval, and then quickly increase with the progression from CAI 5 to CAI 5.5 and CAI 6.

The R-to-B colour ratio proved the best indicator of CAI. The mean R/B ratio was found to decrease from CAI 3 (1.65) through CAI 4 (1.44) to CAI 5 (1.09) and then remain approximately stable or slightly increase to CAI 5.5 (mean 1.15) and CAI 6 (mean 1.26). The available material did not allow us to investigate the RGB intensities and the R/B ratio for CAI 1-2 and CAI 6.5-8. The R/B colour ratio is closely related to CAI ($R^2 = 0.8974$) within the interval from CAI 3 to CAI 5. The slope of the hypothetical reflectance curve calculated from the R and B intensity values also shows a very good correlation with CAI 3 to CAI 5 ($R^2 = 0.9154$). Both the R/B ratio and the reflectance curve slope are similar in concept to the CAI quantification method of Deaton et al. (1996) utilising spectral reflectance of conodonts. The concept of the R/B ratio is also closely related to the original definition of CAI (Epstein et al. 1977; Rejebian et al. 1987), because the shifts towards the red colour (high R/B ratio) are manifested by brown and yellow coloration in CAI < 5, whereas the balanced red, green and blue colours (R/B ratio ~1.0) are manifested by greyscale colours in the RGB colour space (CAI ≥ 5). Application of the RGB based image analysis method may prove useful for thermal alteration studies based on chitinozoans, graptolites, acritarchs and/or plant spores.

The CAI data and R/B data show very similar regional distribution patterns as the vitri-nite reflectance and illite crystallinity data in the Moravo-Silesian Zone. The relationship between the CAI and the vitrinite reflectance data for cross-correlated samples is, how-ever, weak ($R^2 = 0.336$ for CAI; $R^2 = 0.2555$ for R/B ratio). This is presumably influenced by the scarcity of data points and the additional effects of hydrothermal fluids and tectonic deformation on the conodont colour.

The use of the R/B ratio to describe conodont colour is useful even though non-calibrated data is used. This is caused by the fact that proportional colour values effectively compensate for the brightness / illumination variation of the photographed scene (Levin et al. 2005), emphasizing the colour content of RGB data.

Acknowledgements

This work was supported by the project INCHEMBIOL MSM0021622412 and the Czech Science Foundation (GA CR) project No. 205/03/0967. We would like to thank Prof. Vladimír Šucha and Dr. Peter Uhlík, Bratislava, Slovakia, for the XRD analyses. We gratefully acknowledge the helpful comments from journal reviewers Dr. Peter Königshof, Frankfurt/Main, and Dr. Mike Orchard, Vancouver, and the journal editor.

References

Bábek, O., Tomek, Č., Melichar, R., Kalvoda, J. & Otava, J. (2006): Structure of unmetamorphosed Variscan tectonic units of the southern Moravo-Silesian Massif: a review. – Neues Jahrbuch für Geologie und Paläontologie, Abhandlungen, **239**: 37-75.

Bábek, O. & Novotný, R. (1999): The Hnevotín limestone nestratotype locality revisited: A conodont biostratigraphy and carbonate microfacies approach, Moravia, Czech Republic. – Acta Universitatis Palackianae Olomucensis Facultas Rerum Naturalium – Geologica, **36**: 63-68.

Belka, Z. (1993): Thermal and burial history of the Cracow-Silesia region (southern Poland) assessed by conodont CAI analysis. – Tectonophysics, **227**: 161-190.

Belka, Z., Miaskiewicz, K. & Zydorowicz, K. (1987): The electron spin resonance technique in conodont studies: – In: Austin, R. L. (Ed.): Conodonts; investigative techniques and applications: 230-240; British Micropaleontological Society, Chichester (Ellis Horwood).

Briggs, D. E. G., Clarkson, E. N. K. & Aldridge, R. J. (1983): The conodont animal. – Lethaia, **16**: 1-14.

Bustin, R. M., Orchard, M. & Mastalerz, M. (1992): Petrology and preliminary organic geochemistry of conodonts: implications for analyses of organic maturation. – International Journal of Coal Geology, **21**: 261-282.

Cháb, J. (1986): Tectonics of the Moravo-Silesian part of the European upper Paleozoic orogeny; theory. – Věstník Ústředního Ústavu geologického, **61**: 113-119. (In Czech).

Chadima, M., Hrouda, F. & Melichar, R. (2006): Magnetic fabric study of the SE Rhenohercynian Zone (Bohemian Massif): Implications for dynamics of the Paleozoic accretionary wedge. – Tectonophysics, **418**: 93-109.

Chlupác, I. (1988): The Devonian of Czechoslovakia and its stratigraphical significance: – In: McMillan, N. J., Embry, A. F. & Glass, D. J. (Eds.): Devonian of the World. – Proceedings of the Second International Symposium on the Devonian System. Memoir of the Canadian Society of Petroleum Geologists, **14**: 481-497.

Čížek, P., Tomek, C. (1991): Large-Scale thin-skinned tectonics in the eastern boundary of the Bohemian Massif. – Tectonics, **10**: 273-286.

Dallmeyer, R. D., Neubauer, F. & Höck, V. (1992): 40Ar/39Ar mineral age controls on the chronology of late Paleozoic tectonothermal activity in the southeastern Bohemian Massif, Austria (Moldanubian and Moravo-Silesian Zones). – Tectonophysics, **202**: 135-153.

Dean, C., Warner, T. A. & McGraw, J. B. (2000): Suitability of the DCS460c colour digital camera for quantitative remote sensing analysis of vegetation. – ISPRS Journal of Photogrammetry and Remote Sensing, **55**: 105-118.

Deaton, B. C., Nestell, M. & Balsam, W. L. (1996): Spectral reflectance of conodonts: A step toward quantitative color alteration and thermal maturity indexes. – American Association of Petroleum Geologists Bulletin, **80**: 999-1007.

Dudek, A. (1980): Crystalline basement of the Outer Western Carpathians in Moravia: The Brunovistulicum. – Rozpravy Československé Akademie Věd, **90**: 1-85. (In Czech).

Dvořák, J. (1989): Anchimetamorphism in the Variscan tectogene in Central Europe – its relationship to tectogenesis. – Věstník Ústředního Ústavu geologického, **64**: 17-30. (In Czech).

Dvořák, J. & Paproth, E. (1969): Über die Position und die Tektogenese des Rhenoherzynikums und des Sudetikums in den mitteleuropäischen Varisziden. – Neues Jahrbuch für Geologie und Paläontologie, Monatshefte, **1969**: 65-88.

Dvořák, J. & Wolf, M. (1979): Thermal metamorphism in the Moravian Paleozoic (Sudeticum, CSSR). – Neues Jahrbuch für Geologie und Paläontologie, Monatshefte, **1979**: 596-607.

Ellison, S. (1944): The composition of conodonts. – Journal of Paleontology, **18**: 133-140.

Epstein, A. G., Epstein, J. B. & Harris, L. D. (1977): Conodont colour alteration – an index to organic metamorphism. – United States Geological Survey Professional Paper, **995**: 1-27.

Franců, J., Müller, P., Šucha, V. & Ztkalíková, V. (1990): Organic matter and clay minerals as indicators of thermal history in the Transcarpathian depression (East Slovakia Neogene Basin) and the Vienna Basin. – Geologický Zborník, Geologica Carpathica, **41**: 535-546.

Franců, E., Franců, J. & Kalvoda, J. (1999): Illite crystallinity and vitrinite reflectance in Paleozoic siliciclastics in the SE Bohemian Massif as evidence of thermal history. – Geologica Carpathica, **50**: 365-372.

Franců, E., Franců, J., Kalvoda, J., Polcheau, H. S. & Otava, J. (2002): Burial and uplift history of the Palaeozoic Flysch in the Variscan foreland basin (SE Bohemian Massif, Czech Republic). – EGS Stephen Mueller Special Publication Series, **1**: 259-278.

Franke, W. (1995): Rhenohercynian foldbelt; Autochthon and nonmetamorphic nappe units; Stratigraphy. – In: Dallmeyer, R. D., Franke, W. & Weber, K. (Eds.): Pre-Permian geology of Central and Eastern Europe: 33-49; Berlin (Springer).

Fritz, H. & Neubauer, F. (1995): Moravo-Silesian Zone; Autochthon; Structure. – In: Dallmeyer, R. D., Franke, W. & Weber, K. (Eds.): Pre-Permian geology of Central and Eastern Europe: 490-494; Berlin (Springer).

Garcia-Lopez, S., Brime, C., Bastida, F. & Sarmiento, G. N. (1997): Simultaneous use of thermal indicators to analyse the transition from diagenesis to metamorphism: an example from the Variscan Belt of northwest Spain. – Geological Magazine, **134**: 323-334.

Gawlick, H.-J., Krystyn, L. & Lein, R. (1994): Conodont colour alteration indices: Palaeotemperatures and metamorphism in the Northern Calcareous Alps – a general view. – Geologische Rundschau, **83**: 660-664.

Goddijn, L. M. & White, M. (2006): Using a digital camera for water quality measurements in Galway Bay. – Estuarine and Coastal Shelf Science, **66**: 429-436.

Götte, T. & Richter, D. K. (2005): Cathodoluminescence typisation of Quartz in sand sediments from Wangerooge Island. – Senckenbergiana Maritima, **35**: 121-131.

– (2006): Cathodoluminescence characterization of quartz particles in mature arenites. – Sedimentology, **53**: 1347-1359.

Hartley, A. J. & Otava, J. (2001): Sediment provenance and dispersal in a deep marine foreland basin: The Lower Carboniferous Culm Basin, Czech Republic. – Journal of the Geological Society (London), **158**: 137-150.

Helsen, S. (1995): Burial history of Palaeozoic strata in Belgium as revealed by conodont colour alteration data and thickness distributions. – Geologische Rundschau, **84**: 738-747.

Helsen, S. & Königshof, P. (1994): Conodont thermal alteration patterns in Palaeozoic rocks from Belgium, northern France and western Germany. – Geological Magazine, **131**: 369-386.

Helsen, S., David, P. & Fermont, W. J. J. (1995): Calibration of conodont color alteration using color image analysis. – Journal of Geology, **103**: 257-267.

Hladil, J. (1994): Moravian Middle and Late Devonian buildups: evolution in time and space with respect to the Laurussian shelf. – Courier Forschungsinstitut Senckenberg, **172**: 111-125.

Jackson, M. L. (1975): Soil chemical analysis – advanced course. – 930 pp; Madison (Parallel Press).

Jones, G. L. (1990): Irish Carboniferous conodonts record maturation levels and the influence of tectonicsm, igneous activity and mineralization. – Terra Nova, **4**: 238-244.

Kalvoda, J., Leichmann, J., Bábek, O. & Melichar, R. (2003): Brunovistulian terrane (Central Europe) and Istanbul Zone (NW Turkey): Late Proterozoic and Paleozoic tectonostratigraphic development and paleogeography. – Geologica Carpathica, **54**: 1-14.

Kalvoda, J., Bábek, O., Fatka, O., Leichmann, J., Melcichar, R., Nehyba, S. & Spacek, P. (2007): Brunovistulian Terrane (Bohemian Massif, Central Europe) from Late Proterozoic to Late Palaeozoic – a review. – International Journal of Earth Sciences, DOI: 10.1007/ s00531-007-0183-1.

Kashiyama, Y., Fastovsky, D. E., Rutherford, S., King, J. & Montellano, M. (2004): Genesis of a locality of exceptional fossil preservation: Paleoenvironments of Tepexi de Rodriguez (mid-Cretaceous, Puebla, Mexico). – Cretaceous Research, **25**: 153-177.

Königshof, P. (1991): Conodont colour alteration adjacent to a granitic intrusion, Harz mountains. – Neues Jahrbuch für Geologie und Palaöntologie, Monatshefte, **1991**: 84-90.

– (1992): Der Farbänderungsindex von Conodonten (CAI) in paläozoischen Gesteinen (Mitteldevon bis Unterkarbon) des Rheinischen Schiefergebirges – eine Ergänzung zur Vitrinitreflexion. – Courier Forschungsinstitut Senckenberg, **146**: 1-115.

– (2003): Conodont deformation patterns and textural alteration in Paleozoic conodonts: examples from Germany and France. – Senckenbergiana lethaea, **83**: 149-156.

Kovács, S., Rálisch-Felgenhauer, E. & Bóna, J. (2006): Conodont colour alteration related to a half-graben structure: an example from the Mesozoic of the Mecsek and Villány Hills area (Tisza Megaunit, Southern Hungary). – Geologica Carpathica, **57**: 257-268.

Krejčí, Z. (1991) Upper Devonian conodont assemblages in Moravia. 100 pp; unpublished Ph. D. thesis (Masaryk University Brno, Czech Republic) (In Czech).

Kübler, B. (1967): La crystallinité de l´illite et les zones tout a fait superieures du metamorphisme. Etages tectoniques (Colloque de Neuchatel, 18-21 avril 1966). – Neuchatel University, Institute of Geology, Neuchatel: 105-122; Neuchatel (Institute of Geology).

Kumpera, O. & Martinec, P. (1995): The development of the Carboniferous accretionary wedge in the Moravian-Silesian Paleozoic Basin. – Journal of the Czech Geological Society, **40**: 47-60.

Legall, F. D., Barnes, C. R. & Macqueen, R. W. (1981): Thermal maturation, burial history and hotspot development, Paleozoic strata of southern Ontario – Quebec, from conodont and acritarch color alteration studies. – Bulletin of Canadian Petroleum Geologists, **29**: 492-439.

Levin, N., Ben-Dor, E. & Singer, A. (2005): A digital camera as a tool to measure colour indices and related properties of sandy soils in semi-arid environments. – International Journal of Remote Sensing, **26**: 5475-5492.

Lindström, M. (1964): Conodonts. – 196 pp; Amsterdam (Elsevier).

Marshall, C. P., Rose, H. R., Lee, G. S. H., Mar, G. L. & Wilson, M. A. (1999): Structure of organic matter in conodonts with different colour alteration indices. – Organic Geochemistry, **30**: 1339-1352.

Marshall, C. P., Mar, G. L., Nicoll, R. S. & Wilson, M. A. (2001): Organic geochemistry of artificially matured conodonts. – Organic Geochemistry, **30**: 1055-1071.

Mastalerz, M., Bustin, R. M., Orchard, M. & Forster, P. J. L. (1992): Fluorescence of conodonts: implications for organic maturation analysis. – Organic Geochemistry, **18**: 93-101.

Mathieu, R., Pouget, M., Cervelle, B. & Escadafal, R. (1998): Relationship between satellite-based radiometric indices simulated using laboratory reflectance data and typic soil colour of an arid environment. – Remote Sensing and the Environment, **66**: 17-28.

Nicoll, R. S. (1981): Conodont colour alteration adjacent to a volcanic plug, Canning Basin, Western Australia. – BMR Journal of Australian Geology and Geophysics, **6**: 265-267.

Nicoll, R. S. & Gorter, J. D. (1984): Interpretation of additional conodont colour alteration data and the thermal maturation and geothermal history of the Canning Basin, Western Australia. – In: Purcell, P. G. (Ed.): The Canning Basin, W. A. – Geological Society of Australia: 411-425.

Nöth, S. & Richter, K. (1992): Infrared spectroscopy of Triassic conodonts: a new tool for assessing conodont diagenesis. – Terra Nova, **4**: 668-675.

Nowlan, G. S. & Barnes, C. R. (1987): Application of conodont colour alteration indices to regional and economic geology. – In: Austin, R. L. (Ed.): Conodonts; investigative techniques and applications. – British Micropaleontological Society: 188-202.

Obara, B. (2005): Application of the image analysis method to the detection of transcrystalline microcracks observed in microscope images of dolomite and granite structures. – Archives of Mining Sciences, Archiwum Gornictwa, **50**: 537-551.

Pearson, M. J. & Small, J. S. (1988): Illite-smectite diagenesis and paleotemperatures in northern North Sea Quaternary to Mesozoic shale sequences. – Clay Minerals, **23**: 109-132.

Pollastro, R. M. (1993): Considerations and applications of the illite-smectite geothermometer in hydrocarbon-bearing rocks of Miocene to Mississippian age. – Clays and Clay Minerals, **41**: 119-133.

Rajlich, P. (1990): Strain and tectonic styles related to Variscan transpression and transtension in the Moravo-Silesian Culmian basin, Bohemian Massif, Czechoslovakia. – Tectonophysics, **174**: 351-367.

Rejebian, V. A., Harris, A. G. & Huebner, J. S. (1987): Conodont colour and textural alteration: an index to regional metamorphism, contact metamorphism and hydrothermal alteration. – Geological Society of America Bulletin, **99**: 471-497.

Robert, P. (1988): Organic metamorphism and geothermal history: microscopic study of organic matter and thermal evolution of sedimentary basins. – 311 pp; Dordrecht (ELF-Aquitaine and D. Reidl).

Schulmann, K., Ledru, P., Autran, A., Melka, R., Lardeaux, J. M., Urban, M. & Lobkowicz, M. (1991): Evolution of nappes in the Eastern Margin of the Bohemian Massif: a kinematic interpretation. – Geologische Rundschau, **80**: 73-92.

Simons, F. J., Verhelst, F. & Swennen, R. (1997): Quantitative characterization of coal by means of microfocal X-ray computed microtomography (CMT) and color image analysis (CIA). – International Journal of Coal Geology, **34**: 69-88.uchez

Slobodnik, M., Muchez, Ph., Král J., Keppens, E. (2006): Record of fluid circulation and Variscan tectonothermal events in Upper Palaeozoic limestones of the Moravian Karst, Czech Republic. – Geological Magazine, **143**: 491-508.

Środoń, J. (1995): Reconstruction of maximum paleotemperatures at present erosional surface of the Upper Silesia Basin, based on the composition of illite-smectite in shales. – Studia Geologica Polonica, **108**: 9-20.

Sudar, M. & Kovács, S. (2006): Metamorphosed and ductilely deformed conodonts from Triassic limestones situated beneath ophiolite complexes: Kopaonik Mountain (Serbia) and Bükk Mountains (NE Hungary) – a preliminary comparison. – Geologica Carpathica, **57**: 157-176.

Sweet, T. W. C. (1988): The conodonta: morphology, taxonomy, paleoecology and evolutionary history of a long-extinct animal phyllum. – 212 pp.; Oxford Monographs on Geology and Geophysics; Oxford (Clarendon Press).

Teichmüller, M., Taylor, G. H. & Littke, R. (1998): The nature of organic matter – macerals and associated minerals. – In: Taylor, G. H., Teichmüller, M., Davis, A., Diessel, C. F. K., Littke, R. & Robert, P. (Eds.): Organic petrology. – 175-274; Berlin (Gebrüder Bornträger).

Torrent, J., Schwertmann, U., Fechter, H. & Alferez, F. (1983): Quantitative relationship between soil colour and hematite content. – Soil Science, **136**: 354-358.

Underwood, M. B., Laughland, M. M. & Kang, S. M. (1993): A comparison among organic and inorganic indicators of diagenesis and low-temperature metamorphism, Tertiary Shimanoto belt, Shikoku, Japan. – Geological Society of America, Special Paper, **273**: 45-61.

van de Laar, J. G. M. & David, P. (1998): Determination of spore colour alteration by means of colour image analysis. – In: Boyd, W. E. & Hall, V. A. (Eds.): New frontiers and applications in palynology. – Reviews of Palaeobotany and Palynology, **103**: 41-44.

Van Geet, M., Swennen, R. & David, P. (2001): Quantitative coal characterisation by means of microfocus X-ray computer tomography, colour image analysis and back-scattered scanning electron microscopy. – International Journal of Coal Geology, **46**: 11-25.

Van Huyssteen, C. W., le Roux, P. A. L. & Hensley, M. (2006): Interpretation of digital soil photographs using spatial analysis: I. Methodology. – South-African Journal of Plant and Soil, **23**: 7-13.

Viscarra-Rossel, R. A., Minasny, B., Roudier, P. & McBratney, A. B. (2006): Colour space models for soil science. – Geoderma, **133**: 320-337.

Warr, L. N. & Rice, A. H. N. (1994): Interlaboratory standardization and calibration of clay mineral crystallinity and crystallite size data. – Journal of Metamorphic Geology, **12**: 141-152.

Webster, M. A. & Mollon, J. D. (1997): Adaptation and the colour statistics of natural images. – Vision Research, **37**: 3283-3298.

Wiederer, U., Königshof, P., Feist, R., Franke, W. & Doublier, M. (2002): Low-grade metamorphism in the Montagne Noire (S-France): Conodont Alteration Index (CAI) in Palaeozoic carbonates and implications for the exhumation of a hot metamorphic core complex. – Schweizerische Mineralogische und Petrographische Mitteilungen, **82**: 393-407.

Ziegler, P. A. (1988): Laurussia – the Old Red Continent. – In: McMillan, N. J., Embry, A. F. & Glass, D. J. (Eds.): Devonian of the World. – Proceedings of the Second International Symposium on the Devonian System, Memoir of Canadian Society of Petroleum Geologists, **14**: 15-48; Calgary.

Manuscript received: September 24, 2007.
Revised version received: January 28, 2008.
Accepted by the Munich editors: February 08, 2008.

Addresses of the authors:

Assoc. Prof. Ondřej Bábek, Institute of Geological Sciences, Masaryk University, Kotlářská 2, 61137 Brno, Czech Republic, and Department of Geology, Palacký University, Tř. Svobody 26, 77146 Olomouc, Czech Republic.
Tel.: ++420-549-49-4756, Fax: ++420-541-211-214,
e-mail: babek@sci.muni.cz

Prof. Dr. Jiří Kalvoda, Institute of Geological Sciences, Masaryk University, Kotlářská 2, 611 37 Brno, Czech Republic.

Eva Franců Ph. D., Czech Geological Survey, Leitnerova 22, 65869 Brno, Czech Republic.

Prof. Dr. Franz Neubauer, Fachbereich Geographie, Geologie und Mineralogie, Universität Salzburg, Hellbrunnerstrase 34, A-5020 Salzburg.

Příloha 7

Špaček P., Kalvoda J., Franců E., Melichar R. (2001) Variation of deformation mechanisms within the progressive-retrogressive mylonitization cycle of limestones: Brunovistulian sedimentary cover (The Variscan orogeny of the souteastern Bohemian Massif). – Geologica Carpathica. 52, 5, 263-275.

GEOLOGICA CARPATHICA, 52, 5, BRATISLAVA, OCTOBER 2001
263–275

VARIATION OF DEFORMATION MECHANISMS WITHIN THE PROGRESSIVE-RETROGRESSIVE MYLONITIZATION CYCLE OF LIMESTONES: BRUNOVISTULIAN SEDIMENTARY COVER (THE VARISCAN OROGENY OF THE SOUTHEASTERN BOHEMIAN MASSIF)

PETR ŠPAČEK[1*], JIŘÍ KALVODA[1], EVA FRANCŮ[2] and ROSTISLAV MELICHAR[1]

[1]Department of Geology and Paleontology, Masaryk University, Kotlářská 2, 61137 Brno, Czech Republic; *vajgl@sci.muni.cz
[2]Czech Geological Survey, Leitnerova 22, 60200 Brno, Czech Republic

(Manuscript received December 7, 2000; accepted in revised form June 13, 2001)

Abstract: This study deals with the calcite mylonites of the Brunovistulian sedimentary cover developed in the frontal thrust area of the Moravian nappe units. The inhomogeneous structure of sedimentary protoliths allowed the analysis of the contrasting behaviour of calcite in matrix and porphyroclasts and the interpretation of microfabric evolution during deformation under low temperature conditions. Several stages of microfabric evolution characterizing progressive as well as retrogressive deformation are distinguished. Generally, the progressive phase of mylonitization is characterized by grain growth in the matrix and the grain size reduction of the porphyroclasts leading to a stress-induced equilibration of grain size. During the initial deformational stages the calcitic porphyroclasts deformed brittlely and the strain was strongly localized into the ductile matrix. With continuing evolution the onset of the dynamic recrystallization of porphyroclasts occurred, which obviously preceded a significant grain growth in the matrix. With rising temperature during deformation, grain growth predominated after grain size homogenization was finished. The lack of effective dynamic recovery along the stages of the progressive low temperature phase of deformation is discussed. Core-and-mantle structures which are characteristic of the initial stages of progressive deformation carry microfabric features which document the dominance of grain boundary bulging and/or nucleation recrystallization. Formation of subgrains within the porphyroclasts is only a rarely observed feature which probably could not lead to significant grain size reduction. The higher effectiveness of nucleation and recrystallization via migration of grain boundaries compared to subgrain rotation mechanism could be a consequence of high fluid content. Large-scale thrusting within the Brunovistulian basement is shown by the juxtaposition of calcitic and quartzitic mylonites with deformational microstructures reflecting pronounced contrasts of deformational styles. Fully plastic vs. fully brittle behaviour of quartz represents the most pronounced indicator of different deformational conditions between the lower unit of the Svratka Dome and the other domains of the Brunovistulian basement. In the lower tectonic unit of the Svratka Dome the microtructures of calcite mylonites indicate stresses which were about four times lower than in the other two parts of the Brunovistulicum. Despite the deformational contrasts, the values of illite crystallinity measured do not show any spatial gradient which could be linked with the distribution of the contrasting deformational microstructures. The paleothermometric data which are available to date suggest maximum paleotemperatures of 250–300 °C for all three studied domains of the Brunovistulian basement and it is suggested that the difference of Variscan peak temperatures between the three compared domains of the basement was not higher than several dozens of °C. The observed deformational contrasts can thus be explained by an abrupt change of deformation mechanisms in both calcite and quartz at temperatures around 300 °C.

Key words: Eastern Variscan front, Brunovistulicum, inhomogeneous limestones, mylonitization, dynamic recrystallization, microstructures.

Introduction

Microfabric studies of strained homogeneous calcite aggregates have been described relatively frequently, both in nature (e.g. Dietrich & Song 1984; Heitzmann 1987; Burkhard 1990; Covey-Crump & Rutter 1989; Busch & Van der Pluijm 1995) and experiments (e.g. Schmid et al. 1977, 1980, 1987; Rutter 1974; Rutter et al. 1994; Walker et al. 1990). However, research into the mylonitization of inhomogeneous carbonates, which are the most abundant in nature, is rather sparse. Therefore we attempted to give a detailed study of the development of such inhomogeneous limestones in low-temperature (LT) deformational stages.

In the southeastern part of the Bohemian Massif, the tectonic contact of the allochthonous domain of Variscan orogen (the Moldanubian and Moravian nappe units) and the per-autochthonous pre-Variscan basement (the Brunovistulicum) is exposed (Matte et al. 1990). The Devonian and Lower Carboniferous carbonate-clastic sedimentary cover of the Brunovistulicum is strongly sheared in the thrust area under anchimetamorphic and very low-grade metamorphic conditions (Schulmann et al. 1991). Calcite mylonites from this highly deformed sedimentary sequence were studied along orogen-perpendicular profiles, which cross-cut the foot-wall of the Moravian nappe units and proximal parts of their foreland.

As the microstructure of sedimentary protoliths was generally inhomogeneous, the mylonites served as a suitable object for the comparison of the deformational behaviour of the matrix vs. the porphyroclasts within the given spectra of LT deformational conditions. The analysis of deformational microfabric allowed the interpretation of its evolution during the progressive transformation of limestones into mylonites and

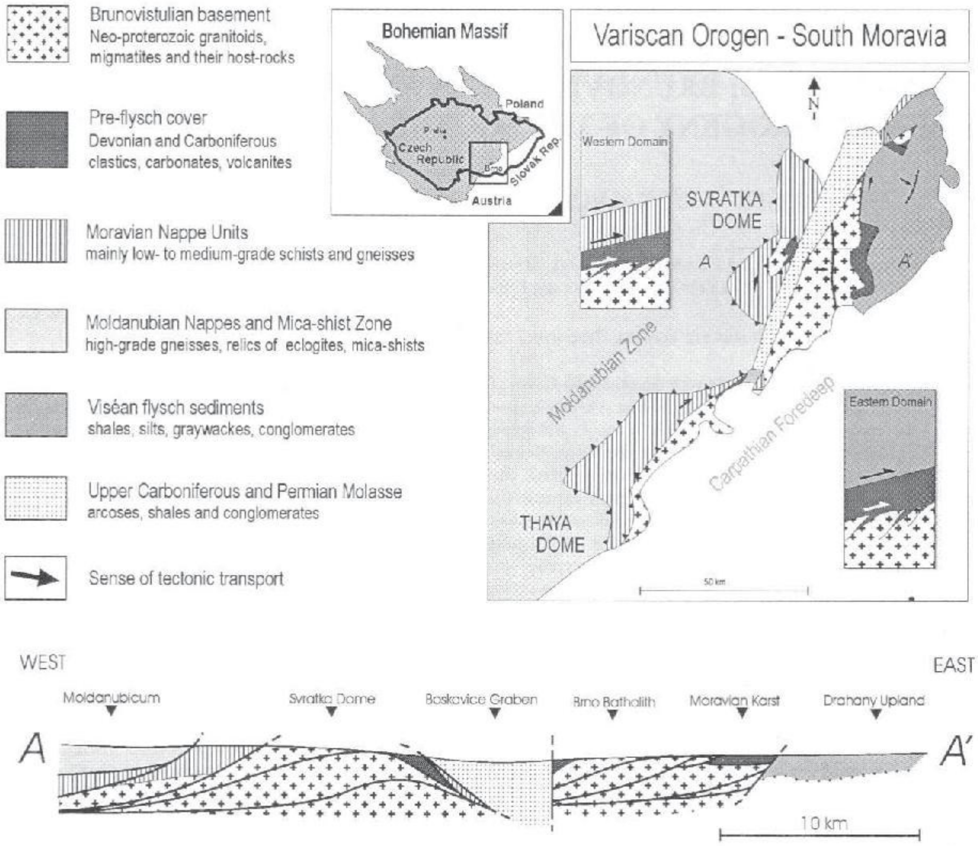

Fig. 1. Schematic map of the area studied and a conceptual profile through the main units of the collision zone.

during retrogressive degradation under decreasing temperatures. On the basis of the observed deformational microstructures it was possible to make a comparison between three domains of the Brunovistulicum in terms of dominant deformational regimes in calcite aggregates.

Geological settings

The Variscan assembly of the allochthonous units and the Brunovistulian basement within the eastern Bohemian Massif are related to the Devonian-Late Carboniferous dextral oblique collision of the Armorican terranes (Moldanubian and Saxothuringian Terrane) with the Brunovistulian Terrane — outer part of Laurussia (Matte et al. 1990; Kalvoda 1995, 2001). Three main units have been distinguished in the collisional zone: Moldanubicum (Suess 1912) with high grade Variscan metamorphism (Suess 1912, 1926; Cháb & Suk 1977), Moravian Zone (Suess 1912) with medium grade Variscan metamorphism (Suess 1912, 1926; Štípská & Schulmann 1995) and Brunovistulicum (Dudek 1980), in which the Variscan metamorphism is low-grade and occurs only in a close contact with the overlying tectonic units (Schulmann et al. 1991; Franců et al. 1999). According to some authors the nappe units of the Moravian Zone were derived from the highest parts of the imbricated Brunovistulian basement (e.g. Frasl 1983; Fritz & Neubauer 1993; Štípská & Schulmann 1995), as indicated mainly by similar radiometric ages of the Brunovistulian granitoids and sheared orthogneiss bodies of the Moravian nappes (van Bremen et al. 1982; Morauf & Jäger 1982).

The structure of the southern part of the collisional zone is well exposed in two incomplete tectonic windows: the Thaya Dome in the south and the Svratka Dome in the north (Fig. 1). A similar lithotectonic zonation has developed in both of them, as described, for example, by Schulmann et al. (1991, 1994) and Fritz & Neubauer (1993):

1 (bottom). Granitoids, metagranitoids and migmatites of the Brunovistulian Cadomian basement with their metasedimentary host rocks and Paleozoic sedimentary cover (Dudek 1980; Finger et al. 1989, 1995; Bosák 1980; Batík & Skoček 1981),

2. Moravian nappe units composed mostly of metasediments, pre-Variscan Bíteš orthogneiss and its metasedimentary host rocks (e.g. Schulmann et al. 1991),

3. Mica-schist zone with metasediments, amphibolites and orthogneiss bodies (Suess 1908),

4 (top). Moldanubian nappes with high-grade granulites, paragneisses, migmatites and relics of eclogites (Matějovská 1975; Jenček & Dudek 1971; Vrána et al. 1995).

Characteristic features of this sequence are inverted Barrovian metamorphic zoning, metamorphic foliation parallel with lithological boundaries and N to NE trending lineations subparallel to the axes of tight folds (Schulmann et al. 1991). In the upper units, E-W stretching lineations are common (Fritz & Neubauer 1993).

In the foreland of the Moravian and Moldanubian nappe units, the Brunovistulian basement is exposed in the Brno batholith and has been verified through many boreholes beneath the Paleozoic cover on the eastern slopes of the Bohemian Massif. In this eastern part of the collisional zone different lithotectonic zonation is developed:

1 (bottom). Cadomian granitoids of the Brunovistulicum with its metamorphosed host-rocks and Devonian-Lower Carboniferous pre-flysh sedimentary cover (e.g. Dudek 1980; Leichmann 1996; Hanžl & Melichar 1997; Finger et al. 2000; Dvořák 1995),

2. several km thick flysh sequence of Viséan age (Dvořák 1973; Rajlich 1990; Čížek & Tomek 1991).

The Viséan flysh sequence is strongly folded (e.g. Rajlich 1990) and Čížek & Tomek (1991) proved the existence of large-scale east-vergent thrusts imbricating both the flysh sequence and the Brunovistulian basement with its tectonized pre-flysh sedimentary cover. In this part of the orogen, the ductile deformation of the rocks is non-penetrative and thick zones of mylonitization occur only in close proximity to the Moravian nappes. Stretching lineation and associated kinematic indicators show top-to-the-NNE shearing (e.g. Bábek & Janoška 1997). In general, the degree of Variscan deformation and metamorphism is very low and further decreases to the east where Paleozoic sequences rest autochthonously on the Brunovistulian basement.

Within the Brunovistulian basement, two parts with different development during the Variscan orogenesis can thus be distinguished. The first is in the westernmost part with the Moravian nappes in the hanging wall and the second in the eastern part is covered by Viséan flysch nappes. The boundary of these two sections is covered by Westphalian-Autunian sediments of the Boskovice Graben. The exact meaning of the tectonic contact of units beneath the sedimentary infill of the graben is still not well understood.

For the tectonic evolution of the collisional zone the forward thrust propagation model was suggested by Schulmann et al. (1991), Fritz & Neubauer (1993) and Fritz et al. (1996). The thrusting began under HT conditions and continued during gradual cooling to LT conditions. The deformation regimes were changing continuously from top-to-the-N shear through top-to-the-E shear to E-W coaxial extension. The simultaneous activity of non-coaxial shearing in the lower units and the coaxial extension in the upper units has been assumed. This model explains the complex structural evolution and systematic decrease of isotopic ages of metamorphism from the uppermost tectonic to the lowest tectonic levels.

Analytical methods

The transformations of the primary structures of inhomogeneous carbonate sediments into a deformation fabric of carbonate mylonites were analysed. Dozens of samples were collected in both parts of the basement — from the foot-wall of Moravian nappe unit in the western part and from the foreland of the Moravian nappes in the eastern part of the basement (Figs. 1 and 6). The key steps in the analytical procedure, which should have provided data for the interpretation of deformation mechanisms and conditions, were:

1) the description and quantification of the optical deformation microstructures and lattice preferred orientations (LPOs);

2) the correlation of the microfabric with the temperatures of deformation.

Microstructures

Thin and ultra-thin (< 10 μm) sections were prepared from oriented samples cut parallel to XZ and ZY planes of finite strain and were examined under optical and SEM microscopes. Grain-shape analyses of the coarse-grained domains were carried out using a polarizing microscope–digital camera–computer arrangement. Images of the thin sections were captured in two or three different polarizer/analyzer positions in order to identify the maximum number of grain-boundaries (Burkhard 1990). The two or three images obtained were projected on a horizontally oriented screen in a slideshow mode and the grain boundary networks were then produced by manually outlining the grains onto transparent foil. For the SEM morphological analyses of the fine-grained aggregates, polished XZ and XY slabs of the selected samples were etched in a 1% hydrochloric acid solution for 10 seconds and coated with gold-film. Secondary electron photomicrographs were obtained from 30–50° tilted samples after tilt-correction.

Quantitative processing of the grain boundary networks was carried out using *ImageTool 2.0* software. In this paper, only the grain size parameter is used for the characterization of microstructures. The grain size (D) is defined as the diameter of a circle with the same area as the grain being measured, that is

$D = \mathrm{sqrt}(4 \times \text{grain area}/\pi)$.

Such a definition of grain size gives the most realistic values which are independent of grain shape. For stress calculations we used the Rutter paleopizometer (Rutter 1995) calculated for the grain boundary migration (GBM) recrystallization mechanism:

$\log \sigma = 2.22 + 0.37 \log d - 0.30 (\log d)^2$,

where σ is the differential stress and d is the grain size, and the median values of grain size were used as suggested by Ranalli (1984).

The content of dolomite and other secondary phases was examined with an electron microprobe in selected samples in order to assess their potential influence on the deformational processes.

The stretch (S = original length/finite length of the deformed object) was measured at pressure fringes, deformed peloids and ooids, boudinaged clasts and other strain-markers in order to demonstrate the strain magnitude of the distinguished microstructural types.

Lattice Preferred Orientations (LPO)

If the evolution of the mylonites was to be reconstructed, it was necessary to determine the mechanisms operative during the deformation. Therefore the LPO were measured. Their intensity is related to the magnitude of the intracrystalline deformational mechanisms and their ratio to the other mechanisms of deformation (e.g. Casey & McGrew 1999). X-ray diffraction texture analysis was used for the comparison of the fabric geometries and intensities of the distinguished microstructural types. The measurements were carried out in the laboratory of of Military Technical Institute of Protection in Brno, using a Siemens D-500 texture goniometer. Textures were measured using reflection geometry on thin slabs of the rock which had been cut parallel to the macroscopic foliation (XY plane). Filtered $CuK\alpha_{1+2}$ rays were used and maximum tilt was 80°. The data were further tilt-corrected, using a tilt scan on a powder sample and processed with *popLA* software (Kallend et al. 1991).

Preliminary results have shown that the LPO patterns of all samples are very similar and that it was not necessary to calculate orientation distribution functions. The LPO intensities of the samples measured were compared in the incomplete ($\Phi = 0$–$80°$) pole figures of (018) planes (*e*-poles).

Additionally, crystallographic orientations of the coarse grains were measured in several thin sections using optical polarizing microscope with a U-stage. This "semi-domainal" LPO analysis allowed the LPO of the porphyroclasts and that of the whole samples to be measured separately.

Paleothermometry

The illite crystallinity of clay fractions from shales associated with the mylonitized limestones was measured in order to estimate the maximum reached paleotemperatures. Clay-size material was separated from 8 rock samples after removing the cements such as carbonates, organic matter and iron oxides (Jackson 1975). Clay fraction < 2 µm was collected by centrifugation for determination of illite crystallinity. Oriented slides were analysed both air-dry and after vapour glycolation using X-ray diffractometer Philips PW 1830 (generator) and PW 3020 (goniometer) with 0.02° step from 2 to 50 °2Q. Illite crystallinity index (IC) was measured as peak width in $\Delta\,2\Theta$ at half maximum (PWHM) of the (001) basal reflection of illite (Kübler 1967) using background stripping and peak-fitting. The results were calibrated to international standards (Warr & Rice 1994).

Microstructures and their interpretations

The results of microfabric analyses allow several basic groups of (proto-)mylonites with similar features to be distinguished. In the following discussion, these groups of microstructures will be identified with the letters A–E. The interpreted mechanisms of deformation are shown in a schematic diagram in Fig. 3.

Microstructures A. **Weakly deformed protoliths**

Rocks of this type retain their original inhomogeneous structure and the sedimentary attributes of their protoliths. The most typical composition includes a micritic matrix (d ~ 4 µm) and a wide-ranging assemblage of various parts of fossil organisms, which together with boudinaged veins and other constituents composed of sparite, will be referred to as "porphyroclasts".

Strain markers, for example, the calcite-filled pressure fringes around quartz clasts and deformed peloids, indicate that matrix suffered substantial strains with minimum stretch values up to S = 4.5. In spite of this high degree of strain, the micrite in the matrix does not exhibit substantial microstructural changes.

The coarse-grained porphyroclasts are not substantially internally strained and figure as rigid bodies passively flowing in a ductile environment. Locally, book-shelf fracturing, microboudinage, twinning and only slight undulose extinction within the coarse grains can be observed in the samples with higher finite strains or with the load-bearing framework of coarse grains. The distribution of the *c*-axes measured in porphyroclasts is random to strong with a single maximum near the pole to the foliation, depending on the strain magnitude (not shown in the figure, in strongly deformed types the *c*-axes distribution is very similar to that in Fig. 2d). Bulk (whole sample) X-ray LPO is much weaker, increasing with the higher volume of the clasts (Fig. 2a).

Fabric development of this microstructure took place in a semi-ductile regime. Strain partitioning due to grain size inhomogeneity, with preferential localization into fine-grained matrix, is characteristic. For the matrix, the interpreted dominant mechanism of the deformation is grain boundary sliding (GBS) with accommodation by diffusion transfer at grain boundaries. The main arguments for GBS are negligible microstructural changes in spite of high strains and the weak LPO. The high water content in the limestones during deformation is indicated by frequent pressure fringes and stylolites in the micrite. It is very likely that the fluids have played an important role in the diffusive matter-interchange between the grains and could thus have caused a substantial weakening of the matrix. During the deformation, the strength of coarse grained porphyroclasts was much higher than that of the fine-grained matrix (compare Fig. 7a). Local high stress conditions resulted in brittle fracturing, twinning and incipient intracrystalline slip within the porphyroclasts.

Microstructures B. **Protomylonites**

A mantled porphyroclasts/matrix structure is characteristic for this group (Fig. 7b). Core-and-mantle structure grains are free of clay minerals and in most cases can be easily distinguished from the matrix which appears darker under transmitted light. The bulging of the grain boundaries and the formation of oval-shape recrystallized grains (Fig. 7c) takes place preferentially at twin lamellae and boundaries of clasts.

This type of microstructure is interpreted as a result of grain boundary bulging (GBB) or nucleation recrystallization (Drury & Urai 1990; Mercier et al. 1977). High aspect ratios of the porphyroclasts were generated mainly by the superposition of GBM on the twin lamellae (Fig. 7b). Within the matrix, non-distinctive grain growth up to d < 10 µm also indicates the incipient activity of grain boundary migration. The formation of subgrains and rotation recrystallization are less pronounced and do not lead to significant reduction in grain size. Despite the occurrence of mantled porphyroclasts, which one is tempted to interpret as the product of subgrain rotation, the lack of recovery in the grains suggests the dominance of the GBB

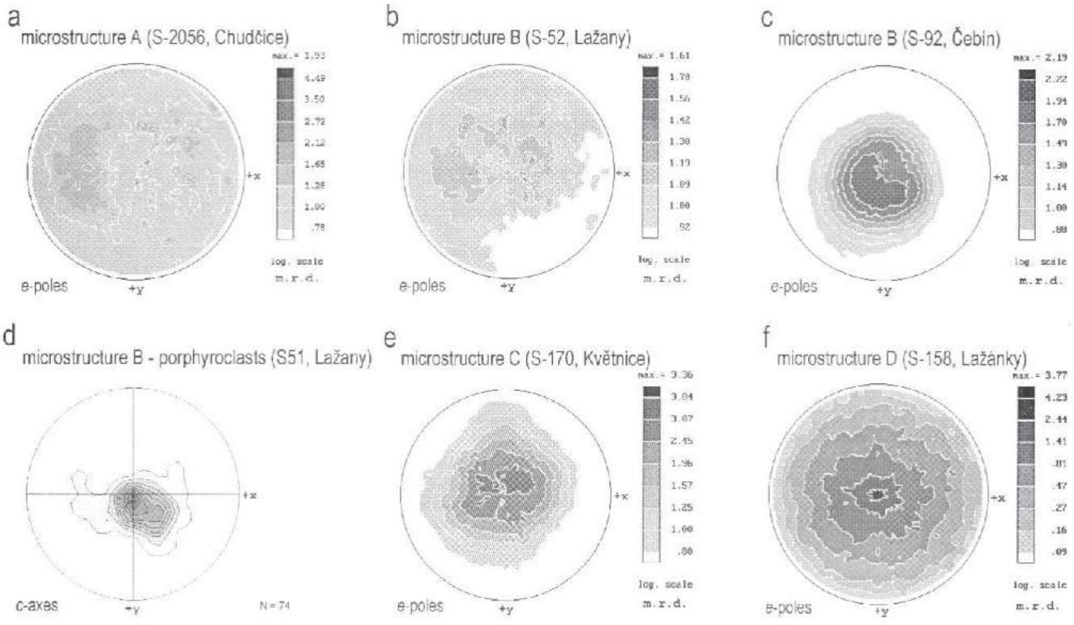

Fig. 2. Sample pole figures of *e*-planes and *c*-axes of the main microstructural types. All data are projected to the plane of foliation in equal-area projection, lower hemisphere. **a–c, e, f** — X-ray diffraction data in incomplete pole figures; intensities are expressed as multiples of a random distribution (m.r.d.). **d** — *c*-axes distribution of porphyroclasts in microstructure B. Contours at 0, 2, 4, 6, 8, 10, 12, 14, 16 and 18 %. Notice the strong LPO of porphyroclasts vs. weak LPO of whole sample in the microstructural types B and the increasing intensity of the preferred orientation from Type B to Type D with relatively constant distribution geometry. The patchy pattern of the distribution is due to the high content of large grains in the samples.

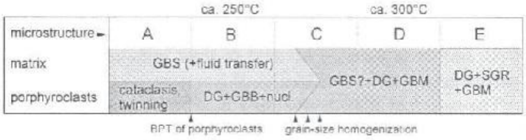

Fig. 3. The interpreted dominant deformational mechanisms operative in the distinguished stages of mylonitized limestones. **GBS** — grain boundary sliding, **GBB** — grain boundary bulging, **DG** — dislocation glide, **GBM** — grain boundary migration, **SGR** — subgrain rotation recrystallization, **nucl.** — nucleation, **BPT** — brittle-plastic transition.

and/or nucleation mechanisms of recrystallization. The recrystallized grains produced by grain size reduction of the porphyroclasts are usually larger in size than those resulting from the grain growth of the matrix micrite (Table 1). This discrepancy can be explained by the low rate of GBM in the matrix grains as a result of their low level of internal strain and/or the inhibitory effect of the secondary phase (Olgaard & Evans 1988). The LPO of these types of protomylonites have features similar to that of the microstructures A: a strong single maximum of the *c*-axes close to the pole of foliation in the porphyroclasts, which is weakened in the LPO of the whole sample (Fig. 2b,c,d). The activity of GBS is likely to have persisted in both the matrix and the domains of recrystallized grains as indicated by the lack of microstructural change in spite of strong deformation of the fine-grained domains. Boudinaged bioclasts indicate minimum stretch values of S = 6.1.

Microstructures C. Mylonites

These types of rocks are composed of a relatively coarse-grained matrix (d = 20–50 μm) with relict porphyroclasts. Pressure fringes indicate minimum stretch values of S = 6.0. Grain aspect ratios vary between 1.5 and 4. All the grains of the matrix and the porphyroclasts are optically strain free, grain boundaries are almost straight, slightly curved or bulbous. Twin lamellae are rare, straight and were probably produced during cooling due to high thermoelastic anisotropy of calcite (Rosenholtz & Smith 1949). The LPO is similar both for matrix and porphyroclasts, showing single maximum of *e*-poles (and *c*-axes respectively) close to the pole of foliation (Fig. 2e). Because the grains lack undulose extinction and a subgrain microstructure and the grain boundaries are frequently bulbous, we attribute the finite microstructure to GBM-dominant recrystallization. Nevertheless, twinning and/or dislocation glide are also likely to have played a substantial role during earlier phases of the deformation as indicated by high aspect ratios and straight boundaries of the grains and the enhanced intensity of LPO.

Locally, sharply terminated prolate lens-shaped domains are developed in these types of mylonites, representing strained stems of *Amphipora* sp. These domains are composed of rela-

Table 1: Grain size values and calculated paleostresses of selected typical samples of the calcite mylonites studied. In some domains, stresses were not calculated for the reasons expressed by abbreviations: ***sp*** — high content of secondary phase (possible inhibition of grain growth), ***nu*** — not well understood mechanisms of origin (inhomogeneous tectonofacies with ambivalent characteristics), ***ss*** — non-recrystallized primary sedimentary structures, ***crm*** — combination of recrystallization mechanisms.

tectonic domain	microstructure	sample no., locality	microstructural domain (and responsive deformation phase)	d (μm, median)	$\sigma_{diff.}$ (MPa)
eastern	B	s88b, Čebín	matrix	4.0	ss
eastern	B	s88b, Čebín	recrystallized grain mantles (peak metamorphosis)	6.2	211
eastern	B	s90-1, Čebín	matrix	5.0	ss
eastern	B	s90-1, Čebín	recrystallized grain mantles (peak metamorphosis)	8.2	203
eastern	B	s51a, Lažany	matrix	5.41	ss
eastern	B	s51a, Lažany	recrystallized grain mantles (peak metamorphosis)	6.7	209
eastern	B	s188, Šebetov	recrystallized grain mantles (peak metamorphosis)	8.0	204
western	B	s45-1, Kadov	matrix	4.3	ss
western	B	s45-1, Kadov	recrystallized grain mantles (peak metamorphosis)	7.2	207
western	C	s170, Květnice	fine grained domains	12.3	nu
western	C	s170, Květnice	coarse grained domains	26.9	nu
western	C	s 239, Vohančice	fine grained domains	19.6	nu
western	C	s 239, Vohančice	coarse grained domains	27.3	nu
western	D	s166-1, Dranč	coarse grained domains (peak metamorphosis)	100.5	57
western	D	s171, Lažánky	fine grained domains	30.6	sp
western	D	s171, Lažánky	coarse grained domains (peak metamorphosis)	115.6	51
western	D	s158, Lažánky	coarse grained domains (peak metamorphosis)	89.4	63
western	D	s151, Dřínová	coarse grained domains (peak metamorphosis)	102.4	56
western	D	s157, Vohančice	coarse grained domains (peak metamorphosis)	111.5	52
western	E	s157, Vohančice	fine grained domains (incipient retrogression)	38.9	crm
western	E	s157, Vohančice	fine grained domains (advanced retrogression)	24.4	crm

tively coarse grained calcite aggregates of equant, strain free grains with slightly curved boundaries.

Microstructures D. Coarse grained marbles

In the most mature mylonites mesoscopic indicators (sheath folds, boudinaged clusters of dolomite) suggest stretch values of S > 10. In these types characteristic homogeneous domains are developed with a uniform grain size which varies with the volume of the dispersed phyllosilicates and dolomite (Table 1). Porphyroclasts composed of calcite are absent. In the domains with a small amount of secondary phases, the grain size usually reaches 100–120 μm. All grains are strain free, having slightly curved to lobate boundaries. Grain aspect ratios are usually > 2.5 and occasionally domains with equant coarse grains with grain boundaries meeting in 100–140° triple junctions can be observed (Fig. 7d). The *c*-axes distribution pattern shows a strong single maximum close to the pole of foliation (Fig. 2f). Rare twin lamellae are straight, and were probably produced during cooling. The microstructural features of these types suggest the dominance of GBM recrystallization mechanism. However, strong LPO indicates substantial activity of intracrystalline deformation during the evolution of these types, whose microstructures could have been overprinted in the latest phases of the deformation.

Microstructures E. Retrogressively deformed marbles

In some areas, grain size reduction of the coarse grains occurs within D types and narrow shear zones are developed affecting coarse-grained aggregates of microstructure D (Table 1). The old grains are polygonized into subgrains and newly formed grains usually have a crystallographic orientation very close to that of their host grains (Fig. 7e). As the grain boundaries of the recrystallized grains are interpenetrating and bulbous, we suggest that the grain size reduction is an effect of the combination of both subgrain rotation and GBM mechanisms. These structures are attributed to the onset of retrogressive deformation during incipient cooling. Further low temperature deformation of some domains generated strong twinning and undulose extinction of the coarse grains.

Paleothermometry

Illite crystallinity was measured in clay fractions of eight samples from both the Svratka and Thaya Domes and western margin of the Brno batholith. Two samples were excluded from further processing because of their high content of expandable smectite and chlorite.

The values of illite crystallinity index (IC) range from 0.20 to 0.35° Δ2Θ (Table 2) and indicate higher part of very low-grade metamorphic (VLGM) conditions with probable maximum paleotemperatures of 250–320 °C (calibration after Frey & Robinson 2000). The thermal alteration is more advanced than in most Paleozoic rocks of the Drahany Upland which show mainly lower VLGM conditions (Franců et al. 1999). The results of IC thermometry are consistent with the data of Bosák (1984) who analysed the degree of kerogen graphitization in dark carbonate rocks of the lower units of the Svratka Dome and of the western margin of the Brno batholith. He concluded that in most samples from the Svratka Dome the maximum temperature did not exceed 300 °C and that the grade of thermal alteration of organic matter was considerably lower in the carbonates of the Brno batholith's western margin. Similar conclusions were made recently by Ulrich (2000) who analysed the carbon and oxygen isotopic composition of six carbonate samples from two localities in the lowermost unit of the Svratka Dome. Using the graphite-calcite thermometer and calibration of Covey-Crump & Rutter (1989) he stated that the maximum temperatures in the graphite-rich marbles did not exceed 300 °C for a longer period of time. In the limestones of the Brno batholith's western margin paleotemperatures of 250–300 °C are indicated by the degree of conodont

Table 2: Illite crystallinity values of clay fractions from shales associated with the mylonitized limestones. **BB** — Brno batholith's western margin, **TD** — lower tectonic unit of the Thaya Dome, **SD** — lower tectonic unit of the Svratka Dome. (*) — associated tectonofacies are marked with capital letters in parentheses.

tectonic domain*	lithology	locality	IC (Δ°2Θ)
BB (A)	clayey limestone	Újezd u B. (s168)	0.30
BB (A)	shale	Újezd u B. (s168b)	0.28
BB (B)	clayey limestone	Šebetov (s111)	0.25
BB (A)	shale	Chudčice (s161)	0.20
TD (B)	shale	Skalice (s221)	0.35
SD (D)	shale	Lažánky (s237)	0.24

alteration. The black colour of the conodonts without the tones of brown corresponds to conodont colour alteration index (CAI) 5–5.5 (see Frey & Robinson 2000 for calibration).

Indirectly, and with limited reliability, the available paleothermometric data which are summarized in Table 3 can be supported by the features of deformation microstructures observed in quartz. In metamorphosed basement crystalline rocks and Devonian conglomerates and sandstones of the lower tectonic unit of the Svratka Dome, quartz aggregates carry clusters of recrystallized quartz grains with a similar *c*-axis orientation and intensely sutured grain boundaries. Well-developed low-angle boundaries and subgrains inside relic old grains are commonly found (Fig. 7g). This fabric is indicative of deformation by dislocation creep with recovery, subgrain rotation recrystallization and grain boundary migration being operative. The features of the microstructure thus correspond to the fully plastic deformation regime 3 of Hirth & Tullis (1992). After Stöckhert et al. (1999), the steady-state medium stress dislocation creep of quartz in the fully plastic regime can only be effective at temperatures above the closure temperature for K-Ar and Rb-Sr systems of biotite, that is above ca. 310±30 °C. In contrast, in the eastern tectonic domain, quartz is brittlely deformed, lacking any traces of intracrystalline slip (Fig. 7h). We consider similar pressure of fluids during the deformation of the quartz aggregates in both units. It seems to be a reasonable assumption that in the eastern part of the Brunovistulian basement (external part of the orogen) the brittle quartz was not deformed at higher strain rates than the plastic quartz in the lower tectonic units of the Svratka Dome (more internal part of the orogen). Assuming this, the observed deformational microstructures of quartz indicate that in the eastern part of the Brunovistulian basement (Brno batholith's western margin), the deformation was taking place under temperatures which were probably lower than 310±30 °C.

The lack of significant IC differences between the compared domains of the Brunovistulian basement (Table 3) suggests that the metamorphic transformation of smectite into illite reached similar stages in the studied rocks of the Brno batholith's western margin, the Thaya Dome and the Svratka Dome and that the paleotemperature differences are below the detection limit of the IC paleothermometer.

Considering potential errors of the paleothermometers and the variation of the IC values measured, it can be stated that the maximum paleotemperatures under which the studied rocks were deformed probably lie between 250 and 300 °C (Table 3). As was discussed above, the deformational features of both quartz and calcite indicate that in the Brno batholith and the lower unit of the Thaya Dome the maximum paleotemperatures were somewhat lower than in the lower unit of the Svratka Dome. However, the paleothermometric data constrain the maximum difference of Variscan peak temperatures between the three compared domains of the basement to several dozens of °C only (see Table 3).

The development of mylonitic stages

The sequence of microstructures A–E which has been distinguished above can be seen as a succession of frozen-in stages within the process of the deformational and metamorphic transformation of sediments. Several facts justify such an opinion: the analogous lithostratigraphic position of calcite mylonites, their overlapping biostratigraphic ranges and the mutual transitions of microstructural stages. A schematic diagram of the model is presented in Fig. 4. It is necessary to stress the fact that unquestionable primary sedimentary markers — fossil organisms — are common within the microstructures A, B and C. Microprobe analyses revealed a calcitic composition of the fossils. This is the main argument for interpreting the A–D sequence as a product of progressive mylonitization under increasing metamorphic conditions. During the retrogressive deformation phases, the fine-grained matrix of Type C was probably reworked again, but a significant change in the microstructure did not occur. The Type C microstructures never acquired the features of D types during its

Table 3: Table of paleothermometric data of the studied area which are collected from the available literature.

Brno batholith's western margin	Lower tect. unit of the Thaya Dome	Lower tect. unit of the Svratka Dome
	graphite/calcite thermometer (Ulrich 2001 with calibration after Covey-Crump & Rutter 1989)	
–	–	max. 300 °C
	CAI (Špaček 2001, calibration after Frey & Robinson 1999)	
>250 °C	–	–
	graphitization of kerogen (Bosák 1984)	
<300 °C	<300 °C	max. 300 °C
	illite crystallinity (this work, calibration after Frey & Robinson 1999)	
250–320 °C	250–320 °C	250–320 °C
	dynamic recrystallization of calcite (this work, after Burkhard 1990)	
min. 250 °C	min. 250 °C	>250 °C
	plastic deformation of quartz (this work, after Stöckhert et al. 1999)	
–	–	>310±30 °C

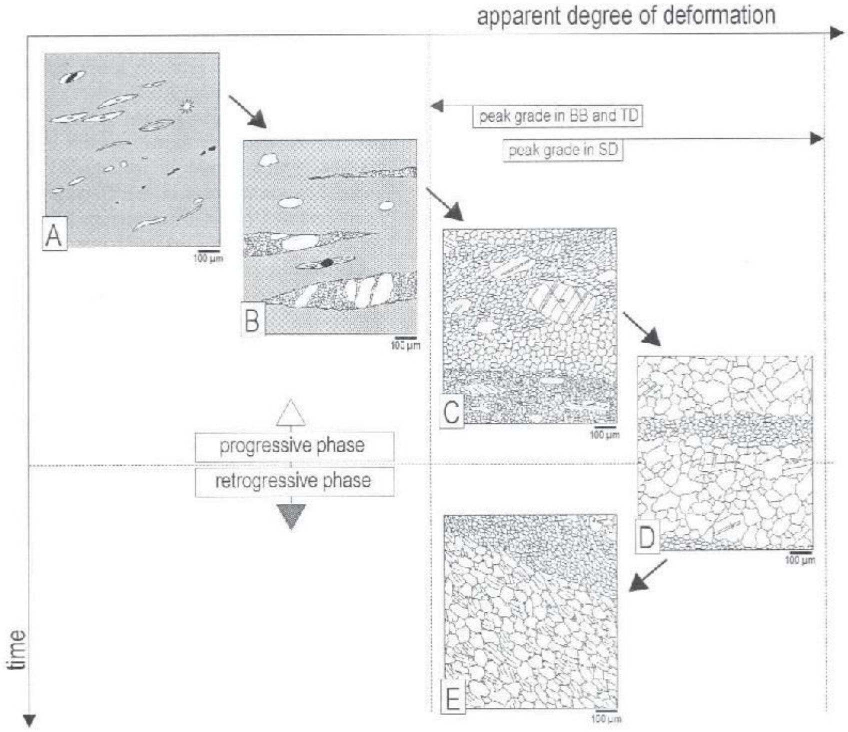

Fig. 4. Schematic diagram of microfabric development in mylonitized sequence of limestones. Notice the different peak grades reached in the lower tectonic unit of the Svratka Dome and the other two domains of the Brunovistulian basement. Objects in diagrams: **black** — quartz, **gray** — micrite and microsparite, **white** — coarse-grained calcite. **BB** — Brno batholith's western margin, **TD** — lower tectonic unit of the Thaya Dome, **SD** — lower tectonic unit of the Svratka Dome.

evolution. It was never fully homogenized and primary sedimentary structures were not completely destroyed. Thus, only the phase during which the microstructures E were produced is interpreted as retrogressive. Generally, the progressive phase of mylonitization is characterized by the grain growth of the matrix and a grain size reduction of the clasts leading to a stress-determined equilibrium of the grain size. With rising temperature during deformation, the homogenization of grain size was finished and grain growth predominated. In retrogressive phase, grain size reduction occurred due to a decreasing temperature and increasing stress.

Mechanisms of recrystallization

One of the most surprising features one can observe in the mylonitized sequence of carbonates studied is the dominance of GBM and the lack of effective dynamic recovery within the microstructures of the progressive low temperature phase of deformation.

Recovery represents the process of ordering the lattice defects, originated during intracrystalline slip, into subgrain boundaries which leads to a decrease in the internal strain energy of the crystal. When dislocations are continuously added to subgrain boundaries, the misorientation of the subgrains increases and new grains are formed. This process of new grains formation is referred to as subgrain rotation recrystallization (SGR) and produces diagnostic core-and-mantle structures with (sub-)grains increasingly misoriented towards the external parts of mantle (Guillopé & Poirier 1979; Lloyd & Freeman 1994). If the temperature is high enough to enable ordering of the lattice defects, continuous recovery-accommodated dislocation creep can operate. However, when the temperature is too low, recovery cannot keep pace with the tangling of the dislocations during intracrystalline slip, newly formed dislocations cannot move and strain hardening of the lattice occurs (e.g. White 1977).

In our study, small (d~8 µm) recrystallized grains of the mantled porphyroclasts in high stress mylonites B do not show any optical filiation to the host grains and their shape indicates the activity of GBB and/or nucleation (Fig. 7b,c). Although ultra-thin sections were used for the observation of microstructures, the formation of small-sized subgrains within the coarse grains was found only sporadically.

We therefore explain the recrystallization of the clasts in microstructures B as the product of a GBB-dominant process. Our observations lead us to the conclusion that during the progressive, low temperature deformation of the limestones studied, SGR was not capable of reducing the coarse grains into a steady-state size. Recovery and SGR produced only relatively large (sub-)grains which must have been further reduced by more effective GBB.

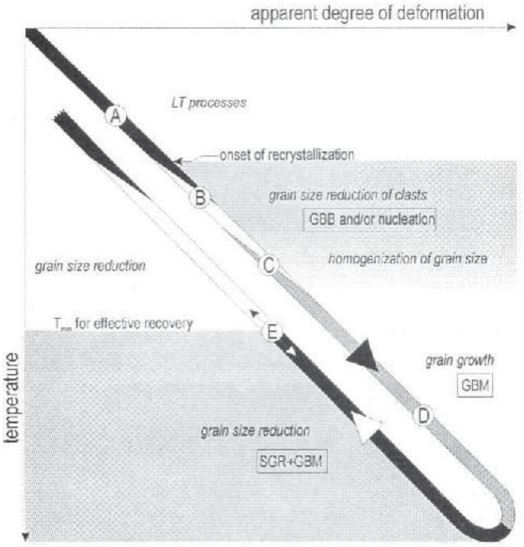

Fig. 5. The suggested model of recrystallization mechanisms in a complete deformation path of mylonitized limestones. Individual microstructures are marked with capital letters A–E. See text for explanations.

A suggested model of recrystallization development is shown in the Fig. 5. According to Lloyd & Freeman (1994), the velocity of grain boundary migration processes is determined by the relative crystallographic characteristics of adjacent grains, the driving forces, temperature and the structure of the boundary. Driving forces include mainly lattice defects, elastic energy and grain-boundary energy, and always lead to a decrease in internal strain energy. In our case, as the SGR did not lead to sufficient grain size reduction, each increment of continuing deformation raised the internal strain of the large grains and could accelerate the grain boundary bulging. Hippertt & Egydio-Silva (1996) presented arguments for the activity of solution-reprecipitation process during the deformation of quartz which can be concurrent with solid state recrystallization. Thus the high content of water in the system, which is indicated by frequent markers of solution transfer, probably also significantly increased the GBB or nucleation rate (compare also with Tullis & Yund 1982). The facilitating of grain boundary migration resulting from a high water content would explain the contradiction of our model to observations of some other authors who suggest that SGR is more effective than GBB under lower temperatures (Schmid et al. 1987). The recrystallization mechanisms of calcite in LT conditions could be analogous to those of quartz, in which grain boundary migration-dominant structures have even been described for dry samples (Hirth & Tullis 1992).

Deformational contrasts and the imbrication of the Brunovistulicum

It has been demonstrated by many authors that inverse proportionality between stress and recrystallized grain size exists (e.g. Twiss 1977; Kohlstedt & Weathers 1980). Thus, under a constant strain rate, the increase in recrystallized grain size is due to a decrease in material strength. Analogously, grain size distribution within a mylonitized sequence can be viewed as the result of metamorphic grade (i.e. temperature) variation. We therefore attempted to assess the differences between the deformation grade of the two domains of the deformed Brunovistulian basement. The most effective and reliable method of relative paleostress estimation seems to be the comparative measurement of grain size in the peak grade microstructures of individual tectonic domains. Uniform recrystallized grain size within broad domains justifies the presumption of steady state creep (e.g. Twiss 1977; Michibayaschi 1993). Facies with small-scale grain size variations were not taken into account in the paleostress calculations. It was assumed that the coarsest recrystallized grain size within the defined groups of microstructures represents the peak metamorphic conditions. In many coarse grained domains of facies D, the lack of anneal-

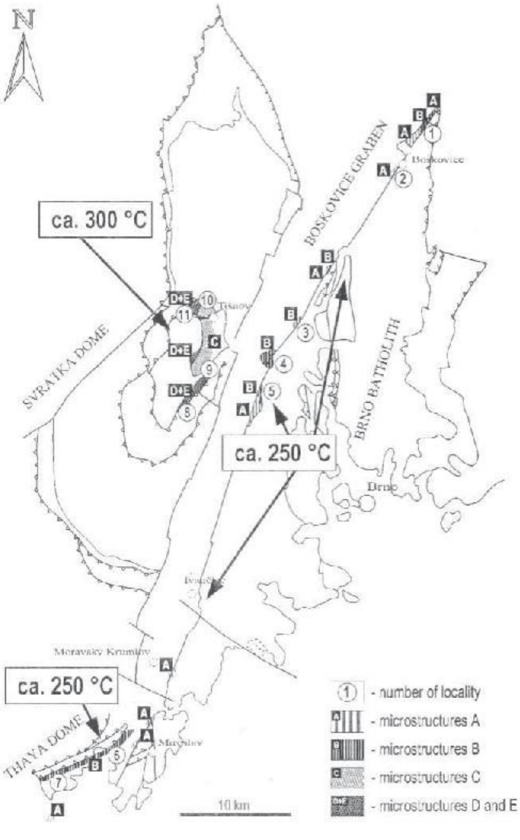

Fig. 6. Simplified sketch of the studied area showing the distribution of distinguished microstructural types. Circles with numbers indicate sampled localities which are referred to in the tables and figures. **1** — Šebetov (s111), **2** — Újezd u Boskovic (s168, s168b), **3** — Lažany (s51a), **4** — Čebín (s88b, s90-1), **5** — Chudčice (s2056, s161), **6** — Kadov (s45-1), **7** — Skalice (s221), **8** — Lažánky (s171, s158, s237), **9** — Vohančice (s157, s239), **10** — Květnice (s170), **11** — Dřínová (s151) and Dranč (s166-1).

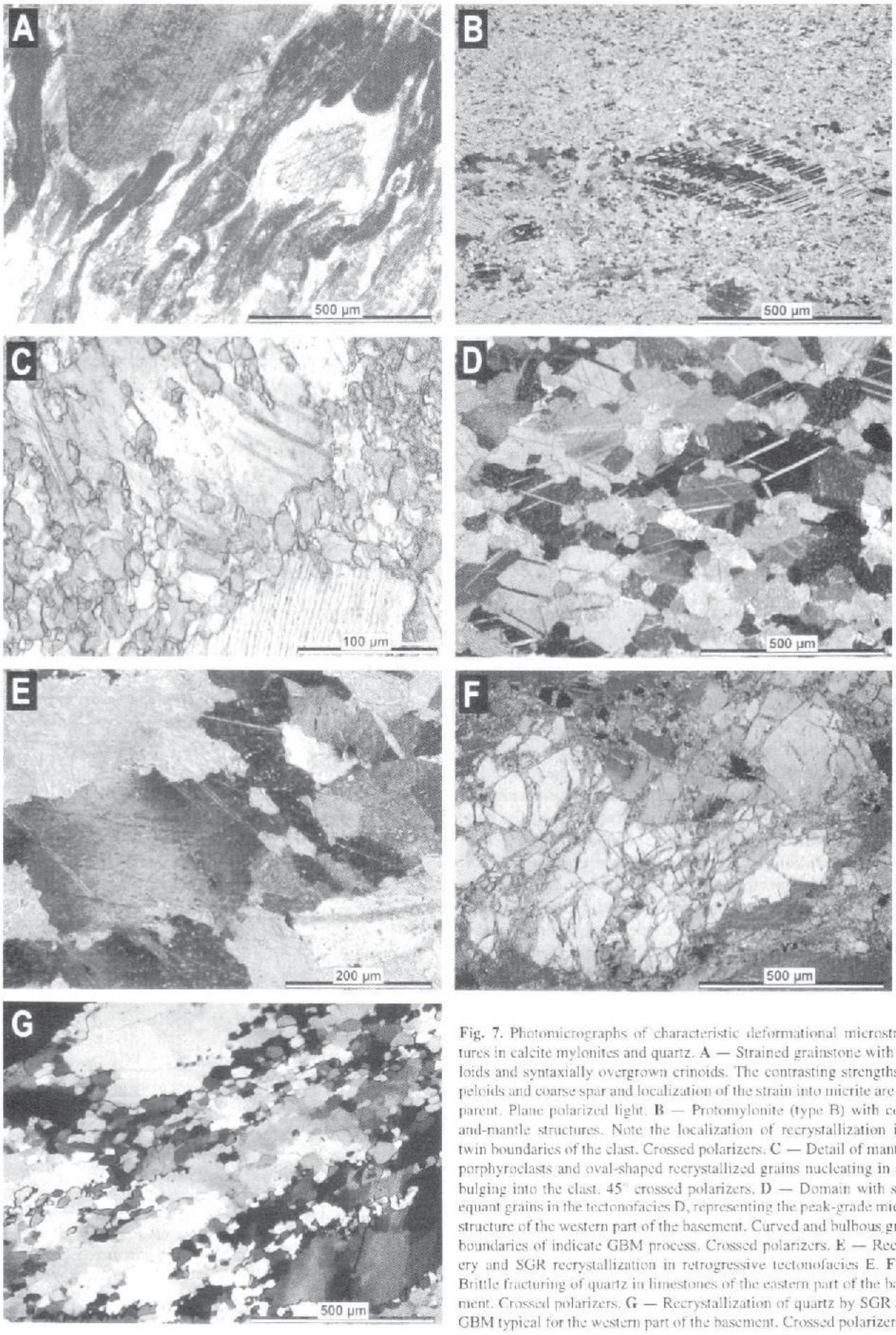

Fig. 7. Photomicrographs of characteristic deformational microstructures in calcite mylonites and quartz. **A** — Strained grainstone with peloids and syntaxially overgrown crinoids. The contrasting strengths of peloids and coarse spar and localization of the strain into micrite are apparent. Plane polarized light. **B** — Protomylonite (type B) with core-and-mantle structures. Note the localization of recrystallization into twin boundaries of the clast. Crossed polarizers. **C** — Detail of mantled porphyroclasts and oval-shaped recrystallized grains nucleating in and bulging into the clast. 45° crossed polarizers. **D** — Domain with subequant grains in the tectonofacies D, representing the peak-grade microstructure of the western part of the basement. Curved and bulbous grain boundaries of indicate GBM process. Crossed polarizers. **E** — Recovery and SGR recrystallization in retrogressive tectonofacies E. **F** — Brittle fracturing of quartz in limestones of the eastern part of the basement. Crossed polarizers. **G** — Recrystallization of quartz by SGR and GBM typical for the western part of the basement. Crossed polarizers.

ing is evidenced with the shape of the grain boundaries, internal strain and polygonization of the grains. It can be stated that after reaching peak temperatures and the localization of the retrogressive deformation into narrow zones, no substantial grain growth took place in the domains which are now coarse grained. The stress calculations thus should not be affected by static recrystallization. In Table 1, the calculated paleostresses are given for several typical samples, using the Rutter paleopiezometer (Rutter 1995) for the GBM recrystallization mechanism.

If we compare the stress values of the facies B and D, which represent the peak metamorphic conditions in the eastern and western parts of the Brunovistulian basement respectively, we can see a significant difference. Stresses four times lower in the lower tectonic unit of the Svratka Dome than in the other two parts of the Brunovistulicum are in accordance with the observed deformation regimes of quartz. As the three compared parts of the Brunovistulian basement are eroded to a similar lithostratigraphic level, the tectonic juxtaposition of the contrasting facies must have occurred during late tectonic phases. The main contrasts however, are not seen between the two parts of the Brunovistulicum with different tectonostratigraphic zonation, which were defined above, but they lie between the lower tectonic unit of the Svratka Dome and the other two domains of the Brunovistulicum — the Brno batholith's western margin and the lower tectonic unit of the Thaya Dome (Fig. 6).

Summary and concluding remarks

The analysis of the mylonites assembly developed within the major thrust system of the Central European Variscan orogeny revealed several characteristic features:

1) A lack of effective dynamic recovery within the progressive low temperature phase of deformation. Microstructural features of core-and-mantle structures developed in calcite protomylonites provided evidence of GBB-dominance of the recrystallization process. In this phase, the SGR mechanism produced only relatively large grains, which must have been further reduced by GBB and/or nucleation. Recovery was effective only during grain size reduction in the retrogressive phase. This can be explained with a higher rate of GBB under lower temperatures, which could have been increased as a result of a high fluid content.

2) The onset of grain size reduction of porphyroclasts prior to distinct grain growth in matrix.

During the incipient mylonitization of inhomogeneous micritic limestones, the porphyroclasts and matrix display contrasting rheological behaviour and strong strain localization into a superplastic matrix occurs. At a certain point of mylonite development, which is probably temperature-determined, GBB is facilitated and the steady-state dynamic recrystallization of clasts sets in. The recrystallized grain size is very close to the grain size in the matrix. Assuming that an inverse proportionality between grain size and stress is valid, the existence of approximate stress homogeneity must be considered in naturally deformed calcite aggregates. A distinct to almost complete dynamic recrystallization of the porphyroclasts and minimum microstructural changes of the matrix indicates significant strain rate differences between the porphyroclasts and the matrix.

3) Variscan large-scale thrusting within the Brunovistulian basement is indicated by the juxtaposition of facies with contrasting microstructures which reflect incompatible peak-grade conditions. The main deformational contrasts can be observed between the lower tectonic unit of the Svratka Dome and the other two domains of the Brunovistulicum — the Brno batholith's western margin and the lower tectonic unit of the Thaya Dome.

It seems very likely that the recrystallized grain size within the mylonitized sequence of limestones studied is due to differential stress variations. Assuming this, it is quite surprising that temperature differences probably not exceeding 50 °C resulted in such dramatic changes of differential stresses and responsive microstructures (compare microstructures A and B with D). Actually, we are not the first to have observed indications of such contrasting behaviour of calcite aggregates under natural LT deformation conditions. Burkhard (1990) examined the change of the microfabric of micritic limestones strained under a natural temperature gradient. He found out that up to 250 °C, grain size distributions were indistinguishable from the sedimentary protolith. Above 280 °C, an increase in grain size in micritic limestones occurred along with an increase in the preferred orientation of the lattice and grain-shape. Behrmann (1983) described distinct variations in the microfabric of calcite mylonites strained at about 300 °C. Microstructural features of the tectonofacial succession, which were described above, provide evidence of the dominance of GBB process or nucleation during the progressive part of LT mylonitization. Burkhard (1990) also suggested a grain boundary migration mechanism for grain growth in epizonally strained micrites. Grain boundary migration has a first order dependence on temperature (e.g. Guillopé & Poirier 1979) and it can be expected that the variation of finite microstructures within the limestones strained under LT conditions is due to a significant change of GBB effectiveness at temperatures around 300 °C.

Acknowledgments: We thank the creators of *ImageTool 2.0* for its free provision at *http://www.uthscsa.edu/dig/itdesc.html*. The constructive reviews of K. Schulmann, D. Plašienka and an anonymous reviewer are highly acknowledged. The research was supported by Grant Agency of Czech Republic through Grant No. 205/98/0751 and by research plan J07/98:143100004.

References

Bábek O. & Janoška M. 1997: Tectonic evolution of the Konice-Mladeč belt: Structural analysis and facies disjunction. *Fac. Rer. Nat., Acta Univ. Palackianae Olomuc., Geol.* 35, 31–35.

Batík P. & Skoček V. 1981: Lithological development of the Paleozoics in the Thaya Batholith eastern margin. *Věst. ÚÚG* 56, 6, 337–347 (in Czech).

Behrmann J.H. 1983: Microstructure and fabric transitions in calcite tectonites from the Sierra Alhamilla (Spain). *Geol. Rdsch.* 72, 2, 605–618.

Bosák P. 1980: Sedimentology of the Devonian in the Tišnov Brunnides and Brno Unit s.s., Tišnov area. *Unpublished PhD. Thesis. Charles University*, Prague, 1–200 (in Czech).

Bosák P. 1984: Organic matter in the Devonian carbonates of the Tišnov area. *Čas. Mineral. Geol.* 29, 1, 41–53 (in Czech).

Burkhard M. 1990: Ductile deformation mechanisms in micritic limestones naturally deformed at low temperatures (150-350 °C). In: Knipe R.J. & Rutter E.H. (Eds.): Deformation mechanisms, rheology and tectonics. *Geol. Soc. Spec. Publ.* 54, 241-257.

Busch J.P. & Van der Pluijm B.A. 1995: Calcite textures, microstructures and rheological properties of marble mylonites in the Bancroft shear zone, Ontario, Canada. *J. Struct. Geol.* 17, 677-688.

Casey M. & McGrew A.J. 1999: One-dimensional kinematic model of preferred orientation development. *Tectonophysics* 303, 131-140.

Cháb J. & Suk M. 1977: Regional metamorphism in Bohemia and Moravia. *Knih. ÚÚG* 50, 156 (in Czech).

Čížek P. & Tomek C. 1991: Large-scale thin-skinned tectonics in the eastern boundary of the Bohemian Massif. *Tectonics* 10, 273-286.

Covey-Crump S.J. & Rutter E.H. 1989: Thermally induced grain growth of calcite marbles on Naxos island, Greece. *Contr. Mineral. Petrology* 101, 69-86.

Dietrich D. & Song H. 1984: Calcite fabrics in natural shear environment, the Helvetic nappes of western Switzerland. *J. Struct. Geol.* 6, 19-32.

Drury M.R. & Urai J.L. 1990: Deformation-related recrystallization processes. *Tectonophysics* 172, 235-253.

Dvořák J. 1973: Synsedimentary tectonics of the Paleozoic of the Drahany Upland (Sudeticum, Moravia, Czechoslovakia). *Tectonophysics* 17, 359-391.

Dvořák J. 1995: Stratigraphy of the Moravo-Silesian zone. In: Dallmeyer R.D., Franke W. & Weber K. (Eds.): Pre-Permian geology of Central and Eastern Europe. *Springer*, Berlin, 477-489.

Dudek A. 1980: The crystalline basement block of the outer Carpathians in Moravia — Brunovistulicum. *Rozpr. Čs. Akad. Věd, Ř. Mat. Přír.* 90, 8, 85.

Finger F., Höck V. & Steyrer H.P. 1989: The granitoids of the Moravian Zone of north-east Austria — Products of a Cadomian active continental margin? *Precambrian Res.* 45, 235-245.

Finger F., Frasl G., Dudek A., Jelinek E. & Thöni M. 1995: Cadomian Plutonism in the Moravo-Silesian Basement. In: Dallmeyer R.D., Franke W. & Weber K. (Eds.): Pre-Permian geology of Central and Eastern Europe. *Springer*, Berlin, 495-507.

Finger F., Hanžl P., Pin C., Von Quadt A. & Steyrer H.P. 2000: The Brunovistulian: Avalonian Precambrian sequence at the eastern end of the Central European Variscides? In: Franke W., Haak V., Oncken O. & Tanner D. (Eds.): Orogenic Processes: Quantification and Modelling in the Variscan Belt. *Geol. Soc. London Spec. Publ.* 179, 103-112.

Franců E., Franců J. & Kalvoda J. 1999: Illite crystallinity and vitrinite reflectance in Paleozoic siliciclastics in the SE Bohemian Massif. *Geol. Carpathica* 50, 5, 365-372.

Frasl G. 1983: Zur Geologie des Kristallins und Tertiars der weiteren Umgebung von Eggenburg. Österreichische Geologische Bundesanstalt, *Excursion Guide*.

Frey M. & Robinson D. (Eds.) 1999: Low-grade metamorphism. *Blackwell Science*, London, 1-313.

Fritz H., Dallmeyer R.D. & Neubauer F. 1996: Thick-skinned versus thin-skinned thrusting: Rheology controlled thrust propagation in the Variscan collisional belt (The southeastern Bohemian Massif, Czech Republic-Austria). *Tectonics* 15, 6, 1389-1413.

Fritz H. & Neubauer F. 1993: Kinematics of crustal stacking and dispersion in the southeastern Bohemian Massif. *Geol. Rdsch.* 82, 556-565.

Guillopé M. & Poirier J.P. 1979: Dynamic recrystallization during creep of single crystalline halite: an experimental study. *J. Geophys. Res.* 84, 5557-5567.

Hanžl P. & Melichar R. 1997: Brno Massif: a section through the active continental margin or a composed terrane? *Krystalinikum* 23, 33-58.

Heitzmann P. 1987: Calcite mylonites in the Central Alpine root zone. *Tectonophysics* 135, 207-215.

Hippertt J. & Egydio-Silva M. 1996: New polygonal grains formed by dissolution-redeposition in quartz mylonite. *J. Struct. Geol.* 18, 1345-1352.

Hirth G. & Tullis J. 1992: Dislocation creep regimes in quartz aggregates. *J. Struct. Geol.* 14, 145-159.

Jackson M.L. 1975: Soil chemical analysis. Advanced course. Published by the author. *Dept. Soil Sci., Univ. Wisconsin*, Madison, 1-895.

Jenček V. & Dudek A. 1971: Relationship of the Moravicum and Moldanubicum at the western border of the Dyje Dome. *Věst. ÚÚG* 46, 6, 331-338.

Kallend J.S., Kocks U.F., Rollet A.D. & Wenk H.R. 1991: Operational Texture Analysis. *Mater. Sci. Engin., A132* 1-11.

Kalvoda J. 1995: Devonian sedimentary basins of East Avalonian margin in Moravia. *Geologické výzkumy na Moravě a ve Slezsku v roce 1994*, 48-50 (in Czech).

Kalvoda J. 2001: Upper Devonian-Lower Carboniferous foraminiferal paleobiogeography and Perigondwana terranes at the Baltica-Gondwana interface. *Geol. Carpathica* 4, 52, 205-215.

Kohlstedt D.L. & Weathers M. 1980: Deformation-induced microstructures, paleopiezometers, and differential stresses in deeply eroded fault zones. *J. Geophys. Res.* 85, B11, 6269-6285.

Kübler B. 1967: La crystallinite de l'illite et les zones tout a fait superieures du metamorphisme. In: Etages Tectoniques, Colloque de Neuchatel, 1966, *A la Baconniere*, Neuchâtel, 105-122.

Leichmann J. 1996: Geologie und Petrologie des Brünner Massifs. *Unpublished PhD* Thesis, *University of Salzburg*.

Lloyd G.E. & Freeman B. 1994: Dynamic recrystallization of quartz under greenschist conditions. *J. Struct. Geol.* 16, 6, 867-881.

Matějovská O. 1975: The Moldanubicum gneiss series of southwestern Moravia and its relation to granulites. *Věstník ÚÚG* 50, 345-351.

Matte P., Maluski H., Rajlich P. & Franke W. 1990: Terrane boundaries in the Bohemian Massif: Result of large-scale Variscan shearing. *Tectonophysics* 177, 151-170.

Mercier J.C.C., Anderson D.A. & Carter N.L. 1977: Stress in the litosphere: inferences form steady steate flow of rock. *Pure Appl. Geophys.* 115, 199-226.

Michibayaschi K. 1993: Syntectonic development of a strain-independent steady-state grain size during mylonitization. *Tectonophysics* 222, 151-164.

Morauf W. & Jäger F. 1982: Rb-Sr whole rock ages for Bitesch Gneiss, Moravicum, Austria. *Terra Cognita* 2, 60-61.

Olgaard D.L. & Evans B. 1988: Grain growth in synthetic marbles with added mica and water. *Contr. Mineral. Petrology* 100, 246-260.

Rajlich P. 1990: Strain and tectonic styles related to Variscan transpression and transtension in the Moravo-Silesian Culmian basin, Bohemian Massif, Czech Republic. *Tectonophysics* 174, 351-367.

Ranalli G. 1984: Grain size distribution and flow stress in tectonites. *J. Struct. Geol.* 6, 443-447.

Rosenholtz J.L. & Smith D.T. 1949: Linear thermal expansion of calcite, var. Iceland spar and Yule marble. *Amer. Mineralogist* 34, 846-854.

Rutter E.H. 1974: The influence of temperature, strain rate and interstitial water in the experimental deformation of calcite rocks. *Tectonophysics* 22, 311-334.

Rutter E.H. 1995: Experimental study of the influence of stress, temperature, and strain on the dynamic recrystallization of Carrara marble. *J. Geophys. Res.* 100, 24651-24663.

Rutter E.H., Casey M. & Burlini L. 1994: Preferred crystallographic orientation development during the plastic and superplastic flow of calcite rocks. *J. Struct. Geol.* 16, 1431-1446.

Schmid S.M., Boland J.N. & Paterson M.S. 1977: Superplastic flow in finegrained limestone. *Tectonophysics* 43, 257-291.

Schmid S.M., Paterson M.S. & Boland J.N. 1980: High temperature flow and dynamic recrystallization in Carrara marble. *Tectonophysics* 65, 245-280.

Schmid S.M., Panozzo R. & Bauer S. 1987: Simple shear experiments on calcite rocks: rheology and mirofabric. *J. Struct. Geol.* 9, 747-778.

Schulmann K., Ledru P., Autran A., Melka R., Lardeaux J.M., Urban M. & Lobkovicz M. 1991: Evolution of nappes in the eastern margin of the Bohemian Massif: a kinematic interpretation. *Geol. Rdsch.* 80/1, 73-92.

Schulmann K., Melka R., Lobkowicz M., Ledru P., Lardeaux J.M. & Autran A. 1994: Contrasting styles of deformation during progressive nappe stacking at the southeastern margin of the Bohemian Massif (Thaya Dome). *J. Struct. Geol.* 16, 355-370.

Špaček P. 2001: Microtectonics and stratigraphy of the Paleozoic limestones in the Brunovistulian SW margin. *Unpublished PhD. Thesis, Masaryk University*, Brno (in Czech).

Štípská P. & Schulmann K. 1995: Inverted metamorphic zonation in a basement-derived nappe sequence, eastern margin of the Bohemian Massif. *Geol. J.* 30, 385–413.

Stöckhert B., Brix M.R., Kleinschrodt R., Hurford A.J. & Wirth R. 1999: Thermochronometry and microstructures of quartz — a comparison with experimental flow laws and predictions on the temperature of brittle-plastic transition. *J. Struct. Geol.* 21, 351–369.

Suess F.E. 1908: Die Beziehungen zwischen dem moldanubischen und moravischen Grundgebirge in dem Gebiet von Frain und Geras. *Verh. Geol. Reichsanst.* 393–412.

Suess F.E. 1912: Die moravischen Fenster und ihre Beziehung zum Grundgebirge des Hohen Gesenks. *Denkschr. K. Akad. Wiss., Wien*, 88, 541–631.

Suess F.E. 1926: Intrusionstektonik und Wandertektonik im varizeischen Grundgebirge. Wien, 268.

Tullis J. & Yund A. 1982: Grain growth kinetics of quartz and calcite aggregates. *J. Geology* 90, 301–318.

Twiss R.J. 1977: Theory and applicability of a recrystallized grain-size palaeopiezometer. *Pure Appl. Geophys.* 115, 227–244.

Ulrich S. 2000: Deformation microstructures and comparative rheology of marble and quartzite in natural strain gradient. *Unpublished PhD. thesis. Charles University*, Prague.

Van Bremen O., Aflalion A., Bowes D.R., Dudek A., Mísař Z., Povondra P. & Vrána S. 1982: Geochronological studies of the Bohemian Massif, Czechoslovakia, and their significance in the evolution of Central Europe. *Transactions of the Royal Society of Edinburgh: Earth Sci.* 73, 89–108.

Vrána S., Blumel P. & Petrakakis K. 1995: Moldanubian Zone, metamorphic evolution. In: Dallmeyer R.D., Franke W. & Weber K. (Eds.): Pre-Permian geology of Central and Eastern Europe. *Springer*, Berlin, 453–466.

Walker A.N., Rutter E.H. & Brodie K.H. 1990: Experimental study of grain-size sensitive flow of synthetic, hot-pressed calcite rocks. In: Knipe R.J. & Rutter E.H. (Eds.): Deformation mechanisms, rheology and tectonics. *Geol. Soc. Spec. Publ. No. 54*, 259–284.

Warr L.N. & Rice H.N. 1994: Interlaboratory standardization and calibration of clay mineral crystallinity and crystallite size data. *J. Metamorphic Geol.* 12, 141–152.

White S.H. 1977: Geological significance of recovery and recrystallization processes in quartz. *Tectonophysics* 39, 143–170.

Příloha 8

Geršlová E., Opletal V., Sýkorová I., Sedláková I., Geršl M. (2015) A Geochemical and Petrographical Characterization of Organic Matter in the Jurassic Mikulov Marls from the Czech Republic. International Journal of Coal Geology 141-142, 42-50.

International Journal of Coal Geology 141–142 (2015) 42–50

Contents lists available at ScienceDirect

International Journal of Coal Geology

journal homepage: www.elsevier.com/locate/ijcoalgeo

A geochemical and petrographical characterization of organic matter in the Jurassic Mikulov Marls from the Czech Republic

Eva Geršlová [a,*], Vladimír Opletal [b], Ivana Sýkorová [c], Iva Sedláková [a], Milan Geršl [d]

[a] Department of Geological Sciences, Faculty of Natural Science, Masaryk University, Kotlářská 2, 611 37 Brno, Czech Republic
[b] MND a.s., Úprkova 807/6, 695 01 Hodonín, Czech Republic
[c] Institute of Rock Structure and Mechanics, Academy of Sciences, V Holešovičkách 41, 18201 Praha, Czech Republic
[d] Department of Agricultural, Food and Environmental Engineering, Faculty of Agronomy, Mendel University in Brno, Zemědělská 1, 613 00 Brno, Czech Republic

ARTICLE INFO

Article history:
Received 7 November 2014
Received in revised form 25 February 2015
Accepted 3 March 2015
Available online 10 March 2015

Keywords:
Mikulov Marls
Kerogen type
Thermal maturity
Vitrinite reflectance
Rock-Eval pyrolysis

ABSTRACT

In this study a Rock-Eval pyrolysis, a petrographic composition of organic matter, vitrinite reflectance and gas chromatography were undertaken on borehole cores from the Mikulov Marls in order to define the organic matter type and determine the thermal maturity. The analyzed samples covered a depth interval of between 2300 m and 4500 m. The studied sediments were dark-colored, moderately laminated shales throughout which appear uniform upon visual examination. The geochemical analyses revealed that the source rock potential of the Mikulov Marls is from fair to good. According to the Rock-Eval pyrolysis, the organic matter in the samples was classified as kerogen type II–III. This classification is not supported by the results from the other used methods. The evaluation of the organic macerals demonstrated the dominant role of liptinite with prevailing liptodetrinite accompanied by a variable content of alginite, bituminite, and sporadic sporinite and resinite. The alginite consists mainly of lamalginite, derived from colonial planktonic or benthonic algae. Based on these results, the Mikulov Marls represent the kerogen type II. These results are also supported with a strong n-alkane odd-carbon-number predominance at n-C$_{15}$, n-C$_{17}$ and n-C$_{19}$ range on the gas chromatography.

1. Introduction and regional setting

Organic matter in sedimentary rocks (kerogen) is used as an indicator of thermal stress over a range of 50–300 °C (Ebukanson and Kinghorn, 1985; Littke et al., 2008; Tissot and Welte, 1984). Maturation degree depends on the overall thermal history of the evaluated rocks, i.e. the temperatures and their duration. Rock-Eval pyrolysis and vitrinite reflectance are commonly used screening methods for thermal maturity evaluation in the rock sequences (Behar et al., 2001; Dahl et al., 2004; Hakimi and Wan Hasiah, 2013; Lafargue et al., 1998; Littke et al., 2008; Teichmüller et al., 1998). Both methods have limits, however, which have been described by a number of authors all over the world (Akinlua et al., 2005; Bordenave et al., 1993; Katz, 1983). Vitrinite reflectance (R_r) is a thermal maturity parameter of organic matter which can be measured in most dark colored shales and siltstones. Its application is limited by the absence of terrestrial plant debris in the pre-Devonian or marine rocks. In these samples, reflectance is measured on zooclasts or bitumens, if present (Goodarzi and Higgins, 1987; Goodarzi and Norford, 1985; Riediger et al., 2011). Different analytical methods such as gas chromatography mass spectrometry are used in the sedimentary environments where the vitrinite particles are missing (Peters et al., 2005).

The Upper Jurassic Mikulov Marls represent the autochthonous cover of the Bohemian Massif. The unit lies either directly on the pre-Mesozoic basement or on the Middle to Upper Jurassic sequences (Gresten Formation, Nikolcice Beds and Vranovice Dolomite). The known thickness reaches up to 1500 m (Picha et al., 2006). The Mikulov Marls itself represents a basinal facies (Adamek, 2005) of the Upper Jurassic continental slope formed primarily by a monotonous sequence of dark gray, organic rich marls where the carbonate content varies in both the vertical and horizontal directions. According to the recent 3D seismic interpretation of the studied area the NW part, the line along the villages Dolni Vestonice, Tesany and Milesovice (SSW-NNE striking zone) generally forms the boundary where the basinal facies of the Mikulov Marls pass into the shallower platform facies represented by organodetritic limestones and dolomites which can be studied in the outcrops as far away as the near vicinity of Brno. During the Miocene, the Mikulov Marls in the studied area, along with the rest of the Pre-Tertiary and Paleogene rocks were overthrust by a system of nappes – the Western Carpathian Flysch Belt. During the Lower Miocene, the Carpathian Foredeep was simultaneously formed in the area as the peripheral foreland basin of the Carpathian Thrusts (Nehyba and Šikula, 2007). Jurassic marls have been identified as the major source rock for oil and gas in the Vienna basin (Blížkovský et al.,

---

[*] Corresponding author. Tel.: + 420 774 796 218.
E-mail address: gerslova.eva@gmail.com (E. Geršlová).

http://dx.doi.org/10.1016/j.coal.2015.03.002
0166-5162/

Table 1
Bulk geochemical data of Rock-Eval and TOC analysis with calculated parameters.

Signatura	Depth (m)	TOC (wt.%)	S_1 (mg/g)	S_2 (mg/g)	T_{max} (°C)	HI	OI	PI
Bul1	3252	2.05	0.21	5.14	431	251		0.04
Bul1	3297	1.81	0.63	4.58	432	253		0.12
Bul1	3411	3.08	0.14	3.18	433	103		0.04
Bul1	3470	2.44	0.25	7.04	431	289		0.03
Bul1	3500	1.75	0.04	2.06	432	118		0.02
Je2	2320	0.83	0.03	1.66	430	200	58	0.02
Kob1	3136	1.59	0.38	4.98	437	313	41	0.07
Kob1	3137	2.10	0.15	7.06	425	336		0.02
Kob1	3138	1.04	0.09	2.47	435	238	54	0.04
Kob1	3179	1.05	0.16	3.28	427	313		0.05
Kob1	3180	1.05	0.23	1.96	430	187	53	0.11
Kob1	3203	0.93	0.01	3.47	432	373		0.00
Kob1	3232	1.26	0.03	3.69	429	293		0.01
Kob1	3237	1.90	0.02	5.72	431	301		0.00
Kob1	3241	1.52	0.42	3.60	431	237	48	0.10
Kob1	3259	1.34	0.02	5.72	431	301		0.00
Kob1	3290	0.96	0.01	4.50	426	469		0.00
Kob1	3299	0.99	0.01	2.92	427	295		0.00
Kob1	3324	2.24	0.27	7.62	424	340		0.03
Kob1	3350	1.65	0.02	9.10	429	551		0.00
Kob1	3390	1.14	0.01	4.57	427	401		0.00
Kob1	3407	1.58	0.01	8.14	423	515		0.00
Kob1	3411	0.96	0.23	8.17	434	851	90	0.03
Kob1	3415	1.77	0.19	5.52	431	312	40	0.03
Kob1	3730	1.39	0.18	3.17	431	229	40	0.05
Kob1	3780	1.33	0.16	3.33	437	250	55	0.05
Kob1	3986	1.54	0.26	5.64	435	366	32	0.04
Kob1	4018	1.43	0.20	4.51	438	315	43	0.04
Kob1	4020	1.32	0.21	3.10	436	236	41	0.06
Kob1	4055	2.05	0.39	7.21	434	352	32	0.05
Kob1	4131	1.28	0.20	4.01	437	313	30	0.05
Kob1	4183	1.29	0.28	2.87	436	223	49	0.09
Kob1	4277	0.79	0.14	2.08	438	263	44	0.06
Kob1	3294	1.24	0.02	6.13	429	465		0.00
Mork1	2997	1.23	0.07	4.30	433	350	33	0.02
Mu2	1494	1.80	0.30	4.72	425	262	26	0.06
Nem1	2756	1.10	0.19	4.51	427	410	162	0.04
Nem1	2757	3.40	0.88	13.74	430	404	49	0.06
Nem1	2758	2.42	0.10	5.98	428	244		0.02
Nem1	2761	2.57	0.16	10.04	427	391	43	0.02
Nem1	2964	1.21	0.17	4.13	428	341		0.04
Nem1	2966	0.96	0.02	1.56	419	163		0.01
Nem1	2992	0.40	0.02	0.26	434	65		0.07
Nem1	3180	1.21	0.02	4.9	433	405		0.00
Nem1	3342	1.46	0.11	4.31	432	295	47	0.02
Nem1	3343	1.50	0.13	6.41	436	427	65	0.02
Nem1	3345	1.30	0.13	3.28	433	252	50	0.04
Nem1	3346	1.21	0.09	5.07	430	419		0.02
Nem1	3506	1.36	0.10	3.53	436	260	35	0.03
Nem1	3508	0.94	0.13	3.52	430	374		0.04
Nem1	3510	1.31	0.12	2.90	434	222	38	0.04
Nem1	3744	1.38	0.22	5.87	435	425	12	0.04
Nem1	3745	1.47	0.24	4.27	434	290	42	0.05
Nem1	3746	1.73	0.39	7.22	434	417		0.05
Nem1	3900	1.06	0.26	3.11	430	293		0.08
Nem1	4034	1.48	0.12	3.5	434	236	13	0.03
Nem1	4103	1.38	0.16	3.32	440	241	33	0.05
Nem1	4104	1.21	0.37	3.67	430	304		0.09
Nem1	4105	1.23	0.21	2.53	437	206	36	0.08
Nem1	4137	1.13	0.38	4.79	438	424		0.07
Nem4	2546	2.40	0.23	12.79	424	533	29	0.02
Něm5	2445	1.39	0.15	5.36	428	387	37	0.03
Něm5	2446	1.26	0.10	5.82	430	462	32	0.02
Něm5	2448	1.45	0.09	3.68	431	254		0.02
Nik1	1500	1.90	0.18	6.97	427	368	50	0.03
Nik1	1700	0.86	0.03	2.02	427	236	56	0.01
Nik8	1891	0.80	0.05	1.55	432	194	71	0.03
Nik8	1995	1.70	0.04	5.32	433	313		0.01
Nik8	1999	1.20	0.03	2.68	432	224	50	0.01
NM1	3168	1.22	0.07	3.76	435	308	25	0.02
NM1	3491	1.39	0.09	3.78	434	272	22	0.02
NM2	2900	1.24	0.07	3.84	429	310		0.02
NM2	2904	1.07	0.05	2.62	431	245	41	0.02
Sed1	4303	2.00	0.38	6.28	439	333	28	0.06

(continued on next page)

Table 1 (*continued*)

Signatura	Depth (m)	TOC (wt.%)	S_1 (mg/g)	S_2 (mg/g)	T_{max} (°C)	HI	OI	PI
Sed1	4305	1.39	0.11	2.44	426	175		0.04
Sed1	4551	1.11	0.26	3.21	443	289	28	0.07
Sed1	4553	1.00	0.26	1.8	439	178	29	0.13
Uh17	2063	1.55	0.18	5.58	423	360		0.03
Uh17	2275	1.04	0.01	3.73	423	358		0.00
Uh17	2547	0.73	0.06	2.65	427	364		0.02
Uh17	2631	0.96	0.05	3.28	421	341		0.02
Uh17	2635	1.10	0.08	4.2	423	382		0.02
Uh18	2143	0.75	0.03	1.7	429	226		0.02
Uh18	2439	0.37	0.04	1.77	421	479		0.02
Uh18	2605	1.60	0.07	7.6	427	475	28	0.01
Uh19	2439	1.13	0.06	4.21	428	373	32	0.01
Uh19	2443	0.64	0.05	2.26	428	353		0.02

TOC: Total organic Carbon, wt.%.
S1: Volatile hydrocarbon (HC) content, mg HC/g rock.
S2: Remaining HC generative potential, mg HC/g rock.
Tmax: Temperature at maximum of S2 peak.
HI: Hydrogen Index = S2 *100/TOC, mg HC/g TOC.
OI: Oxygen Index = S3 * 100/TOC, mg CO_2/g TOC.

1994; Eliáš and Wessely, 1990; Ladwein, 1988; Picha et al., 2006). Based on the recent studies, they also contribute significantly to the hydrocarbon provinces adjacent to the Bohemian Massif lying in an N and NE direction from the Vienna Basin (Nesvacilka Paleovalley, Zdanice elevation area, etc.). The origin of the organic matter in the Jurassic marls was suggested as planktonic algae mixed with a minor portion of reworked and partly oxidized terrestrial plant debris based on Rock-Eval pyrolysis, organic petrography and chromatography (Francu et al., 1996).

This study was aimed at providing a more systematic evaluation of the variation, and sensitivity, of thermal maturity parameters with increasing depth for the Mikulov Marls. The relationship between individual parameters was also evaluated.

2. Methods

The source rock analyses were conducted on the 22 samples taken from eleven exploration wells. All the collected samples were analyzed for total organic carbon (TOC) and Rock-Eval pyrolysis. There were used archival results from Rock-Eval pyrolysis (65 in total) included to the evaluated dataset (Table 1). Random vitrinite reflectance and maceral description (Table 2) were performed on 19 samples. The molecular analyses of the saturated hydrocarbons were performed on 18 (GC, Table 3) and 16 samples (GC/MS, Table 4) respectively.

The studied sediments were dark-colored, moderately laminated shales which appeared remarkably uniform throughout upon visual examination. The total organic carbon was determined using Analytik Jena multi N/C 2100S HT 1300 with a detection limit 0.05%. Carbonates were removed from the sample using 9% water solution HCl. The pyrolysis was conducted using a Rock-Eval 6 instrument. The free and bound hydrocarbons (S1 and S2) and the peak temperature of the pyrolysis (T_{max}) were determined.

The polished surfaces were prepared from rock chips and the reflectance measurement was carried out in oil in non-polarized light (R_r) using a Opton Zeiss microscope-photometer, with 50× and 100× objectives and optical standards of 0.58%, 0.89%, 1.71%, 3.12% and 5.42% reflectance. The maceral composition was determined using the same equipment at the same conditions according to ICCP (1998, 2001). The liptinite composition was determined using the microscope with a fluorescence mode and a set of filters FL05. Maceral identification followed the recommendation described by Hutton (1987) and Taylor et al. (1998).

Table 2
Summary of n-alkane and isoprenoids ratios from Mikulov Marls.

Vrt	Depth (m)	Pri/Phy	Pri/C17	Phy/C18	CPI
Kob1	3136	1.24	0.37	0.35	1.01
Kob1	3179	1.05	0.41	0.39	1.01
Kob1	3324	1.88	1.01	0.74	1.31
Kob1	3407	1.74	0.90	0.75	1.37
Kob1	3411	1.88	0.92	0.68	1.34
Kob1	3435	1.27	0.91	0.90	1.27
Kob1	3645	1.50	0.43	0.35	1.01
Kob1	3874	1.68	0.41	0.30	1.09
Kob1	4018	1.92	0.43	0.29	1.08
Kob1	4131	1.85	0.74	0.56	1.23
Kob1	4334	1.74	0.34	0.24	1.01
Nem1	2756	1.65	1.25	1.27	2.10
Nem1	2997	1.54	1.22	1.25	1.63
Nem1	3179	1.53	1.15	1.13	1.55
Nem1	3506	2.00	0.86	0.59	1.32
Nem1	4103	2.44	0.58	0.29	1.07
Sed1	4305	1.96	0.57	0.34	1.05
Sed1	4551	2.31	0.42	0.22	1.04

Pr: pristane iC19.
Pr: pristane iC19.
Pr: pristane iC19.
C17: nC17 alkane.
C18: nC18 alkane.
CPI: carbon preference index = 2*(nC23 + nC25 + nC27 + nC29)/(nC22 + 2*(nC24 + nC26 + nC28) + nC30).

Table 3
Biomarker ratios calculated from m/z 191 mass fragmentograms from the Mikulov Marl.

Vrt	Depth (m)	Ts/(Ts + Tm)	S/(S + R) C31	S/(S + R) C32	C31R/C30H
Kob1	3136	0.49	0.42	0.45	0.43
Kob1	3179	0.43	0.38	0.44	0.48
Kob1	3411	0.39	0.35	0.30	0.63
Kob1	3780	0.38	0.54	0.48	0.39
Kob1	3986	0.40	0.58	0.55	0.36
Kob1	4018	0.41	0.57	0.57	0.33
Kob1	4131	0.46	0.58	0.57	0.32
Kob1	4277	0.48	0.58	0.60	0.27
Mork1	2997	0.31	0.24	0.22	0.63
Nem1	3342	0.41	0.43	0.43	0.32
Nem1	3506	0.36	0.50	0.45	0.33
Nem1	3744	0.37	0.56	0.52	0.34
Nem1	4103	0.40	0.59	0.60	0.33
NM1	3168	0.39	0.38	0.42	0.40
NM1	3491	0.37	0.52	0.52	0.33
Sed1	4551	0.51	0.55	0.57	0.31

Ts: 18a(H)-trisnorhopane.
Tm: 17a(H)-trisnorhopane.
C31S: C31 22S 17a(H) homohopane.
C31R: 22R 17a(H) homohopane.
C32S: 22S 17a(H) bishomohopane.
C32R: 22R 17a(H) bishomohopane.
C30H: 17a(H)-hopane.

Table 4
Random reflectance of vitrinite (%) and maceral composition (vol.%) of organic matter in the Mikulov Marl.

	Depth (m)	Rr (%)	∑V	T	Ct	Vd	G	∑L	Sp	TAl	LAl	Re	Ld	Bi	∑I	Fu	Smf	Ma	Se	Id
Nem5	2445	0.56	**11.5**	1.5	2.3	6.9	0.8	**73.9**	0.0	1.1	24.3	1.6	45.4	1.5	**14.6**	0.8	0.0	1.6	0.0	12.2
Nem4	2546	0.66	**12.5**	0.0	0.0	5.4	7.1	**50.8**	0.0	1.3	15.6	3.4	29.2	1.3	**35.6**	6.8	5.1	8.5	0.0	15.2
Nem1	2756	0.55	**4.3**	0.0	1.1	3.2	0.0	**69.8**	0.0	1.8	18.2	4.7	39.2	5.9	**25.9**	1.2	0.0	9.4	1.1	14.2
Mork1	2997	0.68	**14.3**	1.8	0.0	5.4	7.1	**50.0**	0.0	0.9	16.8	1.8	29.6	0.9	**35.7**	7.1	3.6	7.1	1.8	16.1
Kob1	3136	0.65	**8.9**	0.0	2.5	5.1	1.3	**74.7**	1.3	2.5	13.9	0.0	51.9	5.1	**16.4**	3.8	0.0	3.9	0.0	8.7
NM1	3168	0.66	**11.5**	1.5	2.3	6.9	0.8	**50.6**	0.0	2.1	24.0	1.6	45.4	1.5	**38.0**	15.2	0.0	6.6	0.0	16.2
Kob1	3179	0.62	**16.7**	0.0	5.4	7.0	4.3	**50.0**	0.0	1.9	16.2	0.0	28.0	3.9	**33.3**	2.8	5.6	6.9	0.0	18.0
Nem1	3342	0.69	**13.0**	2.0	3.0	7.0	1.0	**58.0**	0.0	1.1	18.9	0.0	33.2	4.8	**29.0**	9.0	0.0	9.0	0.0	11.0
Kob1	3411	0.65	**12.2**	0.0	2.7	1.3	8.2	**58.1**	0.0	0.7	14.2	0.0	37.3	5.9	**29.7**	2.7	0.0	8.1	0.0	18.9
NM1	3491	0.72	**9.1**	0.8	2.5	5.1	0.7	**62.0**	0.0	2.6	22.0	1.8	34.5	1.1	**28.9**	2.5	0.0	9.9	0.0	16.5
Nem1	3506	0.69	**6.3**	0.0	1.4	2.1	2.8	**67.7**	0.8	1.4	23.2	0.0	38.0	4.3	**26.8**	2.1	2.8	5.6	0.0	16.3
Nem1	3744	0.70	**13.7**	0.0	1.6	4.9	7.2	**70.5**	1.4	0.8	14.1	3.3	45.3	5.6	**15.8**	1.6	0.0	1.5	0.0	12.7
Kob1	3780	0.66	**10.1**	0.0	1.1	2.3	6.7	**50.6**	0.0	0.6	9.5	0.0	37.3	3.2	**39.3**	16.8	0.0	7.9	0.0	14.6
Kob1	3986	0.68	**9.8**	0.0	2.2	4.3	3.3	**60.1**	0.0	2.3	17.3	2.1	33.0	5.4	**28.3**	6.5	0.0	6.1	2.6	13.1
Kob1	4018	0.70	**13.3**	0.0	1.7	3.4	8.2	**60.0**	0.0	0.7	16.0	0.0	39.0	4.3	**26.7**	3.4	0.0	6.8	0.0	16.5
Nem1	4103	0.72	**13.0**	0.0	1.2	8.2	3.6	**52.5**	2.4	0.4	15.2	1.2	30.1	3.2	**34.5**	4.8	2.4	7.1	0.0	20.2
Kob1	4131	0.72	**14.3**	0.0	0.0	4.8	9.5	**52.4**	1.6	0.8	13.8	0.0	30.0	6.2	**33.3**	4.8	0.0	15.8	0.0	12.7
Kob1	4277	0.72	**9.5**	0.0	0.9	2.9	5.7	**67.6**	0.0	3.1	19.7	1.9	38.0	4.9	**22.9**	2.8	0.0	4.8	0.0	15.3
Sed1	4551	0.75	**4.6**	0.0	0.0	4.6	0.0	**65.5**	0.0	1.3	24.0	1.3	37.5	1.4	**29.9**	3.4	0.0	8.1	0.0	18.4

R_r = Random reflectance of vitrinite, ∑V = Vitrinite content, T = telinite, Ct = Collotelinite, Vd = vitrodetrinite,
G = gelinite; ∑L = Liptinite content, Sp = Sporinite, TAl = Telalginite, LAl = Lamalginite,
Re = Resinite, Ld = Liptodetrinite, Bi = Bituminite; ∑I = Inertinite content, Fu = Fusinite, Smf = Semifusinite, Ma = Macrinite, Se = Secretinite, Id = Inertodetrinite

Sample aliquots of 10 g were spiked with 25 μL of internal standard solution with concentration of 5 ng/mL of *o*-terphenyl. The extraction was performed with 250 mL DCM/MeOH (93:7) in a Soxhlet apparatus for 12 h. The raw extracts were evaporated to dryness under a gentle stream of N_2, and redissolved in 10 mL of n-hexane. Prior to GC and GC/MS analyses, an aliquot of 2 mL of the raw extract was placed on a 2 g silicagel column to separate the aliphatic and aromatic hydrocarbon fractions by liquid chromatography using n-hexane and DCM as eluents. The obtained saturated fraction was subjected to gas chromatographic analyses on an AT 5890 (Agilent Technologies, USA) equipped with a

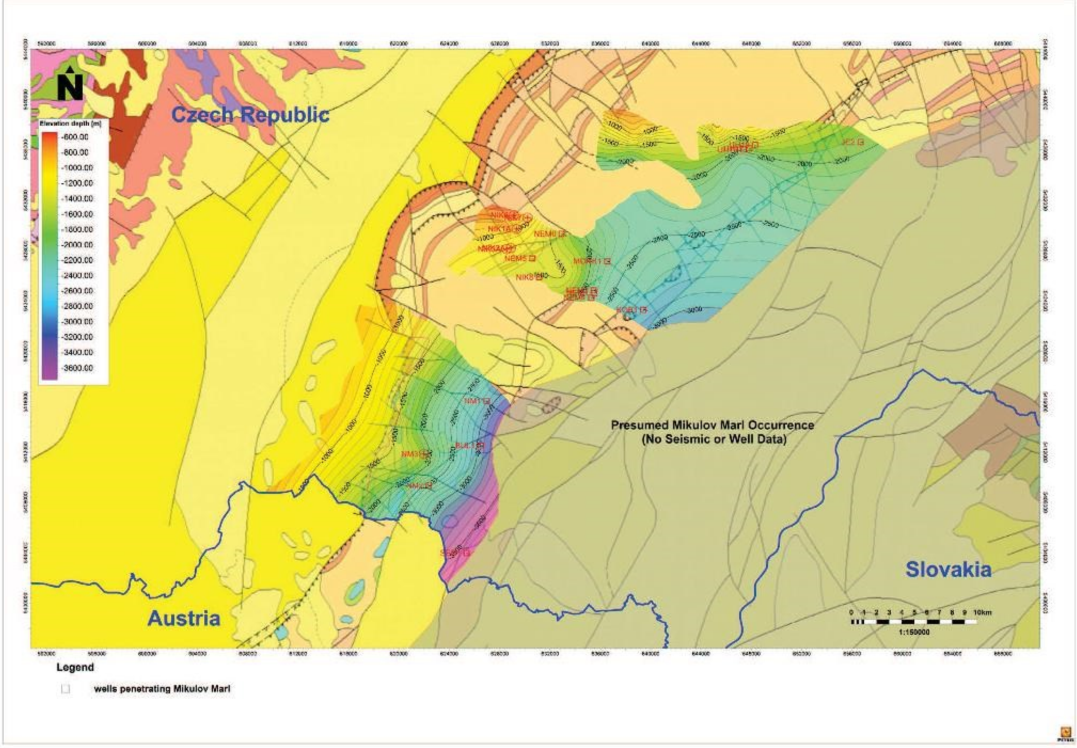

Fig. 1. Subcrop map of the Western Carpathians and their foreland in the eastern part of the Czech Republic. The studied area is marked by a bold frame.

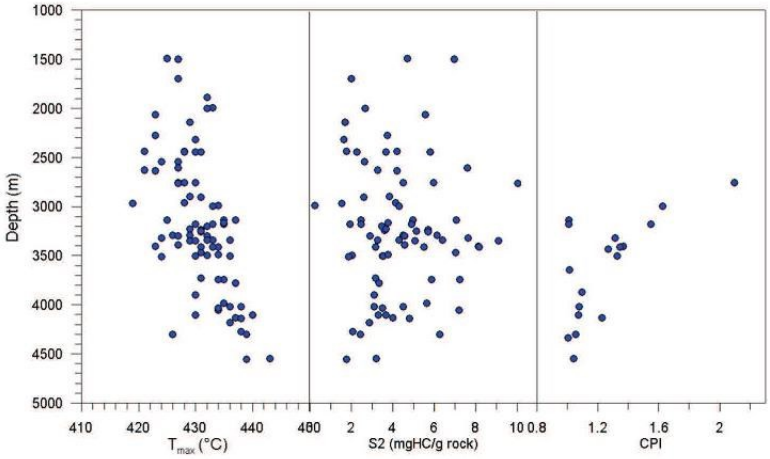

Fig. 2. Selected parameters (T_{max} – maximum pyrolytic temperature, S2 – bound hydrocarbons, CPI – carbon preference index) as a function of depth in the evaluated borehole profiles.

flame ionization detector (FID) and a FSOT capillary column with a non-polar HP5 phase (25 m, i.d. 0.25 mm and 0.5 μm film thicknesses).

A Hewlett-Packard 6890N GC coupled to a HP 5973N MSD operating in the electron impact mode (EI+) was used. The measurements were performed in a full scan mode scanning from m/z 50 to m/z 550. The samples were injected splitless onto a HP-1MS capillary column (60 m length × 0.25 mm i.d. × 0.25 μm film thicknesses, Agilent Technologies, USA). The separation was carried out using helium at a constant flow of 1.2 mL/min with the following oven temperature program: 50 °C (held for 1.2 min), then at 5 °C/min to a final temperature of 300 °C (held for 3 min). The GC/MS interface temperature was held at 280 °C and the ion source temperature at 280 °C. Identification of the compounds was based on a comparison of mass spectral data with those of authentic reference material. The index CPI was calculated as $CPI = 2^*(n\text{-}C_{23} + n\text{-}C_{25} + n\text{-}C_{27} + n\text{-}C_{29})/(n\text{-}C_{22} + 2^*(n\text{-}C_{24} + n\text{-}C_{26} + n\text{-}C_{28}) + n\text{-}C_{30})$.

3. Results

The Rock-Eval pyrolysis provided parameters for evaluation of the hydrocarbon potential, organic matter type and thermal maturity level within the tested data set. The organic carbon content (TOC) in the samples varies from 0.4 to 3.4%. The bound hydrocarbons (S2) range from 0.3 to 13.7 mgHC/g rock. Based on the relationship of TOC to S2 for the majority of the samples, the source rock potential ranges from fair to good (Table 1).

The maximum pyrolytic temperature (T_{max}) varies from 419 to 443 °C. According to T_{max} values and production index (PI) samples from the Mikulov Marls belong to immature to oil window range (Table 1). Values of T_{max} increase moderately with depth (Fig. 2). Hydrogen index (HI) values range from 65 to 851 mg HC/g TOC and reveal pronounced differences among the individual samples. The oxygen index (OI) varies from 12 to 162 mg CO_2/g TOC. By plotting

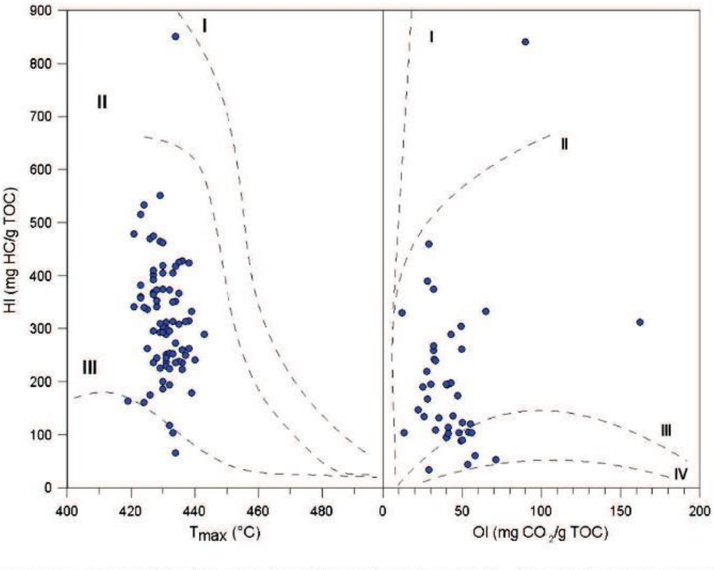

Fig. 3. Kerogen types based on hydrogen index (HI), oxygen index (OI) and thermal maturity (T_{max}) from the Rock-Eval pyrolysis for Mikulov Marl.

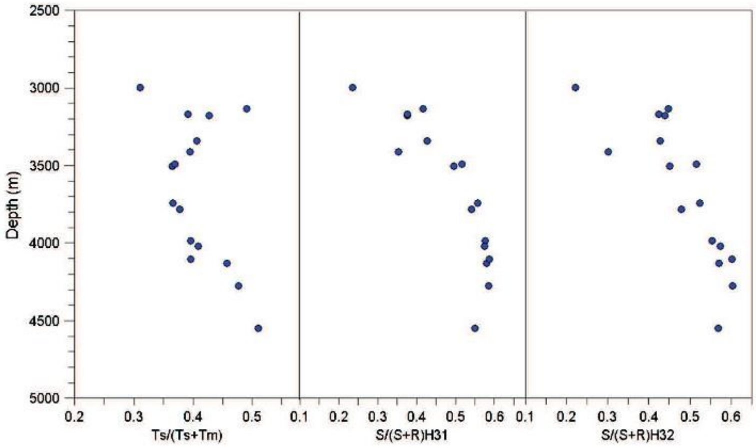

Fig. 4. Biomarker parameters Ts/(Ts + Tm), S/(S + R)H31 and S/(S + R)H32 as a function of depth in the Mikulov Marls.

the T_{max} against HI and OI versus HI (Fig. 3) as proposed by Peters et al. (2005) and Dahl et al. (2004), the analyzed samples represent kerogen type II–III.

3.1. Molecular composition

The chromatograms of the saturate fractions for the extracts from the 18 rock samples reveal a strong odd-carbon-number predominance at n-C_{15}, n-C_{17} and n-C_{19} range. The predominance of odd carbon-numbered-low-molecular-weight n-alkanes in the carbon chain length range is a distinctive characteristic of marine algae as well as cyanobacteria inputs. The carbon preference index (CPI) was adjusted to the specific n-alkane range of carbon numbers in the studied samples. The CPI values are slowly decreasing with depth from 2.1 at the 2756 m to 1.04 at the 4551 m with exception in depth interval in 3136 and 3179 m (Table 2, Fig. 2).

The proportion of the C31 homohopane (22S) to the C31 homohopane (22R) was used to estimate the thermal maturity. The parameter S/(S + R)H31 (Table 3, Fig. 4) regularly increases with a depth from 0.24 to 0.59. An identical depth trend was observed for the homohopane index S/(S + R)H32. The ratio of T_s = C27 18a, 21b-trisnorhopane and T_m = C27 17a, 21b-trisnorhopane was applied as another thermal maturity parameter (Fig. 4). This parameter is applicable over the broad range of maturity (Peters et al., 2005). The parameter Ts/(Ts + Tm) decreases to 0.37 at a depth of 3744 m and increases up to 0.51 at a depth of 4551 m. The evaluated samples had a homogeneous lithology with a stable proportion of the clay fraction, thus the observed fluctuation of Ts/(Ts + Tm) is related likely to the thermal maturity changes.

3.2. Organic petrology

Microscopically, the composition of the Mikulov marls demonstrated the dominant role of the mineral matter (67.0–87.0%). The organic matter consists of macerals from the liptinite group (6.5–22.0%) with admixtures of inertinite (3.0–10.0%) as well as vitrinite (1.0–3.5%). The samples are fairly homogeneous, both lithologically and with respect to their maceral composition (Table 4). The precise classification of the organic particles was limited to the extremely fine grained nature of the majority of the studied samples. All the organic particles are rarely dispersed in the mineral matrix (Fig. 5). The dominant macerals within the liptinite group are liptodetrinite accompanied by a variable content of alginite, bituminite, sporadic sporinite and resinite (Fig. 5A, B). The liptodetrinite represents the fine grained dark gray fragments of liptinite macerals with a size lower than 5 μm and yellow to orange fluorescence color in reflected light. Liptodetrinite in fine-grained mineral matrix occurs together with the fine-grained or amorphous bituminite with dark orange to brown color fluorescence and brown color in reflected light. The identification of bituminite and liptodetrinite was very difficult due to the small size of these particles and their very close association with the clay minerals.

The alginite consists mainly of lamalginite (Fig. 5C, D), derived from small, unicellular or thin-walled colonial planktonic or benthonic algae, with a distinctive lamellar form with little recognizable structure. The translucency of the lamalginite is high, particularly in the fined grained parts of the sediments and is not distinguishable from the mineral matrix under normal reflected light. Its presence was identified under light irradiation due to strong yellow fluorescence (Taylor et al., 1998).

The telalginite represents alginite derived from large colonial or thick-walled unicellular algae with strong fluorescence and with a distinctive external structure. Telalginite was derived in our sample from Tasmanales algea (Fig. 5A, B) which was also sporadically found. The inner space of the alginite is occasionally filled with iron sulfide (pyrite).

The vitrinite macerals (Fig. 5E, F, and G) are present as collotelinite, vitrodetrinite, gelinite and rare telinite. The identification of the vitrinite macerals was extremely difficult due to their small size up to 30 μm and low amount. The dominant maceral was vitrodetrinite which is formed by fine fragments of vitrinite lower than 10 μm. The amorphous humic particles higher than 10 μm were classified as a gelinite and humic particles with an identical botanical structure were classified as a collotelinite. The random vitrinite reflectance was measured on the small number of particles (n = 5–23) and ranges between 0.55% and 0.75% R_r.

Inertinite macerals (Fig. 5H) are the second most abundant component of organic matter in samples. Dominant was inertodetrinite, which included inertinite macerals particles smaller than 10 μm. The particle size of white macrinite, fusinite, semifusinite, secretinite with reflectance values between 0.91% and 5.16% ranged from 10 mm to 150 μm and the reflectance values from 0.90% to 2.5%. There was not observed any micrinite in the examined samples.

4. Discussion

The optical analyses performed on borehole cores did not support data from Rock-Eval pyrolysis. According to the data, organic matter from the studied samples was classified as kerogen type II–III. These assumptions are broadly accepted throughout the literature (Francu et al.,

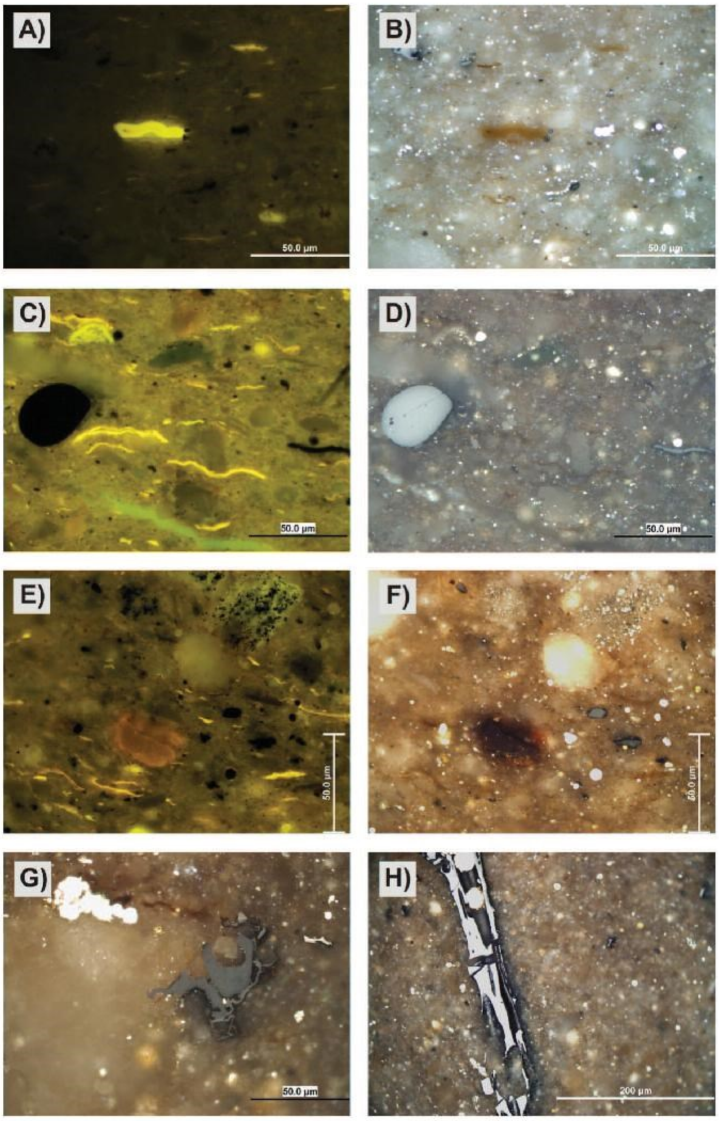

Fig. 5. Telalginite derived from Tasmanites in a mineral groundmass with dispersed liptodetrinite, fragments of lamalginite and inertodetrinite (depth 4131 m) in fluorescence mode A) and polarized light B); Lamalginite and nonfluorescing macrinite in a mineral groundmass with liptodetrinite and bituminite (depth 4277 m) in fluorescence mode C) and polarized light D). Probable brown resinite and vitrinite fragments and pyrite in a mineral matrix with dispersed liptodetrinite and bituminite (depth 3342 m) in fluorescence mode E) and polarized light F). Vitrinite-like structure ($Rr = 0.62\%$) in a mineral matrix (depth 3780 m) G). Fusinite with pyrite framboids in a mineral matrix (depth 4103 m) H). (For interpretation of the references to color in this figure legend, the reader is referred to the web version of this article.)

1996; Picha et al., 2006). A detailed examination of the polished surfaces demonstrated the dominant role of the macerals from the liptinite group with admixtures of inertinite (Fig. 6). The amount of the terrigenous maceral, such as vitrinite and terrigenous liptinite and sporinite, was extremely low.

The results from the gas chromatography reveal the dominance of n-C_{15}, n-C_{17} and n-C_{19} n-alkanes. These n-alkanes are regarded as being derived from marine algae. A minor proportion of the n-C_{21-25} n-alkanes was observed corresponding to a low amount of the terrestrial material found in the polished surfaces.

The misleading interpretation of the HI and OI indexes from the Rock-Eval pyrolysis can be explained as follows. The organic matter in the majority of the samples is on the narrow boundary of the immature/mature range. The HI may thus be representative of the original material and the initial quality of the deposited organic matter (Espitalie et al., 1984). The reduction of the HI can also be due to presence of active minerals such as smectite and illite (Davis and Stanley, 1982; Dembecki, 1992; Peters, 1986). There is a high amount of the clay minerals (up to 20%) in all the examined samples. Minerals such as illite and kaolinite are predominating in the clay fraction.

The vitrinite reflectance increases steadily from 0.56% at a depth of 2445 m to 0.75% at a depth of 4551 m (Fig. 6). At a corresponding depth, the T_{max} fluctuates between 429 and 433 °C. The parameter $S/(S + R)$ H32, which is widely used for estimation of the thermal

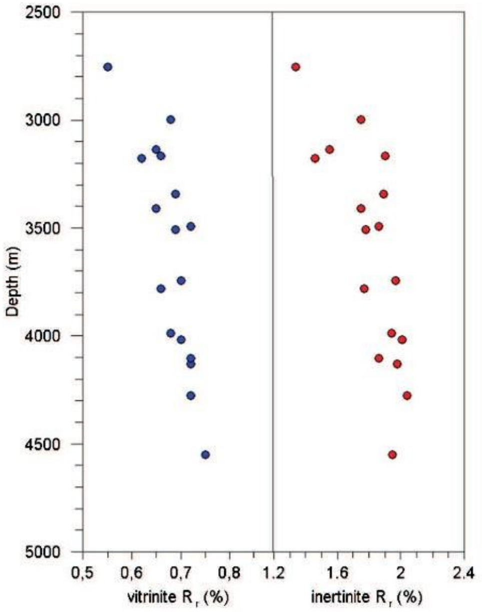

Fig. 6. Increase in the thermal maturity with a depth measured as random vitrinite reflectance (a) and random inertinite reflectance (b) for the Mikulov Marls.

maturity (Farrimond et al., 1998) particularly within the early stages of the maturation reaches 0.52 at a depth of 3491 m. The corresponding vitrinite reflectance is 0.7 R_r % in Mikulov Marls. According to Schoell et al. (1983), the equilibrium for the 32 hopanes occurs at a vitrinite reflectance of cca 0.5%. Observed shift can be related to the small number of particles available for vitrinite reflectance measurement.

The data from petrographic maceral analyses were plotted to the ternary plot (Fig. 7) based on Littke and Sachsenhofer (1994). The Mikulov Marls are interpreted as the basinal facies of the Upper Jurassic continental slope (Picha et al., 2006). The maceral composition with prevailing alginite, low vitrinite and inertinite suggest that the Mikulov Marls were deposited in the marine environment with important role of upwelling processes.

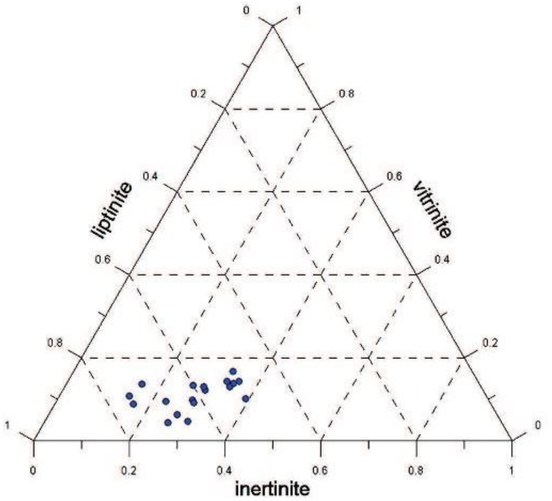

Fig. 7. Petrographic composition of organic matter in the Mikulov Marls source rock on the ternary plot according to Littke and Sachsenhofer (1994).

5. Conclusions

Organic petrographic investigation on the Jurassic Mikulov Marls reveals that organic matter is homogeneous in composition. The dominant maceral group in all examined samples are macerals from liptinite group namely – liptodetrinite, alginite, bituminite. The alginite consists mainly of lamalginite, derived from colonial planktonic or benthonic algae. The amount of the terrigenous maceral such as vitrinite and sporinite is extremely low (average 11%). Based on these observations the organic matter in the Mikulov Marls belong to the kerogen type II. The fact restricts the use of the CPI parameter for thermal maturity. The CPI is an index used for evaluating the thermal maturity of source rocks. In the case of the Mikulov Marls, however, CPI cannot be used because the proportion of organic matter from terrestrial plants is minor and its initial value is very low (1 to 2). For these reasons, it is not predictive of the thermal maturity of the organic matter present and thus even does not correlate with other parameters of thermal conversion.

The maceral consistency in all examined samples allowed an evaluation of thermal maturity using $Ts/(Ts + Tm)$ and hopane isomerization ratios. The beginning of the oil window was positioned at 3491 m based on hopane isomerization. At this depth the $S/(S + R)$ C31 index reach 0.52 and $Ts/(Ts + Tm)$ is equal to 0.37. The corresponding vitrinite reflectance for the beginning of oil generation is 0.7 R_r % and inertinite reflectance 1.8%. The parameter T_{max} varies at the depth 3491 m from 423 to 436 °C. The low correlation between parameters in the shallower depth (0–3500 m) is explained as the effect of the immature organic matter.

Acknowledgments

This study benefited from the Masaryk University project MUNI/M/0081/2013 and could not have been completed without the support from MND a.s. Special thanks go to Jana Hamršmídová who has been extremely helpful during the various phases of the research.

References

Adamek, J., 2005. The Jurassic floor of the Bohemian Massif in Moravia — geology and paleogeography. Bull. Geosci. 80 (4), 291–305.

Akinlua, A., Ajayi, T.R., Jarvie, D.M., Adeleke, B.B., 2005. A re-appraisal of the application of Rock-Eval pyrolysis to source rock studies in the Niger Delta. J. Pet. Geol. 28, 39–47.

Behar, F., Beaumont, V., De, B., Penteado, H.L., 2001. Rock-Eval 6 technology: performances and developments. Oil Gas Sci. Technol. Rev. IFP 56, 111–134.

Blížkovský, M., Kocak, A., Morskovský, M., Novotný, A., Gaza, B., Kostelníček, P., Hlavatý, V., Lunga, S., Vass, D., Franců, J., Müller, P., 1994. Exploration History, Geology and Hydrocarbon Potential in the Czech Republic and Slovakia. In: Popescu, B.M. (Ed.), Hydrocarbons of Eastern Central Europe, Habitat, Exploration and Production History. Springer-Verlag, Berlin, pp. 71–117.

Bordenave, M.L., Espitalie, J., Leplat, P., Oudin, J.L., Vandenbroucke, M., 1993. Screening techniques for source rock evaluation; tools for source rock routine analysis; Rock-Eval pyrolysis. In: Bordenave, M.L. (Ed.), Applied petroleum geochemistry, pp. 217–278.

Dahl, B., Bojesen-Koefoed, J., Holm, A., Justwan, H., Rasmussen, E., Thomsen, E., 2004. A new approach to interpreting Rock-Eval S2 and TOC data for kerogen quality assessment. Org. Geochem. 35, 1461–1477.

Davis, J.B., Stanley, J.P., 1982. Catalytic effect of smectite clays in hydrocarbon generation revealed by pyrolysis-gas chromatography. J. Anal. Appl. Pyrolysis 4, 227–240.

Dembecki Jr., H., 1992. The effects of the mineral matrix on the determination of kinetic parameters using modified Rock-Eval pyrolysis. Org. Geochem. 18, 531–539.

Ebukanson, E.J., Kinghorn, R.R.F., 1985. Kerogen facies in the Major Jurassic Mudrock Formations of Southern England and the implication on the depositional environments of their precursors. J. Pet. Geol. 8, 435–462.

Eliáš, M., Wessely, G., 1990. The autochtonous Mesozoic on the east flank of the Bohemian Massif — an object of mutual geological efforts between Austria and Czechoslovakia. In: Minaříková, H., Lobitzer, H. (Eds.), Thirty years of geological cooperation between Austria and Czechoslovakia. Federal Geological Survey Vienna – Geological Survey Prague, pp. 78–83.

Espitalie, J., Senga Makadi, K., Trichet, J., 1984. Role of the mineral matrix during kerogen pyrolysis. Org. Geochem. 6, 365–382.

Farrimond, P., Taylor, A., Telnaes, N., 1998. Biomarker maturity parameters: the role of generation and thermal degradation. Org. Geochem. 29, 1181–1197.

Francu, J., Radke, M., Schafer, R.G., Poelchau, H.S., Čáslavslý, J., Boháček, Z., 1996. Oil–oil and oil-source rock correlation in the northern Vienna basin and adjacent Carpathian Flysch Zone (Czech and Slovak area). In: Wessely, G., Liebl, W. (Eds.), Oil and gas in Alpidic thrustbelt and basins of Central and Eastern Europe. EAGE Special Publication 5. Geological Society, London, p. 456.

Goodarzi, F., Higgins, A.C., 1987. Optical properties of scolecodonts and their use as indicators of thermal maturity. Mar. Pet. Geol. 4, 353–359.

Goodarzi, F., Norford, B.S., 1985. Graptolites as indicators of the temperature histories of rocks. J. Geol. Soc. Lond. 142 (6), 1089–1099.

Hakimi, M.H., Wan Hasiah, A., 2013. Organic geochemical characteristics and oil generating potential of the Upper Jurassic Safer shale sediments in the Marib-Shabowan basin, western Yemen. Org. Geochem. 54, 115–124.

Hutton, A.C., 1987. Petrographic classification of oil shale's. Int. J. Coal Geol. 8, 203–231.

International Committee for Coal and Organic Petrology, 1998. The new vitrinite classification (ICCP system 1994). Fuel 77, 349–358.

International Committee for Coal and Organic Petrology, 2001. The new inertinite classification (ICCP system 1994). Fuel 80, 459–471.

Katz, B.J., 1983. Limitations of 'Rock-Eval' pyrolysis for typing organic matter. Org. Geochem. 4, 195–199.

Ladwein, H.W., 1988. Organic geochemistry of Vienna Basin. Model for hydrocarbon generation overthrust belts. AAPG Bull. 72, 586–599.

Lafargue, E., Marquis, F., Pillot, D., 1998. Rock-Eval 6 applications in hydrocarbon exploration, production, and soil contamination studies. Oil Gas Sci. Technol. Rev. IFP 53, 421–437.

Littke, R., Sachsenhofer, R.F., 1994. Organic petrology of deep sea sediments: a compilation of results from the Ocean Drilling Program and the Deep Sea Drilling Project. Energy Fuel 8, 1498–1512.

Littke, R., Bayer, U., Gajewski, D., Nelskamp, S., 2008. Dynamics of Complex Intracontinental Basins The Central European Basin System. Springer.

Nehyba, S., Šikula, J., 2007. Depositional architecture, sequence stratigraphy and geodynamic development of the Carpathian Foredeep (Czech Republic). Geol. Carpath. 58 (1), 53–69.

Peters, K.E., 1986. Guidelines for evaluating petroleum source rock using programmed pyrolysis. AAPG Bull. 70, 318–329.

Peters, K.E., Walters, C.C., Moldowan, J.M., 2005. The Biomarker Guide. Cambridge University Press.

Picha, F.J., Stranik, Z., Krejci, O., 2006. Geology and hydrocarbon resources of the Outer Western Carpathians and their foreland, Czech Republic. In: Golonka, J., Picha, F.J. (Eds.), The Carpathians and their foreland: geology and hydrocarbon resources. AAPG Memoir 84, pp. 49–175.

Riediger, C., Goodarzi, F., Macqueen, R.W., 2011. Graptolites as indicators of regional maturity in lower Paleozoic sediments, Selwyn Basin, Yukon and Northwest Territories, Canada. Can. J. Earth Sci. 26 (10), 2003–2015.

Schoell, M., Teschner, M., Wehner, H., Durand, B., Quedin, J.L., 1983. Maturity related biomarker and stable isotope variations and their application to oil/source rock correlation in the Mahakam Delta, Kalimantan. In: Bjoroy, M., Albrecht, C., Cornford, C. (Eds.), Advances in Organic Geochemistry 1981. John Wiley and sons, New York, pp. 156–163.

Taylor, G.H., Teichmüller, M., Davis, A., Diessel, C.F.K., Littke, R., Robert, P., 1998. Organic Petrology. Gebrüder Borntraeger, Berlin.

Teichmüller, M., Taylor, G.H., Littke, R., 1998. The nature of organic matter – macerals and associated minerals. In: Taylor, G.H., Teichmüller, M., Davis, A., Diessel, C.F.K., Littke, R., Robert, P. (Eds.), Organic Petrology. Gebrüder Borntraeger, Berlin, pp. 175–274.

Tissot, B.P., Welte, D.H., 1984. Petroleum Formation and Occurrence. 2nd edn. Springer, Berlin Heidelberg New York.

Příloha 9

Geršlová E., Schwarzbauer J. (2014) Hydrocarbon-based indicators for characterizing potential sources of coal-derived pollution in the vicinity of the Ostrava City. Environmental Earth Sciences, Springer, 71, 7,

Hydrocarbon-based indicators for characterizing potential sources of coal-derived pollution in the vicinity of the Ostrava City

Eva Geršlova & Jan Schwarzbauer

Environmental Earth Sciences

ISSN 1866-6280
Volume 71
Number 7

Environ Earth Sci (2014) 71:3211-3222
DOI 10.1007/s12665-013-2709-0

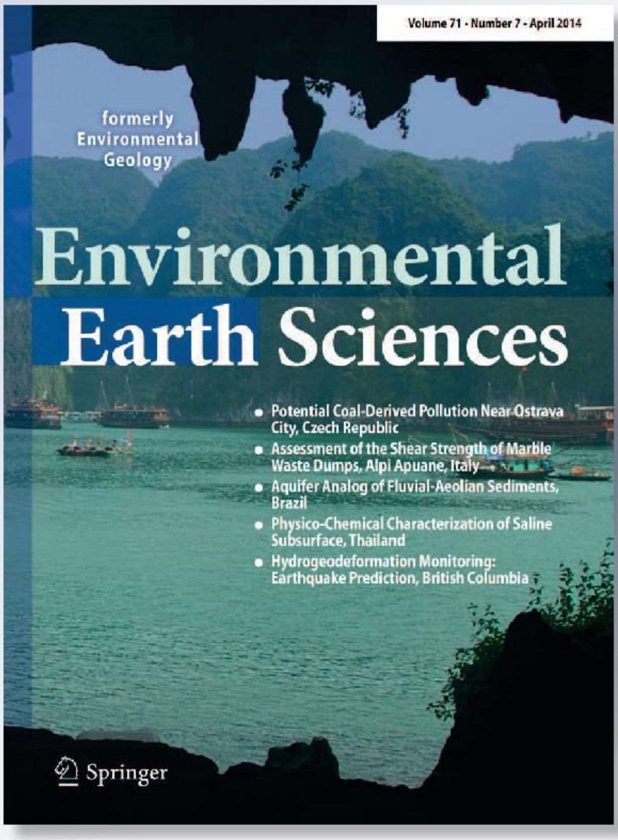

Springer

Environ Earth Sci (2014) 71:3211–3222
DOI 10.1007/s12665-013-2709-0

ORIGINAL ARTICLE

Hydrocarbon-based indicators for characterizing potential sources of coal-derived pollution in the vicinity of the Ostrava City

Eva Geršlova · Jan Schwarzbauer

Received: 25 April 2013 / Accepted: 31 July 2013

Abstract Coaly material enters various environmental compartments from different emission sources and on diverse pathways. The complexity of both the emission processes and the quality of contamination in the Ostrava region avoids a simple source correlation for coal-derived pollution. Hence, this study focused on the application of different geochemical approaches for source apportionment using bulk parameters, aliphatic biomarkers and source-specific PAH ratios. Major aim was to prove the effectiveness of the applied methods for characterizing the impact of coal-derived contamination in complex emission systems such as in the Ostrava region. Individual emission sources were discriminated sufficiently by TOC vs. TEH relationship and two-dimensional correlations of PAH ratios. Additionally, aliphatic biomarkers revealed individual signatures for all classes of samples and pointed to a widespread distribution of fossil material also in the hydrosphere. On the contrary, indicative PAH ratios documented a dominance of pyrogenic over petrogenic-derived organic matter in the lake sediments investigated. These contradictory descriptions demonstrate clearly that only a comprehensive application of different marker systems allows a detailed view on the quality and quantity of coal-derived pollution. Lastly, it remains unclear whether coaly material in aquatic sediments acts as sink or source for PAHs. A proposed indicative marker, the ratio of phenanthrene over retene, failed.

Keywords Coal-derived contamination · Emission sources · PAHs · Biomarker · Sediments

E. Geršlova
Masaryk University, Kotlářská 2, 602 00 Brno, Czech Republic

J. Schwarzbauer (✉)
Institute of Geology and Geochemistry of Petroleum and Coal, Aachen University of Technology (RWTH), Lochnerstr. 4-20, 52056 Aachen, Germany
e-mail: jan.schwarzbauer@emr.rwth-aachen.de

Introduction

The usage of coal as fossil fuel results in a huge impact on the environment, where the emission of coal material and associated pollutants is of elevated environmental relevance. Coaly material enters environmental compartments from different emission sources and on diverse pathways. Atmospheric deposition, leaching from waste deposits and direct emissions from mining areas are the main pathways on which coaly material and associated pollutants enter the aquatic environment. Interestingly, studies on coal particle emission to the aquatic environment are less reported and focused on heavily affected regions like harbors or coal production sites. Further on, dominantly the association of coaly material with corresponding pollutants, in particular polycyclic aromatic hydrocarbons PAHs has been investigated (e.g., Ghosh et al. 2000; Wang et al. 2001; Gu et al. 2003; Pies et al. 2008a).

Coaly material spread to the environment might be of interest not only due to the primary emission of coal-specific pollutants (e.g., Achten and Hofmann 2009), but also due to its role in sorption and transport of pollutants as a secondary aspect of environmental relevance. Several studies pointed to coal particles as major domain for accumulation of lipophilic contaminants, in particular PAHs (e.g., Yang et al. 2008). Since PAHs are both constituents of coals and widespread distributed pollutants from other source (e.g., in situ formation by pyrolytic processes), an unambiguous designation of coal-associated PAHs as intrinsic pollutants or migrated contamination has been reported only very rarely (e.g., Achten et al. 2011).

From a chemical point of view, coal-derived emissions are not homogeneous. It has been pointed out that some intrinsic properties (e.g., maturity, maceral composition) affect the chemical composition of the coal and its releasable contamination (e.g., Stout and Emsbo-Mattingly 2008). Further on, secondary processes, that coal material is subjected to after release from its natural seams (e.g., weathering, technical production and leaching), alter also the coaly material. Hence, both the composition of emitted pollutants and the adsorption properties of environmentally relevant coaly material vary highly.

Noteworthy, in old mining areas coal particles have different environmental fates resulting in different chemical compositions and contamination potentials. This accounts also for the Upper Silesian Coal Basin as one of the larger bituminous coal basins in Europe where the mining history started in the second half of the nineteenth century with extensive production increase in the 1950–1970s (Starý 2004). The average annual coal production is currently around 12 million tons. The barren rock from the mines amounts to 0.65 billion tons since 1963 (Martinec et al. 2006) and is partly left in the mines as backfill, partly taken to the surface and dumped on the spoil banks, as well as used for other purposes, e.g., landfills.

In the Ostrava region, as part of the Upper Silesian Coal Basin area, the massive transfer of material from the mines to the surface results in a modified landscape with subsided depressions, accumulated spoil heaps, and associated flow of mining water into the rivers and mine gas transfer to the atmosphere. In particular, the spoil banks and settling lakes become primary objects of remediation since they are suspected to have an elevated contamination potential for the Ostrava region.

These spoil banks are highly individual in composition, age, position in the landscape and industrial sources of contaminants. The barren rocks in the spoil banks consist of conglomerates, sandstones, graywakes, arcoses, siltstones and shale's of mainly Carboniferous and party Cretaceous-to-Miocene age excavated from the collieries. Carboniferous barren rocks include coal particles ranging from centimeter to micrometer size. The barren rocks are deposited together with the process water in the settling lakes as fine-grained flotation and coal slurry. The coal-to-country rock ratio in the spoil banks is controlled by the petrographic composition of the exploited layer, mining technology, and the coal beneficiation treatments used.

Besides potential emissions from spoil banks and other deposits also contamination by fly ashes are suspected as the result of coal combustion processes. Coal has been used in electrical power plants in this area since 1850 and huge amounts of fly ashes have been dumped for decades.

In order to characterize or distinguish emission sources some organic geochemical approaches have been used. With respect to fossil material the analysis of indicative hydrocarbons are preferred. On the one hand, specific PAH ratios have been intensively used to distinguish petrogenic and pyrolytic emission sources in various environments (e.g., Barra et al. 2008; Wang et al. 1999, 2012; Ding et al. 2007; Pies et al. 2008b; Zhang et al. 2008, Lehndorff and Schwark 2009; Halek et al. 2010; Navarro-Ortega et al. 2011; Hu et al. 2011; Shukla et al. 2012; Tay and Biney 2013). Particularly, Yunker et al. (2002) investigated very detailed the effectiveness and practicability of individual PAH ratios as proxy for differentiating diverse pyrolytic sources from petrogenic pollution in sediments and soils. On the other hand, also aliphatic hydrocarbons, in particular *n*-alkanes, hopanes and steranes, have been used to trace the impact of contaminations by petroleum or coaly material (e.g., Aboul-Kassim and Simoneit 1995; Faure et al. 2000; Yunker and Macdonald 2003; Faure et al. 2006; Farias et al. 2008).

The complexity of both the emission processes and the quality of contamination in the Ostrava region avoids a simple source correlation. Hence, this study focused on the application of different geochemical approaches for source apportionment ranging from comparison of bulk parameters to specific PAH ratios. Major aim is to prove the effectiveness of the applied methods for characterizing the impact of coal-derived contamination in complex emission systems such as in the Ostrava region.

Methods

Sample material

In autumn 2006 a set of 63 sediment and coal samples from the Ostrava area were collected. The environmental samples were taken from different compartments, which were known or suspected to be influenced by or related to the coal mining activities. After sampling the particulate material was stored in hermetically closed glass jars, and cooled at 4 °C. All equipment used for sampling was intensively rinsed with solvents prior to usage.

The sampling was aimed to cover all kinds of the coal-related spots. Accordingly, the sample set can be subdivided into five groups having similar features:

- *Coal seams (9 samples, CS1-9)* The coal samples from the two main formation in the Upper Silesian Basin Ostrava and Karvina covering range of the vitrinite reflectance from 1.1 to 1.8 % of Ro.

- *Coaly waste deposit (4 samples CW1-4)* Places not public accessible, containing mixture of eye visible coal particles from mining with other industrial waste mainly originating from coking and plants.
- *Spoil dumps (15 samples, SD1-15)* Mostly remediated and for recreation purpose used dry land areas on the former dumps behind coal preparation plants. These samples contain fine-to-coarse coaly particles unaffected by high-temperature processes. However, a first group of samples represented dry material (SD1-8), whereas SD9-15 was characterized as wet material.
- *Fly ash dumps (7 samples, FA1-7)* Material from the dumps behind the separators of the particulate matter in the power plants and steel works. The matrix is built by cinder and slag partly decomposed and converted to clay material in the lake.
- *Lake sediments (28 samples, LS1-28)* Four core and two surface sediment samples from recreation and fishing lakes, brooks and a reservoir. These sediments may be contaminated by the coal emission sources. In the brooks and other open spots the place was cleaned from vegetation and first 5 cm of the sediment were removed and the fresh samples were collected.

Chemical analysis of sediments

Bulk analysis

The natural wet samples were dried, pulverized, homogenized and sieved through a 1-mm mesh prior to all following analyses (bulk analyses, GC analyses, etc.). All samples were subjected to elemental analysis of total organic (TOC), total inorganic carbon (TIC) and total sulphur (TS) using an Eltra Metalyt CS 100/1000S apparatus.

Sample preparation

Sample aliquots of 5 g were mixed with anhydrous Na_2SO_4, spiked with 25 μL of internal standard solution containing 5 ng/mL of *o*-terphenyl and 10 ng/μL of androstane. Extraction was performed with DCM/MeOH (93:7) by accelerated solvent extraction (Dionex ASE® 100 apparatus). The parameters of the ACE procedure were: temperature 80 °C, static time 8 min, flush volume 60 %, purge time 100 s and static cycle 1. The raw extracts were evaporated to dryness under a gentle stream of N_2, and redissolved in 10 mL of *n*-hexane.

GC analysis

For the determination of total extractable hydrocarbons (TEH) aliquots of 0.5 mL of the raw extracts were dried and fractionated by liquid chromatography using 2 g of activated florisil and 2 g of Na_2SO_4 as stationary phase and hexane as eluent. Polar compounds were removed by this procedure and the obtained fraction with aliphatic and aromatic hydrocarbons were subjected to gas chromatographic analyses on an AT 5890 (Agilent Technologies, USA) equipped with flame ionization detector (FID) and a FSOT capillary column with non-polar HP5 phase (25 m, i.d. 0.25 mm and 0.5 μm stationary phase). The amount hydrocarbons eluting in the retention time window between n-C_{10} to n-C_{40} was calculated by peak integration and external standard calibration.

GC/MS analysis

Prior to GC/MS analyses an aliquot of 2 mL of the raw extract was placed on a 2 g silica gel column to separate the aliphatic and aromatic hydrocarbon fractions by liquid chromatography using *n*-hexane and DCM as eluents. Powder copper was added overnight to the aliphatic fraction in order to remove elemental sulfur.

A Hewlett-Packard 6890N GC with a HP 5973N MSD operated in the electron impact mode (EI^+) was used. Measurements were performed in full scan mode scanning from *m/z* 50 to *m/z* 550. Samples were injected splitless onto a HP-1MS capillary column (60 m length × 0.25 mm i.d. × 0.25 μm film thickness, Agilent Technologies, USA). Separation was carried out using helium at a constant flow of 1.2 ml/min with the following oven temperature program: 50 °C (held for 1.2 min), then at 5 °C/min to the final temperature of 300 °C (held for 3 min). The GC/MS interface temperature was held at 280 °C and the ion source temperature at 280 °C. Identification of the compounds was based on comparison of mass spectral data with those of authentic reference materials.

Quantitative data of PAHs were obtained by integration of specific ion chromatograms using calibration by an internal standard (*o*-terphenyl). Results were validated using commercially available reference material Metranal2. From this validation measurements standard deviations for selected PAHs were determined between 10 and 20 %. Limit of quantitation was 0.05 mg/g. Determination of hopanes was based on integration of a specific ion chromatogram (*m/z* 191), calibrated by androstane as the internal standard.

Results and discussion

The environment in the Ostrava region is significantly affected over decades by coaly material as a result of intensive mining activities. Not only active coal mining but in particular the coal waste management has to be considered as main pollution source. Hence, the type of coaly contamination differs according to technical treatment or the depositional conditions of coaly waste as described in the introduction. Geochemical alterations of coal-derived organic matter in the different sample sets investigated in this study influenced the chemical composition. Accordingly, geochemical signatures of different types of coaly waste samples should be a useful tool to differentiate environmentally relevant pollution sources. This forensic approach has been applied by investigating four different types of coaly waste, comprising coal seam material, spoil banks, fly ash dumps and an old coaly waste deposit. Further on, a potential impact on the environment has been studied by analyses of lake sediments.

Discrimination of sample material by bulk parameters

The geochemical bulk parameters illustrated the variability and specificity of the five selected sample groups (Table 1). Overall ranges were 0.2–87.9 % for total organic carbon (TOC) values, <0.1–7.2 % for total inorganic carbon (TIC) values and <0.1–2.1 % for sulphur content. However, a more detailed view on the different data sets derived from the specific sample groups revealed a more systematic change of bulk properties.

The samples of the *coal seams* exhibited elevated TOC values around 63–88 %, very low carbonate content (0.1–0.9 % TIC) and also low total extractable hydrocarbon yields (20–187 mg/kg TEH). The black sediments from the *coaly waste residues* are rich in TOC (43–64 %), probably due to high amount of carbonaceous material. Also higher TEH (825–1,890 mg/kg) and sulfur values (0.5–0.7 %) have been measured. Spoil dump samples, containing abundant visible coal particles, had TOC values higher than 11 %, variable inorganic carbon values from almost zero to 7 % TIC, and TEH values of 40–2,428 mg/kg.

Fly ash dump samples differ totally from the other sample groups due to very low amount of sulfur and TEHs. Interestingly, the TOC values detected were not around zero as expected for residues after high-temperature combustion, but ranged from 0.6 to 4.7 %. This fact indicates that the combustion of coal was either not complete or that in some cases the material was contaminated by external organic matter as a result of long-lasting dumping. The *lake sediments* had low TOC values from 0.2 to 9.3 %, TIC values from 0.1 to 1.6 %, TEH content from the limit of quantification up to 1,890 mg/kg, and sulphur content ranging from <0.1 to 2.1 %).

However, although bulk parameters are useful and fast analytical tools to characterize organic matter samples differentiation based on one parameter remain insufficient with respect to more comprehensive environmental investigations. Solely the TOC parameter seemed to have a remarkable potential for distinguishing the different sample sets due to its broad range of detected values and its slightly significant differences for individual sample sets. However, a two-dimensional correlation of these bulk parameters might act as a more appropriate discriminating tool.

For these purposes TOC values have been chosen as primary parameter due to its slight separation potential. The correlation of TOC with TIC, TS and TEH has been illustrated in Figs. 1, 2, 3. Correlation of TOC over TIC (Fig. 1) revealed no individual grouping because TIC cover a wide range in nearly all subsample sets, e.g., for spoil dump samples from <0.1 to 7.2 %. Only a slightly better correlation was found for TS over TOC (Fig. 2). Generally a positive and very similar correlation for the coaly material (SD, CS, CW) was obvious for all samples with exception of fly ash samples, which exhibited constantly very low TS values. However, a distinct separation of the individual sample sets was not achieved.

The highest potential to distinguish the five sample sets was achieved by the correlation of the TOC and TEH as illustrated in Fig. 3. The generally more wide spread distribution of the lake samples reflects the multiple emissions affecting this aquatic system. All four sample sets, representing the potential emission sources for coal-related pollutions in the Ostrava region, showed closer distributions with either higher TOC or TEH values, respectively. Interestingly, the TEH values discriminate the dry and wet spoil dumps from one another. Obviously, dryness results in loss of extractable hydrocarbons maybe as a result of evaporation or enhanced aerobic microbial transformation.

Generally, the correlation of the bulk parameters was used to better classify the studied types of samples. There is a clear correlation of fairly high sulfur and TEH values with the TOC in the coaly materials (CS, SD, CW, FA samples). On the contrary, the lake sediments showed a significant offset towards lower TOC for similar TS, PAH, and TEH values. Nevertheless, solely the TOC vs TEH correlation was appropriate to distinguish between different sample sets and, therefore, to discriminate the corresponding potential emission sources of coaly material in the Ostrava region.

Aliphatic biomarker compounds

For a more detailed assessment of fossil matter-derived environmental contamination, the investigation of aliphatic molecular marker substances has been successfully introduced as a geochemical forensic tool (e.g., Kaplan et al. 1997). Therefore, in this study organic geochemical analyses focused partially on some source-specific aliphatic biomarker compounds. *n*-Alkanes and selected isoprenoids

Table 1 Bulk parameters measured in samples from Ostrava region

Sample		TIC % m/m	TOC % m/m	TS % m/m	TEH mg/kg
CS1		0.3	81.7	0.5	<20
CS2		0.4	87.9	0.5	<20
CS3		0.4	87.1	0.6	42
CS4		0.4	75.0	0.6	187
CS5		0.9	72.2	1.2	33
CS6		0.4	71.9	0.6	66
CS7		0.5	86.3	0.3	<20
CS8		0.1	86.4		
CS9		0.1	63.4	1.4	<20
SD1		7.2	23.2	0.2	132
SD2		0.0	23.7	0.1	47
SD3		3.5	15.1	0.1	40
SD4		0.9	13.4	0.1	48
SD5		0.0	17.4	0.1	63
SD6		2.5	15.8	0.2	72
SD7		0.8	11.4	0.2	81
SD8		5.2	17.3	0.2	72
SD9		0.1	29.8	0.4	866
SD10		0.2	27.2	0.3	664
SD11		0.3	28.0	0.2	799
SD12		0.5	28.3	0.3	1,152
SD13		1.4	27.7	0.3	677
SD14		0.1	50.2	0.5	1,435
SD15		0.1	48.1	0.4	2,428
FA1		3.2	3.3	0.0	<35
FA2		0.2	4.5	0.0	<20
FA3		0.2	4.6	0.0	<20
FA4		0.1	0.6	0.0	<20
FA5		0.3	1.3	0.0	<20
FA6		0.2	3.0	0.0	31
FA7		0.3	4.7	0.0	<20
CW1		0.1	43.5	0.6	825
CW2		0.1	43.1	0.5	1,798
CW3		0.1	45.9	0.6	887
CW4		1.5	64.7	0.7	1,890
LS1	Core 1: 0–30 cm	0.1	9.3	2.0	1,890
LS2	Core 1: 30–40 cm	0.2	6.8	2.1	238
LS3	Core 1: 40–50 cm	0.1	3.6	1.0	202
LS4	Core 1: 50–60 cm	0.0	2.3	0.3	83
LS5	Core 1: 60–70 cm	0.1	1.6	0.1	61
LS6	Core 2: 0–15 cm	1.2	3.9	0.1	280
LS7	Core 2: 15–30 cm	1.6	3.9	0.2	419
LS8	Core 2: 30–45 cm	1.3	3.6	0.3	331
LS9	Core 2: 45–60 cm	1.0	3.7	0.3	294
LS10	Core 2: 60–75 cm	1.2	3.9	0.3	361
LS11	Core 2: 75–90 cm	0.9	4.0	0.3	468
LS12	Core 2: 90–120 cm	1.4	3.9	0.2	459
LS13	Core 2: 120–140 cm	1.5	4.0	0.2	421
LS14	Core 2: 140–160 cm	0.8	3.8	0.3	266
LS15	Core 2: 160–180 cm	0.7	3.1	0.2	243
LS16	Core 2: 180–185 cm	0.1	0.7	0.0	<20
LS17	Surface sediment	0.1	7.3	0.3	910
LS18	Surface sediment	0.1	8.0	0.2	660
LS19	Core 3: 0–4 cm	0.2	2.2	0.0	53
LS20	Core 3: 4–9 cm	0.1	1.3	0.2	28
LS21	Core 3: 9–13 cm	0.1	0.7	0.1	<20
LS22	Core 3: 13–19 cm	0.1	0.4	0.0	<20
LS23	Core 3: 30–40 cm	0.1	0.2	0.0	<20
LS24	Core 4: 10–15 cm	0.1	4.2	0.1	76
LS25	Core 4: 25–35 cm	0.1	2.9	0.3	111
LS26	Core 4: 45–56 cm	0.1	0.4	0.0	<20
LS27	Core 4: 56–66 cm	0.1	4.2	0.3	201
LS28	Core 4: 67–81 cm	0.1	8.4	0.3	181

CS coal seam samples, *SD* spoil dumps, *FA* fly ash samples, *CW* coaly waste deposits, *LS* lake sediments, *TIC* total inorganic carbon, *TOC* total organic carbon, *TS* total sulphur, *TEH* total extractable hydrocarbons

showed characteristic fingerprints (Fig. 4) that allowed to discriminate the various types of samples. In particular, coal-related samples, lake sediments and fly ash samples were distinguished based on the signature of their aliphatic fractions.

Coal-related samples (coal seam, spoil dump, coaly waste deposit) were enriched in *n*-alkanes in the *n*-C_{13} to *n*-C_{21} range with a balanced odd/even ratio of the homologues. With respect to acyclic isoprenoids the relative contribution of pristane and phytane were also more or less balanced. However, the *n*-alkanes prevail over the isoprenoids indicating only a minor degree of biodegradation. On the contrary, lake sediments differ significantly regarding their aliphatic signature. Firstly, a high variation within this subsample set was observed. Further on, *n*-alkanes were of minor importance, but isoprenoids dominated frequently this fraction. Solely *n*-C_{17} appeared as dominant alkane in numerous samples reflecting the contribution of fresh algae material.

The pattern of aliphatic hydrocarbons allowed to distinguish between samples with high contribution of coaly material and environmental samples. However, this observation does not allow to estimate the contribution of coaly material to lake sediments, since transformation and degradation processes might affect heavily the pattern of aliphatic hydrocarbons in the subaquatic samples.

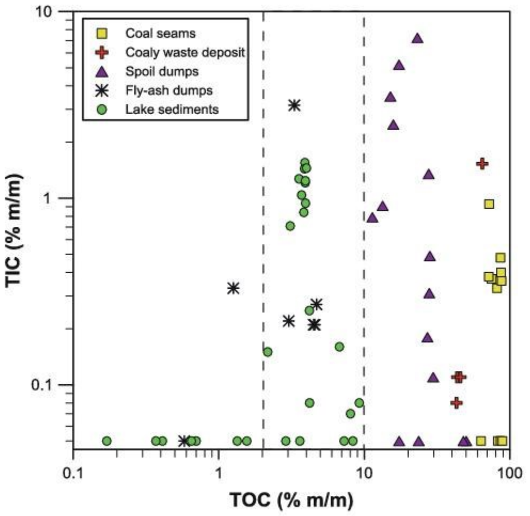

Fig. 1 Correlation of total organic carbon (TOC) and total inorganic carbon (TIC)

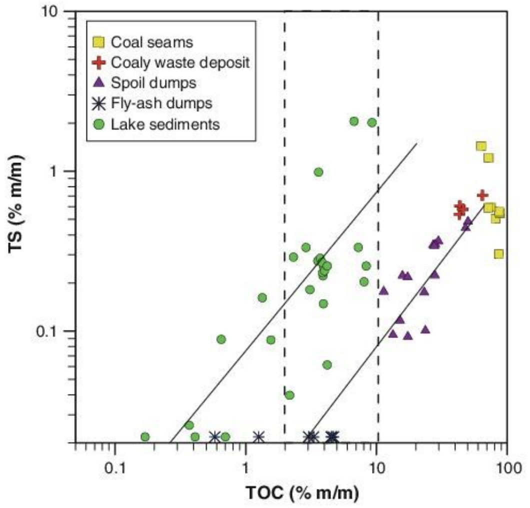

Fig. 2 Total organic carbon (TOC) correlated with total sulfur (TS)

Besides n-alkanes and some acyclic isoprenoids a significant contribution of the so-called unresolved complex mixture (UCM) appeared in the gas chromatograms. A more bimodal shape of the UCM is obvious with slight variation in samples from coal seams, spoil dump, and coaly waste residues (Fig. 4). A first maximum in the range of n-C_{18} to n-C_{24} is followed by a second maximum coeluting with hopanes. Noteworthy, in lake sediment samples solely the second UCM appears.

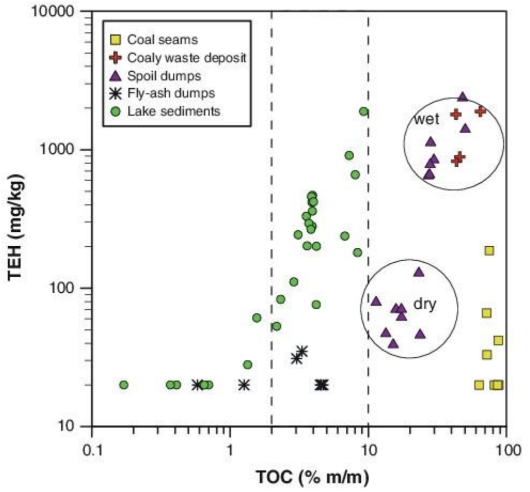

Fig. 3 Total extractable hydrocarbons (TEH) correlated with total organic carbon (TOC)

A second approach based on biomarker compounds focuses on the determination of specific cyclic isoprenoids. Hopane and sterane ratios reflect the thermal maturity of fossil matter. In this study three hopane and one sterane parameter have been calculated (see Table 2). These values provide information on the relative quantity of biogenic but less thermodynamically stable isomers as compared to geogenic and more stable isomers. This is, for example, reflected by the trisnorhopanes for which the transformation from T_m to T_s with increasing thermal maturity can be observed leading to an equilibration of both isomers. Hence, the T_s to T_m ratio (calculated as $T_s/(T_s + T_m)$ starts at zero and is around 0.5 in the steady-state. Therefore, the detected values around 0.4–0.5 in the coaly material (see also average values in Table 2) reflect the thermal maturity of Ostrava coal. The same range of values (see also average values in Table 2) in the spoil dumps reflects also the contribution of fossil matter, the mature coal material. On the contrary, lake sediments with values between 0.2 and 0.4 (average value 0.31, see Table 2) represent the mixture of recent and fossil matter, since we can assume that thermodynamically driven diagenetic processes, which may produce values of 0.2–0.4, will not occur in recent sediments. Interestingly, a slightly different view is provided by the 22R/22S values of higher hopanes. Equilibrium value around 0.5 were determined in both coaly samples and lake sediments. An explanation for these two different observations might be related to the sensitivity range of the parameters.

Generally, the aliphatic biomarker compounds were useful to distinguish coal-related samples from lake

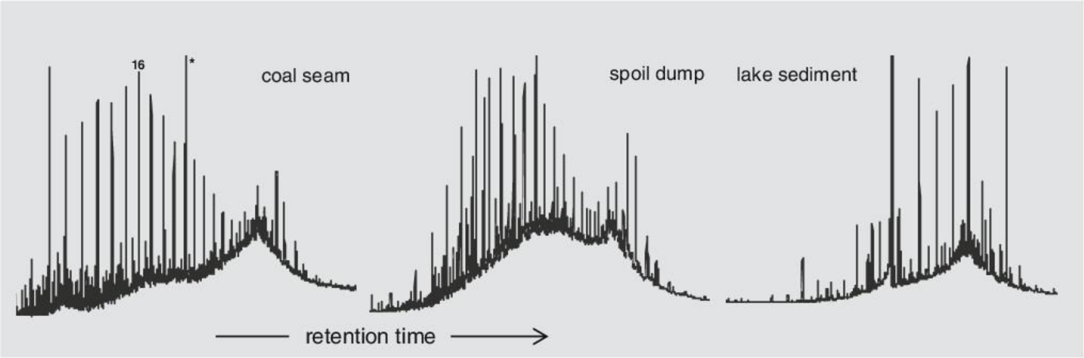

Fig. 4 Selected gas chromatograms of the saturated fraction from samples of different type (*asterisk* internal standard; 16 = n-C_{16})

sediments, but hopane and sterane analyses pointed to the ubiquitous appearance of fossil matter, also in the aquatic sediments. Noteworthy, in contrast to all other samples fly ash samples are characterized by a very low contribution of aliphatics to the organic matter. Just minor amounts in the range of n-C_{23} to n-C_{33} were detectable.

Polycyclic aromatic hydrocarbons

A well-established tool for differentiating petrogenic and pyrogenic sources is the two-dimensional correlation of source-specific polycyclic aromatic hydrocarbons (PAHs) as critically discussed by Yunker et al. (2002). This approach has been applied also to the Ostrava sample set based on quantitative analyses of all abundant 2–5-ring PAHs (phenanthrene, anthracene, fluroanthene, pyrene, benz(a)anthracene and chrysene) and their most prominent methylated homologues. Some compounds of minor concentrations but with a high potential for source apportionment (1,7-dimethylphenanthrene, 2,6-dimethylphenanthrene) have been also considered (Yunker et al. 2002). However, it has to be noted, that PAH ratios have their limitations to act as source indicators. Some restrictions are summarized by Katsoyiannis et al. (2007) as well as Tobiszewski and Namiesnik (2012). Since most restrictions are related to mixing (e.g., in waste waters) or transport discrimination over long distances (e.g., during atmospheric transport), these limitations by applying the PAH ratio approach in the Ostrava region seemed to be of minor importance.

The quantitative data as given in Table 3 points to a dominance of phenanthrene in all samples. The highest values were determined in coals samples (up to 4,860 μg/g) followed by coaly waste residues with values between 150 and 400 μg/g. Lake sediments exhibited the lowest amounts around a few μg/g.

A first indicative set of parameters are given in Table 4. The distribution of parent PAHs and methylated homologues are calculated as relative amount of parent PAHs to the sum of parent compound and methylated derivatives. The relative proportion of phenanthrene and anthracene (PAHs with mass of 178 Da) ranged in coal samples from 31 to 52 %, in spoil dumps from 34 to 41 % and increased up to values between 49 and 78 % in coaly waste residues and lake sediments (average values see Table 4). A similar trend from lower proportion of parent PAHs in coal and spoil dump samples to prevailing parent compounds in lake sediments and coaly waste residues was measured for fluoranthene and pyrene (PAHs with mass 202 Da) as well as dibenzothiophene (mass 184 Da), indicated also by the average values (see Table 4). A higher amount of alkylated homologues points to a higher contribution of petrogenic PAHs, since pyrogenic PAHs are depleted in substituted homologues. Hence, these values confirmed a high proportion of coal material in the spoil dumps and less coaly matter in the other sample sets. An exception has to be stated for fly ash samples in which only parent PAHs were detected mostly and, therefore, values of 1 have been determined as the result of the pyrolysis processes.

A more precise analyses of PAH sources were derived from two-dimensional correlations of indicative PAH ratios. The most valuable correlations are illustrated in Figs. 5 and 6 and correspond to the critical appraisal by Yunker et al. (2002). Based on the fluoranthene and pyrene proportion, cross-plots with corresponding anthracene and phenanthrene as well as benz(a)antharacene and chrysene ratios as illustrated in Fig. 6 discriminated petrogenic from pyrogenic sources but considered also combustion processes of fossil matter. The same approach was used for correlations of parent PAH ratios with indicative dimethyl phenanthrene isomers (Fig. 5). Also in these cross-plots, areas were indicative for petrogenic, pyrogenic and mixed sources.

Table 2 Specific biomarker ratios based on hopanes and steranes

Sample	$T_s/T_S + T_m$	22R/22R + 22S H32	22R/22R + 22S H33	ββ/αα + ββ Ster
CS1		0.51	0.58	0.51
CS2		0.55	0.53	0.52
CS3		0.58	0.55	0.49
CS4		0.54	0.51	nd
CS5		0.53	0.56	0.52
CS6	0.35	0.52	0.52	0.52
CS7		0.51	0.54	nd
CS8		0.53	0.52	0.49
CS9	0.50	0.50	0.50	nd
Average CS		0.53 (±0.02)	0.53 (±0.03)	0.51 (±0.01)
SD1	0.42	0.58	0.56	0.50
SD5	0.44	0.56	0.50	0.50
SD7	0.44	0.56	0.50	0.33
SD9	0.49	0.57	0.56	0.46
SD13	0.45	0.58	0.58	0.47
SD14	0.27	0.55	0.61	nd
Average SD	0.41 (±0.08)	0.57 (±0.01)	0.55 (±0.04)	0.45 (±0.07)
FA1	nd	nd	nd	nd
FA2	nd	nd	nd	nd
FA3	nd	nd	nd	nd
Average FA				
CW1	0.34	0.57	0.60	nd
CW2	0.36	0.56	0.62	nd
CW3	0.37	0.54	0.57	nd
CW4	0.77	0.48	0.62	nd
Average CW	0.46 (±0.21)	0.54 (±0.04)	0.60 (±0.02)	0.45 (±0.08)
LS1	0.32	0.54	0.59	0.45
LS3	0.28	0.52	0.57	0.45
LS5	0.26	0.50	0.59	0.45
LS9	0.31	nd	nd	nd
LS14	0.30	nd	nd	nd
LS16	nd	nd	nd	nd
LS17	0.35	0.57	0.60	0.46
LS18	0.36	0.54	0.60	0.44
LS24	0.17	0.51	0.62	nd
LS26	0.50	0.50	0.50	nd
LS28	0.22	0.51	0.59	nd
Average LS	0.31 (±0.09)	0.52 (±0.02)	0.58 (±0.04)	0.45 (±0.01)

Average values are given with standard deviations (in brackets)

CS coal seam samples, *SD* spoil dumps, *FA* fly ash samples, *CW* coaly waste deposits, *LS* lake sediments

T_s = 18α-trisnorhopane; T_m = 17α-trisnorhopane; 22R or 22S H32 and H33 = 22(R)- or 22(S) C_{32}- and C_{33}-hopanes; αα- or ββ-ster = αα- or ββ-steranes

Due to a restricted number of data points the phenanthrene/anthracene correlations were of minor significance. Well separated sample sets were achieved in all other cross-plots. Coal samples and spoil dumps have been characterized to be dominantly of fossil matter origin with some outliners. On the contrary, lake sediments have been attributed to combustion processes of natural material. Interestingly, in many cases the fly ash samples plotted in the region of combustion of fossil matter. The samples of the coaly waste residues have been linked either with the lake samples (Fig. 6) or were attributed to both natural combustion and petroleum sources (Fig. 5). The later correlation points to the restriction of this approach, since the conclusion, e.g., drawn from the dimethylphenanthrene and the fluoranthen/pyrene parameters are contradictory. Nevertheless, all cross-plots clearly separated coal samples and spoil dump samples from Lake sediments and coaly waste residues. Whereas, fly ash samples represent a unique sample set. These results indicated only minor coaly emissions towards the aquatic environment in the Ostrava

Table 3 PAH content and source-specific PAH ratios

Sample	*P* [μg/g]	An [μg/g]	Fl [μg/g]	Py [μg/g]	BaA [μg/g]	Ch [μg/g]	An/(An + P)	Fl/(Fl + Py)	BaA/(BaA + Ch)	1,7-DMP/ (2,6+ 1,7-DMP)	P/Ret
CS1	2200	2.7	1020	756	5.7	407	0.001	0.57	0.01	0.23	99
CS2	2750	3.1	62	128	27	548	0.001	0.33	0.05	0.22	122
CS3	3570	4.4	98	208	12	626	0.001	0.32	0.02	0.41	20
CS4	3250	4.1	109	238	31	701	0.001	0.31	0.04	0.59	45
CS5	4860	3.6	164	362	56	1000	0.001	0.31	0.05	0.37	86
CS6	2230	7.1	84	182	64	475	0.003	0.32	0.12	0.53	6
CS7	654	11	41	78	63	181	0.017	0.34	0.26	0.57	46
CS8	584	95	161	205	161	165	0.140	0.44	0.49	0.74	5
CS9	9.1	0.05	1.3	1.7	0.3	6.4	0.005	0.43	0.04	0.26	108
SD1	18	0.1	1.5	2.2	0.5	5.5	0.006	0.41	0.08	0.44	54
SD5	15	0.05	0.8	1.4	0.2	4.1	0.003	0.36	0.05	0.48	104
SD7	11	0.05	0.4	0.9	0.1	2.5	0.005	0.31	0.04	0.47	114
SD9	53	0.3	3.1	5.5	0.9	16	0.006	0.36	0.05	0.44	47
SD13	48	0.3	2.7	4.9	0.5	13	0.006	0.36	0.04	0.39	54
SD14	41	1.2	6.3	8.5	4.8	13	0.028	0.43	0.27	0.75	nd
FA1	208	20	174	129	74	88	0.088	0.57	0.46	0.64	nd
FA2	2.2	0.05	0.3	0.4	0.1	0.1	0.022	0.43	0.50	0.49	nd
FA3	6.0	0.1	0.7	0.6	0.2	0.5	0.016	0.54	0.29	0.67	nd
CW1	471	42	212	143	38	95	0.082	0.60	0.29	0.45	63
CW2	114	17	52	39	16	26	0.130	0.57	0.38	0.42	49
CW3	484	40	228	152	42	95	0.076	0.60	0.31	0.39	55
CW4	142	18	33	25	6.2	26	0.113	0.57	0.19	0.39	151
LS1	2.0	0.3	2.9	1.9	0.7	1.2	0.130	0.60	0.37	0.57	51
LS3	1.2	0.2	2.2	1.2	0.4	0.8	0.143	0.65	0.33	0.62	39
LS5	0.6	0.1	0.9	0.5	nd	nd	0.143	0.64	nd	nd	180
LS9	2.2	0.3	2.8	2.0	0.7	1.1	0.120	0.58	0.39	0.54	30
LS14	3.3	0.6	4.9	3.3	1.1	1.7	0.154	0.60	0.39	0.56	44
LS16	0.1	0.05	0.1	0.1	0.05	0.1	0.333	0.50	0.33	1.00	36
LS17	4.1	0.4	5.7	4.5	2.0	3.1	0.089	0.56	0.39	0.73	24
LS18	30	3.4	60	43	17	22.1	0.102	0.58	0.43	0.61	157
LS24	10	3.4	14	10	5.6	6.3	0.254	0.58	0.47	0.72	38
LS26	1.5	0.5	1.6	1.4	0.6	0.7	0.250	0.53	0.46	0.65	110
LS28	51	18	59	44	23	24	0.261	0.57	0.49	0.64	84

P phenanthrene, *A* anthracenem *Fl* fluroanthene, *Py* pyrene, *BaA* benz(a)anthracene, *Ch* chrysene, *DMP* dimethylphenanthrene, *Ret* retene
CS coal seam samples, *SD* spoil dumps, *FA* fly ash samples, *CW* coaly waste deposits, *LS* lake sediments

region. The dominant contribution of pyrogenic contamination in the Lake sediments is obvious. However, it has to be noted that these parameters characterize solely the PAH contamination. Further on, it has to be noted, that not only a widespread distribution, but also a long-lasting contamination is evident as indicated by the core sample data.

All these aspects have to be considered for a comprehensive characterization of the state of pollution. In this study, contradicting facts have been observed that PAH in sediments are dominantly of pyrogenic origin, whereas biomarkers like hopanes clearly demonstrated the contribution of fossil matter. For an explanation of this antagonism the chemical composition of the coaly waste deposit sample might give an interesting clue. As illustrated in Figs. 5 and 6, these samples plot at the interface between sediment samples and coaly samples. This position is also evident following the likely environmental fate for coal material from the seams, towards spoil banks, followed by dispersion in waste deposits and lastly their emission in aquatic systems. Based on this appraisal it can be assumed, that the original coaly material acts as geosorbents accumulating pyrogenic PAH and further lipophilic contaminations over time and along the environmental pathways. Hence, exclusively focusing on

Table 4 Relative amounts of PAHs and their methylated derivatives (178 = sum of phenanthrene and anthracene; 198 = sum of methylphenathrenes and -anthracenes; 202 = sum of fluoranthene and pyrene; 216 = sum of methylfluoranthrenes and -pyrenes; DBT = dibenzozhiophene; MDBT = methyldibenzothiophenes)

Sample	178/178 + 192	202/202 + 216	DBT/DBT + MDBT
CS1	0.44	0.43	0.44
CS2	0.48	0.45	0.48
CS3	0.31	0.39	0.43
CS4	0.36	0.41	0.43
CS5	0.41	0.39	0.42
CS6	0.52	0.48	0.46
CS7	0.33	0.37	0.38
CS8	0.35	0.34	nd
CS9	0.32	0.39	0.32
Average CS	0.39 (±0.08)	0.41 (±0.04)	0.42 (±0.05)
SD1	0.37	0.28	0.35
SD5	0.38	0.26	0.32
SD7	0.41	0.25	0.33
SD9	0.37	0.24	0.31
SD13	0.37	0.24	0.32
SD14	0.34	0.27	0.32
Average SD	0.37 (±0.02)	0.26 (±0.02)	0.33 (±0.01)
FA1	1.00	1.00	1.00
FA2	0.68	0.65	1.00
FA3	1.00	1.00	1.00
Average FA	0.89 (±0.18)	0.881 (±0.20)	1.00 (±0.00)
CW1	0.61	0.73	0.48
CW2	0.67	0.76	0.49
CW3	0.61	0.73	0.48
CW4	0.68	0.65	0.49
Average CW	0.64 (±0.04)	0.71 (±0.05)	0.49 (±0.01)
LS1	0.55	0.77	0.47
LS3	0.60	0.81	0.54
LS5	0.69	nd	0.78
LS9	0.53	0.76	nd
LS14	0.58	0.78	0.50
LS16	0.65	nd	<0.01
LS17	0.49	0.73	0.41
LS18	0.76	0.87	0.64
LS24	0.74	0.77	0.68
LS26	0.78	0.80	0.82
LS28	0.75	0.78	nd
Average LS	0.64 (±0.10)	0.79 (±0.04)	0.61 (±0.15)

Average values are given with standard deviations (in brackets)

CS coal seam samples, *SD* spoil dumps, *FA* fly ash samples, *CW* coaly waste deposits, *LS* lake sediments

the PAHs leads to the wrong assumption of solely pyrogenic contamination but neglects the superimposition of 'natural' coaly PAH pattern by pyrogenic contributions over time. Furthermore, this assumption provides the potential role of coal particles as sink for PAHs in soils and sediments as suggested by several studies (e.g., Wang et al. 2001; Yang et al. 2008).

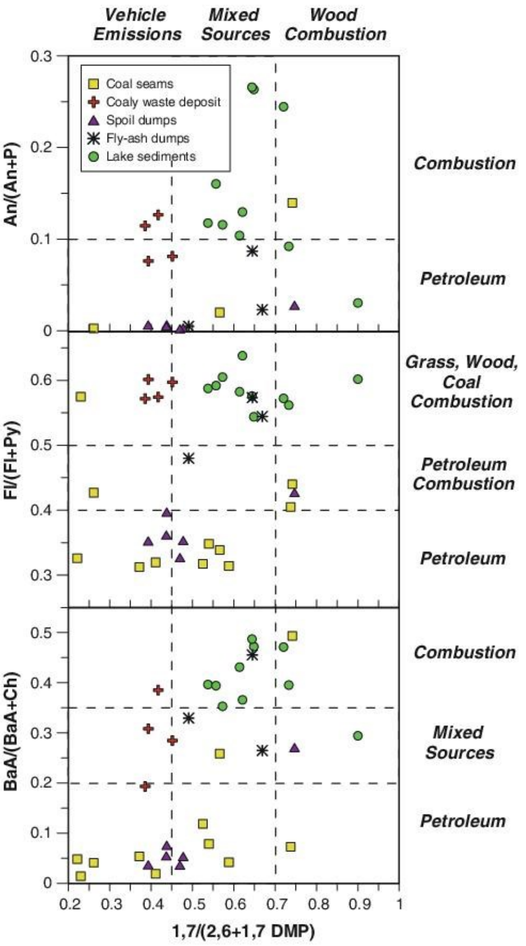

Fig. 5 Indicative cross-plots of source-specific PAH ratios (according Yunker et al. 2002)

A potential tool to evaluate whether coaly particle in the lake sediments of Ostrava region act as sink or source of PAH might be the comparison of exclusively coaly PAH with pyrogenic PAH. For this purposes we have discussed to introduce the parameter phenanthrene/retene as indicator for additionally absorbed PAH. The idea behind this ratio is to compare retene (1-methyl-7-isopropylphenanthrene), as diagenetic product of abietinic acid (a resin constituent in conifers) and abundant in coals, with the structurally similar phenanthrene which is a prominent pyrogenic PAH. An increasing phenanthrene/retene would indicate an ongoing accumulation of pyrogenic PAH in coaly material. These ratios were calculated for those samples in which retene

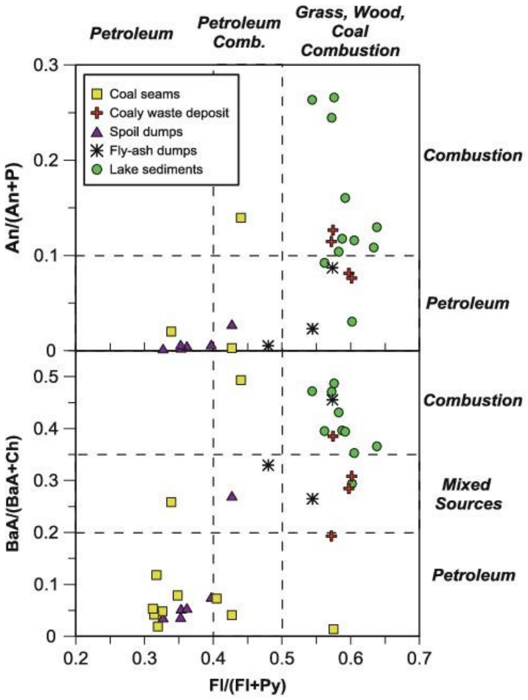

Fig. 6 Indicative cross-plots of source-specific PAH ratios (according to Yunker et al. 2002)

was detected (see Table 3). Unfortunately, the values varied between 5 and 122 in coal samples and spoil dump samples, but also between 24 and 180 in lake sediment samples. Hence, there was no trend and, therefore, no postulated accumulation indicated by this value. However, since this parameter has been introduced here for the first time and, consequently, has not been tested before, the question whether coals in the Ostrava environment act as sink or source for PAH remains open.

Conclusions

This study points critically to the application of geochemical indicators for tracing coal-derived contamination as exemplified for the Ostrava region. The usefulness of simple bulk parameters, specific organic geochemical biomarkers as well as indicative PAHs and their relative abundances has been proven for distinguishing several potential emission sources of coal-derived contamination. In Ostrava region material from coal seams, spoil dumps, fly ash material as well as deposited coaly waste as potential pollution sources were discriminated well by TOC vs TEH relationship and two-dimensional correlations of PAH ratios. Additionally, aliphatic biomarkers revealed individual signatures for all classes of samples and pointed to a widespread distribution of fossil material also in the hydrosphere. On the contrary, indicative PAH ratios documented a dominance of pyrogenic over petrogenic-derived organic matter in the lake sediments investigated. These contradictory descriptions demonstrate clearly that only a comprehensive application of different marker systems allows a detailed view on the quality and quantity of coal-derived pollution. Lastly, it remains unclear whether coaly material in aquatic sediments acts as sink or source for PAHs. A proposed indicative marker, the ratio of phenanthrene over retene, failed.

Acknowledgments This study was funded by The Czech Ministry of Environment (Grant No. MŽP-OG-115/06/SS). The study was also kindly supported by the Institutional research support of Masaryk University in the year 2012.

References

Aboul-Kassim TAT, Simoneit BRT (1995) Petroleum hydrocarbon fingerprinting and sediment transport assessed by molecular biomarker and multivariate statistical analyses in the eastern harbour of Alexandria, Egypt. Marine Pollut Bull 30(1):63–73

Achten C, Hofmann T (2009) Native polycyclic aromatic hydrocarbons (PAH) in coals—a hardly recognized source of environmental contamination. Sci Total Environ 40(8):2461–2473

Achten C, Cheng S, Straub KL, Hofmann T (2011) The lack of microbial degradation of polycyclic aromatic hydrocarbons from coal-rich soils. Environ Pollut 159:623–629

Barra R, Quiroz R, Saez K, Araneda A, Urrutia R, Popp P (2008) Source of polycyclic aromatic hydrocarbons (PAHs) in sediments of the Biobio River in south central Chile. Environ Chem Lett 7(2):133–139

Ding X, Wang XM, Xie ZQ, Xiang CH, Mai BX, Sun LG, Zheng M, Sheng GY, Fu JM, Pöschl U (2007) Atmospheric polycyclic aromatic hydrocarbons observed over the North Pacific Ocean and the Arctic area: spatial distribution and source identification. Atmospheric Environ 41(10):2061–2072

Farias C-O, Hamacher C, de Wagener AL-R, de Scofield AL (2008) Origin and degradation of hydrocarbons in mangrove sediments (Rio de Janeiro, Brazil) contaminated by an oil spill. Org Geochem 39(3):289

Faure P, Landais P, Schlepp L, Michels R (2000) Evidence for diffusive contamination of river sediments by road asphalt particles. Environ Sci Technol 34(7):1174–1181

Faure P, Mansuy-Huault L, Su X (2006) Alkanes and hopanes for pollution source apportionment in coking plant soils. Environ Chem Lett 5(1):41–46

Ghosh U, Gillette JS, Luthy RG, Zare RN (2000) Microscale location, characterization, and association of polycyclic aromatic hydrocarbons on harbor sediment particles. Environ Sci Technol 34(9):1729–1736

Gu S-H, Kralovec AC, Christensen ER, Van Camp RP (2003) Source apportionment of PAHs in dated sediments from the Black River, Ohio. Wat Res 37(9):2149–2161

Halek F, Kianpour M, Kavousi A (2010) Characterization and source apportionment of polycyclic aromatic hydrocarbons in the ambient air (Tehran, Iran). Environ Chem Lett 8(1):39–44

Hu NJ, Shi XF, Huang P, Liu JH (2011) Polycyclic aromatic hydrocarbons in surface sediments of Laizhou Bay, Bohai Sea, China. Environ Earth Sci 63(1):121–133

Kaplan IR, Dalperin Y, Lu ST, Lee RP (1997) Forensic environmental geochemistry: differentiation of fuel-types, their sources and release time. Org Geochem 27(5–6):289–313

Katsoyiannis A, Terzi E, Cai QY (2007) On the use of PAH molecular diagnostic ratios in sewage sludge for the understanding of the PAH sources. Is this use appropriate? Chemosphere 69(8): 1337–1339

Lehndorff E, Schwark L (2009) Biomonitoring airborne parent and alkylated three-ring PAHs in the greater cologne conurbation II: regional distribution pattern. Environ Pollut 157(5):1706–1713

Martinec P et al (2006) Termination of underground coal mining and its impact on the environment. Anagram s.r.o, Ostrava, p 128

Navarro-Ortega A, Ratola N, Hildebrandt A, Alves A, Lacorte S, Barcélo D (2011) Environmental distribution of PAHs in pine needles, soils, and sediments. Environ Sci Pollut Res 19(3): 677–688

Pies C, Hoffmann B, Petrowsky J, Yang Y, Ternes TA, Hofmann T (2008a) Characterization and source identification of polycyclic aromatic hydrocarbons (PAHs) in river bank soils. Chemosphere 72(10):1594–1601

Pies C, Ternes T-A, Hofmann T (2008b) Identifying sources of polycyclic aromatic hydrocarbons (PAHs) in soils: distinguishing point and non-point sources using an extended PAH spectrum and *n*-alkanes. J Soils Sediments 8(5):312–322

Shukla V, Patel DK, Upreti DK, Yunus M (2012) Lichens to distinguish urban from industrial PAHs. Envrion Chem Lett 10(2):159–164

Starý J (2004) Mineral Commodity Summaries of the Czech Republic 2004 Yearbook, Ministry of Environment of the Czech Republic, Czech

Stout SA, Emsbo-Mattingly SD (2008) Concentration and character of PAHs and other hydrocarbons in coals of varying rank—implications for environmental studies of soils and sediments containing particulate coal. Org Geochem 39(7):801–819

Tay CK, Biney CA (2013) Levels and sources of polycyclic aromatic hydrocarbons (PAHs) in selected irrigated urban agricultural soils in Accra, Ghana. Environ Earth Sci 68(6):1773–1782

Tobiszewski M, Namiesnik J (2012) PAH diagnostic ratios for the identification of pollution sources. Environ Pollut 162:110–119

Wang Z, Fingas M, Shu Y–Y, Sigouin L, Landriault M, Lambert P (1999) Quantitative characterization of PAHs in burn residue and soot samples and differentiation of pyrogenic PAHs from petrogenic PAHs—the 1994 mobile burn study. Environ Sci Technol 33(18):3100–3109

Wang X-C, Zhang Y-X, Chen RF (2001) Distribution and partitioning of polycyclic aromatic hydrocarbons (PAHs) in different size fractions in sediments from Boston Harbor, United States. Marine Poll Bull 42(11):1139–1149

Wang Z, Yang P, Wang Y, Ma X (2012) Urban fractionation of polycyclic aromatic hydrocarbons from Dalian soils. Environ Chem Lett 10(2):183–187

Yang Y, Ligouis B, Pies C, Achten C, Hofmann T (2008) Identification of carbonaceous geosorbents for PAHs by organic petrography in river floodplain soils. Chemosphere 71(11):2158–2167

Yunker M-B, Macdonald R-W (2003) Petroleum biomarker sources in suspended particulate matter and sediments from the Fraser river Basin and Strait of Georgia, Canada. Org Geochem 34(11):1525–1541

Yunker M-B, Macdonald R-W, Roxanne V, Mitchell R-H, Goyette D, Sylvestre S (2002) PAHs in the Fraser River basin: a critical appraisal of PAH ratios as indicators of PAH source and composition. Org Geochem 33(4):489–515

Zhang W, Zhang S, Wan C, Yue D, Ye Y, Wang X (2008) Source diagnostics of polycyclic aromatic hydrocarbons in urban road runoff, dust, rain and canopy throughfall. Environ Pollut 153(3):594–601

Příloha 10

Nehyba S., Nyvlt D., Schkade U., Kirchner G., Francu E. (2010) Depositional rates and dating techniques of modern deposits in the Brno reservoir (Czech Republic) during the last 70 years. J Paleolimnol 45, 1, 41-55.

J Paleolimnol
DOI 10.1007/s10933-010-9478-5

ORIGINAL PAPER

Depositional rates and dating techniques of modern deposits in the Brno reservoir (Czech Republic) during the last 70 years

Slavomír Nehyba · Daniel Nývlt · Uwe Schkade · Gerald Kirchner · Eva Franců

Received: 3 February 2010 / Accepted: 20 October 2010

Abstract Facies analysis, magnetic susceptibility, and analysis of grain size, TOC content and isotopes (^{137}Cs, ^{210}Pb, ^{226}Ra, ^{228}Ra, and ^{238}U concentrations) were used to determine the history of the modern deposits of the Brno reservoir. The sedimentary succession can be subdivided into two main units. The lower unit is formed predominantly by medium- to coarse-grained silty sands and is interpreted as a fluvial succession deposited before the Svratka River was dammed. The upper unit consists of brownish planar laminated silts and rarely of clayey or sandy silts and is interpreted as a product of the reservoir deposition. The concentrations of ^{238}U reflect the history of uranium mining in the upper part of the Svratka River catchment. As a consequence, ^{210}Pb radionuclide concentrations cannot be used for establishing a sediment chronology. Concentrations of ^{137}Cs show two marked peaks, the upper of which is attributed to the Chernobyl reactor accident in 1986, and the lower one is attributed to the maximum rate of atomic weapons testing in 1963. From these peaks, mean depositional rates of 3.2 cm year^{-1} for the time period of 1986–2007 and of 3.4 cm year^{-1} between 1963 and 1986 are calculated. Based on the known age of the reservoir, which was constructed in 1939, we can also calculate mean depositional rate for the time period of 1939–1963, which is 3.1 cm year^{-1}.

Keywords Reservoir deposits · Radiometric dating · Depositional rate · Hydrological changes · Human impact

Introduction

Artificial lakes and reservoirs are known to act as effective traps for fluvial material and may represent a continuous record of deposition of modern sediments. Reservoir deposits can be used for the evaluation of climatic conditions, contamination history of the area and past environmental changes caused by both natural and artificial events (Foster and Walling 1994; Shotbolt et al. 2005; Yeloff et al. 2005; Bennett and Rhoton 2007). The sediments

---

S. Nehyba (✉)
Department of Geological Sciences, Faculty of Science, Masaryk University, Kotlářská 2, 611 37 Brno, Czech Republic
e-mail: slavek@sci.muni.cz

D. Nývlt · E. Franců
Czech Geological Survey, Brno Branch, Leitnerova 22, 658 69 Brno, Czech Republic
e-mail: daniel.nyvlt@geology.cz

E. Franců
e-mail: eva.francu@geology.cz

U. Schkade · G. Kirchner
Bundesamt für Strahlenschutz, Postfach 10 01 49, 38201 Salzgitter, Germany
e-mail: gkirchner@bfs.de

deposited in reservoirs can, thus, represent a valuable archive that can be used to reveal the erosion history of watersheds.

The depositional rate of reservoir sediments is influenced by various factors (Kashiwaya et al. 1997; Bell 1998; Brothers et al. 2008; Wren and Davidson 2008; Begy et al. 2009) and reflects processes taking place both in the source and depositional area. Modern deposits can be dated by several methods (Walker 2006). Sediment geochronologies based on the radionuclides ^{137}Cs and ^{210}Pb have been established for marine, lacustrine and intertidal environments (Koide et al. 1971; Robbins and Edgington 1975; Smith and Walton 1980; Lynch et al. 1989; Callaway et al. 1996; Håkanson 2007; Appleby 2008; Sikorski and Bluszcz 2008; Begy et al. 2009) and applied to study historical trends of contaminant emissions at industrial sites, effects of single events, e.g. a storm surge or flood, and local palaeoclimatic conditions (Ritchie et al. 1973; French et al. 1994; Callaway et al. 1996; Kirchner and Ehlers 1998; Barra et al. 2001; Oldfield et al. 2003; Lüder et al. 2006; Bennett and Rhoton 2007; Di Gregorio et al. 2007; Begy et al. 2009). The combined use of ^{210}Pb and ^{137}Cs for estimating sediment ages has been strongly recommended because information available from these tracer nuclides complements each other (Kirchner and Ehlers 1998), and validation of the ^{210}Pb-based geochronology by other time markers is essential (Anderson et al. 1987; Reinikainen et al. 1997; Smith 2001).

The present study focuses on the following: (1) depositional rate determination of the Brno reservoir deposits during the last 70 years, (2) definition of a geochronology of the reservoir deposits using ^{137}Cs, ^{210}Pb and other ^{238}U decay-chain radionuclides, and (**3**) identification of the role of hydrological processes in the sedimentary record of this particular reservoir.

Study area

The Brno reservoir was constructed on the Svratka River during the period of 1936–1939 and was completely filled for the first time by the summer flood in 1940. The reservoir has the characteristic geometry of the relatively long and narrow basin due to artificial flooding of the incised river valley. The flooded valley is relatively broad close to the reservoir dam, whereas distally it narrows rapidly with rather steep walls. The maximum depth of the artificial lake is 19 m and its length is ~10 km. The total volume of retained water can reach a maximum of 18.4 million m^3, but the constant reservoir storage volume is calculated at 7.6 million m^3, with a maximum areal extent of approximately 2.59 km^2 (unpublished Povodí Moravy data, Vlček 1984). The reservoir was constructed for several purposes including stabilisation of the Svratka River discharge, reduction of the flood effect, electricity production, to act as a water source, and for recreational and commercial activities. The Svratka River is the only important tributary into the reservoir. The other tributaries are small and mostly ephemeral streams. The dominant role of the Svratka River for the fluvial and sediment flux of the dam is demonstrated by the following data: the reservoir catchment area is 1,575 km^2, and the Svratka River catchment area above the studied reservoir is more than 1,490 km^2. The average annual flow rate below the dam is 8.03 m^3 s^{-1}, and the average discharge of the Svratka River is approximately 8.00 m^3 s^{-1}.

Granodiorites and diorites of the Brno batholith (Cadomian; Neoproterozoic in age) constitute the major part of the reservoir bedrock. The areal extent of younger deposits (Permian, Neogene and Quaternary in age) along the reservoir margins is limited (Müller and Novák 2000). Input of rock debris from the steep walls is mainly the result of subaerial gravitational flows. Moreover, several transverse erosive short valleys are cut into the walls of the reservoir. Wind-generated currents and breaking waves are responsible for erosion of Quaternary loess and colluvial deposits in the central part of the reservoir, for cliff retreat and for redistribution of the material into the basin.

Methods

Our sediment sampling strategy was directed by the reservoir morphometry, distributions of deposits and position of the accumulation zone (Shotbolt et al. 2005). The complex bathymetry of the reservoir has caused complicated sediment distribution patterns. Therefore, the coring site of the core BP-4 was located in the upper part of the Brno reservoir (Fig. 1) where high trap efficiency potential is presumed. This was also confirmed by field screening (Franců et al.

Fig. 1 Sketch map of the studied area with the location of the coring hole

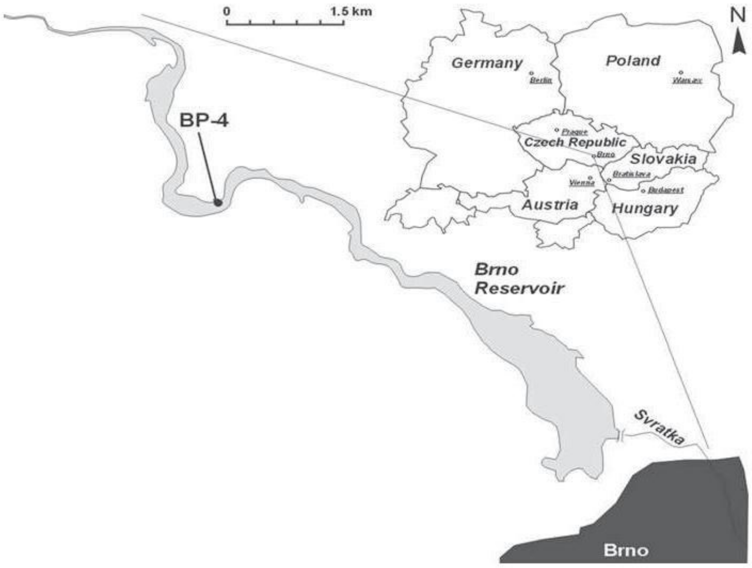

2010), which showed that sampling in the central part of the reservoir would be inappropriate due to the erosional effect of the stream and regular reservoir management. The sediment thickness in the central part of the reservoir (close to the dam) is generally <1 m (Franců et al. 2010). The distance of the coring site from the ordinary inflow point, where the reservoir water level affected the Svratka River inflow (area of raised water level) is approximately 2 km. Our drilling was oriented in the path of the fluvial inflow away from the possible transverse input of material from reservoir walls. The Svratka River has an incised meandering fluvial pattern here (49°15′30.26″N, 16°27′42.05″E and 220.5 ± 0.5 m a.s.l.), and the apical left-bank point bar position was selected for drilling. The coring site was temporarily accessible due to the exceptional reservoir level decrease of more than 10 m in the winter to early spring of 2008 due to a water release to revitalise the reservoir because of a summer cyanobacterial bloom made its recreational use impossible.

Sampling was performed in March 2008 using a Makita vibration hammer and Eijkelkamp coring tubes. The obtained core of 292.5 cm in length was placed into a plastic sleeve and divided immediately into two equal parts. One part of the core was frozen and stored, and the other part was photo documented, lithologically described and subdivided into 121 samples, each about 2.5 cm thick.

Facies analysis, magnetic susceptibility, analysis of grain size, TOC content and both ^{137}Cs and ^{210}Pb concentrations were used to establish a geological framework of the core. Grain size was measured by laser diffraction methods using a Cilas 1064 granulometer for the 0.0004–0.5-mm fraction. Ultrasonic dispersion and washing in sodium polyphosphate were used prior to the grain size analyses to avoid flocculation of analysed particles. The average grain size is demonstrated by the graphic mean (Mz) and the uniformity of the grain size distribution by the standard deviation (σI) (Folk and Ward 1957). Lithofacies analysis followed the rules of Walker and James (1992), Tucker (1988) and Nemec (2005). Environmental magnetic susceptibility (MS) was measured as mass susceptibility (χ) in 10^{-9} m^3 kg^{-1} using an MFK1-FA Kappabridge at a magnetic field of 200 A m^{-1} in the AGICO, Ltd. For further summary of magnetic parameters and terminology, see Evans and Heller (2003). All samples were subjected to elemental analysis of total organic (TOC) and inorganic carbon (TIC) using a Metalyt CS 1000 S apparatus (ELTRA GmbH, Neuss, Germany). The method of total carbon assessment is based on the infrared detection of carbon dioxide released by combustion at 1,200°C. Inorganic carbon content is measured as carbon dioxide exhibiting phosphoric acid acidification. Subtracting the inorganic carbon from the total carbon yielded TOC. Historical changes of organic pollutant levels were studied throughout the core by Franců et al. (2010). The magnetic susceptibility values were not corrected for the diluting effect of organic carbon as TOC levels were low.

Maximum daily discharge measurements from the period of 1939 to 2007 were evaluated (unpublished Povodí Moravy data) for the gauging station Veverská Bítýška at 228.1 m a.s.l., which is located approximately 2 km upstream from study site. Continuous data from the 68-year period of the dam's history were analysed using the Pearson method (Brázdil 1995).

For the gamma-spectrometric analyses, a high-purity Germanium well detector with a relative efficiency of 36.6% and a usable energy range between 40 and 2 MeV was applied. Sediment samples were dried, homogenised and loaded into glass vials prior to measurement. Depending on the mass of sediment available, measurement times varied between 1 and 6 days to limit some statistical counting uncertainties for all of the radionuclides in our range of interest. In addition to the anthropogenic ^{137}Cs (with a gamma energy of 661.7 keV), activity concentrations of natural ^{210}Pb (46.5 keV), ^{228}Ra (via its decay product ^{228}Ac at 911.2 keV) and ^{238}U (via its short-lived decay products ^{234}Th at 63.3 keV and ^{234m}Th at 1001.0 keV) were determined. For ^{226}Ra, its 186.2 keV decay energy was used after subtraction of the contributions of ^{235}U at this energy, which were determined from the 143.8 keV energy of this uranium isotope. This procedure was preferred to the measurement of ^{226}Ra via its short-lived progeny, ^{214}Pb, because loss of some ^{222}Rn from the glass vials could not be excluded. Count rates were corrected for summation effects where necessary.

Radionuclide chronology

The radionuclide ^{137}Cs (30.1 year half-life) is artificially produced by a nuclear fission processes. The nuclear weapons tests performed in the atmosphere between 1945 and 1980 caused global dispersion and deposition of this radionuclide. Due to the varying annual number and yield of atmospheric tests, deposition rates in the environment showed a pronounced maximum in 1963 (UNSCEAR 2000). Because ^{137}Cs is strongly associated with minerals (Alberts et al. 1989), the 1963 weapons testing peak has been preserved in most sediments to the present. In much of Europe and the Middle East, deposition of ^{137}Cs originating from the Chernobyl reactor accident in 1986 provides a further time marker that may be even more pronounced than the 1963 weapons peak.

The use of the natural isotope ^{210}Pb (22.3 year half-life) is based on its removal from the atmosphere by precipitation and integration into sediments where it subsequently decays to the stable isotope ^{206}Pb. In addition to this atmospherically derived ^{210}Pb (often called excess or unsupported ^{210}Pb), which is used for dating, there is a background concentration of this isotope (called supported ^{210}Pb) originating from the ^{226}Ra present in the sediment minerals.

There are two standard approaches to estimate sediment ages and sedimentation rates from the activity concentrations of excess ^{210}Pb measured in a sediment core, the constant initial concentration (CIC) and the constant rate of supply (CRS) model (Appleby 2001). Both models are based on the assumption of a constant annual flux in the density of excess ^{210}Pb fixed to particles across the water–sediment interface. The CIC model is applicable if sedimentation rates and sediment densities are also time invariant. For such a stationary sedimentation regime, excess ^{210}Pb shows an exponential decline within the sediment, which reflects its sedimentation rate. The CRS model focuses on varying sedimentation rates. Sediment ages are derived from the fraction of the depth-integrated excess ^{210}Pb present above the position considered. Thus, any deviations from an exponential decrease with depth of excess ^{210}Pb are interpreted by the CRS model to reflect a variation of the sedimentation rate.

Results

Facies analyses and depositional environment

The sedimentary succession can be subdivided into two main units (Fig. 2). The lower unit lies below a depth of 199.5 cm. Brown, greyish to greenish medium- to coarse-grained silty sands predominate within this unit. Sand is usually poorly sorted with

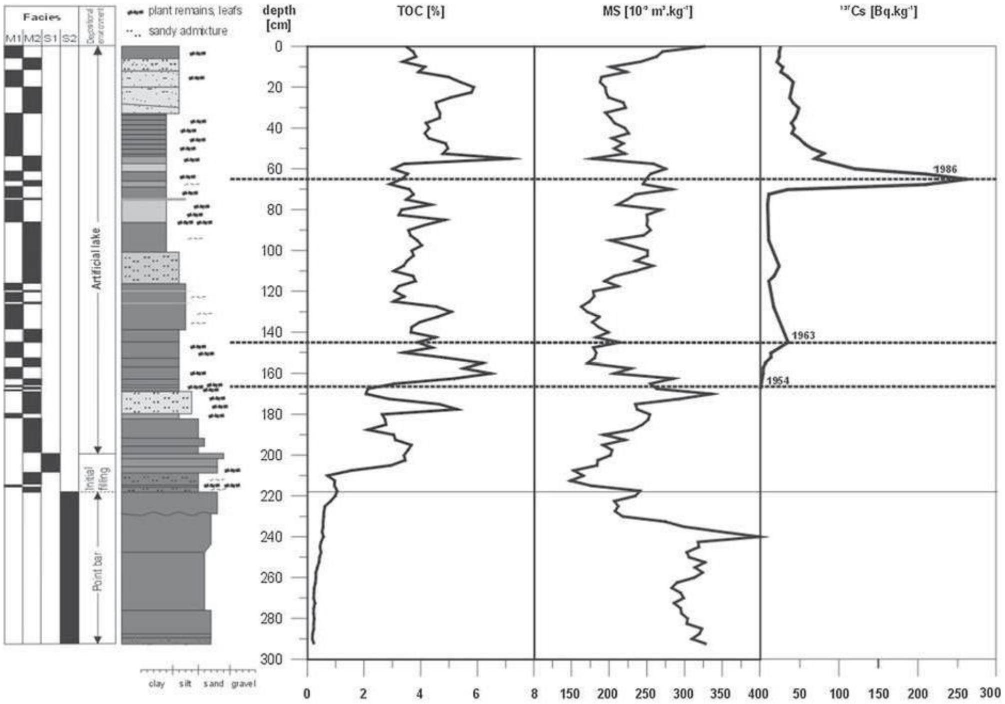

Fig. 2 Lithological profile of the studied core, facies distribution, total organic carbon (TOC) content, magnetic susceptibility (MS) values and the concentrations of ^{137}Cs throughout the studied profile

some admixture of granules and a reduced occurrence of plant detritus. The bases of sandy beds are irregular or gradational. Sandy silt laminae with abundant plant detritus are sometimes intercalated in sandy facies. This unit is interpreted as fluvial succession deposited before filling of the dam from the contact and saltation load (bedload). This fluvial unit can be further subdivided into two subunits. The lower subunit (218.5–292.5 cm) comprises thicker (10–30 cm) beds of poorly sorted sand with reduced content of plant detritus (facies S2). This subunit was interpreted as a product of lateral accretion of fluvial material on the point bar (associated with the migration of the thalweg towards the right cut bank of the Svratka River in this part of the valley). The upper subunit was recognised at a depth of 199.5–218.5 cm and is formed by thin (<5 cm) sandy beds (S1 facies) alternating with silt laminae (M2 and M1 facies). Facies changes represent the alternating periods of quiet deposition (facies M1, M2) and more agitated deposition, with the migration of flow ripples and small dunes (facies S1). The formation of this subunit is interpreted as a response of the start of reservoir filling and the possible impact of the several floods during the initial reservoir water infill period of 1939–1941. This interpretation is supported by the upward coarsening trend of the subunit and the absence of fluvial sediments higher in succession. Three factors suggest that the initial prograding deltaic deposition in the marginal zone of the reservoir did not influence deposition at our study site, and these factors include the distance between our study site and the area of raised water level, the abrupt change in the grain size at the start of the deposition, and the lack of evidence for instability and slumping.

The upper unit (above 199.5 cm) consists of brownish, grey to greenish planar laminated silts and rarely of clayey or sandy silts. Graphic mean Mz (17 samples) varies between 0.025 and 0.012 mm (average

0.018 mm). Silts are relatively poorly sorted; their σI varies between 1.3 and 1.7 ϕ (average 1.5 ϕ). Thin sandy interlayers and sand admixture occur especially in the lower part of the succession (depths of 101–116.5 and 169–180 cm). Planar lamination is connected with alternation of slightly coarser and lighter laminae and those which are relatively finer grained and darker (higher content of organic matter). Two facies (M1 and M2) were selected according to the content of plant detritus and colour. The M1 facies is notably darker due to higher organic content (mainly plant detritus) than the lighter coloured M2 facies. Alternation of these facies can be followed within the succession. The upper unit is interpreted as the post-dam phase with sediments deposited mainly from graded and uniformly suspended loads. Alternation of the M1 and M2 facies and the presence of some intercalated sandy silt layers indicate the impact of various natural and anthropogenic processes affecting reservoir deposition. Such processes include variations in seasonal fluvial discharge (especially occasional floods), the annual vegetation cycle, variations in agricultural and industrial activities in the surrounding areas and fluctuations in the reservoir water level. Relatively monotonous facies arrangement and grain size within the upper unit point to generally stable sedimentary environment. Considerable consistency in particle size distribution throughout the upper unit of the core demonstrates that reservoir drawdown events have not resulted in redistribution of coarse sediments. The upper unit sediments were deposited in the reservoir accumulation zone and do not represent any type of marginal sediments affected dominantly by processes other than those involved in reservoir deposition. Input from rain splash and slope wash was not recognised because such processes preferentially remove fine particles, though coarser sediments may also be removed during high-intensity rainfall events or from steeply sloping marginal deposits (Shotbolt et al. 2005).

Organic carbon content and magnetic susceptibility

Changes in total organic carbon (TOC) content and environmental magnetic susceptibility (MS) throughout the profile reflect major changes in conditions during sedimentation. The lower fluvial subunit (below 218.5 cm), which is interpreted as being deposited by lateral fluvial accretion on the point bar, shows the lowest TOC content (typically $<1\%$) with a slight increase towards the top (Fig. 2). In contrast, MS values are high (usually $>290.10^{-9}$ m^3 kg^{-1}) with a maximum of 407.10^{-9} m^3 kg^{-1} at the depth of 240 cm. Changes in MS reflect different inputs of ferromagnetic minerals from the Svratka River catchment, which correspond to changes in the grain size of sediments. Low organic carbon content is typical for fluvial deposition; its vertical increase may reflect shallowing of water due to lateral accretion on the point bar. The upper fluvial subunit (218.5–199.5 cm) shows a slight increase of TOC at its base, followed by its gradual decrease up to 210 cm and finally a rapid increase up to $\sim 3.5\%$ at its top. This fluvial subunit has the lowest MS values of the entire profile, reaching levels of $\sim 150.10^{-9}$ m^3 kg^{-1}. These variations indicate discharge changes in the time of the initial water filling of the reservoir.

Reservoir sediments (above 199.5 cm) reflect cyclic changes in both TOC and MS. These usually show negative correlations because higher organic carbon content implies a low energy sedimentary environment allowing deposition of fine-grained organic material. Conversely, larger and heavier ferromagnetic minerals are eroded and transported primarily during higher discharge events and deposited during more dynamic conditions. Variations in TOC and MS content are principally related to the discharge changes throughout the reservoir history. Large flood events or reservoir level drawdowns can be especially important.

MS can also be used for identification of the reservoir accumulation zone (Shotbolt et al. 2005). The zone is characterised by fine sediment deposited under low-energy conditions with no reworking and continuous stable sedimentation. The replicability of magnetic characteristics of core profiles was often used to identify this zone (Blais and Kalff 1995). There is visual similarity of the MS profiles of the studied core with published MS profiles from cores drilled approximately 1 km down in the studied (Sedláček and Bábek 2009), which further confirms that coring site was located in the accumulation zone.

Hydrology

Depositional rates in artificial lakes are generally proportional to rainfall intensities (Kashiwaya et al. 1997). The highest fluvial discharge of the Svratka

River at the gauging station Veverská Bítýška during the studied 68-year period was 240 $m^3\ s^{-1}$ (March 10, 1941). Variations in fluvial discharges can be used to evaluate the significance of floods for the reservoir infill. Analysed data from the 68-year period of the dam history are presented in Table 1.

Significant differences between the maximum and average fluvial discharge favour variations in volume and grain size of transported material being successively deposited within the reservoir. This also affects the other proxy data, such as TOC, MS and concentrations of radionuclides originating from atmospheric deposition within the sedimentary sequence. Furthermore, strong seasonal variabilities are expected to result from the noticeable differences in discharge between the late winter/spring and autumn periods. These differences are typical for rivers with their upper catchment reaches in a humid climate. Here the maximum discharges mostly appear during the longer periods following snow melting (mostly in the period from February to April) and in some short periods following summer thunderstorm events with higher precipitation rates (from June to July). During autumn (October to November), the reduced discharge connected with lower precipitation prevails in Central Europe.

Fluctuating water levels represent serious limitation for continuous deposition in the reservoirs and impact on the sedimentary record. Moreover, changes in the location of the water's edge effectively extend and change the area of sediment exposed to redistributing processes. The extent and frequency of drawdown during the last 43 years (i.e. 1965–2008) can be followed according to data from the Povodí Moravy state enterprise. Annual water-level fluctuations are approximately 3–4 m, and only 5 fluctuations of approximately 5 m were recognised during this period, with the minimum measured level at

Table 1 Maximum fluvial discharges (Qmax.) during the studied years and their return value (*T*)

Year	Qmax. [m^3/s]	*T*	Year	Qmax. [m^3/s]	*T*	Year	Qmax. [m^3/s]	*T*
1939	69.90	2.42	1962	116.00	5.07	1985	123.00	5.93
1940	126.00	6.49	1963	20.60	1.06	1986	108.00	4.16
1941	240.00	100.12	1964	23.40	1.11	1987	105.00	3.71
1942	47.00	1.52	1965	55.40	1.75	1988	91.20	3.2
1943	27.40	1.14	1966	56.20	1.84	1989	58.90	2.06
1944	75.20	2.6	1967	50.30	1.59	1990	22.10	1.09
1945	134.00	7.98	1968	40.00	1.29	1991	18.10	1.01
1946	170.00	25.77	1969	74.60	2.51	1992	63.00	10.37
1947	169.00	18.79	1970	55.00	1.71	1993	61.50	2.26
1948	100.00	3.52	1971	38.30	1.25	1994	53.80	1.66
1949	43.70	1.37	1972	37.00	1.22	1995	59.10	2.12
1950	44.60	1.4	1973	18.10	1.03	1996	55.60	1.79
1951	51.20	1.63	1974	42.10	1.34	1997	115.00	4.72
1952	49.00	1.55	1975	59.50	2.19	1998	78.40	2.81
1953	106.00	3.92	1976	85.50	1.26	1999	110.00	4.42
1954	42.00	1.32	1977	140.00	12.19	2000	91.20	3.35
1955	121.00	5.47	1978	30.10	1.16	2001	21.70	1.07
1956	128.00	7.16	1979	82.00	2.93	2002	56.90	1.89
1957	57.00	1.94	1980	46.20	1.49	2003	135.00	9.02
1958	24.40	1.125	1981	148.00	14.79	2004	58.00	2
1959	18.40	1.04	1982	76.20	2.7	2005	137.00	10.37
1960	39.00	1.27	1983	46.00	1.46	2006	192.00	40.98
1961	35.40	1.18	1984	45.30	1.43	2007	36.60	1.2

T—return value

222.3 m a.s.l. Our coring site was located at 220.5 ± 0.5 m a.s.l., ~2.5 m below the constant reservoir water level (i.e. 223.1 m a.s.l.). The reservoir water-level fluctuation data shows that this coring site was first subaerially exposed during the 2007/8 winter and spring, when the water was released more than 5 m below the constant reservoir level.

Results of the grain size and MS study reveal that water-level fluctuations did not result in significant disturbances of studied deposits. Although drawdowns could sometimes have affected the coring site, no significant role of marginal and shallow water processes (wave action, rain splash and slope slaps) and redistribution of coarse material into the basin was recognised in the core. For much of the drawdown periods, there could only have been low and predominantly fine inputs of sediment to the submerged area where the coring site was located. An important role in such a limited redistribution of material from the studied position might be played by the time of the drawdown period (usually winter) and cohesiveness of bottom sediment, which limited erosion.

Radiometric dating and depositional rates

Trace concentrations of ^{137}Cs have been detected down to a sediment depth of 165 cm. The depth distribution of this anthropogenic radionuclide shows two marked peaks (Fig. 3). These can be unambiguously attributed to deposition of ^{137}Cs from the weapons testing fallout maximum in 1963 (at the 142.5–145.0-cm depth) and from the Chernobyl reactor accident in 1986 (at the 65.0–67.5-cm depth), respectively. From these peaks, mean depositional rates of 3.2 cm year^{-1} for the time period of 1986–2007 and of 3.4 cm year^{-1} between 1963 and 1986 are calculated. These results indicate that the sedimentation regime has been almost constant for the last 45 years. From the change in the sediment composition at 218.5 cm, which reflects the known start of reservoir filling in 1939, we can calculate a mean sedimentation rate of 3.1 cm year^{-1} for the time period of 1939–1963.

In general, the concentrations of ^{238}U show higher values in the upper half of the analysed core than below, with a marked peak at the 130.0–132.5-cm layer. Using the ^{137}Cs chronology, this layer corresponds to the year 1967 (Fig. 3). Such a peak is also present for ^{226}Ra at the same position, but no concentration increase was measured for ^{228}Ra (Fig. 3). This suggests uranium-mining residues as a likely source of increased radionuclide concentrations at the 130–140-cm depth because such material is commonly enriched in ^{238}U and ^{226}Ra, but not in ^{228}Ra, a member of the ^{232}Th decay chain. This interpretation is supported by the results of a Spearman's rank correlation test, which showed no significant association of the concentration of ^{228}Ra and ^{238}U within the analysed sediment core (one-sided, $r_s = -0.077$, p » 0.05).

Concentrations of unsupported ^{210}Pb are highly scattered, showing almost no relationship with sediment depth (Fig. 3). Spearman rank correlation tests result in highly significant associations of the ^{238}U concentrations within the analysed core with both total and unsupported ^{210}Pb (one-sided, $p < 0.001$, with $r_s = 0.854$ for total and $r_s = 0.675$ for unsupported ^{210}Pb). This finding indicates that the major source of both ^{210}Pb fractions is material enriched in uranium and its decay products and not deposition from the atmosphere. This conclusion is supported by the fact that like ^{238}U and ^{226}Ra, both ^{210}Pb fractions show marked peak concentrations in the 130.0–132.5-cm layer.

The CRS model available for depth-to-age conversion of unsupported ^{210}Pb showing a non-exponential decline with depth within a sediment core is based on a time-invariant flux density of this tracer radionuclide across the water–sediment interface. This assumption, which has been validated for ^{210}Pb deposited annually from the atmosphere (Turekhian et al. 1977; Rangarajan et al. 1986), becomes highly questionable if the dominating source of unsupported ^{210}Pb in the sediment is likely to be uranium ore mining residues. Because the CRS model erroneously converts variations in time of the flux density of unsupported ^{210}Pb into the sediment into variations in sedimentation rates, ^{210}Pb concentrations in the Brno reservoir sediment cannot be applied for establishing a geochronology.

For the uranium decay chain members (^{238}U, ^{226}Ra and total ^{210}Pb), but not for ^{228}Ra, there is a pronounced step increase in concentrations above the ~210-cm depth, followed by another less pronounced increase above the ~150-cm depth (Fig. 3).

In the upper part of the Svratka River catchment, underground uranium ore mining commenced in

Fig. 3 Activity concentrations of the radionuclides of interest in the sedimentary profile. For ^{210}Pb, the supported and unsupported fractions are displayed separately. Uncertainties are usually <20%

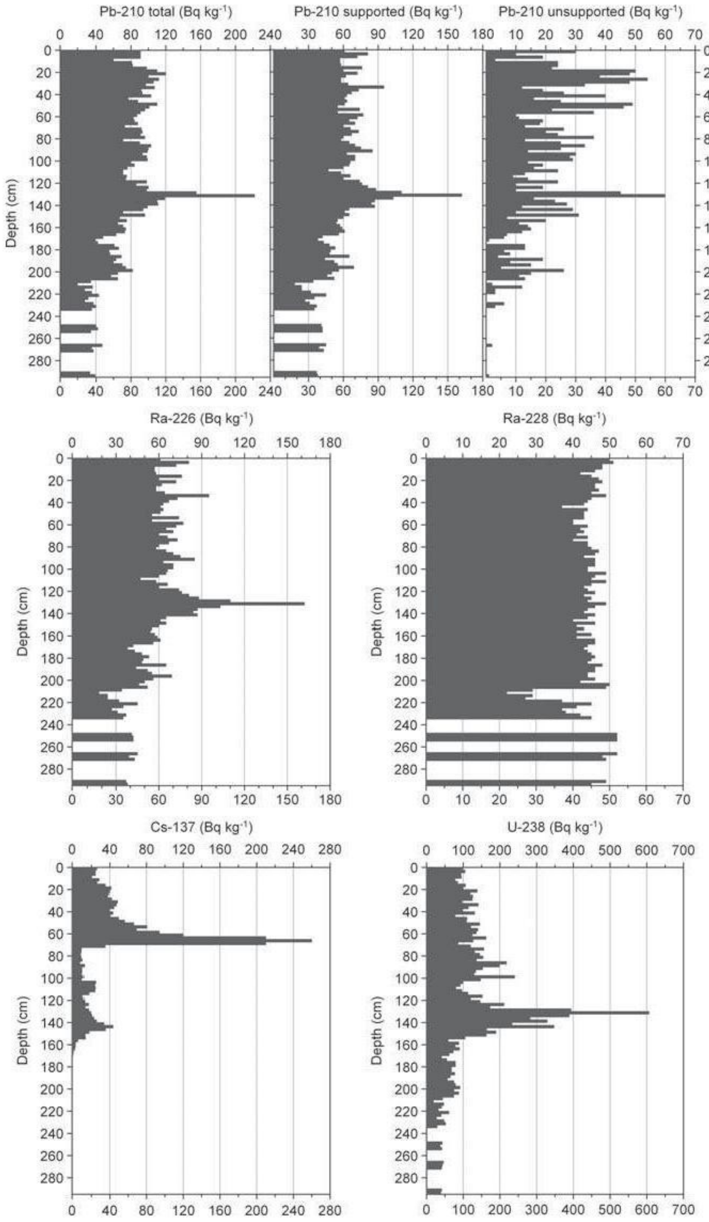

1957 (ore deposit Rožná) and in 1959 (ore deposit Olší), producing extensive amounts of pit tips and pit waters. Based on our ^{137}Cs-based geochronology, the increase of ^{238}U, ^{226}Ra and ^{210}Pb at the ~150-cm depth corresponds to the years 1960 and 1961, which is in excellent agreement with the initiation of these industrial activities. The increase of these radionuclides at ~210 cm is likely to reflect changes of the watershed flow regime caused by the reservoir dam construction.

According to the Czech Hydrometeorological Institute, enhanced discharge in late winter 1966/67 caused a major redistribution of pit tips in the upper reach of the Svratka River catchment. This event is reflected in the marked peak of ^{238}U and its decay products in the 130.0–132.5-cm layer. Its ^{137}Cs-derived age shows exact correspondence.

Discussion

Detailed stratigraphic analysis has enabled us to track the sedimentary history of the reservoir infill in detail and to postulate the processes involved in this deposition. Sedimentation rates in reservoirs vary greatly. Phillips and Nelson (1981) described the average sedimentation rate of the artificial Lake Matahina at approximately 20 mm year^{-1}. Similarly Mulholland and Elwood (1982) suggested an average sedimentation rate for reservoirs of around 20 mm year^{-1}. Van Metre et al. (2001) found sedimentation rates in eight US reservoirs to vary between 6 and 66 mm year^{-1}, and Shotbolt et al. (2005) declared that the average sedimentation rate for UK reservoirs lies between 3 and 54 mm year^{-1}. Our analysis shows that the sedimentation rate was relatively high in the case studied here. A higher sedimentation rate limits the time that sediment spends at the reactive sediment–water interface.

Our study is based on a single core, so it cannot represent the sedimentation rate for the entire reservoir basin, but our results proved that the recorded sedimentary processes reflect deposition in an accumulation zone (Shotbolt et al. 2005) and, thus, sediments from the upper part of reservoirs with high trap efficiency potential can also produce valuable information. Mean depositional rates of 3.2 cm year^{-1} for the time period of 1986–2007 and of 3.4 cm year^{-1} between 1963 and 1986 were calculated. The step increase of ^{238}U, ^{226}Ra and ^{210}Pb above the 210-cm depth likely reflects reservoir completion and water filling (1940–1941). This could result from adsorption of the radionuclides to suspended organic material because TOC shows a parallel increase (Fig. 2). However, the almost unchanged concentrations of ^{228}Ra (and thus ^{232}Th) in the sediment indicate that an increased transport of uranium-rich minerals by the watershed and into the reservoir is likely to be of higher importance.

Although the sedimentation rates in the Brno reservoirs were relatively stable during the last 68 years, some slightly enhanced and decreased rates can be observed. Variations in depositional rate are primarily affected by fluctuations in sediment supply. According to Kashiwaya et al. (1997), the depositional rate in the reservoirs is roughly proportional to the rainfall intensity. Precipitation is related to surface erosion and sediment transport, although this relationship is obliterated by other factors, such as erodibility of the surface material, geology and geomorphology of the catchment area, precipitation season, etc. Depending on the energy of the floodwater, the reservoir sediments can be eroded as well as deposited. Floods are often the most dominant sediment contributor to the reservoirs (Zhang et al. 1998). A higher sedimentation rate can be connected with a greater role of stratified flows during the floods, whereas non-stratified flows dominate under normal flow conditions (Shotbolt et al. 2005). Therefore, the flood events are recorded not only from the changes of sediment type, but also from changes in depositional rate. Occurrence of thin sandy interlayers and sand admixture within the predominantly silty deposits of the reservoir in the studied profile (depths of 101–116.5 and 169–180 cm) could point to higher fluvial discharge during the flooding periods.

Maximum fluvial discharge can be used for evaluation of the significance of flooding for reservoir infill. Depositional rates of the studied reservoir deposits can be compared with periods of higher fluvial discharge of the Svratka River. The highest occurrence of pronounced flood events (i.e. >5-years water) was documented for the period from 1939 to 1963, and this period exhibits a slightly lower depositional rate. The highest depositional rate was observed for the time period 1963–1986, which is the period with the lowest occurrence of pronounced floods (Table 2). Gasiorowski and Hercman (2005) showed that the proximity to the major river channel and a position close to the mean water level are most suitable for the direct recording of the flood events. The inverse relationship of the depositional rate and the occurrence of pronounced floods further confirms that sediments in the studied core were not affected by redepositional processes and reflect a uniform

Table 2 Occurrence of pronounced flood events (i.e. >5-years water discharges) in the Svratka River gauging station Veverská Bítýška (immediately above the Brno reservoir) during the time period 1939–2006

Period	>20 years water	>10 years water	>5 years water	>3 years water	Average Q(max) m^3/s
1939–1963	2	1	5	2	82.2
1963–1986		2	1		64.4
1986–2006	1	1	2	5	77.0

sedimentary accumulation zone of the reservoir. Major floods may erode reservoir floors and generate sedimentary unconformities in some reservoirs (Haag et al. 2001). Such unconformities were not recognised in the studied core, and the higher depositional rate during the initial period of reservoir infill is supposedly due, in general, to an increase of accommodation space connected with the rise in the reservoir water level. The formation of available accommodation space was stable in later periods, and the depositional rate declined compared to the initial period. It can be speculated that the slightly lower mean depositional rate during the period of 1939–1963 could reflect some erosion events of reservoir deposits, possibly during the high 1962 discharge connected with the late-spring flood.

Identification of periods with high fluvial discharges/floods within the sedimentary record is a tentative problem. Such a speculative interpretation of the studied deposits is presented in Fig. 4. The sedimentary record was subdivided into the main above-mentioned periods based on radiometric dating, and individual years were selected according to the depositional rate calculated for each period. The curve of the maximum fluvial discharge was drawn for the 68-year period. Points with low levels of TOC and high levels of MS were detected within the sedimentary record and compared with higher fluvial discharges/floods. This approach allows us to deduce that approximately 15 floods can be recognised within the sedimentary record. It was found that 3–5-years water discharges are sufficient to affect the TOC and MS record. Moreover, the timing of the floods during the year plays an important role because only winter and early spring flooding events were identified in the sedimentary record. It should be stressed that, during the first period of reservoir infill, important floods (3–5-years water) occurred during the winter (February to early March). Since the mid 1980s, spring to summer floods have become more common.

Although the coring site was located in the upper part of the reservoir, the sedimentary record represents the accumulating zone (almost uniform fine grained deposits that are spatially consistent over a reasonable area with no major reworking of material and no admixture of coarse grains), which is representative of most of the reservoir showing an uninterrupted depositional record. Sediment input during water drawdowns is generally coarser, but fine sediments could be re-entrained at the margins during prolonged drawdown periods (Shotbolt et al. 2005). Such a situation could be identified by the increase in sedimentation rate. Our observation of no significant disturbances in the deposition rate confirm the consistency of sedimentation in the studied case. However, the occurrence of thin sandy interlayers and sand admixture within silts at depths of 101–116.5 cm in the studied profile could point to some role of fluctuation of the water level. This interval corresponds to the years 1969–1973 based on the ^{137}Cs geochronology. Two significant decreases of the water level of approximately 5 m were recorded during these years, and these years were generally dry in the Svratka River catchment with only low-level discharges (Fig. 4). The same is true for the sandy interlayer at depths of 169–180 cm, which must have been deposited during the drier years between 1948 and 1952 without any high-level discharge events. Despite fluctuations in water levels, the studied core contains undisturbed and consistently deposited sediments. The water-level fluctuations were not a very efficient agent for initiation of the redistribution of sediment. Although sedimentation rates were not entirely consistent, these variations did not significantly affect the usefulness of the sediment records because the majority of sediment was deposited under low energy conditions, and zones of atypical sediment influx were very rare, very thin and identifiable (Shotbolt et al. 2006).

Sediment is assumed to be deposited continuously and consistently throughout the year. In reality, the

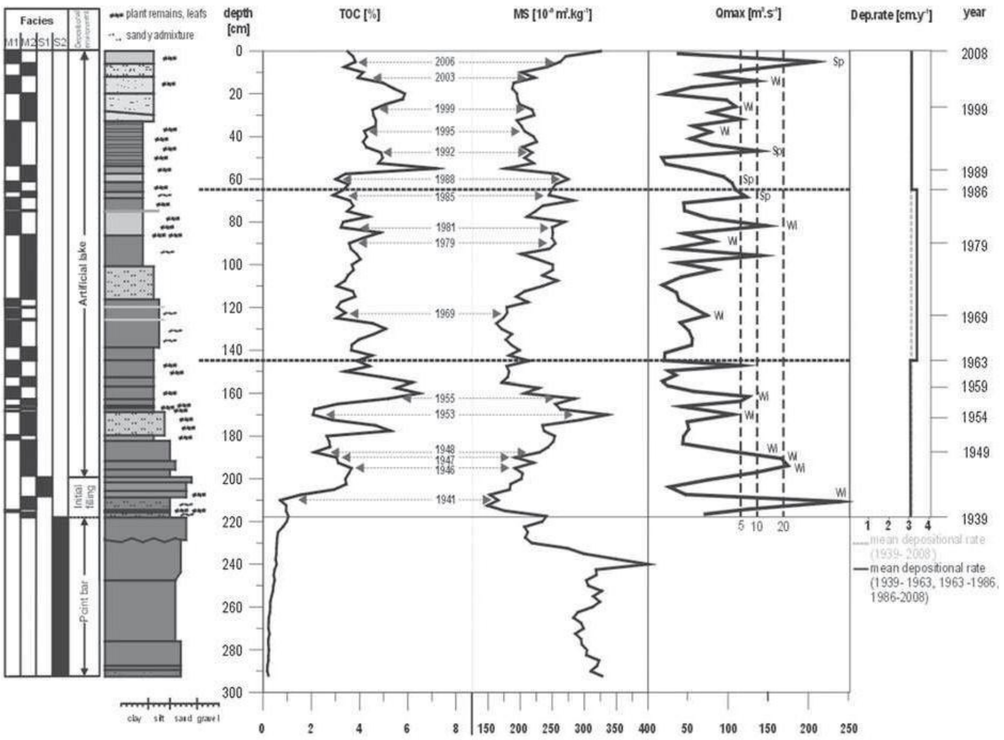

Fig. 4 Lithological profile of the studied core, facies distribution, total organic carbon (TOC) content, magnetic susceptibility (MS) value, maximum annual discharges (Qmax.), with indication of n-year water for the x-axis and the flood season (*Wi* winter, *Sp* spring) and possible correlation of the flood record with TOC and MS. The average depositional rate for the complete reservoir infill (1939–2007) and the mean depositional rate for the identified time periods (1939–1963, 1963–1986, and 1986–2007) are shown. *Thick dashed lines* represent ^{137}Cs-based time markers

sedimentary record is an amalgamation of deposits under different energy conditions and will contain particles of different size that are deposited at different rates during particular seasons of the year (Shotbolt et al. 2006).

With regard to radiometric dating, the sediment core that we analysed in this study has been found to be exceptional for two reasons. First, excess ^{210}Pb originates mainly from ^{210}Pb present in the watershed area from natural and industrial sources. Applicability of this radionuclide for dating recent sediments is, therefore, limited. Second, in areas with comparatively high uranium content in rocks and soils, changes in both the watershed flow regime and industrial mining activities influence the concentrations of ^{238}U and its long-lived decay products. Elevated concentrations of ^{238}U, ^{226}Ra and ^{210}Pb originating from uranium ore mining and milling were also observed in fluvial sediments in south-eastern Germany (Hoppe et al. 1996; Michel et al. 2005) and could be related to documented events (failure of the dam of a sedimentation pond, high water, termination of industrial activities). This finding confirms that such events may serve as time markers, which should be used to validate a ^{137}Cs-based geochronology.

Although uranium emissions into the watershed decreased after the initiation of a uranium dressing plant in Dolní Rožínka in 1968 (Kříbek and Hájek 2005) and after the conclusion of mining activities at Olší in 1989, ^{238}U in the analysed sediment decreased only gradually during the last 40 years. This reflects both the elevated concentrations of this radionuclide and its decay products in the watershed and the impacts of the Rožná mine, which is still in operation.

Conclusions

Modern deposits of the Brno reservoir were studied in detail with the aim of reconstructing the sedimentary history of the reservoir and identifying of processes involved in deposition there.

The studied sedimentary succession can be subdivided into two main units. The lower unit, interpreted as a fluvial succession deposited before the Svratka River was dammed, is formed predominantly by medium- to coarse-grained silty sands that are usually poorly sorted with some admixture of granules and reduced occurrence of plant detritus. Sandy silt laminae with abundant plant detritus are locally intercalated in sands. This fluvial unit can be subdivided into two subunits. The lower subunit is interpreted as a product of lateral accretion of the point bar. The upper subunit was deposited in response to the beginning of reservoir filling and the possible impact of the several flood events during the years of 1939–1941. The upper unit of succession consists of brownish, grey to greenish planar laminated silts and rarely clayey or sandy silts. Thin sandy interlayers and sand admixture occur especially in the lower part of the upper unit. Planar lamination is connected with alternation of slightly coarser and lighter laminae and those that are relatively finer grained and darker (with higher content of organic matter). The upper unit is interpreted as reservoir sediments. Reservoir sediments reflect cyclic changes in both TOC and MS, which are usually negatively correlated.

Mean depositional rates of 3.2 cm year^{-1} for the time period from 1986 to 2007 and 3.4 cm year^{-1} between 1963 and 1986 were calculated. Based on the known age of the reservoir, which was constructed in 1939, the mean depositional rate was also calculated for the time period from 1939 to 1963, which is 3.1 cm year^{-1}. These results indicate that the sedimentation regime has been almost constant for the 68 years of the Brno reservoir's existence.

This study documents an environmental situation that precludes using only ^{210}Pb for sediment dating. Its main source here is ^{210}Pb present naturally in the catchment and from uranium mining activities. Because flux rates into the sediment are not time-invariant and depend on surface water runoff, application of the CRS model for depth-to-age conversion of excess ^{210}Pb is not possible.

Elevated concentrations of ^{238}U, ^{226}Ra and ^{210}Pb in the sediment core can be identified with particular events that are likely to have mobilised these radionuclides (completion of the reservoir, initiation of mining, enhanced fluvial discharge). These time markers can be used to validate the ^{137}Cs-derived chronology and to extend the geochronology back to the time of Brno reservoir construction in 1939. Therefore, when studies show uranium-rich minerals in sediments, we recommend that investigators determine whether specific human activities are responsible for elevated radionuclide concentrations because that information might prove helpful for establishing sediment chronologies.

Acknowledgments The authors would like to thank two unknown reviewers and the journal editors Neil Rose, Mark Brenner and Thomas Whitmore for their critical and stimulating comments, which greatly helped to improve the manuscript. We are very grateful to Petr Dobrovolný for his kind help with analysis of the hydrological data. We thank Povodí Moravy, State enterprise, for reservoir level fluctuation and discharge data. This study was funded by The Czech Ministry of Environment (Grant No. SP/1b7/156/07). The study was also kindly supported by the research project MSM 0021622412.

References

Alberts JJ, Wahlgren MA, Orlandini KA, Durbahn CA (1989) The distributions of ^{239}, ^{240}Pu, ^{238}Pu, ^{241}Am and 137Cs among chemically-defined components of sediments, settling particulates and net plankton of Lake Michigan. J Environ Radioact 9:89–103

Anderson RF, Schiff SL, Hesslein RH (1987) Determining sediment accumulation and mixing rates using ^{210}Pb, ^{137}Cs, and other tracers: problems due to postdepositional mobility or coring artifacts. Can J Fish Aquat Sci 44(Suppl 1):231–250

Appleby PG (2001) Chronostratigraphic techniques in recent sediments. In: Last WM, Smol J (eds) Tracking enviromental change using lake sediments. Kluwer, Dordrecht, pp 171–203

Appleby PG (2008) Three decades of dating recent sediments by fallout radionuclides: a review. Holocene 18:83–93

Barra R, Cisternas M, Urrutia R, Pozo K, Pacheto P, Parra O, Focardi S (2001) First report on chlorinated pesticide deposition in a sediment core from a small lake in Central Chile. Chemosphere 45:749–757

Begy R, Cosma C, Timar A (2009) Recent changes in Red Lake (Romania) sedimentation rate determined from depth profiles of 210Pb and 137Cs radioisotopes. J Environ Radioact 100:644–648

Bell FG (1998) Enviromental geology: principles and practice. Wiley, London, pp 1–594

Bennett SJ, Rhoton FE (2007) Reservoir sedimentation and environmental degradation: assessing trends in sediment-associated trace elements in Grenada Lake, Mississippi. J Environ Qual 36:815–825

Blais JM, Kalff J (1995) The influence of lake morphometry on sediment focusing. Limnol Oceanogr 40:582–588

Brázdil R ed (1995) Statistické metody v geografii. Brno, pp 1–80 (In Czech)

Brothers S, Vermaire JC, Gregory-Eaves I (2008) Empirical models for describing recent sedimentation rates in lakes distributed across broad spatial scales. J Paleolimnol 40:1003–1019

Callaway JC, DeLaune RD, Patrick W (1996) Chernobyl ^{137}Cs used to determine sediment accretion rates at selected northern European coastal wetlands. Limnol Oceanogr 41:444–450

Di Gregorio DE, Fernández Niello JO, Huck H, Somacal H, Curutchet G (2007) ^{210}Pb dating of sediments in a heavily contaminated drainage channel to the La Plata estuary in Buones Aires, Argentina. Appl Radiat Isot 65:126–130

Evans ME, Heller F (2003) Environmental magnetism. Academic Press, Oxford, pp 1–312

Folk RL, Ward W (1957) Brazos River bar: a study in the significance of grain-size parameters. J Sediment Petrol 27:3–26

Foster IDL, Walling DE (1994) Using reservoir deposits to reconstruct changing sediment yields and sources in catchment of the Old Mill Reservoir, South Devon, UK, over the past 50 years. Hydrol Sci 39:347–368

Franců E, Schwarzbauer J, Lána R, Nývlt D, Nehyba S (2010) Historical changes in levels of organic pollutants in sediment cores from Brno Reservoir, Czech Republic. Water Air Soil Pollut 209:81–91

French PW, Allen JRL, Appleby PG (1994) 210-Lead dating of a modern period saltmarsh deposit from the Severn estuary (Southeast Britain) and its implications. Mar Geol 118:327–334

Gasiorowski M, Hercman H (2005) Recent changes of sedimentation rate in three Vistula oxbow lakes determined by 210Pb dating. Geochronometria 24:33–39

Haag I, Kern U, Westrich B (2001) Erosion investigation and sediment quality measurements for a comprehensive risk assessment of contaminated aquatic sediments. Sci Total Environ 266:249–257

Håkanson L (2007) Lake environments. In: Perry C, Taylor K (eds) Environmental sedimentology. Blackwell Publ, Oxford, pp 109–143

Hoppe T, Kluge A, Jurk M, Schkade U (1996) Radioaktive isotope in Sedimenten—Freiberger Mulde, Zwickauer Mulde, vereinte Mulde. Z Umweltchem Ökotox 8:83–88

Kashiwaya K, Okimura T, Harada T (1997) Land transformation and pond sediment information. Earth Surf Processes Landforms 22:913–922

Kirchner G, Ehlers H (1998) Sediment geochronology in changing coastal environments: potentials and limitations of the ^{137}Cs and ^{210}Pb methods. J Coastal Res 14:483–492

Koide M, Soutar A, Goldberg ED (1971) Marine geochronology with ^{210}Pb. Earth Planet Sci Lett 14:442–446

Křibek B, Hájek A (2005) Uranové ložisko Rožná. Model pozdně variských a povariských mineralizací. Czech Geological Survey, Prague, pp 1–98 (In Czech)

Lüder B, Kirchner G, Lücke A, Zolitschka B (2006) Paleoenvironmental reconstructions based on geochemical parameters from annually laminated sediments of Sacrower See (northeastern Germany) since the 17th century. J Paleolimnol 35:897–912

Lynch JC, Meriwether JR, McKee BA, Vera-Herrera F, Twilley RR (1989) Recent accretion in mangrove ecosystems based on ^{137}Cs and ^{210}Pb. Estuaries 12:284–299

Michel R, Feuerborn J, Knöchel A, Miller F, Ritzel S, Treutler H-C, von Tümpling W, Wanke C (2005) Radionuclides in the Mulde river system after the August 2002 flood. Acta Hydrochim Hydrobiol 33:492–506

Mulholland PJ, Elwood JW (1982) The role of lake and reservoir sediments as sinks in the perturbed global carbon cycle. Tellus 34:490–499

Müller P, Novák Z et al. (2000) Geologie Brna a okolí. Czech Geological Survey, Brno, pp 1–90 (In Czech)

Nemec W (2005) Principles of lithostratigraphic logging and facies analyses. Institutt for geovitenskap, Uni Bergen, pp 1–28

Oldfield F, Wake R, Boyle J, Jones R, Nolan S, Gibbs Z, Appleby P, Fisher E, Wolff G (2003) The late-Holocene history of Gormire Lake (NE England) and its catchment: a multiproxy reconstruction of past human impact. Holocene 13:677–690

Phillips CJ, Nelson CS (1981) Sedimentation in an artificial lake. Lake Matahina, Bay of Plenty. N Z J Mar Freshwater Res 15:459–473

Rangarajan C, Madhavan R, Gopalakrishnan SmtS (1986) Spatial and temporal distribution of lead-210 in the surface layers of the atmosphere. J Environ Radioact 3:23–33

Reinikainen P, Meriläinen JJ, Virtanen A, Veijola H, Äystö J (1997) Accuracy of ^{210}Pb dating in two annually laminated lake sediments with high Cs background. Appl Radiat Isot 48:1009–1019

Ritchie JC, McHenry JR, Gill AC (1973) Dating recent reservoir sediments. Limnol Oceanogr 18:254–263

Robbins JA, Edgington DN (1975) Determination of recent sedimentation rates in Lake Michigan using Pb-210 and Cs-137. Geochim Cosmochim Acta 39:285–304

Sedláček J, Bábek O (2009) Předběžné zhodnocení rychlosti sedimentace ve vybraných přehradních nádržích v povodí Moravy. Geologické výzkumy na Moravě a ve Slezsku 16:31–34 (In Czech)

Shotbolt LA, Thomas AD, Hutchinson SM (2005) The use of reservoir sediments as environmental archives of catchment inputs and atmospheric pollution. Prog Phys Geogr 29:337–361

Shotbolt LA, Hutchinson SM, Thomas AD (2006) Sediment stratigraphy and heavy metal fluxes to reservoirs in the southern Pennine uplands, UK. J Paleolimnol 35:305–322

Sikorski J, Bluszcz A (2008) Application of α and γ spectrometry in the ^{210}Pb method to model sedimentation in artificial retention reservoir. Geochronometria 31:65–75

Smith JN (2001) Why should we believe ^{210}Pb sediment geochronologies? J Environ Radioact 55:121–123

Smith JN, Walton A (1980) Sediment accumulation rates and geochronologies measured in the Sagenay Fjord using the Pb-210 dating method. Geochim Cosmochim Acta 44:225–240

Tucker M (ed) (1988) Techniques in sedimentology. Blackwell Science, Oxford, pp 1–394

Turekhian KK, Nozaki Y, Benninger LK (1977) Geochemistry of atmospheric radon and radon products. Ann Rev Earth Planet Sci 5:227–255

UNSCEAR—United Nations Scientific Committee on the Effects of Atomic Radiation (2000) Sources and effects of ionizing radiation. UNSCEAR 2000 Report to the General Assembly, vol I: Sources. United Nations sales publication E.00.IX.3, New York

Van Metre PC, Callender E, Mahler BJ, Wilson JT, Dorsey ME (2001) Differences in lake and reservoir sedimentation—implications for sediment coring studies. In: Reno NV (eds) Proceedings of the seventh federal interagency sedimentation conference, IX:12–19

Vlček V (ed) (1984) Zeměpisný lexikon ČSR. Vodní toky a nádrže. Academia, Praha, pp 1–316

Walker M (2006) Quaternary dating methods. Wiley, Chichester, pp 1–286

Walker RG, James NP (1992) Facies models. Response to sea level changes. Geol Ass Canada, Toronto, pp 1–380

Wren DG, Davidson GR (2008) Practical implications of quantifying ancient sedimentation rates in lakes. J Soil Water Conserv 63:89A

Yeloff DE, Labadz JC, Hunt CO (2005) The suitability of south Pennine (UK) reservoir as an archive of recent environmental change. J Paleolimnol 34:339–348

Zhang X, Walling DE, Quine TA, Wen A (1998) Use of reservoir deposits and Caesium—137 measurements to investigate the erosional response of a small drainage basin in the Rolling Loess Plateau region of China. Land Degrad Dev 8:1–16

Příloha 11

Franců E., Schwarzbauer J., Lána R., Nývlt D., Nehyba S. (2009) Historical Changes in Levels of Organic Pollutants in Sediment Cores from Brno Reservoir, Czech Republic. Water, Air and Soil Pollution 209, 1-4, s. 81-91.

Water Air Soil Pollut
DOI 10.1007/s11270-009-0182-x

Historical Changes in Levels of Organic Pollutants in Sediment Cores from Brno Reservoir, Czech Republic

E. Franců · J. Schwarzbauer · R. Lána · D. Nývlt · S. Nehyba

Received: 11 May 2009 / Accepted: 14 August 2009

Abstract Results of a comprehensive study are presented on the spatial and depth-related distribution of persistent organic pollutants (POPs) in sediments of the Brno reservoir, Czech Republic. Based on sedimentological observations, three major historic phases were identified related to the evolution of the depositional environment, flow rate, and material input. Data on organic carbon, polycyclic aromatic hydrocarbons, polychlorinated biphenyls, and organochlorine pesticides showed specific distribution patterns in a 3-m-deep core. The analysis of the depth trends of the geochemical data combined with sedimentology made it possible to distinguish between remote sources of the pollutants, early weathering alterations of POPs, transport by river associated with organic matter as sorbent on one hand, and local sources weakly related to lithology on the other hand. The integrated sedimentological and environmental geochemical archive provided an improved dynamic view of the pollution in historical terms.

Keywords PCBs · PAHs · Organochlorine pesticides · Sediment profile

1 Introduction

Persistent organic pollutants (POPs), such as polychlorinated biphenyls (PCBs) and organochlorine pesticides (OCPs), are incessantly being found in water, sediments, and biota throughout the world despite the fact that their production and usage have been restricted since the 1970s (Konat and Kowalewska 2001; Sapozhnikova et al. 2004; Covaci et al. 2006). POPs are known to have a strong affinity to particles, and thus, river and lake sediments represent an important sink for these contaminants (Zennegg et al. 2007). Many authors have successfully used undisturbed sediment cores as pollution archives to restore the historical changes in the levels and patterns of POPs in aquatic environments (e.g., Hong et al. 2003; Frignani et al. 2005; Heim et al. 2005; Evenset et al. 2007; Kim et al. 2007).

The bulk analysis of POPs is often extended to more precise information on the pollution sources

---

E. Franců (✉) · R. Lána · D. Nývlt
Czech Geological Survey,
Leitnerova 22,
65869 Brno, Czech Republic
e-mail: eva.francu@geology.cz

J. Schwarzbauer
Institute of Geology and Geochemistry of Petroleum and Coal, Aachen University of Technology (RWTH),
Lochnerstr. 4-20,
52056 Aachen, Germany

S. Nehyba
Department of Geological Sciences,
Masaryk University of Brno,
Kotlarska 2,
61137 Brno, Czech Republic

and their fate in the environment using more detailed analysis, e.g., by isomer- or congener-specific analyses of PCBs, OCPs, or PAHs (e.g., Götz et al. 2007; Zennegg et al. 2007). The multicomponent analysis of different substance classes provides a basis for a comprehensive assessment of relationships among different types of contaminants and their sources.

Owing to an intensive agricultural and industrial production in past few decades, in particular, river and reservoir sediments in the Czech Republic are loaded with POPs and their levels are only slowly decreasing (Holoubek et al. 2000, 2003, 2007). In contrast to soil contamination monitored regularly in the Czech Republic since the late 1970s (Svobodova et al. 2003), there are very limited data available on POPs in sediment cores, especially no data prior to the 1970s (e.g., Bábek et al. 2008). This makes it difficult to assess the historical trends in the amounts of POPs entering the aquatic environment and to evaluate the effect of implementation of legal measures toward the POPs reduction on their real occurrence.

A great number of papers published during the past decade present valuable data on the pollutant distribution in surface sediments and cores (e.g., Dsikowitzky et al. 2002; Yunker et al. 2002; Navarro et al. 2006; Li et al. 2009). In many papers, however, there is a limited analysis of the sedimentological features of the pollutant distribution, which may play a key role in distinguishing among the different sources, transport processes, and state of preservation of the contaminants in the specific environment (Eyre and McConchie 1993; Pereira et al. 1999; Lüder et al. 2006).

Brno reservoir is an important artificial lake within the southern Moravian water management system. It was built on the Svratka River in 1936–1939 and filled in the early 1940s (Bayer et al. 1954). This type of basin provides a unique opportunity to study an undisturbed sedimentary sequence not only to illustrate the spatial distribution in the reservoir but also describe depth trends in POPs. For this purpose, more comprehensive analysis comprising congener- and isomer-specific analyses as well as multicomponent approaches have been applied together with sedimentological characteristics of the sediment cores to document a sedimentation period from the 1920s to the construction of the Brno reservoir and its evolution until present time.

2 Sampling and Methods

2.1 Sampling

A preliminary sampling campaign was performed to explore an optimal location for drilling a deep core. Therefore, 12 shallow cores were collected (Fig. 1) using a hand-coring device. Each core was cut into slices of about 5 cm; the total cored depth interval ranged from less than 100 to 250 cm. Based on these results, a 292.5-cm-deep core (BP4) was drilled in March 2008 using Makita vibration hammer and Eijkelkamp coring tubes (Fig. 1). The drilling site of the BP4 core is located in the upper part of the Brno reservoir below the Veveří Castle, where the Svratka River has incised meandering fluvial pattern. The core was placed in a plastic sleeve and divided immediately into two equal parts. One part was frozen and stored and the other one was photo documented, lithologically described, and divided into 121 subsamples, each about 2.5 cm thick.

2.2 Bulk Characterization

The samples were dried, pulverized, homogenized, and sieved through a 1-mm mesh. All samples were subjected to elemental analysis of total organic (TOC) and inorganic carbon using a Metalyt CS 1000 S apparatus (ELTRA GmbH, Neuss, Germany). Environmental magnetic susceptibility (MSS) was measured as mass susceptibility (χ) in $10^{-9}\mathrm{m}^3\mathrm{kg}^{-1}$ dividing the volume susceptibility by material density using the MFK1-FA Kappabridge at the magnetic field of 200 A m^{-1} in the AGICO, Ltd. For further summary of magnetic parameters and terminology, see Evans and Heller (2003).

2.3 Extraction and Fractionation

n-Pentane, *n*-hexane, *n*-heptane, and dichloromethane (DCM; all of residue analysis grade) as well as silica gel were purchased from Merck (Darmstadt, Germany); anhydrous sodium sulfate for analysis (activated at 600°C for 6 h prior use) was obtained from Penta (Chrudim, Czech Republic). Sample aliquots of 5 g were mixed with a portion of activated Na_2SO_4 and spiked with 25 µL of surrogate recovery standard solution containing 2,4,5,6-tetrachloro-*m*-xylene, PCB 209, d10-

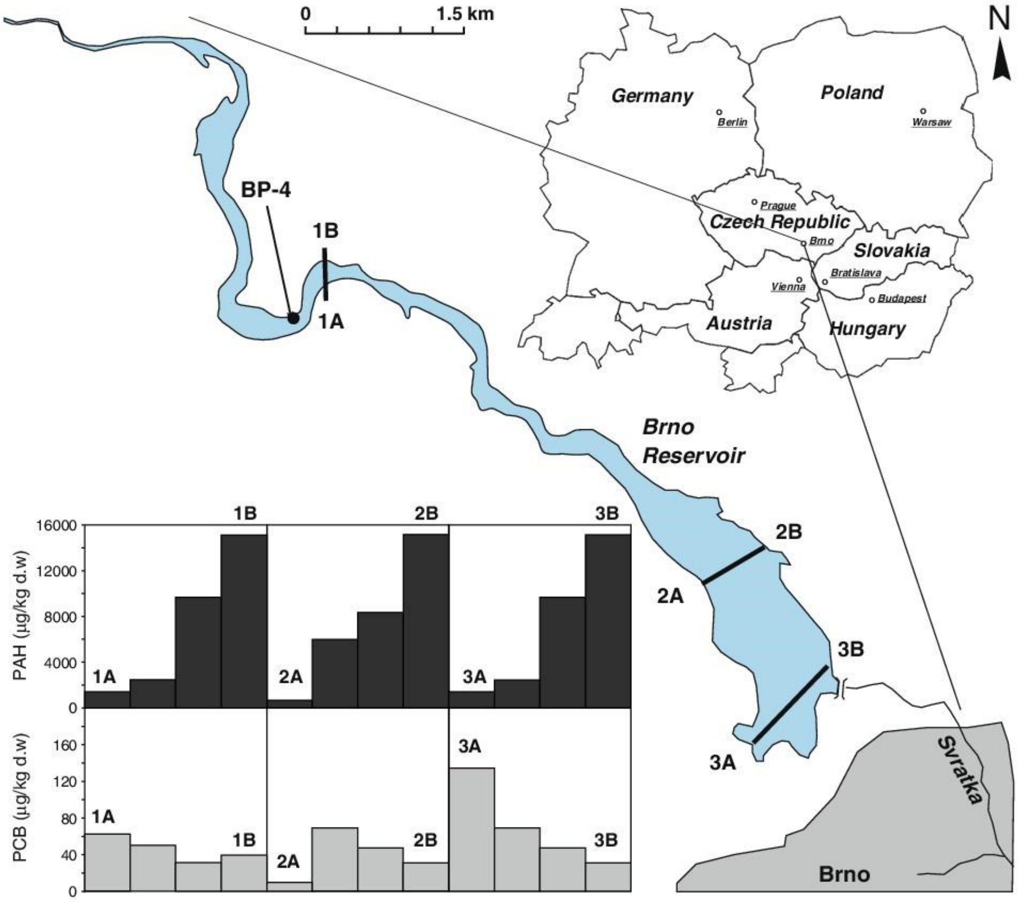

Fig. 1 Sampling locations and PCB and PAH concentrations for surface sediments in Brno reservoir

anthracene and d12-chrysene. Extraction was performed with *n*-hexane/acetone (1:1) by accelerated solvent extraction on a ASE 100 system (Dionex, USA). The extractions were performed at 100°C and 2,000 psi with two static extraction cycles (4 min each), then the extraction cell was flushed with solvent (60%) and purged with nitrogen (2 min). The raw extracts were reduced to 0.5 mL using a gentle stream of nitrogen, and the volume was adjusted to 10 mL with *n*-hexane. For analysis of halogenated compounds, an aliquot of 2 mL of the extract was taken to a vial, 2 mL of *n*-heptane together with 50 µL of internal standard containing octachloronaphthalene (to control the cleanup step, 1 ng/µL in *n*-heptane) was added, and after concentration to 0.5 mL and readjustment to 2 mL with *n*-heptane, activated powder copper was added in order to remove sulfur (overnight). The cleanup was carried out on a glass column with 0.5 g of activated silica, 0.5 g of silica impregnated with $AgNO_3$, 0.5 g of silica impregnated with NaOH, another 0.5 g cm of silica, then 1.5 g of silica impregnated with 96% H_2SO_4, and finally 0.5 g of silica. The target analytes were eluted with 28 mL of pentane, evaporated to 0.5 mL using nitrogen, transferred to a gas chromatography GC vial, and the volume was adjusted to 1 mL with *n*-heptane. For the PAH analysis, an extract aliquot of 2 mL was placed on a silica gel column to separate the aliphatic and aromatic hydrocarbon fractions by liquid chromatography using *n*-hexane and DCM as eluents; powder copper was added in order to remove elemental sulfur (overnight).

2.4 Quantification of PCBs and OCPs

PCBs and OCPs were determined using a Hewlett-Packard 6890 gas chromatograph, equipped with an electron capture detector and a HP-5ms fused silica capillary column (60 m×0.25 mm i.d.×0.25 μm, J&W Scientific, USA). Hydrogen was used as the carrier gas (constant flow 1.1 mL/min), and the GC oven temperature was programmed as follows: initial temperature 50°C held for 2 min–increase to 150°C at a rate of 50°C/min–final increase to 300°C at 5°C/min and held for 11 min. The following halogenated organic contaminants were analyzed: seven PCB congeners (28, 52, 101, 118, 138, 153, and 180), dichlorodiphenyltrichloroethane (DDT) and selected metabolites (*o,p′*- and *p,p′*-DDT, *o,p′*- and *p,p′*-dichlorodiphenyldichloroethylene (DDE), and *o,p′*- and *p,p′*-dichlorodiphenyldichloroethane (DDD)) as well as hexachlorobenzene (HCB). All reference standards were purchased from Dr. Ehrenstorfer (Augsburg, Germany), and quantification was based on an external eight-point calibration (0.5–500 ng/mL of each component in *n*-heptane).

2.5 Quantification of PAHs

Determination of 16 EPA PAHs including naphthalene (N), acenaphthylene (Ayl), acenaphthene (Aen), fluorene (F), phenanthrene (P), anthracene (An), fluoranthene (Fl), pyrene (Py), benzo[*a*]anthracene (B*a*A), chrysene (Ch), benzo[*b*]fluoranthene (B*b*F), benzo[*k*]fluoranthene (B*k*F), benzo[*a*]pyrene (B*a*P), indeno[1,2,3-*cd*]pyrene (IP), dibenzo[*a,h*]anthracene (D*ah*A), and benzo[*ghi*]perylene (B*ghi*P) was carried out using a Hewlett-Packard 6890N gas chromatograph connected to a HP 5973N MSD quadrupole mass spectrometer (MS) operated in the electron impact mode (EI^+, 70 eV) with a source temperature of 270°C and single ion monitoring. The chemical identity of PAHs was checked both by retention time match and by using selected qualifier ions. The following ions were used for qualification and quantification (in italic form) of the target PAHs (*m/z*): N (127, *128*, 129), Ayl (151, *152*), Aen (152, *153*, 154), F (165, *166*, 167), P + An (176, *178*, 179), Fl + Py (200, *202*, 203), B*a*A + Ch (226, *228*, 229), B*b*F + B*k*F + B*a*P (126, *252*, 253), IP + B*ghi*P (274, *276*), and D*ah*A (276, *278*).

A volume of 1 μL was injected splitless (splitless time 60 s, injection temperature 100°C, then increase to 300°C at 720°C/min) onto a HP-5ms capillary column (30 m×0.25 mm i.d.×0.25 μm). Separation was carried out using helium at a constant flow of 1.2 mL/min with the following oven temperature program: 50°C (held for 1.2 min), then at 10°C/min to 170°C and at 6°C/min to the final temperature of 315°C (held for 3 min). The PAH quantification was also based on an external four-point calibration with authentic reference material.

2.6 Quality Control

The identification of all PCBs and OCPs was verified by the analyses of selected samples using GC/MS (method described above). Blank samples were prepared by submitting pure solvent to the whole analytical procedure with activated Na_2SO_4 instead of sample material (at least with each set of ten samples). Analytical blanks had levels of high-chlorinated PCB congeners (138, 153, 180) and HCB below method detection limits; no other compounds were detected. The analyte recoveries were determined by analyzing certified reference material (Metranal™ 2—River sediment, ANALYTIKA Ltd., Prague, Czech Republic) and for PCBs and OCPs, and PAHs were in the range of 61–100.8% and 70.8–128.9%, respectively. Those samples with recoveries below 50% were not used for quantification. The detection limits, calculated from the calibration solution with the lowest concentration within the linear range of the detector used, were 0.7 μg kg^{-1} for PCBs and OCPs and 1 μg kg^{-1} for PAHs.

3 Results and Discussion

3.1 Spatial Distribution of POPs

For a preliminary insight into the pollution level of Brno reservoir sediments, three horizontal profiles (A to B), perpendicular to the Svratka River flow, at three different locations (1 to 3) were sampled and analyzed for sum of PAHs and PCBs (Fig. 1). The quantitative distribution of the selected contaminant groups in the upper 5 cm below the surface along the three horizontal profiles revealed low amounts indicating an only negligible contamination of the Brno reservoir. Interestingly, total PAH concentrations (between 448 to 15,170 μg kg^{-1} dry weight (dw)) increased from right to left bank in all three profiles (Fig. 1, top) and suggested that local sources, such as numerous small furnaces in recreational weekend houses cumulated on the left bank, prevail over the PAH transported by the Svratka River. On the contrary, the PCB concentrations occurred close to or slightly above the value of 20 μg kg^{-1} dw. They show a rather flat distribution along the three profiles (Fig. 1, bottom) with gentle increase from the left to the right bank, i.e., in the opposite direction to the increasing trend of the PAHs. The maximum amounts of all contaminants are observed in the SW bay in the lower end of the reservoir. The slightly elevated values coincide with the location close to the marina and electric boat harbor.

3.2 Depth Trends

The BP4 core provides the most complete set of sedimentological, geochemical, and physical data in the studied area, which document the principal phases of evolution by three depth intervals with characteristic depth trends of the measured parameters. The data include lithological profile and facies (Fig. 2), TOC content, and MSS (Fig. 3). They reflect the oscillation in the water level, seasonal and annual variations.

3.2.1 Fluvial Succession

The lower part of the core (218.5–292.5 cm) is built mainly by medium- to coarse-grained sands with variable bed thickness up to 29 cm. Sands are usually poorly sorted. The very low TOC content ranging from 0.17% to 1.5% is associated with high magnetic susceptibilities (MSS mostly >250.10^{-9}m^{3}kg^{-1}), which exhibit several local maxima (300, 257.5, and 240 cm) and gradual upward decrease (Figs. 2 and 3). The increased MSS values are associated with higher proportion of ferromagnetic minerals delivered from amphibolites, scarns, and schists of the Moravicum unit (Svoboda 1963) by the main stream of the Svratka River and their deposition in the sand- and gravel-rich sediments. This lowermost part of the

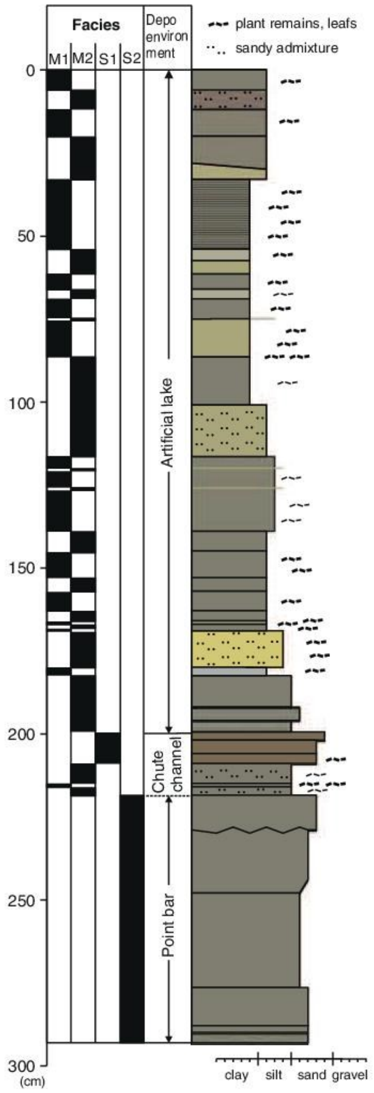

Fig. 2 Lithological profile, depositional environment, and facies in the BP4 borehole. The graphic log on the *right-hand side* presents macroscopically described sedimentological data. Log gives a visual impression of vertical changes in the studied section, including color, sedimentary texture (i.e., grain-size), sedimentary structures, lithology, and nature of bed contacts. The grain size of individual beds is expressed by its thickness —the wider the column, the coarser the sediment. For further explanation of sedimentological logging, see Tucker (1988, 2003)

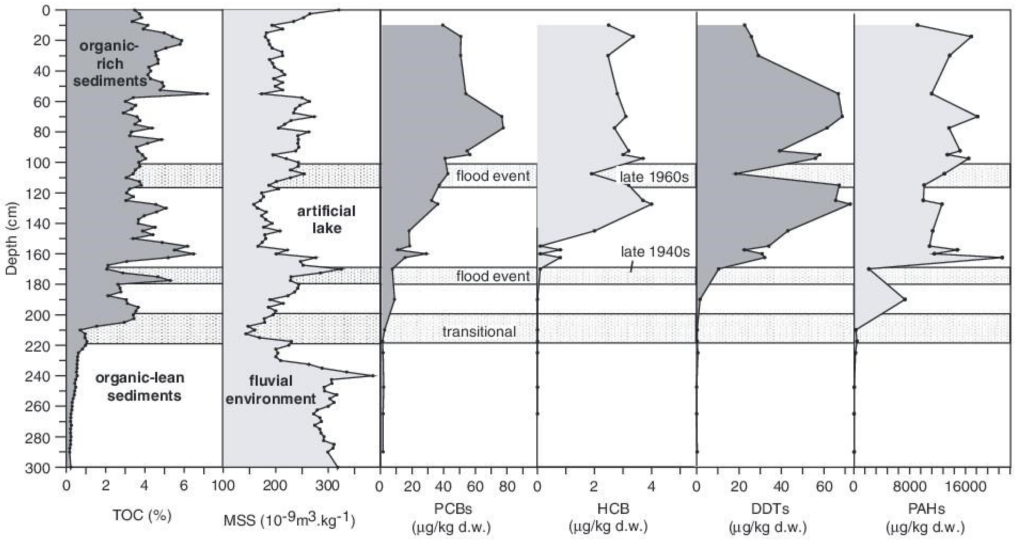

Fig. 3 Total organic carbon (*TOC*), magnetic susceptibility (*MSS*), polychlorinated biphenyls (*PCBs*), polyaromatic hydrocarbons (*PAHs*), DDTs, and hexachlorobenzene (*HCB*) in the BP4 profile

succession is interpreted as S2 facies formed in fluvial environment by lateral accretion of the sandy material in the meander point bar associated with the migration of the flow line toward the right cut bank of the Svratka River in this part of the valley.

3.2.2 Transitional Interval

The above-laying transitional interval (199.5–218.5 cm) is formed by thinner (<5 cm) sandy beds (S1 facies) alternating with sandy–silty laminas of M2 and M1 facies (Fig. 2), the latter being highly enriched in plant remains. It is characterized by sudden upward increase both in TOC up to 3.55% and MSS down to $155\times10^{-9}\mathrm{m}^3\mathrm{kg}^{-1}$. These sediments formed most probably by avulsion (redeposition) associated with possible meander chute channeling during a flood event and reservoir filling in 1939 followed by partial water outflow during the years 1939–1940, which is manifested in the coarsening-upward trend at this part of the succession (Fig. 3).

3.2.3 Artificial Lake Succession

The upper part of the core profile (0–199.5 cm) consists of dark clayey silts, silty clays, and some sandy silt interlayers occurring in the lower part of the succession. The muddy facies with rhythmical bedding, bed thickness of 10–30 cm, and rich or slightly enriched in plant detritus (M1 and M2 subfacies, respectively, Figs. 2 and 3). The organic-rich layers are notably darker and typically more clayey. The predominantly muddy material of the upper part of the profile was deposited in the artificial lake environment. The lithological variations and presence of several intercalated sandy silt layers, e.g., at depth of 101–116.5 and 169–180 cm, are interpreted as natural and/or anthropogenic forcing to the reservoir deposition associated with flood events when coarser material was deposited even in the lateral position off the main water flow line through the reservoir. In contrast to the transitional interval, there is a clear negative correlation between TOC and MSS. High TOC occur in medium–fine-grained silt and clay, where the amount of magnetic minerals is decreased while peak MSS values correlate with drops in the TOC in the sandy–silty layers.

The average accumulation rate estimated from the sediment thickness and total time since the first reservoir filling was ~3 cm year^{-1} with a gently upward decreasing trend and probable fluctuations manifested by uneven layer thickness. Assuming the mentioned rate, the two flooding events in the core might be deposited in the late 1940s and late 1960s of the past century. Precise sediment dating of this profile would be dealt with elsewhere.

3.3 General Trends in POPs in the Core

3.3.1 PCBs

Concentrations of PCBs (sum of PCB congeners 28, 52, 101, 118, 138, 153, and 180) in the whole profile ranged from <LOQ to 77.6 μg kg^{-1} dw (Fig. 3). The occurrence of PCBs in the sedimentary layers in a depth below 220 cm representing the pre-industrial period of time before the filling of the reservoir (1930s and older) may be explained by either molecular diffusion or bioturbation, similar to, e.g., the case described by Evenset et al. (2007). From 220 cm upward, the amount of PCBs increased from 2.74 to 76.7 and 77.6 μg kg^{-1} dw, the maximum PCB levels within the profile were at 77.5–70 cm, respectively. Above this depth, the PCBs declined to the value of 39.4 μg kg^{-1} dw in the top layer of the recent age. This value fits very well with the data obtained from the surface sediment samples (see Section 3.1). Noteworthy, a PCB peak was observed at a depth of 160 cm, which coincided with an increase in the TOC.

The PCB production began in the early 1930s in the western countries (Breivik et al. 2002). Since the commercial production of PCBs in the former Czechoslovakia started during the early 1960s (Holoubek et al. 2003), PCBs found in core segments representing the periods of time after the 1940s (upward from ca. 200 cm) probably originated from imported foreign PCB products. The maximum PCBs corresponded to the late 1970s–mid-1980s. Decreasing trends in PCBs, observed in subrecent sedimentary layers, reflect the implementation of the legal measures toward the reduction of PCB use during past decades.

3.3.2 Organochlorine Pesticides

DDT contamination level started at a depth of approximately 210–200 cm (Fig. 3) reached two maxima of 72.4 and 68.7 μg kg^{-1} dw at depths of 128 and 70 cm, respectively. In contrary to a more stable increase in PCBs, two significant drops at depths of 108 and 93 cm were observed in sandy layers. This might be explained as a result of flood events when sandy material was selectively deposited whereas the fine-grained fraction was washed further away with DDTs (see Section 3.4.2 for detailed discussion).

The concentration of HCB showed increase within the depth interval from 155 to 115 cm. Toward the surface layers, a relatively uniform HCB level at around 3 μg kg^{-1} dw was observed with less significant decrease in recent samples.

3.3.3 PAHs

The evolution trend of the PAHs is similar to that of the PCBs with more abrupt increase from the background values (41–62 μg kg^{-1} dw) to 236 μg kg^{-1} dw at the fluvial-to-transitional environmental boundary (218.5 cm; Fig. 3). The transitional interval is enriched in PAHs by one order of magnitude (300–463 μg kg^{-1} dw) while in the initial fine-grained artificial lake sediments, the total amount of PAHs reaches the highest value of the entire profile (21,278 μg kg^{-1} dw at 164 cm), which is by three orders of magnitude higher than that in the fluvial S2 facies. The sandy silt layers of the transitional interval and initial artificial lake succession are associated with marked decrease in PAHs. This does not apply to the shallower sandy silt layer at depth of 101–116.5 cm, where the PAHs content does not seem to be controlled by lithology.

3.3.4 Comparison with Similar Studies

Vertical changes in POPs from the Brno reservoir sediment core showed comparable trends with other published studies. Yamashita et al. (2000) observed increasing contamination trends for various organochlorines in a sediment core from Tokyo Bay with a beginning in the early 1900s and a maximum in the early 1980s. The maximum levels of PCBs and PAHs were 150 and 2,000 μg kg^{-1} dw, respectively. PCBs (sum of six indicator congeners) in a sediment core from Greifensee, Switzerland, had nearly the same historical trends between the 1930s and 1980s with a maximum of 130 μg kg^{-1} dw in the 1960s (Zennegg et al. 2007). Decreasing concentration trends for PCBs from the 1970s were also observed in sediment cores from the Venice Lagoon, Italy (Frignani et al. 2005). Similarly, slightly declining levels of organochlorines were found in recent sedimentary layers from the Teltow Canal, Germany, and in sedimentary archives from the Lippe and Rhine rivers (Heim et al. 2004, 2005, 2006). Even POPs in sediment cores from remote areas show similar time trend, as demonstrated by Evenset et al. (2007) who found maximum levels of PCBs and DDTs (71.8 and $4\ \mu g\ kg^{-1}$ dw, respectively) as back as the mid-1960s with an increase beginning in the 1930s.

3.4 Compound-Specific Distribution of POPs

3.4.1 PCBs

A detailed study of the congener pattern, e.g., by comparing PCB of different degree of chlorination, might be a helpful tool to evaluate changes in PCB application or changes in environmental conditions (Li et al. 2009). Three predominant congeners in all cores were PCB 138, 153, and 180. The ratio of PCB congeners 28/153, which act as representatives of trichlorinated and hexachlorinated congeners, ranged dominantly from 0.05 to 0.39 with a mean of 0.27 representing a dominance of higher chlorinated congeners (Table 1). Also, the more comprehensive ratio (28+52)/(138+153+180) supported this observation. Higher chlorinated technical formulations are typical constituents in hydraulic fluids or thermostable lubricants, whereas lower chlorinated mixtures are used in less viscous applications. The congener patterns of the investigated PCBs were relatively consistent and without general trend throughout the whole length of the core (Fig. 4). A significant increase of both PCB ratios (up to 1.6 or 0.95,

Table 1 Ratios of the PCB congeners, DDTx metabolites, and selected PAHs—An/(An + P), Fl/(Fl + Py), B*a*A/(B*a*A + Ch) in the BP4 core samples

Depth (cm)	PCB28/ PCB153	PCB (28 + 52)/PCB (138 + 153 + 180)	2,4-/4, 4-DDE	2,4-/4, 4-DDD	2,4-/4, 4-DDT	An/ (An + P)	Fl/ (Fl + Py)	BaA/ (BaA + Ch)
10	0.16	0.11	N/A	3.27	N/A	0.05	0.57	0.46
17.5	0.18	0.13	N/A	3.47	N/A	0.06	0.57	0.46
30	0.18	0.12	N/A	4.75	N/A	0.05	0.57	0.46
55	0.39	0.24	0.02	2.09	0.14	0.06	0.57	0.45
70	0.15	0.10	N/A	0.68	0.09	0.07	0.57	0.46
77.5	0.20	0.13	0.02	1.3	0.12	0.06	0.57	0.45
92.5	1.13	0.71	0.04	3.99	0.43	0.07	0.57	0.49
95	1.60	0.95	0.03	0.91	0.14	0.07	0.57	0.45
97.5	0.27	0.17	0.04	1.49	0.14	0.07	0.57	0.49
107.5	0.07	0.06	N/A	2.71	N/A	0.08	0.57	0.48
115	0.16	0.11	0.03	0.67	0.44	0.07	0.56	0.45
125	0.13	0.10	0.03	1.25	0.2	0.08	0.56	0.48
127.5	0.15	0.12	0.05	0.58	0.28	0.09	0.55	0.45
145	–	–	0.06	0.89	0.39	0.08	0.57	0.45
155	–	–	0.10	0.82	N/A	0.08	0.58	0.46
157.5	0.27	0.24	0.12	1.15	N/A	0.09	0.58	0.50
160	0.09	0.08	0.11	1.04	N/A	0.09	0.58	0.46
162.5	0.21	0.24	0.10	0.72	N/A	0.09	0.58	0.51
170	–	–	N/A	1.00	N/A	0.10	0.58	0.45
190	–	–	N/A	N/A	N/A	0.09	0.57	0.46
210	–	–	N/A	N/A	N/A	0.08	0.57	0.40
217.5	–	–	N/A	N/A	N/A	0.09	0.57	0.41
225	–	–	–	–	–	0.09	0.57	0.41
247.5	–	–	–	–	–	0.13	0.57	–
265	–	–	–	–	–	–	–	–
290	–	–	–	–	–	–	–	–

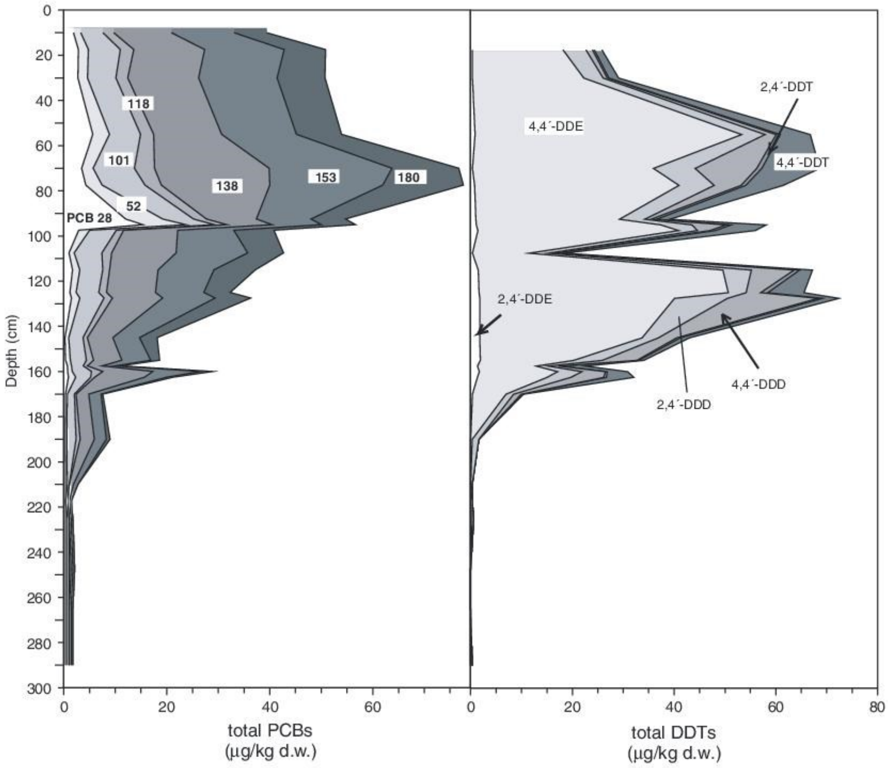

Fig. 4 PCB congener patterns and DDT homologous in the BP4 sediment core (Brno reservoir 2008)

respectively), at depth 95 cm, may suggest a temporary input of technical PCB mixtures with higher content of low chlorinated PCB congeners. An accidental leakage from a former manufacture of transformers and capacitors utilizing a low chlorinated technical mixture of Delor 103 (similar to Aroclor 1242) and situated upstream from the reservoir has been documented for this time period and might, therefore, be the reason for the excursion of the congeneric pattern. Hence, the PCB ratio excursion illustrates the superimposition of diffuse and constant contamination by a local emission event.

3.4.2 DDTs

With respect to the sediment core investigated, an unusual distribution of DDT metabolites was detected. Relative abundances of DDT isomers (Fig. 4) were found to be in order DDE ≫ DDD > DDT in almost all layers of the core. Particularly, the concentration of *p,p′*-DDE accounted for 49.9–81.7% of total ΣDDT concentrations. This was a somewhat unusual observation in dominantly strict anaerobic reservoir sediments where, consequently, a predominance of the *p,p′*-DDD was expected. The observations may indicate an input of highly weathered DDT, as already published by, e.g., Evenset at al. (2007). In our case, the principal source of DDT was agricultural activities upstream to the reservoir during past decades and the following aerobic degradation of DDT on soil that have been then transported to an anaerobic sedimentary environment. The mean ratio of *p,p′*-DDT/*p,p′*-DDE, used to estimate the "age" of DDT inputs, was 0.13 in our core (Table 1). According to Strandberg et al. (1998), the ratio of 0.33 or less in sediments is considered as an aged mixture and this suggests that current input of DDT into the reservoir are of little importance.

3.4.3 PAHs

Source indicative PAHs were used for calculation of the ratios Fl/(Fl + Py), BaA/(BaA + Ch), 1,7-DMP/(2,6 + 1,7-DMP) ratios introduced by Budzinski et al. (1997) and (Yunker et al. 1999). These parameters are used to distinguish the dominant emission source and the associated emission pathways of PAH, in particular its petrogenic or pyrolytic origin. This approach was also applied to the sediment samples of the Brno reservoir. The most significant ratios Fl/(Fl + Py) and BaA/(BaA + Ch) were higher than 0.5 and indicated combustion processes as main PAH source (Table 1; Yunker et al. 2002). Accordingly, the PAHs seem to derive dominantly from diffuse emissions of contaminated airborne particles or from soil erosion also polluted by pyrogenic material.

4 Conclusions

Based on sedimentological and screening analysis, the investigated core profile can be divided into three major sections with different depositional history and pollutant distribution. The lowest interval (218.5–292.5 cm) was deposited in a fluvial environment with low organic carbon and POPs content. Depletion in contamination might probably not reflect lower emission rates but might be the result of rather higher flow rates washing away the fine-grained and normally higher polluted particles. The lower sorption capacity of the accumulated coarser sedimentary material is suspected to be the reason for the low pollution level in the lower core section.

The intermediate interval represented the initial flooding process of the Brno reservoir (218.5–199.5 cm). It was marked by a sudden increase in TOC and with the amounts of analyzed POPs associated with upward coarsening of sediments. This was interpreted as a result of extensive sediment redeposition during one flooding event.

The upper segment deposited in the reservoir environment (199.5–0 cm) was rich in clays and silts, and two sandy layers evidenced two major flood events in the late 1940s and late 1960s. The clay-rich interval was characterized by a pronounced increase in all POPs in contrast to sandy interlayers with low amounts of DDTs and HCB. Surprisingly, these were associated neither with decrease in PCBs nor in PAHs. This discrepancy could be explained by a different input of the mentioned pollutant groups into the reservoir. DDTs and HCB were washed down dominantly from upstream agricultural influenced area and corresponding soils, adsorbed on clays and organic matter, and transported into the reservoir by the Svratka River. During the flood events with elevated flow rates, the sandy material was deposited selectively while the fine-grained fraction was washed away and the associated DDT and HCB contaminants were probably mobilized. Based on the fact that the PCBs and PAHs did not show decrease in the sandy intervals, it might be deduced that they were brought into the reservoir dominantly by precipitation from the air and short distance sheet runoff from the surrounding slopes by means of transport which was less sensitive to grain size fractionation and thinning during floods.

Acknowledgments Special thanks to F. Hrouda and M. Chlupáčová (Agico Ltd.) for magnetic susceptibility measurement. This study was funded by The Czech Ministry of Environment (grant no. SP/1b7/156/07).

References

Bábek, O., Hilscherová, K., Nehyba, S., Zeman, J., Famera, M., Francu, J., et al. (2008). Contamination history of suspended river sediments accumulated in oxbow lakes over the last 25 years. *Journal of Soils and Sediments*, *8*, 165–176.

Bayer, M., Mencl, V., & Pelikán, V. (1954). Erozivní zjevy na březích nádrže na řece Svratce v Kníničkách. Sbor. VŠ Stav. IV, 293–302.

Breivik, K., Sweetman, A., Pacyna, J. M., & Jones, K. C. (2002). Towards a global historical emission inventory for selected PCB congeners—a mass balance approach: 1. Global production and consumption. *The Science of the Total Environment*, *290*, 181–198.

Budzinski, H., Jones, I., Bellocq, J., Pierard, C., & Garrigues, P. (1997). Evaluation of sediment contamination by polycyclic aromatic hydrocarbons in the Gironde estuary. *Marine Chemistry*, *58*, 85–97.

Covaci, A., Gheorghe, A., Hulea, O., & Schepens, P. (2006). Levels and distribution of organochlorine pesticides, polychlorinated biphenyls and polybrominated diphenyl ethers in sediments and biota from the Danube Delta, Romania. *Environmental Pollution*, *140*, 136–149.

Dsikowitzky, L., Schwarzbauer, J., & Littke, R. (2002). Distribution of polycyclic musks in water and sediments of the Lippe River (Germany). *Organic Geochemistry*, *33*, 1747–1758.

Evans, M. E., & Heller, F. (2003). *Environmental magnetism. Principles and applications of enviromagnetics. International Geophysics Series 86*. San Diego: Academic.

Evenset, A., Christensen, G. N., Caroll, J., Zaborska, A., Berger, U., Herzke, D., et al. (2007). Historical trends in persistent organic pollutants and metals recorded in sediment from Reservoir Ellasjøen, Bjørnøya, Norwegian Arctic. *Environmental Pollution*, *146*, 196–205.

Eyre, B., & McConchie, D. (1993). Implications of sedimentological studies for environmental pollution assessment and management: Examples from fluvial systems in North Queensland and Western Australia. *Sedimentary Geology*, *85*, 235–252.

Frignani, M., Bellucci, L. G., Favotto, M., & Albertazzi, S. (2005). Pollution historical trends as recorded by sediments at selected sites of the Venice Lagoon. *Environment International*, *31*, 1011–1022.

Götz, R., Bauer, O. H., Friesel, P., Herrmann, T., Jantzen, E., Kutzke, M., et al. (2007). Vertical profile of PCDD/Fs, dioxin-like PCBs, other PCBs, PAHs, chlorbenzenes, DDX, HCHs, organotin compounds and chlorinated ethers in dated sediment/soil cores from flood-plains of the river Elbe, Germany. *Chemosphere*, *67*, 592–603.

Heim, S., Schwarzbauer, J., Kronimus, A., Littke, R., Woda, C., & Mangini, A. (2004). Geochronology of anthropogenic pollutants in riparian wetland sediments of the Lippe River (Germany). *Organic Geochemistry*, *35*, 1409–1425.

Heim, S., Ricking, M., Schwarzbauer, J., & Littke, R. (2005). Halogenated compounds in a dated sediment core of the Teltow Canal, Berlin: Time related sediment contamination. *Chemosphere*, *61*, 1427–1438.

Heim, S., Hucke, A., Schwarzbauer, J., & Littke, R. (2006). Geochronology of anthropogenic contaminants in a dated sediment core of the Rhine River (Germany): Emission sources and risk assessment. *Acta Hydrochimica et Hydrobiologica*, *34*, 34–52.

Holoubek, I., Ansorgova, A., Kohoutek, J., Korinek, P., & Holoubkova, I. (2000). The regional background monitoring of POPs (PAHs, PCBs, OCPs) in the Czech Republic. *Organohalogen Compounds*, *46*, 387–390. ISSN 1026-4892.

Holoubek, I., Adamec, V., Bartoš, M., Černá, M., Čupr, P., Bláha, K., et al. (2003). Úvodní národní inventura persistentních organických polutantů v České republice. Projekt GF/CEH/01/003: Enabling activities to facilitate early action on the implementation of the Stockholm convention on persistent organic pollutants (POPs) in the Czech Republic. TOCOEN, s.r.o., Brno v zastoupení Konsorcia RECETOX—TOCOEN & Associates, TOCOEN REPORT No. 249, Brno, srpen. Internet: http://www.recetox.muni.cz/.

Holoubek, I., Klanova, J., Jarkovsky, J., Kubik, V., & Helesic, J. (2007). Trends in background levels of persistent organic pollutants at Kosetice observatory, Czech Republic. Part II. Aquatic and terrestrial environments 1996–2005. *Journal of Environmental Monitoring*, *9*, 564–571.

Hong, S. H., Yim, U. H., Shim, W. J., Oh, J. R., & Lee, I. S. (2003). Horizontal and vertical distribution of PCBs and chlorinated pesticides in sediments from Masan Bay, Korea. *Marine Pollution Bulletin*, *46*, 244–253.

Kim, Y. S., Eun, H., Katase, T., & Fujiwara, H. (2007). Vertical distributions of persistent organic pollutants (POPs) caused from organochlorine pesticides in a sediment core taken from Ariake Bay, Japan. *Chemosphere*, *67*, 456–463.

Konat, J., & Kowalewska, G. (2001). Polychlorinated biphenyls (PCBs) in sediments of the southern Baltic Sea—trends and fate. *The Science of the Total Environment*, *280*, 1–15.

Li, A., Rockne, K. J., Sturchio, N., Song, W., Ford, J. C., & Wie, H. (2009). PCBs in sediments of the Great Lakes—distribution and trends, homolog and chlorine patterns, and in situ degradation. *Environmental Pollution*, *157*, 141–147.

Lüder, B., Kirchner, G., Lücke, A., & Zolitschka, B. (2006). Palaeoenvironmental reconstructions based on geochemical parameters from annually laminated sediments of Sacrower See (northeastern Germany) since the 17th century. *Journal of Paleolimnology*, *35*, 897–912.

Navarro, A., Tauler, R., Lacorte, S., & Barceló, D. (2006). Chemometrical investigation of the presence and distribution of organochlorine and polyaromatic compounds in sediments of the Ebro River Basin. *Analytical and Bioanalytical Chemistry*, *385*, 1020–1030.

Pereira, W. E., Hostettler, F. D., Luoma, S. N., Geen, A., Fuller, C. H. C., & Anima, R. J. (1999). Sedimentary record of anthropogenic and biogenic polycyclic aromatic hydrocarbons in San Francisco Bay, California. *Marine Chemistry*, *64*, 99–113.

Sapozhnikova, Y., Bawardi, O., & Schlenk, D. (2004). Pesticides and PCBs in sediments and fish from the Salton Sea, California, USA. *Chemosphere*, *55*, 797–809.

Strandberg, B. O., van Bavel, B., Rergqvist, R.-A., Broman, D., Ishaq, R., Näf, C., et al. (1998). Occurrence, sedimentation and spatial variations of organochlorine contaminants in settling particulate matter and sediments in the northern part of the Baltic Sea. *Environmental Science & Technology*, *32*, 1754–1759.

Svoboda, J. (Ed.) (1963). Geological map of ČSSR. Sheet M-33-XXIII Česká Třebová, scale 1:200,000. ÚÚG Praha.

Svobodova, Z., Zlabek, V., Randak, T., Machova, J., Kolarova, J., Hajslova, J., et al. (2003). Profiles of persistent organic pollutants (POPs) in tissues of marketable common carp and in bottom sediments of selected ponds of South and West Bohemia. *Acta Veterinaria Brno*, *72*, 295–309.

Tucker, M. E. (1988). *Techniques in sedimentology*. Oxford: Blackwell. 408 pp.

Tucker, M. E. (2003). *Sedimentary rocks in the field* (3rd ed., p. 234). Chichester: Wiley. ISBN 0-470-85123-6.

Yamashita, N., Kannan, K., Imagawa, T., Villeneuve, D. I., Hashimoto, S., Miyazaki, A., et al. (2000). Vertical profile of polychlorinated dibenzo-p-dioxins, dibenzofurans, nephtalenes, biphenyls, polycyclic aromatic hydrocarbons, and alkylphenols in a sediment sore from Tokyo Bay, Japan. *Environmental Science & Technology*, *34*, 3560–3567.

Yunker, M. B., Macdonald, R. W., Goyette, D., Paton, D. W., Fowler, B. R., Sullivan, D., et al. (1999). Natural and anthropogenic inputs of hydrocarbons to Strait of Georgia. *Science of the Total Environment*, *225*, 191–209.

Yunker, M. B., Macdonald, R. W., Vingarzan, R., Mitchell, H., Goyette, D., & Sylvestre, S. (2002). PAHs in the Fraser River basin: A critical appraisal of PAH ratios as indicators of PAH. *Organic Geochemistry*, *33*, 489–515.

Zennegg, M., Kohler, M., Hartmann, P. C., Sturm, M., Gujer, E., Schmid, P., et al. (2007). The historical record of PCB and PCDD/F deposition at Greifensee, a lake of the Swiss plateau, between 1848 and 1999. *Chemosphere*, *67*, 1754–1761.